TECHNISCHE UNIVERSITÄT WIEN

Dissertation

Tracker performance studies at the 100 TeV future circular hadron collider at extreme pile-up conditions

Ausgeführt zum Zwecke der Erlangung des akademischen Grades einer Doktorin der technischen Wissenschaften

unter der Leitung von

Univ.Prof. Dipl.-Phys. Dr.rer.nat. **Jochen Schieck**

Institut für Hochenergiephysik
der Österreichischen Akademie der Wissenschaften (ÖAW)

eingereicht an der Technischen Universität Wien
Fakultät für Physik

von

Dipl.-Ing. **Julia Stefanie Hrdinka**, BSc

Matr.Nr.: 1025644
Schwarzenhornstraße 10,
6822 Satteins

Wien, am 20.08.2019

Kurzfassung

Das rechnergestützte Finden der Spuren von geladenen Teilchen, mithilfe des Spurendetektors eines Hochenergiephysikexperiments, ist der anspruchsvollste Teil der Rekonstruktion der Produkte einer Teilchenkollision an einem Beschleuniger. Die Spurrekonstruktion wird besonders anspruchsvoll, wenn mehrere Teilchenpaare innerhalb einer Ereignisspanne kollidieren (*Pile-up*). Das ATLAS experiment am LHC (*Large Hadron Collider*) plant einen Umbau des Detektors (*Phase-II upgrade*), um den neuen experimentellen Bedingungen der nächsten LHC phase (*Run3*) zu genügen. In dieser Phase werden durchschnittlich, anstatt der momentan ungefähr 40, 200 gleichzeitige Kollisionen pro Ereignis erwartet. Daher müssen sowohl der Spurendetektor, als auch die Software zur Rekonstruktion verbessert und erneuert werden.
Zusätzlich werden momentan experimentelle Möglichkeiten für die Zeit nach dem LHC im Rahmen der sogennanten FCC (Future Circular Collider) Design Studie untersucht. Für einen zukünftigen Proton-Proton Teilchenbeschleuniger (*FCC-hh*), mit einer Schwerpunktsenergie von 100 TeV, wird durchschnittlich sogar ein Pile-up von 1000 erwartet. Die Software für Detektorsimulation und Teilchenrekonstrution dieser anspruchsvolleren zukünftigen Experimente soll von der bisherigen Erfahrung und den laufenden Verbesserungen für die LHC-Experimente profitieren. Neben dem extrem erhöhten Pile-up, ist die Auflösung sehr naher Teilchenspuren in hochenergetischen Teilchenjets eine der größten Herausforderungen für die Spurrekonstruktion.
Diese Arbeit wurde im Rahmen der FCC Machbarkeitstudie durchgeführt. Im ersten Abschnitt wird die Entwicklung von Software-Komponenten für Simulation und Teilchenspurrekonstruktion vorgestellt. Wesentlich war dabei die Verwendung moderner Programmiertechniken und die Ausnützung von Parallelisierung. Gleichzeitig sollte die optimale Ausnutzung der experimentellen Möglichkeiten, mit Einbeziehung von Pile-up, gewährleistet sein. Die Software-Suite wurde wesentlich erweitert, um Studien zur Leistung des Spurendetektors zu ermöglichen.
Im zweiten Teil der Arbeit wurden diese Software-Komponenten verwendet, um die Leistung des Teilchenspurdetektors unter den anspruchvollen experimentellen Bedingungen des FCC-hh zu untersuchen. In diesem Zusammenhang wurde die Auslastung der Auslesekanäle und die zu erwartenden Datenraten im Spurendetektor erfasst und die Auflösung von nahen Spuren innerhalb von Bottom-Quark-Jets untersucht. Weiters wurde das Potential um direkt einen WIMP (Weakly Interacting Massive Particle) dunklen Materie Kandidaten zu detektieren, welcher eine verschwindende Teilchenspur im Spurendetektor hinterlässt, abgeschätzt.

Abstract

In high energy physics collider experiments the finding and measurement of trajectories of charged particles in the innermost tracking detector is one of the most challenging aspects of event reconstruction. It is particularly strongly influenced by the presence of pile-up and becomes computationally challenging in such environments. The ATLAS experiment, at the LHC (Large Hadron Collider) is planing a large-scale upgrade (*Phase-II upgrade*) to handle the experimental conditions of the next run *Run3*, which includes a new inner tracking detector. To cope with the environment of up to 200 simultaneous proton-proton collision per bunch-crossing (*pile-up*) both, hardware and software components need to be significantly updated.
At the same time, post LHC circular collider possibilities are examined in the frame of the FCC (future circular collider) design study. For a future proton-proton collider (*FCC-hh*) with a center-of-mass-energy of 100 TeV, 1000 pile-up interactions are expected.
The main challenges for a FCC-hh scenario in terms track reconstruction are expected to be the resolution of close-by tracks in dense jet environments and dealing with the extreme pile-up conditions. Moreover, the complex experimental setup leads to demanding computational aspects in track reconstruction and simulation. At the beginning of the study, a FCC software suite was established, which should profit from the LHC legacy and ongoing research and development for the upcoming detector upgrades.
This work is embedded in the future circular collider study. The first part of this work describes the development of software components for simulation and modern track reconstruction for future scenarios. The usage of modern programming techniques, respecting the evolution of the computing hardware by exploiting parallel computing approaches, while aiming on optimizing the physics potential, in particular for high pile-up environments, was essential. The software suite was substantially extended to allow tracker performance studies.
The optimized and newly developed software was used to study the tracker performance and physics potential of the FCC-hh baseline tracker, considering the extreme pile-up conditions. These aspects have been studied by examining the expected channel occupancy and data rates as well as double track resolution in the core of b-quark particle jets. Finally the potential of directly detecting a possible WIMP (Weakly Interacting Massive Particle) dark matter candidate, with disappearing track signature, was assessed.

Acknowledgments

This work has only been possible with the help and support of many people, whom I would like to thank at this point.
Since I started at CERN as a master student and throughout my whole PhD, Andreas Salzburger has been my supervisor at CERN. Thank you Andi, for being a great mentor and guiding me not only through high energy physics and computing, but also always supporting me on a personal level.
I would like to express my very great appreciation to Jochen Schieck, for the support from Vienna, which made this experience possible for me.
Coralie Neubüser, you have not only been a good friend and colleague, but also a big mental support during my PhD. Thank you, for the encouragement during 'hot phase' and proof-reading my thesis.
Being part of the Acts-Software team is a memorable experience for me. I really appreciated being a member this dynamic team and I learned a lot for my future path.
I also would like to thank the FCC-hh detector team. Especially Werner Riegler for his support, Zbynek Drasal for his assistance during the FCC CDR-phase and the occupancy studies and Clement Helsens, for answering my numerous questions.
Being part of the ATLAS collaboration was a great pleasure for me. I am particularly grateful for the assistance given by Markus Elsing. I want to give my thanks to Anthony Morley, helping me with the, at first glance, seemingly impossible quest of finding disappearing tracks in the distant future. In this context, I also want to thank Masahiko Saito, for never getting tired of answering my questions. Noemi, thank you for always having an open door for me. Thanks to Robert for your personal advice and for thinking through many computational problems together. Elmar, Martin and Paul, thank you for your encouragement. Michael, thank you for being a great office mate and helping me with both, technical and organizational questions.
Since with finishing my PhD, also my active participation in the 'Mampf'-University will come to an end. I enjoyed our lunch and coffee breaks, which have been a welcome change to work.

Ich möchte meiner ganzen Familie für ihr Engagement und ihre Unterstützung danken. Vielen Dank liebe Eltern, dass ihr probiert habt, mir meine unzähligen Fragen zu beantworten und es mir erlaubt habt, neugierig zu bleiben und die Welt zu erkunden. Danke Mama, dass du mich zu einer selbständigen unabhängigen Frau erzogen hast und mich immer ermutigt hast weiter zu machen. Danke Papa, für dein großes Interesse an meiner Arbeit und die unzähligen Diskussionen über den Sinn und den Ursprung des Universums.

Patrick, danke dass du immer (zumindest mental) an meiner Seite warst, während dieser arbenteuerlichen aber zugegebenermaßen auch stressigen Zeit. Du bist der Fels, an dem ich mich immer anlehnen kann, vor allem wenn ich mich wieder zu viel "verkopf". Ich freue mich auf die gemeinsame Zukunft mit dir.

Finally, given even the marginal probability of our universe to exist, I also want to acknowledge the privilege to be born and living in this specific time and place in wealthy Europe, giving me the possibility to think about the origins of my existence.

Contents

Chapter 1

Introduction

Questions as "What are we made of?", "What is the origin and the fate of the universe?" and "What are the underlying principles of nature?" have always been a driving force for humans to study matter, beginning with macroscopic objects, to atoms down to the elementary building blocks of nature. Those particles are beyond observation by human senses, but with the technical advancements in the last century have become detectable. The establishment of particle accelerators allowed to observe and study particles and their interactions in detail and have guided the evolution of particle physics [1]. The findings of particle physics are currently embedded within the theory called the *Standard Model of particle physics (SM)* [2], describing fundamental matter particles and three out of four fundamental interactions.

Particle colliders accelerate charged particles within a vacuum pipe (the beampipe), using electromagnetic fields, close to the speed of light and either collide them with a fixed target or with another particle beam accelerated in opposed direction. At the collision point, the proton's constituents (quarks and gluons) may collide and produce a shower of new particles. Each of the constituents carries a small fraction of the total proton's energy. Following Einstein's well known equation $E = mc^2$ [3], the mass of newly produced particles can have significantly higher masses, than the particles they originate from. By studying these interactions, which resemble the conditions at the beginning of the universe, (the Big Bang [4]) and resulting particles, insight about matter and the origins and fate of the universe can be gained.

From their first implementation to now, particle accelerators have been fundamental to advance particle physics and the understanding of our universe. Particle colliders have proven to be not only from benefit in basic physics research, but to be useful instruments in many different fields, as for instance biology, chemistry, material sciences, industrial applications and medical applications [1, 5]. Furthermore, particle accelerators are driving forces in pushing technologies and knowledge in several fields to its limits, e.g. superconductor development for high-field magnets, cryogenic systems, radio-frequency applications, semi-conductor technologies, data processing and many more [6–8].

To detect particles being produced at a particle collider, a detector is placed at the *interaction point (IP)*. Particle identification and additional measurements are done, by determining the properties of products resulting from the collision, henceforth called the *final states*. Depending on the purpose of an experiment, different properties and particle types need to be measured and hence, various different implementations can exist.

The *Large Hadron Collider (LHC)* [9] is the world's most powerful particle collider, situated at the research center CERN [10], in Geneva (Switzerland). It collides two proton beams with a center-of-mass energy of 13 TeV (designed for at maximum 14 TeV), at four different interaction points. Each of those points hosts a particle detector constituting a particle physics experiment. Two experiments, namely ATLAS [11] and CMS [12], at the LHC are so called, *multi-purpose detectors*[1], while LHCb [13] and ALICE [14] are more specific experimental setups. A multi-purpose detector, is responsible for being able to measure many different particle signatures with

[1] Allows to test the SM for various predictions with high accuracy/precision.

a broad range of energy and different interactions types. Such a detector consists of different sub-systems. Each sub-system has a different main task and exploits a particular mechanism of particle interaction with the detector material to create a measurable signal. Closest to the beam-pipe the first sub-detector is the *tracking detector*, whose purpose is to determine the trajectory as well as the origin of the charged particles. When a magnetic field is present within the tracking volume, the trajectory allows to determine the momentum, the charge and the vertex of the produced particle. In most applications (as in ATLAS and CMS), the trajectory is not directly revealed by the detector. Instead the spatial position of the particle (hit) is determined at many different points by detector modules, which are usually arranged in layers around the beam pipe. Given all hits of an interaction, dedicated computer-based *track reconstruction* [15] algorithms, reconstruct the passage of each particle through the detector. Finding all points belonging to the same particle trajectory is a demanding task. It is done by applying pattern recognition techniques and fitting a curve to the space-points, found to belong to the same track. The detector systems responsible for measuring the energy of particles are *calorimeters*. The concept of calorimeters is to shower the particle within dense material and measure the energy the particle deposited, which allows to determine the particle's initial energy. Two different types are installed subsequently: one for electromagnetically interacting particles and one for hadronically interacting particles. Muons, which mainly interact through ionization penetrate the calorimeters and are detected in dedicated *muon tracking chambers*. Please see [16] for a more general introduction of particle interaction with matter and particle detectors, up-to-date information can be found in [17].

Just after the completion of the second run (*Run2*) [18] (2015-2018) of the Large Hadron Collider (LHC) [9, 19] at 13 TeV center-of-mass energy proton-proton collisions, we arrived at a compelling point in physics. With the discovery of the Higgs boson [20, 21], by the ATLAS [11] and CMS [12] collaborations during *Run1* (2010-2013) a new chapter began, allowing to study the boson's properties and the mechanism of electroweak symmetry breaking (EWSB) [22, 23]. By exceeding its luminosity[2] expectation by approximately 10 % during Run2, the experiments at the LHC collected a total integrated luminosity[3] of 189 fb^{-1} since its start [25, 26].

This allowed precision measurements of many properties of the standard model particles, including the masses of the W-boson [27], the top-quark [28] and the Higgs-boson [29]. Furthermore the the Higgs-Yukawa coupling[4] [30] could be established, by measuring the Higgs couplings to the heaviest third generation quarks [31–33] and leptons [34, 35].

Many Standard Model precision measurements are still missing. These include rare Higgs decays and production channels and the Higgs self-coupling, accessible via double-Higgs production. The latter gives insight to the shape of Higgs potential and Higgs vacuum stability, which - including only current Higgs and top-mass measurements and theoretical predictions - could be meta-stable [36]. Moreover both, theory and experimental observations, suggest, that the standard model has deficiencies and that there needs to be physics *Beyond the Standard Model (BSM)*, which complements or extends the standard model. These indications include that the standard model only describes three out of the four fundamental forces, missing the description of gravity. Furthermore, despite their experimental evidence, dark matter [37] as well neutrino oscillations [38] and the domination of matter over antimatter (baryogenesis) [4] are currently not described by the standard model.

To date, all LHC measurements so far are consistent with Standard Model predictions, comprising the Higgs boson as an elementary light scalar field, which does not require new physics at

[2] Quantifies the possible number of collisions per cm^2 and second (see [24]).
[3] The luminosity integrated over time.
[4] Coupling strength between Higgs field and fermions.

electroweak (EW) scale (~ 246 GeV). Theoretical constraints include, that EWSB was imposed and the mechanism as well as the Higgs mass are not predicted. In addition the Higgs-Yukawa couplings to fermions as well as the large variety in mass of the different hierachies of fermions, the so-called *flavour hiarchy* is not understood. Due to its scalar nature, the Higgs boson would feel quantum corrections through interaction with heavy virtual particles, proportional to the energy scale, leading to possible corrections far exceeding the Higgs mass itself, unless a dedicated fine tuning cancels for those effects [30]. This dilemma is generally referred to as the *hierarchy* or *naturalness problem* [39] and would expect new physics to enter at TeV-scale.

Many BSM theories try to address the deficiencies of the standard model by introducing new physics models. The *supersymmetric* extensions of the standard model (*SUSY*) [40] introduce a new space-time symmetry, giving each standard model particle a supersymmetric partner, with a spin difference of 1/2. SUSY models could not only solve the naturalness problem by automatic cancellation of the quantum corrections, but could also provide a dark matter candidate in the form of *WIMP's* (weakly interacting massive particles) (see chapter 6). *Composite Higgs* models [41], on the other hand solve the naturalness problem by assuming that the Higgs boson is of finite size and no elementary particle. According to theories the composite state would emerge from a new strongly-coupled sector, which is dynamically broken, triggering EWSB and a physical Higgs boson.

Whether any of those models is appropriate and what could be the solution to the current obstacles in particle physics needs to be answered by experiments, since theory can not give a definite answer. Despite intensive searches at the LHC, by looking for even small discrepancies from the SM predictions, no signs of physics beyond the standard model could be found so far [42, 43]. This means that at TeV-scale new physics is either absent or extremely hidden. As a consequence, if valid, SUSY must be broken in practice. In case of composite models, there needs to be a mass gap between the Higgs and the strong resonances.

The LHC is currently preparing for *Run3*, planned for 2021–2023 to collide protons at $\sqrt{s} = 14$ TeV and with doubled nominal luminosity of 2×10^{34} cm^{-2}s^{-1} to achieve a total integrated luminosity of 300 fb^{-1}. Since a continuation of operating the collider at the same luminosity would not give significant statistical enhancement (to halve statistical errors more than ten years would be required), Run3 will be followed by a major upgrade of both, the accelerator and the experiments (*Phase-II upgrade*) to the *High-luminosity LHC (HL-LHC)* [44, 45]. This new accelerator will stay at the same center-of-mass energy of 14 TeV but increase the nominal luminosity by a factor of $5-7$ in order to collect ten times more data and finally arrive at a total integrated luminosity of 3000 fb^{-1}. The HL-LHC is planned to maximize the LHC potential and to run from $2026-2035/40$, with potential detector upgrades similar to the current LHC-program.

The HL-LHC will allow to make direct and indirect searches for new physics, including observation of extremely rare events (e.g. extremely rare flavour transitions) or slight discrepancies of the SM parameters to predictions, indicating presence of new physics. For this purpose the HL-LHC allows to measure the Standard Model parameters with unprecedented precision. Moreover, it allows a significant improvement of the knowledge of the inner structure of the protons, contributing to improvement of connected uncertainties in measurements. Direct searches, apart from SUSY and Composite Higgs candidates include heavy right-handed sterile neutrinos, which are predicted by theories of the seesaw mechanism [46], attempting to solve the puzzle of observed neutrino masses and oscillations. With the improved precision, the HL-LHC can give a definite answer if there is new physics at the EW-scale and set constraints for higher scales, inaccessible to direct searches up to hundreds of TeV. Possible future colliders and experiments can then address the still open questions [47, 48].

A considerable potential, building on the LHC legacy, concerns collider projects in the context of the international *Future Circular Collider (FCC)* study [49]. A first series of conceptual design

reports (CDR) (see [50]) was delivered by the end of 2018, serving as input for the *european strategy for particle physics update (ESPPU)* 2019/2020. More comprehensive reports are planned to be finished within 2019. The study considers a staged research program, similar to the LEP-LHC program, starting with an electron-positron collider (*FCC-ee*) followed by a proton-proton collider (*FCC-hh*) and a possible intermediate step of an electron-proton collider (*FCC-eh*). The colliders would be subsequently installed within the same tunnel of approximately 100 km circumference, which allows to share technical and organizational infrastructure. The FCC-ee would operate for 15 years at multiple center-of-mass energies, beginning with $\sqrt{s} \sim 91$ GeV (Z-resonance), allowing to produce approximately 5×10^{12} Z-bosons, followed by $\sqrt{s} \sim 160$ GeV (production of $\sim 10^8$ WW-pairs), $\sqrt{s} \sim$ 240 GeV, producing more than 10^6 Higgs bosons and would finish with $\sqrt{s} \sim 350 - 365$ GeV (over 10^6 $t\bar{t}$-pairs). The FCC-hh collider would operate at 100 TeV center-of-mass energy and collect data with a total integrated luminosity of 20 ab^{-1} per main experiment (two main experiments planned), producing more than 10^{10} Higgs bosons. Similar to the current LHC, it would also allow for heavy-ion collisions, but at nearly eight times increased centre-of-mass energy, using lead ions at $\sqrt{s} = 39$ TeV. The FCC-eh is optional and would collide protons of 50 TeV with electrons of 60 GeV and could collect 2 ab^{-1} of data, resolving the parton structure of the proton with per mill accuracy. It would run concurrently with the FCC-hh, with an energy-recovery linac (ERL) providing the electron beam for a dedicated experiment. Both FCC-hh and FCC-eh could operate for 25 years.
These three complementary collider options maximize the physics potential, by exceeding both, the luminosity and energy frontier, allowing for measurements with a sensitivity orders of magnitude higher than today. The extraordinary precision of typically several orders of magnitude larger than anything before aims to study the SM model properties in great detail and allows to probe energy scales beyond direct reach. The FCC-program would allow to significantly improve the understanding of the Higgs boson, by measuring its properties in percent or sub-percent accuracy, as shown in fig. 1.1. The FCC-ee could determine the Higgs width in a model-independent manner from the process $e^+e^- \to ZH$ and achieve a first measurement of the Higgs self coupling to 32 % [51]. The FCC-hh program will complement the FCC-ee measurements, measuring even rare Higgs decays, as for instance $H \to \mu^+\mu^-$, $H \to Z\gamma$, $H \to 4\nu$, as well as decays to second generation fermions and an improvement of the Higgs self-coupling measurement, with precision of 5 – 7% [51].
Electroweak precision measurements can give hints to new physics, either through direct effects of heavier particles (e.g. heavy resonances W', Z', heavy sterile neutrios), which interfere or mix with the known SM particles or quantum corrections through loops. With its center-of-mass energy of 100 TeV, the FCC-hh enhances the mass reach to directly discover new particles by one order of magnitude. Many heavy particles are predicted by BSM theories, including heavy resonances, SUSY partners or dark matter candidates up to several tens of TeV [51].

For this document the FCC-hh scenario is considered and studied regarding track reconstruction capabilities and limitations. First, in chapter 2, an overview of the FCC-hh collider, the experimental conditions at $\sqrt{s} = 100$ TeV and a more detailed description of the FCC-hh baseline detector along with its expected performance is presented. Especially track reconstruction will be extremly challenging at FCC-hh and HL-LHC conditions, since the total number of measurements will increase by orders of magnitude compared to current LHC conditions. This requires highly efficient and fast track reconstruction software. At the beginning of this work a new software project (Acts, see section 3.2) had been launched to provide experiment independent, modular track reconstruction tools for the ATLAS phase-II upgrade [53] and FCC-hh. As part of the Acts software team and the FCC software (section 3.1) group, software tools and components have been developed in the context of this thesis, which are presented in chapter 3. Using

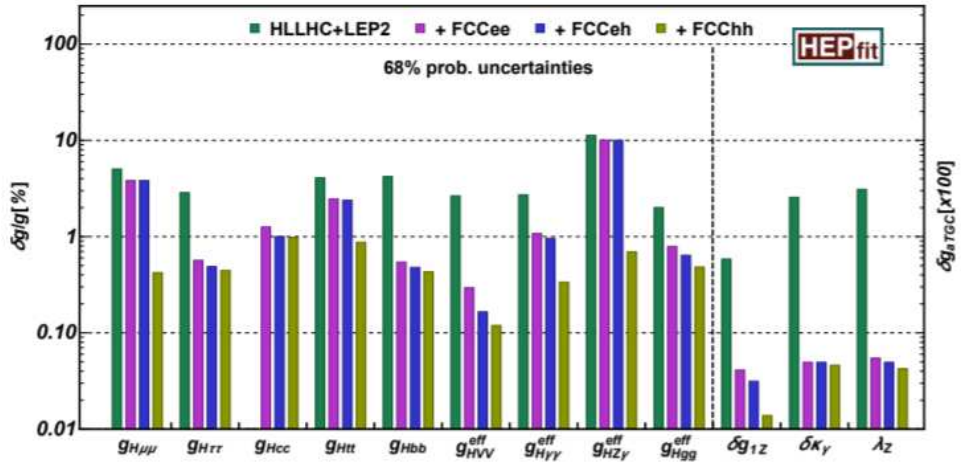

fig. 1.1: One-sigma precision reach at the FCC on the effective single Higgs couplings $g^{\text{eff}}_{\text{Hxx}} \equiv \Gamma_{\text{H}\to\text{X}}/\Gamma^{\text{SM}}_{\text{H}\to\text{X}}$ and anamolous Triple Gauge Couplings (aTGC) $\delta g_{1,\text{Z}}$, $\delta\kappa_\gamma$, λ_Z. An absolute precision in the EW measurements is assumed. The different bars illustrate the improvements that would be possible by combining each FCC stage/collider with the previous knowledge at that time (the precisions, not reported here, at each FCC stage/-collider considered individually would obviously be quite different). Note that, without a run above the $\text{t}\bar{\text{t}}\text{H}$ threshold, circular e^+e^- colliders alone do not directly constrain the g_{Hgg} and g_{Htt} couplings individually. The combination with LHC measurements however resolves this flat direction [52]. Source of figure: [52]

the established software tools, detector performance studies on the FCC-hh reference tracking detector (section 2.3) have been conducted, shortly introduced in the following.
The main challenges for track reconstruction at the FCC-hh scenario are the exceptionally high number of simultaneous proton-proton collisions per bunch-crossing (referred to as *pile-up* and *PU*) and the presence of highly collimated objects. The latter can result in spatially extremely close particle trajectories, putting constraints on separation of single measurements and hence on track reconstruction. This so-called *double track resolution* is studied, using B-Hadron jets in chapter 5. The pile-up is expected to be approximately a factor 25 higher than at current LHC conditions and a factor 5 higher than at HL-LHC. This special environment and the resulting expected channel occupancy and data rates are studied in detail in chapter 4.
FCC-hh gives a unique possibility to directly detect WIMP dark matter candidates in the form of SUSY charginos (bino-wino, higgsino) in the TeV-range. With lifetimes of 0.2 ns (bino-wino) and 0.023 ns (higgsino) [54] these charginos can reach the tracker and decay within the tracking detector into the lightest supersymmetric particle, the neutralino, which leaves the tracker undetected. To find this signature, one searches for disappearing tracks in the tracking detector. Since the transverse momentum of the chargino is very high, it will appear as a straight, short track. Hence, searching for this signature within the high pile-up environment resembles the search of a needle in a haystack. The dedicated study is presented in chapter 6.

Chapter 2

The FCC hadron collider and its baseline detector

To accelerate protons to 50 TeV at a collider with 100 km circumference, superconducting dipole magnets of an unprecedented field strength of 16 T are foreseen. This is double the strength used for the LHC. Similar to the LHC the already present infrastructure at CERN, consisting of *Linac4*, *PS Booster*, *PS* and *SPS* [55] can be used as an injector chain. Either LHC could be used as last acceleration step before the injection into FCC-hh, or, due to the high power consumption of the LHC cryogenics system, a dedicated booster could be installed within the FCC-hh tunnel. The energy stored per beam, will exceed the LHC value by a factor of twenty. For this high energy scenario, synchrotron radiation plays a major role, even for protons. It will be 200 times the value of LHC and together, both beams emit 5 MW of energy. Similar as for the LHC, *beamscreens* cooled to 50 K protect the machine from effects of the power of the synchrotron radiation. The initial luminosity for the first two years of operation is planned to be at $5 \times 10^{34}\,\mathrm{cm}^{-2}\mathrm{s}^{-1}$, which is the same level as planned for HL-LHC. The luminosity will then be raised to the nominal value of $3 \times 10^{35}\,\mathrm{cm}^{-2}\mathrm{s}^{-1}$, delivering an estimated integrated luminosity of $2\,\mathrm{fb}^{-1}$ during the initial phase and $8\,\mathrm{fb}^{-1}$ at the nominal level, per day. While the size of the luminous region will stay roughly the same with $\sigma_z = 49\,\mathrm{mm}$, assuming gaussian distribution along z, the total average number of simultaneous proton-proton collisions (denoted as $\langle\mu\rangle$), per bunch crossing (as for LHC every 25 ns) will be extremely raised compared to the current LHC runs. The initial phase value of $\langle\mu\rangle = 171$ is comparable to HL-LHC values but the value of more than $\langle\mu\rangle = 1000$ in the nominal phase is exceptionally high [52].

Figure 2.1 shows, that the mass reach of FCC-hh is highly extended and possible BSM particles up to tens of TeV can be produced in the central region, while known SM processes (with relatively low mass compared to 100 TeV) can also be produced in the very forward region. The kinematical coverage of the FCC-hh compared to the LHC is depicted, showing x, the fraction of momentum of the colliding parton (quark or gluon) with respect to the proton versus M_X, the invariant mass of the produced final states, with constant dashed lines of rapidity y. The plot also shows, that knowledge of the parton distribution functions (PDFs) in a wide kinematical range is required [56].

The FCC-hh will not only allow to discover potential new physics at higher energy scale, but grant to measure SM properties with exceptional precision. For the different measurements, the cross sections need to be known to estimate possible backgrounds. In fig. 2.2 the cross sections for SM processes (left) in dependence of the hadron collider center-of-mass energy $\sqrt{s}$, for the LHC $\sqrt{s} = 14\,\mathrm{TeV}$ and HE-LHC $\sqrt{s} = 28\,\mathrm{TeV}$ scenario, and up to $\sqrt{s} = 100\,\mathrm{TeV}$ are shown. The total (111 mbarn to 153 mbarn) and inelastic (85 mbarn to 108 mbarn) cross section only raise slightly from LHC to FCC-hh, while the cross section for several standard model processes increase more strongly, especially jet and top-quark production. Most of the Higgs production processes are raised by an order of magnitude. The production of a Higgs boson from a pair of top quarks $t\bar{t}H$, is even increased by two orders of magnitude, which allows to study the

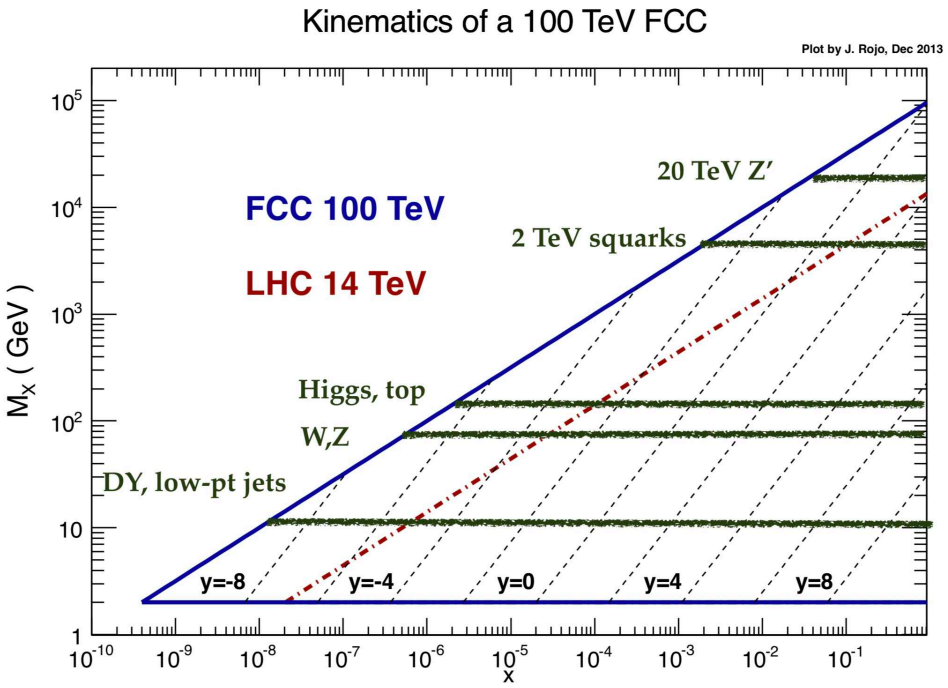

fig. 2.1: Kinematical coverage in the (x, M_X) plane of a $\sqrt{s} = 100\,\text{TeV}$ hadron collider (solid blue line), compared to the corresponding coverage of the LHC at $\sqrt{s} = 14\,\text{TeV}$ (dot-dashed red line). With M_x being the invariant mass of the produced final states and x being the fraction of momentum of the parton with respect to the hadron. The dotted lines indicate regions of constant rapidity y at the FCC. Relevant M_X regions for phenomenologically important processes, from low masses (Drell-Yan, low p_T jets), electroweak scale processes (Higgs, W, Z, top), and possible new high-mass particles (squarks, Z') are indicated. Source of figure: [56]

Higgs-top couplings in further detail. The same applies for double Higgs production, which will become accessible at 100 TeV and can give inside to the shape of the Higgs potential.
For the FCC-hh collider two interaction regions surrounded by general purpose detectors are foreseen. For the conceptual design report phase, a baseline detector (depicted in fig. 2.3 and fig. 2.4) has been designed to allow to study its projected performance, physics potential and to identify possible problems which need dedicated research and development. At this early stage, the baseline design does not incorporate any definite choices for the final design. Assuming a continuation of the trend of the recent decades, significant technology advancements can be expected. The detector design is oriented on the LHC detectors and their upgrades, which represent most recent particle detector developments. In addition, the collision environment has to be taken into account and the detector has to be able to measure specified physics benchmark processes. Particles with small masses compared to 100 TeV (e.g. SM particles) will have significant boost towards the forward region. For instance the jets accompanying vector boson fusion (VBF) production of the Higgs boson peak at $|\eta| = 4.4$ and 90 % are included within $|\eta| = 6$, while at LHC the peak is at $|\eta| = 3.4$ and can reach values up to $|\eta| = 5$. Therefore the detector needs to hermetically cover a region up to $|\eta| = 6$. To be sensitive to both, the known standard model processes in the GeV–range and possible new physics beyond the standard model in the TeV–region, the measurement precision needs to be significantly increased. At the same time, the future experiment should stay sensitive to known SM processes. This

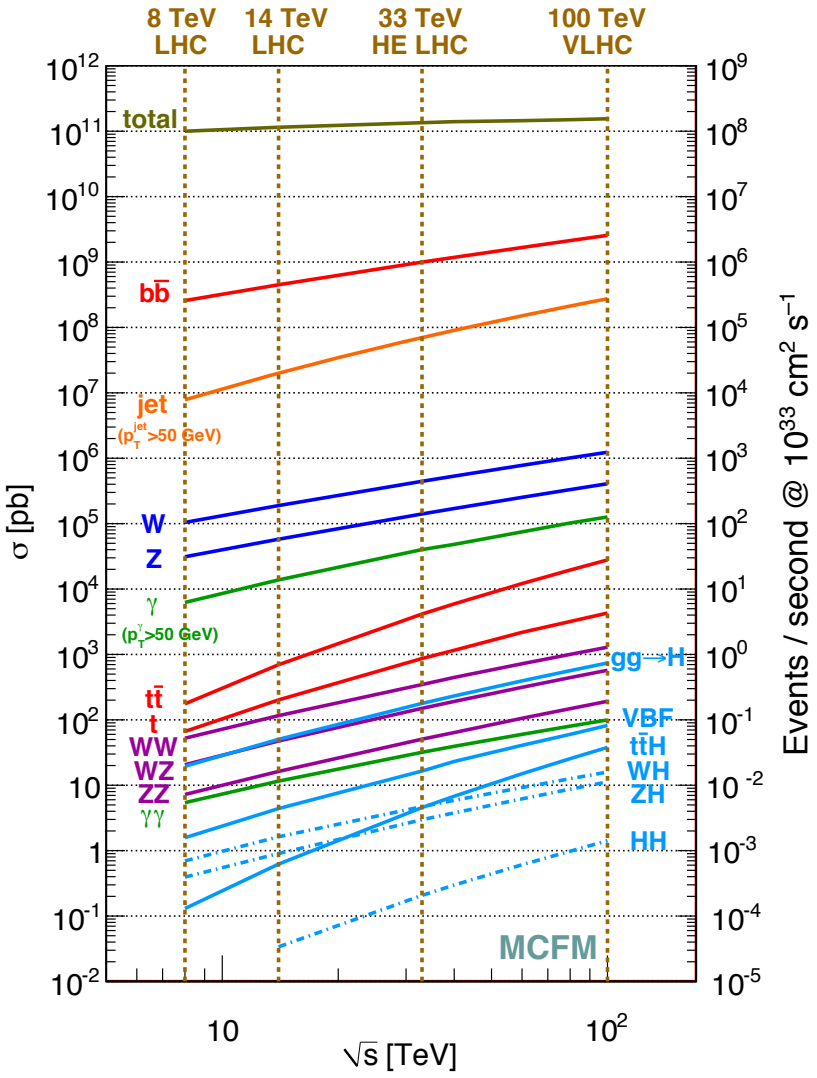

fig. 2.2: Standard Model process cross sections at hadron colliders as a function of centre-of-mass energy ($\sqrt{s}$) and Higgs-boson production cross sections as a function of centre-of-mass energies (light blue). The axis on the right, shows the corresponding number of expected events per second. Source of figure: [52].

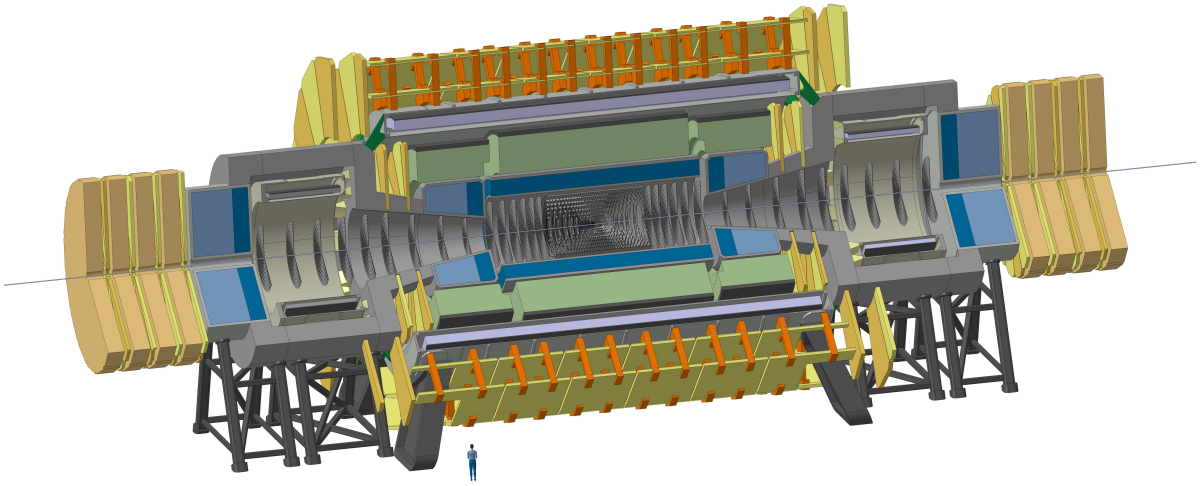

fig. 2.3: The FCC-hh reference detector with 20 m radial extension and 50 m length, hermetically covering the beam-pipe in the center and consisting of the different sub-systems: the tracker (grey) is the detector next to the beam-pipe, followed by the electromagnetic (blue) and hadronic calorimeters (green), surrounded by a 4 T solenoid (metallic) with a bore of 10 m in diameter. The muon system (yellow/orange) is placed outside the magnets. Source of figure: [52].

means that similar p_T and energy thresholds need to be kept for triggering at values comparable to LHC [52].

The size of the baseline detector, with a diameter of 20 m and a length of 50 m, is similar to current ATLAS dimensions. Due to the expected highly boosted objects, the detector consists of a central and a displaced forward part. The beam-pipe is cylindrical, with a radial extension of 20 mm, within a distance of 8 m in z from the interaction point. Thereafter, the beam-pipe shape is foreseen to transition into a conical shape around $\mid \eta \mid = 6.7$ projecting towards the IP with an angle of 2.5 mrad. The central 4 T magnetic field, described in more detail in section 2.2, is provided by a solenoid with a bore of 10 m in diameter. The tracking detector (section section 2.3) and the calorimeters (section 2.5) are placed within the bore. The calorimeters ensure 98 % of containment, in order to limit punch-trough to the muon system, further described in section 2.6 [52].

2.1 The radiation environment

The produced number of tracks is not increased strongly when going from $\sqrt{s} = 14$ TeV ($dN/d\eta \mid_{\eta=0} = 6$) to $\sqrt{s} = 100$ TeV ($dN/d\eta \mid_{\eta=0} = 10$) [57]. However, the increased collision rate with a peak of 31 GHz, compared to 0.8 GHz at LHC and 4 GHz at HL-LHC, together with the increased luminosity raises the radiation in the experimental cavern significantly compared to the LHC and HL-LHC [52]. As explained in the introduction of this chapter the concept of particle detection is based on the interaction of particles with the detector material. Hereby, the particle can interact with the electron shell (e.g. ioniziation, see appendix A.4.1) of the detector material, which is usually used for particle detection and does not lead to permanent effects. Interaction with the lattice atoms, as for instance displacing them, can lead to defects in the sensor and the readout electronics and significantly change the detection quality. According to the *NIEL hypothesis* [58] the radiation damage is linear proportional to the non-ionizing

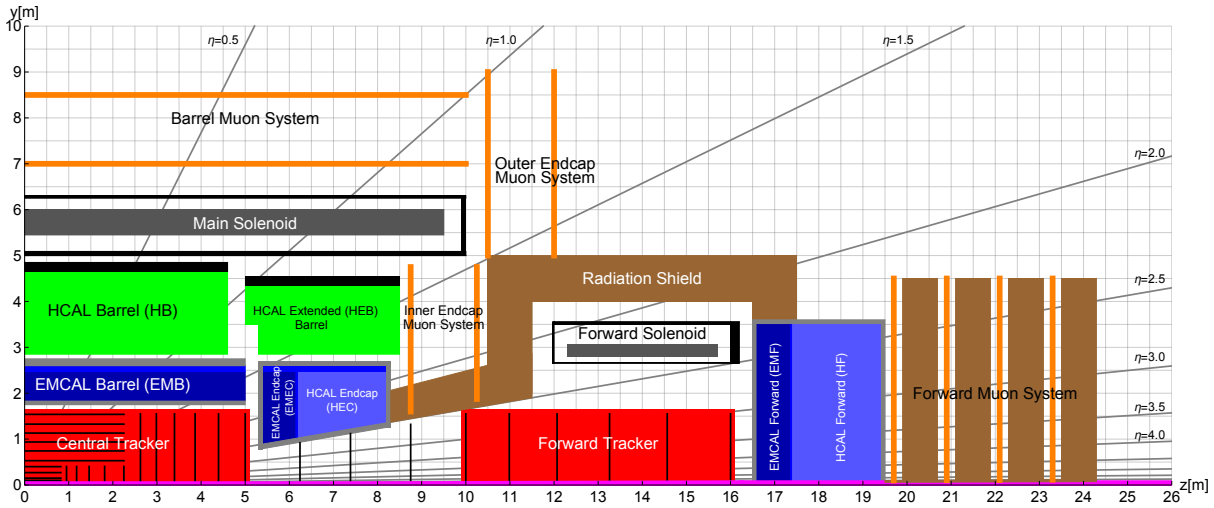

fig. 2.4: The cross section of the FCC-hh reference detector design showing the y coordinate versus z, consisting of the different detector-subsystems, magnetic coils and shieldin is shown. Only the first quadrant of the detector is shown. Source if figure: [52].

energy loss. The long term damage of silicon sensors is usually expressed in a particle fluence (number of particles per surface) commonly normalized to 1 MeV neutron equivalence. The calculation of the quantity is as follows: $N_0 \frac{dN}{d\eta} \frac{1}{2r^2\pi}$, with N_0 being the total number of collisions, with the value of 3.2×10^{18} for the possible integrated luminosity of $30\,ab^{-1}$ (no assumptions on replacement of detector components made). For the FCC-hh tracking detector, the value of this key quantity amounts to its maximum value of $5-8 \times 10^{17}\,cm^{-2}$ at the layer closest to the beam-pipe ($r = 25\,mm$), which is one order of magnitude higher than the expected value at experiments at the HL-LHC and even two orders of magnitude higher than at the current LHC detectors. From 40 cm distance to the beam-pipe outwards, the value is at maximum at the expected HL-LHC values or lower, which means that the same technologies as developed for the HL-LHC (RD53 collaboration [59, 60]) can be used in that case. However, for the innermost tracker region as well as for the innermost part of the forward calorimeters, where extreme values of even $5 \times 10^{18} cm^{-2}$ are reached, a dedicated research and development program has to be put in place to develop radiation hard detector technologies. Those include trends in electronics development as e.g. fibre optic links and wireless technologies, which allow data processing and controlling outside the radiation zones and thin CMOS technology [52].

2.2 The magnetic field

Applying a magnetic field within the tracking volume allows to determine the transverse momentum of a particle, by measuring the track *Sagitta*. If the magnetic field points into longitudinal direction (along the beamline), the particles are bend in transverse plane due to the Lorentz force [61]. By determining the Sagitta, denoted as s in fig. 2.5, via measuring at least three points along the particle trajectory, the particle's transverse momentum can be determined. The Sagitta of the trajectory can be calculated the following:

$$s = r - r\cos\frac{\varphi}{2} = r(1-\cos\frac{\varphi}{2}) \tag{2.1}$$

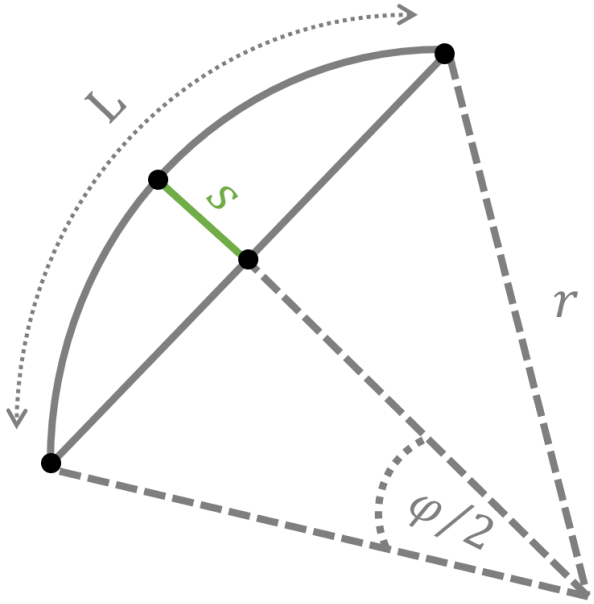

fig. 2.5: Display of the sagitta method to determine the momentum of a particle by measuring the Sagitta s to the particle trajectory.

Using taylor expansion for small φ, the following identity can be obtained

$$1 - \cos\frac{\varphi}{2} \approx 1 - (1 - \frac{1}{2}\frac{\varphi^2}{4}) = \frac{r\varphi^2}{8} \quad \text{for} \quad \varphi \ll 1 \tag{2.2}$$

with $\varphi \approx \frac{L}{r}$ (for small φ) the Sagitta can be written as

$$s = \frac{L^2}{8r} \tag{2.3}$$

and can be related to the momentum by using eq. (4.3)

$$s[m] = \frac{0.3B[T]L^2[m^2]}{8p_T[\frac{GeV}{c}]} \tag{2.4}$$

For the FCC-hh-case the whole central tracking region (and also the calorimeters) are surrounded by a solenoid, which provides an axial magnetic field of 4 T. For the solenoid the same superconducting material as used for the current ATLAS and CMS experiments, which are Al stabilized Nb – Ti/Cu Rutherford cables, is foreseen. The superconducters need to be cooled with He to 4.5 K. For the forward region, two smaller solenoids are foreseen. Alternatively two dipoles (similar to ALICE and LHCb) with a magnetic field integral of 4 Tm are studied, which would be beneficial for tracking performance in the high pseudo-rapidity region. This model however would mean, that rotational symmetry is lost and a compensation system for the hadron beam would be required. There is no shielding of the magnetic field inside the detector cavern foreseen, due to its size and high cost, which is unique to the FCC-hh magnetic field implementation. Hence, services inside the cavern need to be adjusted to the higher stray field. For the service cavern (66 – 96 m away from detector cavern), the expected stray field is less than 5 mT [52]. The FCC-hh magnetic field map can be seen in fig. 3.32.

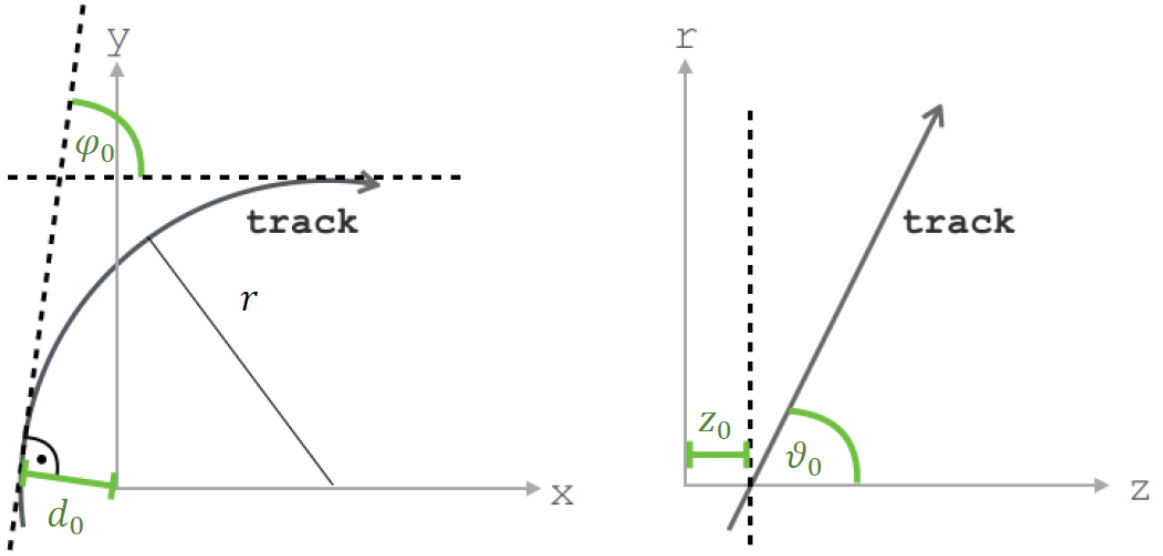

fig. 2.6: Definition of the track parameters. On the left side, the track (grey) is shown in transverse plane, of which the curvature, d_0 and φ_0 can be determined. To the right, the track is shown in r/z-plane which is approximately straight and defines z_0 and ϑ_0.

2.3 Baseline tracker

The tracking detector needs to provide high precision momentum measurement, vertexing and flavour tagging ability for b-, c- and τ-jets.
For this purpose the trajectory of all final states need to be reconstructed from the signals measured by the tracker. A trajectory can be described by five distinct parameters, referred to as the *track parametrization*. This parametrization can slightly vary for different experiments, for the FCC-hh case, the following parameters, illustrated in fig. 2.6, have been chosen:

- φ - azimuthal angle of the direction of the momentum
- ϑ - polar angle of the direction of the momentum
- $\frac{q}{p_T}$ - charge over transverse momentum, describing the curvature, bending direction and momentum in transverse plane
- d_0 - transverse impact parameter
- z_0 - longitudinal impact parameter

Since for the FCC-hh-scenario, the produced particle momenta can reach tens of TeVs (see fig. 2.1), a relative momentum resolution $\delta p_T/p_T = 10 - 20\,\%$ at $p_T = 10\,\text{TeV/c}$ was set as a requirement. For ATLAS and CMS, the requirement for high momenta was 10 % at $p_T = 1\,\text{TeV/c}$. At the same time, the tracking needs to remain sensitive to lower momenta in the GeV/c-range, expanding the sensitive momentum range over four orders of magnitude. Due to the expected presence of highly boosted objects at 100 TeV, an extension of precise tracking up to $|\eta| = 4$ and general tracking capability to $|\eta| = 6$ (ATLAS and CMS Phase-II upgrades require $|\eta| = 4$) is foreseen. Caused by the expected forward boost and the production of objects with high momentum, highly collimated jets (see section 5.2, for jet definition) are expected (please see section 5.4 for further information), with very small separation of the individual

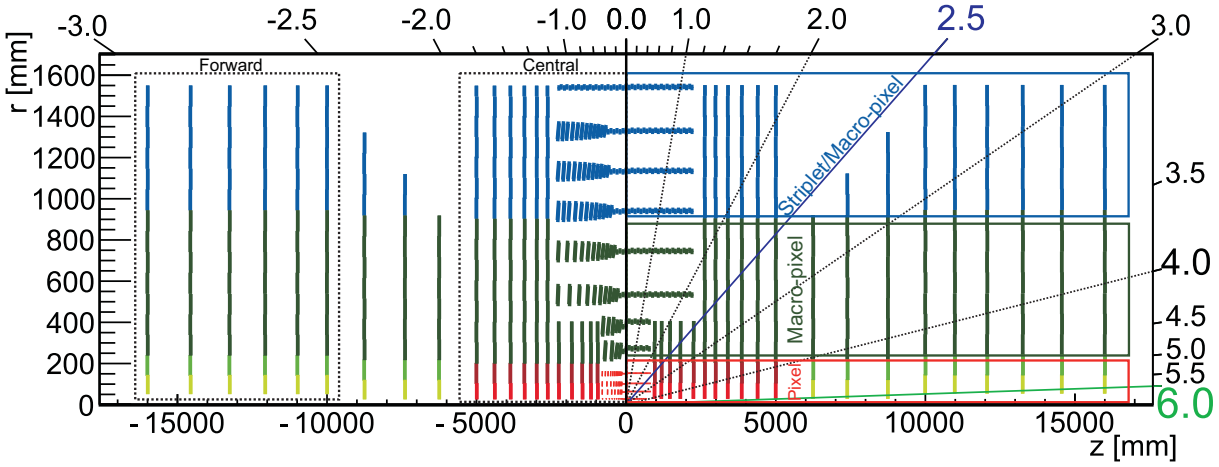

fig. 2.7: The detector modules of the FCC-hh Tracker in r/z-cross section. The tracker consists of a central, a transition and a forward region. The detector modules use silicon technology and are segmented with different granularities into pixel, macro-pixel and striplet modules. The figure is split into two halves, where the right side shows the flat and the left side the tilted layout. The dotted lines show the pseudo-rapidity coverage at different points. Figure by Z. Drasal [52, 62, 63].

tracks within the jet. This so called double track resolution is a driving factor in constraining the detector granularity. In addition the high pile-environment plays a crucial role, which is a factor 25 more than at LHC and 5 times more than at HL-LHC, with an expected line pile-up density of $8.1\,\mathrm{mm}^{-1}$ along the z-axis [52].

The tracking volume, confined by the volume of the electromagnetic calorimeter, extends from the beampipe ($r > 20.8\,\mathrm{mm}$) to 1.6 m in radial direction and up to 16 m in longitudinal direction. It consists of three different parts: *central*, *intermediate* and *forward* tracker. The central tracking region is similar to the ATLAS and CMS Phase-II upgrade plans and covers a pseudorapidity region of $|\eta| \leq 2.5$. The intermediate region serves as a connector between the forward and the central region, providing extra measurements. While the forward tracker allows tracking up to $|\eta| \approx 6$ and resembles the forward regions of LHCb.

Two slightly different realisations of the FCC-hh baseline tracker model exist, which are shown in fig. 2.7. To the left the *tilted* layout, following the example of the current ATLAS and CMS Phase-II upgrade is shown, while to the right, a more traditional *flat* approach, as currently implemented at the LHC experiments, can be seen. The tilted model, inclines the detector modules in the z-plane to be normal to an ideal particle coming from the center of the tracker. In this way the passed material and hence the effect of multiple scattering is reduced, while the number of measurements is kept high. To reduce difficulty of installation, 2 – 3 modules share the same tilt. The flat model has a total active silicon surface of $430\,\mathrm{mm}^2$ (tilted $\sim 10\,\%$ less), which is an increase of 72 % compared to the ATLAS and CMS Phase-II upgrades. The detector modules are arranged to hermetically cover the luminous region and have small overlaps ($\sim 1\,\mathrm{mm}$) to account for possible alignment in the future [52, 62, 63].

Assuming constant magnetic field along z and equidistantly positioned tracker layers in transverse plane, the transverse momentum resolution $\delta p_T/p_T\,[\mathrm{GeV/c}]$ can be obtained from the Sagitta (see eq. (2.4)) resolution. The sagitta uncertainty can be split into two parts: a constant part given by the intrinsic resolution of the measurement and a part from multiple scattering. Describing

those parts with constants a and b leads to the general form of the momentum resolution in dependence of p_T and ϑ or η:

$$\frac{\delta p_T}{p_T} = a\ p_T \oplus \frac{b}{\sin^{\frac{1}{2}}\vartheta} = a\ p_T \oplus b\ \cosh^{\frac{1}{2}}\eta \quad \text{see (49) in [64]} \tag{2.5}$$

The constant term is determined by $N+1$ measurements and their uncertainty in r/φ-direction $\sigma_{r\varphi}$ [m] following the gluckstern formula [65]

$$\frac{\delta p_T}{p_T}\ |_{Res} = \frac{\delta s}{s} = \frac{\sigma_{r\varphi}\ |\ p_T\ |}{0.3BL^2}\sqrt{\frac{720}{N+5}} \quad \text{see (46) in [64]} \tag{2.6}$$

The multiple scattering part can be approximated the following

$$\frac{\delta p_T}{p_T}\ |_{MS} = \frac{0.0136\,\text{GeV/c}}{0.3\beta BL}\sqrt{\frac{x_{tot}}{X_0 \sin\vartheta}} \quad \text{see (48) in [64]}$$

with the thickness in radiation length x_{tot}/X_0 and the relativistic factor $\beta = v/c$. In total 12 barrel layers are situated in the central tracker, with distances similar to the CMS upgrade tracker. This allows 12 measurements in the central region. There is a large increase of the number of measurements in the forward region. While an increase of the number of measurements increases the momentum precision $\propto 1/\sqrt{N}$, more passed material lead to a deflection of the particle $\propto \sqrt{x/X_0}$ (see appendix A.4.4) (due to multiple scattering) and hence decrease of resolution. The formula shows, that there is a direct dependence of the transverse momentum resolution on the lateral granularity. To fulfill the requirement of $\delta p_T/p_T = 20\%$ at $p_T = 10\,\text{TeV/c}$, a lateral resolution of $\sim 9\,\mu\text{m}$ is necessary. In addition, a good d_0-resolution is needed to identify displaced vertices for tagging jets. The d0-resolution can be estimated the following:

$$\delta d_0\ |_{Res+MS} \approx a_{Res} \oplus \frac{b_{MS}\cosh\eta^{1/2}}{p_T} \quad \text{see (64) in [64]} \tag{2.7}$$

The first part a_{Res} is a constant term, depending on the detector geometry and granularity and since the determination of the impact parameters d_0 and also z_0, mainly depends on the first two measurement planes, it can be analytically estimated:

$$a_{res} = \frac{r_1\sigma_2 \oplus r_2\sigma_1}{r_2 - r_1} \quad [66] \tag{2.8}$$

The second part of eq. (2.7), is due to multiple scattering and depends on the passed material of the beampipe $\frac{t_{BP}}{X_{PB}}$ and the first layer $\frac{t_0}{X_0}$ in thickness of radiation length:

$$b_{MS} = \left(\frac{13.6\text{MeV/c}^2}{\beta p_T}\right)^2 \left(\frac{t_{BP}}{X_{PB}} + \frac{t_0}{X_0}\right) r_0^2 \quad [63, 64] \quad \text{for } r_0 << L \tag{2.9}$$

with r_0 being the radius of the innermost layer. The above term depends on the inverse transverse momentum, therefore at high p_T the first term is dominant, while at low p_T the second term plays a major role.
Other important criteria to define the granularity in r/φ (lateral) and z/r (longitudinal) direction include the general goal of keeping the channel occupancy below 1 % and to allow the separation of two close-by tracks within a jet (double-track resolution). The granularity in longitudinal direction is mainly needed to reconstruct the primary vertex and to distinguish it from the

pile-up vertices. Hence, the impact parameter resolution needs to be optimized, which can be expressed the following:

$$\delta z \,|_{\mathrm{Res+MS}} \approx a_{\mathrm{Res}} \oplus \frac{b_{\mathrm{MS}} \cosh^{\frac{3}{2}} \eta}{p_T} \text{ [64]} \tag{2.10}$$

The passed material generally increases with η and degrades the z_0-resolution. The reference tracker has three different granularity regions: *pixel*, *macro-pixel* and *striplet*. Based on above calculations the pitch sizes (p) for the reference flat and tilted layout have been chosen and are listed in table 2.1.

Flat layout:		
Pixels (inner)	**Macro-pixels (middle)**	**Striplets/Macro-pixels (outer)**
$25 \times 50\,\mu m^2$ (1–4th BRL)	$33.3 \times 400\,\mu m^2$	$33.3\,\mu m \times 50\,mm$ (BRL)
$25 \times 50\,\mu m^2$ (1st EC ring)		$33.3\,\mu m \times 10\,mm$ (EC)
$33.3 \times 100\,\mu m^2$ (2nd EC ring)		
$33.3 \times 400\,\mu m^2$ (3–4th EC ring)		
Tilted layout:		
$25 \times 50\,\mu m^2$ (1–4th BRL)	$33.3 \times 400\,\mu m^2$	$33.3\,\mu m \times 1.75\,mm$ (BRL)
$25 \times 50\,\mu m^2$ (1st EC ring)		$33.3\,\mu m \times 1.75\,mm$ (EC)
$33.3 \times 100\,\mu m^2$ (2nd EC ring)		$33.3\,\mu m \times 50\,mm$ (12th BRL layer)
$33.3 \times 400\,\mu m^2$ (3–4th EC ring)		

tab. 2.1: Summary of spatial dimensions (pitch sizes, p) of detector readout cells, as optimized for different categories of sensors: inner vertex detector, middle and outer tracker. The granularity for both tracker layouts are shown: *flat* (top) and *tilted* layout (bottom) [63].

When assuming binary readout the intrinsic point position resolution (neglecting all effects of digitization and clusterization, i.e. cluster size and charge sharing) is $p/\sqrt{12}$ and hence $\sim$ 7.5 µm for the innermost layers and $\sim$ 9.5 µm for the following layers in r/φ-direction [52, 62, 63]. The expected transverse momentum and impact parameter resolutions for the FCC-hh reference tracker are shown in fig. 2.8. Except for a slight degradation due to the transition from barrel to end-cap, the relative transverse momentum resolution $\delta p_T/p_T$ stays low and roughly constant in the region of $0 < |\eta| < 1.9$. In the transition-region between the central and forward part $1.9 < |\eta| < 2.5$, the resolution is up-to 4 times worse than before. In the forward region the resolution is re-established within $2.5 < |\eta| < 3.1$ to degrade for higher η-values. Both impact parameter resolutions degrade with increasing η, since more material is crossed. This effect is particularly strong for the z_0-resolution [52, 62, 63].

The detector technologies are currently undefined and also simple extrapolation from Phase-II upgrade plans is not possibe, due to the high radiation environment. Since the detector material strongly depends on the specific detector technology choice, a very approximate model has been used for the material. This has to be taken into account, in a next design phase, as soon as the technology choices are more concrete. The module material was assumed to be homogeneous along the plane of the module and sandwich-like in thickness, with the following composition:

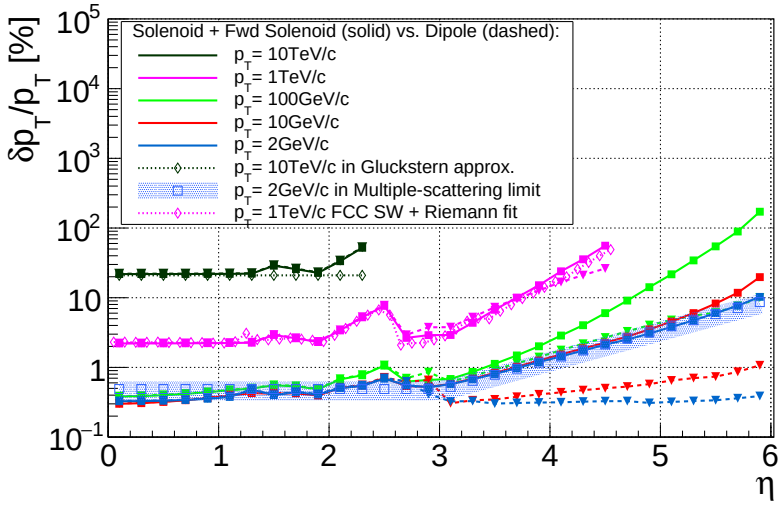

(a) Track $\delta p_T/p_T$ in two scenarios: reference central + forward solenoid (solid curves, rectangles) and alternative central solenoid + dipole (dashed curves, triangles). For illustration, a high p_T limit curve (dotted with open diamonds) as well as low p_T MS limit curve (blue open circles with bands) are shown. 10 TeV/c and 1 TeV/c is calculated in a Gluckstern approximation [64, 67] and FCCSW by Riemann fit, respectively for a scenario with a constant 4 T magnetic field. The MS limit is calculated with an average total material budget at $\eta = 0$: $x_{tot}/X_0 = 0.45 \pm 0.25$. $\delta p_T/p_T$ is shown for $p_T = 10$ TeV/c (dark green), 1 TeV/c (magenta), 100 GeV/c (green), 10 GeV/c (red) and 2 GeV (azure blue).

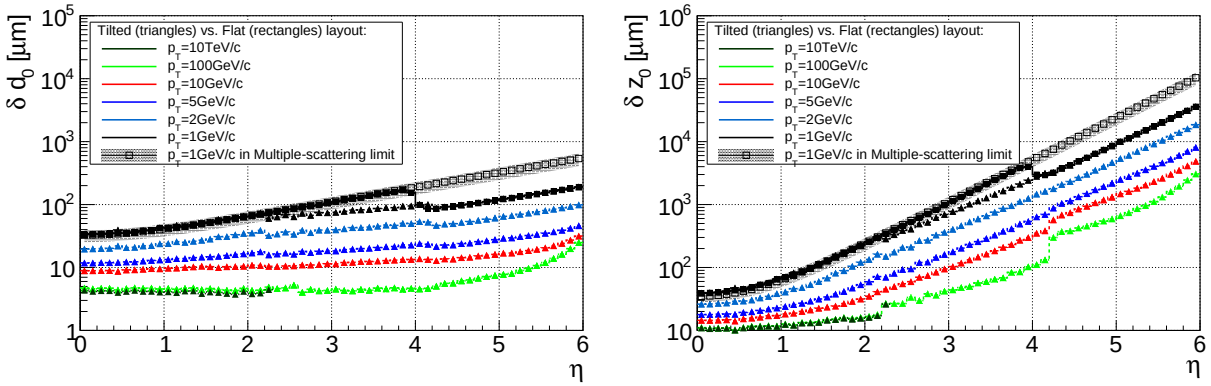

(b) Track impact parameter resolutions in r/φ, δd_0 (left), and in z, δz_0 (right). Two sets of curves are depicted: for flat layout (solid curves, rectangles) and tilted layout (dashed curves, triangles); $p_T = 10$ TeV/c (dark green), 100 GeV/c (green), 10 GeV/c (red), 5 GeV/c (blue), 2 GeV/c (azure blue) and 1 GeV/c (black). For illustration, a low p_T MS limit in a Gluckstern approximation [64, 67] is shown (black open rectangles with bands). It is calculated for a scenario with an ideal constant 4 T magnetic field and $p_T = 1$ GeV/c. To estimate the effect of material budget, the t_0/X_0 of the 1st layer is varied by ±50 % in the MS limit.

fig. 2.8: The expected FCC-hh track parameter resolutions, estimated with the tkLayout SW tool [67], originally developed for CMS Phase-II and adapted for FCC usage. It builds on a 3D spatial detector model, including the beampipe and estimates the track covariance matrix by Generalized Least Squares (GLS) method in a parabolic approximation. The only material effects being considered are multiple Coulomb scattering. Effects of particle energy losses are currently ignored in tkLayout. The magnetic field is approximated by a variable field value along z-direction. Figures created by Z. Drasal [52, 62, 63].

20% Silicon, 42% Carbon, 2% Copper, 6% Aluminium and 30% plastic [52, 62, 63]. To account for the accumulation of services and cooling when going outwards, the material budget is slightly increased with the radius. Effects of accumulation of services along the barrel staves are neglected. The material budget has the following distribution:

- 1% $\frac{x}{X_0}$ per layer in the innermost barrel layers
- 1.5% $\frac{x}{X_0}$ per ring in the innermost EC rings
- 2% $\frac{x}{X_0}$ per layer/ring in the macro-pixel region
- 2.5% $\frac{x}{X_0}$ per layer/ring in the striplet region

In total, the flat tracker baseline design consists of 49 114 modules, with 4908/1080 modules comprising the inner and 18 142/11 376 the outer tracker barrel/endcap region. For the intermediate forward part 3192 are foreseen, while the forward endcap region consists of 10 416 modules. Due to the high line pile-up density of eight pile-up vertices per mm in z, primary vertexing will be challenging. The pile-up particles have relatively low p_T compared to the signal tracks. Therefore the primary vertex can, to a large extend, be determined by selecting the reconstructed vertex with the highest sum of transverse momenta of tracks, contributing to this vertex. However, the hereby assigned primary vertex can still be contaminated by pile-up vertices. The number of pile-up vertices which are effectively contained within the uncertainty of the reconstructed vertex is referred to as the effective pile-up. Hence, 2D-vertexing by also using timing information to discriminate the tracks contributing to a vertex can be considered. In fig. 2.9 a comparison of the effective value for low p_T (1 GeV/c) of the CMS Phase-II and the FCC-hh tilted tracker layout for different timing resolution scenarios and also when not considering timing information is shown. The value is estimated by propagating the track parameters to the interaction region (only taking multiple scattering material effects into account) and counting the number of pile-up vertices which are effectively contained within the surface of the track parameters error ellipse, estimated at 95 % confidence level. The surface of the error ellipse is mainly determined by the material and radius of the beampipe and the first layers. Additionally, it depends on the dimensions of the luminous region.

Due to increased material budget and thus, worse impact parameter resolution, the effective pile-up increases with η. For the CMS Phase-II upgrade the effective pile-up at the highest pseudorapidity-acceptance of $|\eta| = 4$, assuming timing resolution of 25 ps, has a value of 1.2. This value is expected to be manageable, as shown by CMS full simulation [68]. For the FCC-hh tracker, 5 ps timing resolution needs to be assumed to obtain similar values. Currently, no detector technologies with such a good timing resolution exist. Alternatively more than one layer taking timing information with e.g. $\delta t = 25$ ps could be used, because the resolution improves with the number of measurements. Nevertheless, finding the primary vertex in the region of $|\eta| > 4$ will still be challenging. To possibly cover the full pseudorapidity region up to $|\eta| < 6$, increasing the beam bunch size can be considered, which would decrease the line pile-up density, due to a reduced collision probability.

2.4 Trigger scenarios

The signals produced at detectors of colliders need to be readout to be processed and recorded for later analysis. Due to the immense data produced at each collision, the number of recorded events is usually reduced by using triggers, which select only certain events. The implementation of triggers is very experiment specific. The ATLAS [69] and CMS [70] trigger systems have two

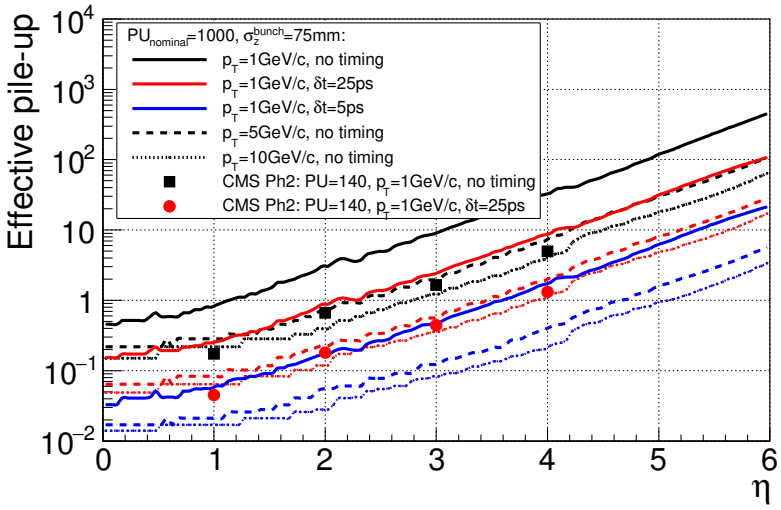

fig. 2.9: Effective pile-up evaluated for the nominal FCC-hh pile-up of 1000, the tracker tilted geometry and several track p_T values: 1 GeV/c (solid line), 5 GeV/c (dashed line) and 10 GeV/c (dotted line). Two options of primary vertexing are studied: 1D vertexing in z (black) and 2D vertexing in z and time. In 2D vertexing, the time resolution per track is set either to $\delta t = 25$ ps (red) or $\delta t = 5$ ps (blue). For reference, the effective pile-up for CMS Phase-II layout v3.6.5 and nominal $\langle\mu\rangle = 140$ is depicted: $p_T = 1$ GeV/c with 1D vertexing (black rectangles), $p_T = 1$ GeV/c with 2D vertexing and $\delta t = 25$ ps (red circles). Figure by Z. Drasal [52, 62, 63].

levels, which select possibly interesting events based on certain criteria e.g. calorimeter activity consistent with an electromagnetic shower, a tau- or hadronic jet, missing transverse Energy or the presence of muons. While the full event data is stored in pipelines for a few µs, the first level (*Level1*) trigger makes a fast decision using hardware processors in the calorimeters and muon systems. The second level (*High Level Trigger (HLT)*) is a software trigger, which then further reduces the events selected by the first level, using more detailed information by applying fast reconstruction algorithms. The triggers of the ATLAS and the CMS experiment reduce the data output rate from 40 MHz to a few kHz.

For the FCC-hh case, the trigger system is not fixed yet, since the trigger strongly depends on the detector technology. One possibility would be continuous readout, using only a high level trigger, similar as planned for the LHCb Phase-II upgrade [71]. The advantage of such a system is flexibility, since the software trigger is adjustable and can easily be adapted to different physics scenarios and theories. Although it would be technically possible to transfer the data of ATLAS and CMS Phase-II detectors (~ 200 TB/s) to the HLT, 150 to 300 k radiation-hard optical links would be required. This would not only be problematic from a cost point of view, but would also significantly decrease the tracking performance, due to increased material needed for links and cooling. For the FCC-hh scenario, similar arguments can be applied and the requirements on radiation hardness are even more constraining [52].

In addition to the increased peak-luminosity at 100 TeV, the SM cross sections increase. Due to this fact, it is expected to find 20 $b\bar{b}$-pairs per bunch crossing and three jets with transverse momenta above 50 GeV/c. Furthermore photon jets need to be distinguished very well, due to a rate of 10^{-4} of photons to jets with pT > 50 GeV [52].

Combined with the much finer granularity of the FCC-hh-baseline detector, this leads to high data rates of approximately 250 TB/s for the calorimeter and muon systems, which is ten times

the value of the Phase-II upgrades of ATLAS and CMS and can possibly be handled in the future. However, it is of question if the tracker data rate of 2 – 3 PB/s (see section 4.5), when assuming binary readout can be processed at the full event rate. Most probably a first selection, using the muon and calorimeter information together with coarse tracker information, needs to be done. When simulating the CMS Phase I calorimeter and muon triggers at 14 TeV and 100 TeV, both with a pile-up of 140 and a luminosity of $5 \times 10^{34}\text{cm}^{-2}\text{s}^{-1}$, the thresholds to operate the muon, electron/photon and jet triggers at a rate of 100 kHz (current CMS and ATLAS Level1 trigger rate) are raised from 25/30/120 GeV to 78/150/300 GeV just from the cross sections [52]. This makes the Level1 trigger for the FCC-hh case quite challenging and demands to find intelligent solutions in form of algorithms to reduce the trigger rate. The upgrade strategy of ATLAS [72] and CMS [73] uses a first level trigger, reducing the tracker readout rate to a maximum of 1 MHz. Apart from the muon and calorimeter triggers at the first level, CMS additionally uses a track trigger, which in conjunction allows to identify primaries. A similar model has been studied for the FCC-hh case, using a triplet of pixel layers (minimum number of measurements needed to form a track) with 30 mm separation at an average radial position of 600 mm from the beampipe. The rather large distance from the interaction region was chosen, to allow to readout at a maximum rate of today's available technologies of $\sim \mathcal{O}(1)\,\text{Gb/s/cm}^2$ and allows only charged particles with a $p_T > 0.36\,\text{GeV/c}$ to reach the trigger layers. The draw-back from choosing such a large distance is, that track parameter uncertainties grow, when extrapolating to the interaction point. The distance between the three layers is a compromise between track parameters uncertainty, which grows with the distance, and fake rate decreasing with distance. The latter could be improved by timing readout information. The standalone performance of such a track trigger has been studied for FCC-hh conditions, taking only multiple scattering into account [74]. It allows to reduce the pile-up contribution by isolating the primary vertex, with a z_0 resolution of 1 – 5 mm at $2 < p_T < 5\,\text{GeV/c}$. At a trigger rate of 100 kHz, it can standalone identify 50 % of the HH and $t\bar{t}H$ signals, taking a pile-up of 1000 into account [52, 62, 63]. Another possible approach would be to use a hardware based tracking sub-system, providing tracking data for the software HLT level, as done for the ATLAS upgrade.

2.5 Calorimetry

For the FCC-hh baseline calorimeters, the sampling calorimeter type is used. In distinction to a homogeneous calorimeter, this type is characterized by using separate materials for initiating the particle shower (*absorber*) and measuring the particles's deposited energy [17]. The energy resolution of a sampling calorimeter can be described the following

$$\frac{\sigma_E}{E} \approx \frac{a}{\sqrt{E}} \oplus \frac{b}{E} \oplus c \tag{2.11}$$

with a describing the stochastic term caused by shower fluctuations and sampling, b is the noise term due to electronics noise and pile-up and c is the constant term, caused by different effects as shower leakage, construction uniformity or cell-to-cell calibration [52].
The FCC-hh baseline electromagnetic calorimeter (EMCAL), has a thickness of $30\,X_0$ and consists of three parts: the barrel (EMB), endcaps (EMEC) and a forward part (EMF). The EMB and EMEC cover a pseudorapidity region of $|\eta| \leq 2.5$ and are placed within the magnetic field. The forward part extends up to $|\eta| \leq 6$. Due to its good intrinsic radiation hardness, Liquid Argon (LAr) technolgy was chosen, inspired by the ATLAS electromagnetic calorimeter [75], using multilayer printed circuit boards for readout. The Liquid Argon gap radially increases from 1.15 mm to 3.09 mm, which varies the sampling fraction and requires separate calibration

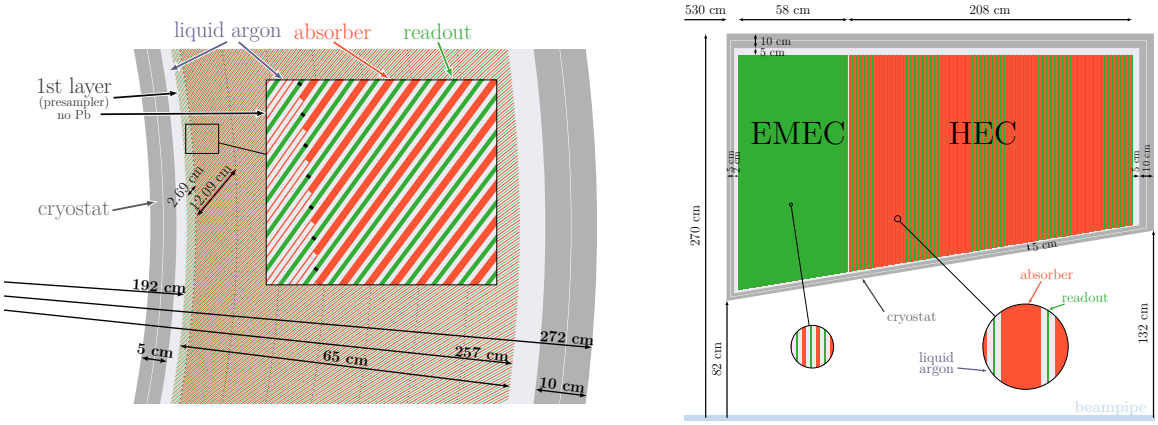

(a) EMCAL **(b)** EMEC

fig. 2.10: The Liquid Argon electromagnetic calorimeter structure of the FCC-hh reference detector for the barrel (left) and endcap (right). Source of figure: [52].

of the eight different layers in the barrel. As an absorber, 2 mm steel plated lead is used. Different than in ATLAS, no accordeon structure is used, instead the plates are inclined by 50° in radial direction (see fig. 2.10). The granularity is increased 2-4 times compared to ATLAS with $\Delta\eta \times \Delta\Phi = 0.01 \times 0.009$ and $\Delta\eta = 0.0025$ for the second layer, which corresponds to 20×20 mm at $|\eta| = 0$, 8×8 mm at $|\eta| = 2$ and 6×6 mm at $|\eta| = 4$. The total radial extension of the EMB is 65 cm, starting at a radius of 185 cm. Since Liquid Argon needs to be cooled, all calorimeter parts are surrounded by an Aluminium cryostat of 5 cm thickness in front of the electromagnetic calorimeters and 10 cm on the back. The EMEC is placed within the same cryostat as the hadronic endcap calorimeter. The cryostat in front of the ECAL comprises 56 % of the radiation length and needs to be compensated for in reconstruction. The EMEC uses 1.5 mm steel lead plates, perpendicular to the beamline, placed in a cone with 0.5 mm LAr gaps and 1 cm copper plates. The EMF uses the same layout with 0.1 mm LAr and 1 cm Copper plates. According to full simulation of single electrons, the calorimeter meets the requirement of energy resolution, which is $\sigma_E/E = 10\,\%\sqrt{\text{GeV}} \oplus 0.7\%$ (same as for current ATLAS Liquid Argon calorimeter). Using an optimized reconstruction (sliding window approach) leads to $a = 8.2\,\%\sqrt{\text{GeV}}$ and $c = 0.15\%$ at $\eta = 0$. The electronics noise was estimated to 1 – 35 MeV per cell by scaling the ATLAS numbers to the used capacitances of the readout electrodes and results in $b = 0.3$ GeV, when using a window size of $\Delta\eta \times \Delta\varphi = 0.07 \times 0.17$. When including pile-up, the window size for reconstruction needed to be optimized to $\Delta\eta \times \Delta\varphi = 0.03 \times 0.08$ and contributes with $b = 1.3 - 2.7$ GeV within $|\eta| < 1.5$ [52].

The hadronic calorimeter (see [76, 77]) needs to be highly granular to resolve collimated objects and needs a good containment of jets of 20 – 30 TeV at $\eta = 0$. Similar to the electromagnetic calorimeter, the hadronic calorimeter (HCAL) is made of a central barrel part (HB) and two extended barrels (HEB), covering a pseudorapidity of $|\eta| \leq 1.81$. The forward hadronic calorimeter uses Liquid Argon technology. For the HB and HEB the radiation does not put as stringent constraints on the technology as for the ECAL. Hence, organic tile scintillation material can be used, as done for the current ATLAS Tile Calorimeter [78]. Layers of the scintillator, and the absorbers; lead and tungsten, are placed orthogonal to the beamline. Wavelength shifting fibres [17] transport the signal to the Silicon photo-multiplier (SiPMs [17]) readout. The containment is $\sim 9\Lambda_0$ at $\eta = 0$. The granularity is four times increased compared to ATLAS with $\Delta\eta \times \Delta\varphi = 0.025 \times 0.025$ with ten longitudinal layers in the barrel and eight in the extended

part. The single pion resolution for $\eta = 0.36$ is $48\,\%/\sqrt{E} \oplus 2.2\,\%$ and within the target goal of maximal 3 % constant term. Since the hadronic calorimeter is placed within the magnetic field, the resolution is slightly degraded, due to losses to the cryostat wall. The effect of pile-up and electronics noise can be correctly integrated, using a topological clustering [79, 80] algorithm and worsens the resolution to $114\,\%\sqrt{E} \oplus 2.1$. This means that the reconstruction and calibration algorithms need to be further optimzed and possibly combined with tracking information (*particle flow*) [52].
The longitudinal segmentation of the calorimeters is preliminary and still needs optimization. Furthermore the pile-up mitigation needs to be studied in more detail. In total, the proposed ECAL and HCAL have 2.5×10^6 channels. At 40 MHz bunch crossing rate, assuming 16 bit readout per cell, this would at maximum result in a rate of 200 TB/s to be transported by optical fibres to the first level trigger, assuming all available channels are fired simultaneously.
An alternative to the proposed LAr option for the electromagnetic calorimeter is a calorimeter, based on silicon technology as active material and lead or tungsten absorber. The readout can either be realized as being analogue, by measuring the energy deposition, or digital. The latter operates by counting the number of particles passing through a cell, which is roughly proportional to the energy deposition, if the material is thin. Using 50 layers with 2.1 mm tungsten and 300 µm Silicon and 5 mm × 5 mm pads yields in a stochastic term of $a = 16\%\sqrt{GeV}$ and a constant term of $c = 0.1\,\%$ in simulation without pile-up. Digital readout, using monolithic active pixel sensors (MAPS) [17], with 50 µm × 50 µm (threshold of 480 e^-) and extremely thin sensor layer thickness of 18 µm gives $a = 12.6\%\sqrt{GeV}$ and $c = 0.3\,\%$. The linearity of response is good up to approximately 300 GeV. Beyond, it needs to be corrected for multiple electrons passing through the same pixel. In total, this calorimeter would have 10^{12} pixels on a surface of 3500 – 6000 m^2 Silicon, depending on the exact implementation. Future research and development and especially the CMS Phase-II planned high granularity forward calorimeter [81], based on analogue silicon technology will show if the technology could be applied for FCC-hh [52].

2.6 Muon system

For the muon system three different options exist: momentum measurement in the tracker plus using the muon system for identification only, standalone muon momentum measurement i.e. measuring the angle between the muon track and the radial line connection to the beam axis or a combined approach. The current muon system model consists of a barrel and outer endcap part, which are located outside the solenoids, an inner endcap part, within the main solenoid and a forward part. The expected standalone muon resolution is limited by multiple scattering in the calorimeter to $\sim 4\,\%$ for tracks with transverse momenta of 10 – 1000 GeV/c, about 6 % for 2 TeV/c and 24 % for 10 TeV/c. Assuming 50 µm position resolution up to $|\eta| = 2.5$, the performance is equal to the tracker resolution and less than 10 % for $p_T \leq 3$ TeV. At $|\eta| = 2.5$ the resolution is limited by multiple scattering to 28 % for tracks with 10 – 100 GeV/c and $\sim 41\,\%$ for 500 GeV/c. Beyond, the momentum resolution exceeds 100 %. Therefore, in the current setup the forward muon system can only be used for muon identification, but not for triggering. To allow momentum resolution in the forward region, the dipole magnet option would need to be used, instead of the solenoid. Considering the energy loss in the calorimeters, only muons with a minimum transverse momentum of 6 – 7 GeV/c can reach the muon systems. The total cross section for muon production coming from c- or b- or t-quark, W- or Z-boson decays amounts in 200 µbarn and a total muon rate of more than 20 MHz for a transverse momentum threshold of 10 GeV/c. Hence, the threshold needs to be set higher, to provide selectivity. The charged particle rates are in a range ($1 - 250\,kHz/cm^2$) to allow to use the same sMDT (small-diameter

muon drift tube) technologies as planned for the ATLAS Phase-II upgrade [82]. Possibly two layers consisting of four rows of gas filled ($Ar - CO_2$) drift tubes with a diameter of 15 mm, an angular resolution of 60 µm and a spatial resolution of 40 µm could be used. These chambers would efficiently cover a total area of 1150 m^2, using 260 k tubes [52].

Chapter 3

Software for simulation and reconstruction

Throughout the whole lifetime of an high energy physics experiment, software is an essential tool. This chapter concentrates on software for detector *simulation* and event *reconstruction*, developed in the context of this thesis.

Simulation includes event generation, the propagation of particles through the magnetic field as well as the particle interactions with the detector material, leading to energy loss, scattering and possibly the creation of new particles. The response of the detector and the creation of the detector signal, referred to as *digitization* also needs be considered. The stochastic nature of physical processes is mirrored in simulation. For instance the multiple coulomb scattering of charged particles is implemented by stochastic scattering. The propagation of a particle through the magnetic field depends on the particle's state (e.g. momentum, direction, position, charge) and is implemented by numerically solving the field integrals. In contrast, the physical processes a particle might undergo during the passage through the detector, have stochastic character. Therefore, simulation in high energy physics is a perfect candidate for using Monte Carlo methods [83].
Simulation is a substantial part of an experiment from the very beginning throughout its whole lifetime. During the design phase it is crucial for developing detector models and studying their performance. Among other applications, simulation is also used to deliver background estimation as well as efficiency and purity values for analysis. The data produced by Monte Carlo simulation is processed as if it was data recorded by the detector. In this way discrepancies between the theoretical models used in simulation and actual data indicate that the underlying physics has not been described properly and thus, can point to new physics.
Simulation is always an approximation of the underlying physics processes. The complexity of this approximation determines the computing complexity and accuracy of the simulation. Depending on the needed accuracy and speed as well as on the stage of the experiment, usually different simulation types, classified according to their quality and speed are used. Figure 3.1 illustrates the application of different simulation types, e.g. *fast* and *full simulation*. When designing an experiment, the complexity of the simulation type increases. This is not only due to the progress in software development but also because more accurate models are needed, while the detector layout gravitates towards the final design. Though, different simulation types are not only needed during the detector design phase, but throughout the whole lifetime of an experiment. For instance, to produce a high amount of data to increase the confidence in statistics for a study, faster simulation types with sufficient accuracy are beneficial.

Full simulation is most detailed, using an accurate description of the detector geometry and its material, doing an in-depth step-by-step particle transport through the detector and simulating the particles' interaction with matter. Yet, the high accuracy requires more CPU-time and therefore long runtime.
Fast simulation is, as the name suggests, faster and less CPU-consuming. To speed up the simulation, various approaches with different levels of simplification exist, for different use-cases.

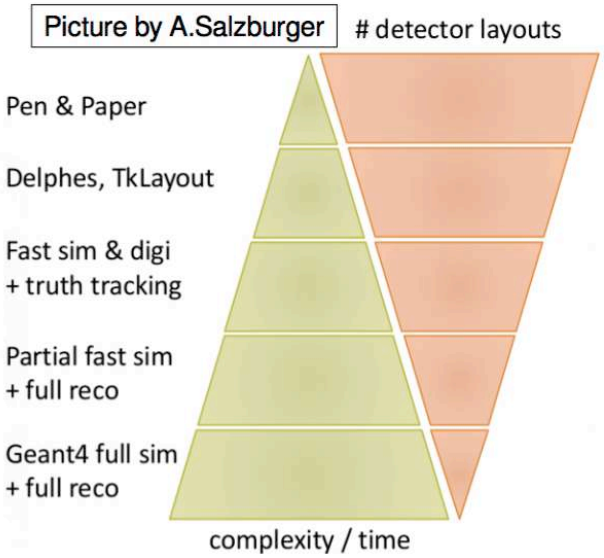

fig. 3.1: Illustration of a simulation pyramid, showing the purpose, speed and complexity of the different simulation types as well as the decrease of possible detector layouts over time. At first, general considerations on the possible detector design are done without software. As a second step analytical software tools (e.g. tkLayout [67, 84]) and simple parametrized simulation models (e.g. DELPHES [85]) are used, mainly for physics potential studies. This is followed by fast simulation types and first tracking applications using the truth information from simulation. Both, the detector design and the simulation type become more and more detailed, allowing to undertake in-depth detector performance studies.

One possibility is to simplify the geometry and the material but still simulate the particle's transport and its interactions within the detector material accurately (see section 3.2.4). There is a spectrum of possible geometric simplifications from describing the sensitive detector modules detailed but just approximating the passive material to describing the whole tracker made of simple cylinders, or using a completely parametric approach. In the latter case, the particle interactions are parametrized by smearing the particle's energy and momentum according to its most probable energy loss obtained from full simulation (e.g. DELPHES [85]).
The simulation setup used for the FCC-hh is described in detail in section 3.1.

Another important software application is *event reconstruction*, whose purpose is to set the measured detector signal into physical context. The reconstruction step is done to obtain physical objects, e.g. particle tracks in the tracking detector or energy depositions in the calorimeters. This allows to determine the properties of particles, as for instance the particle type, mass, energy, momentum or charge.
To understand the concepts of track reconstruction, the design of a tracking detector is explained first. The purpose of a tracking detector is to determine the trajectory of charged particles. Given a magnetic field, the trajectory allows to determine the momentum of a particle and its origin. A semiconductor Silicon tracker (as for instance used in ATLAS [11] and CMS [12]), consists of thousands of silicon modules, subdivided into millions of readout channels which hermetically cover the collision region. However, the tracker does not directly reveal the trajectory. Instead it makes a number of localizations of the particle's trajectory: In simplified terms, each channel can be seen as a small diode in reverse bias, which records an electric pulse as soon as a charged

particle traverses the volume and ionizes along its trajectory (for more detailed information on how semiconductor detectors work, please see [17], *chapter 35.7*). When a particle traverses such a detector module, it will make a charge deposition, creating current in the depletion zone and hence, *activate* one to several neighbouring channels, which form a measurement (also referred to as cluster). This measurements consists of the measurement position and, depending on the readout technology, additional information as energy deposition, charge or time measurement.
The task of track reconstruction software is thereafter to find the trajectories of the charged particles from the measurement positions with high efficiency and quality i.e. good fit quality and a small number of holes[1]. Given the detector measurements, track reconstruction is composed of two parts: *track finding*, which uses pattern recognition algorithms to find the particle trajectories, and *track fitting*, whose purpose is to determine the optimal (best fitting) track parameters e.g. point of origin, direction of flight and momentum. Monte Carlo simulation plays a crucial role for validation of track reconstruction and determination of its efficiency. In contrast to real data, the information about which particle created which hits - the *truth information* - is known [15].

Future scenarios, as a detector for the currently studied FCC-hh collider or ATLAS and CMS, after the Phase-II upgrade for HL-LHC (see [86, 87]) have to satisfy unprecedented requirements, regarding performance of both simulation and track reconstruction. Because of the increased luminosity and the increased number of simultaneous proton-proton collisions per bunch crossing of 200 for HL-LHC and about 1000 for the FCC-hh environment, more particles and therefore a multitude of hits need to be processed in track reconstruction. This can be especially challenging for track finding, because the complexity is not rising linearly with the number particles but combinatorial, with the number of possible hit combinations between the layers. Therefore, track reconstruction software for these scenarios needs to be highly efficient and fast. Among others, these requirements have been a strong motivation to establish a new track reconstruction package *Acts (A common tracking software)* based on the ATLAS track reconstruction software. The Acts package is introduced in further detail in section 3.2, followed by a presentation of the software implemented for the FCC design studies, in section 3.1.

The following part is dedicated to the software which was used for the studies presented in chapters 4 to 6 and whose development was a major part of the work described in this thesis. This included the co-development of the, at the beginning of the effort, newly established software package Acts, with the focus on enabling and supporting the FCC-hh use-case within FCCSW. One focus was on the more experiment specific geometry support, which follows previous experience with the translation of a DD4hep-Geometry (see section 3.1.2.1) into an ATLAS-like first test tracking geometry previously implemented for FCC software (FCCSW). It showed that the general usage of the ATLAS-tracking software is possible in another experiment and framework [88], and additionally motivated this work. The former implemented ATLAS-like tracking geometry in FCCSW is now fully replaced by the Acts package. The used programming language is *C++* [89, 90].
In the first part of this chapter, a general introduction to FCCSW is given and the software components used and developed for the studies are introduced. The second part concentrates on the specific software implementations within Acts.

[1] Passed detector layers along the track, where no measurement has been registered.

3.1 The FCC Software (FCCSW) for event processing, simulation and reconstruction

For all of the possible FCC collider options (ee, eh, hh) a common software suite FCCSW [91, 92] was established, in order to optimize usage of common components and to keep code duplication at a minimum. In addition FCCSW profits from the existing and well-tested LHC-experiment software, adapts useful components for FCC usage and exploits software concepts proven to be successful. For instance FCCSW uses Gaudi [93] as an underlying event processing framework. It is an experiment independent software architecture and framework for high energy physics data applications, which is also used by the LHCb [13] and ATLAS [11] experiment. Gaudi controls the event loop by scheduling components, realized as *services* (providing fundamental functionality to all algorithms and tools), *algorithms* (main processing block) and *tools* (algorithmic code which can be reused by several algorithms) with abstract interfaces, that communicate via a central data store. These Gaudi components allow to introduce configurable parameters. The configurable parameters as well as the components to be used for a specific job, can be declared and modified at runtime using Gaudi job options, which are simple python [94] scripts. Each service, algorithm and tool in Gaudi needs to implement an `initialize()` and a `finalize()` method. The initialization is done before the events of a run are processed and is used for configuration of the components by the given job-option parameters. After the execution of the given number of events, where each algorithm is executed once per event, the finalization of each component is called, allowing to do necessary clean-up. Using Gaudi ensures future deployment of parallelism, since Gaudi is updated to the concurrent GaudiHive [95] framework.
The FCC event data is stored in a common and flexible event data model (EDM) [96], based on simple C++ classes and structs using ROOT [97] for input/output and persistification.

fig. 3.2: The FCCSW simulation-tracking chain showing the different steps in full simulation and reconstruction.

For event simulation and reconstruction a detector geometry description is essential which is described in section 3.1.2. The first step of the simulation chain is event generation. In FCCSW PYTHIA8 [98], with Monash 2013 tune [99] is used to simulate proton-proton collisions with a center-of-mass energy of 100 TeV. To simulate the beam spread, vertex smearing is directly applied during event generation with the gaussian widths of $\sigma_{x/y} = 0.5\,\text{mm}$, $\sigma_z = 40\,\text{mm}$ and $\sigma_t = 180\,\text{mm/c}$.
The generated particles are the input to the FCCSW-simulation-tracking-chain, displayed in fig. 3.2. The particles are traversed through the detector, taking the magnetic field into account (section 3.1.3), by simulation, followed by digitization and clusterization (section 3.1.4). The created cluster positions (space-points) serve as input to track seeding[2], using a cellular automaton approach [100] as done for the CMS upgrade. These seeds are the input to track reconstruction and fitting, for which Acts will be used.
Following the example of the ATLAS integrated simulation framework (ISF) [101], full and fast simulation options can be coherently combined in different detector regions. The simulation

[2]Seeding is the first part of track pattern recognition, aiming to find possible track candidates.

package Geant4 [102] serves as simulation kernel and is used for full and a fast parametrized simulation option (see [103]). For the full simulation studies presented in this thesis, Geant4 version 10.03.p01 with the physics list `FTFP_BERT` was used. A particle production cut[3] of 0.1 mm is the default in FCCSW simulation.
In order to simulate FCC-hh conditions with pile-up of 1000, a pool of minimum bias events at 100 TeV is simulated separately from the signal events. In a second step 1000 randomly chosen minimum bias events are merged with the signal event using a pile-up merging algorithm. This algorithm then calls dedicated tools defined by the user which do the merging of the requested EDM-classes relevant for the specific study. The particle identification in FCCSW is currently directly taken from Geant4 (using the `trackID`) and is shifted for the pile-up events. In this way, the pile-up can be distinguished from the signal events. In future, a dedicated particle identification scheme needs to be implemented for better handling of the Monte Carlo truth information. The pile-up merging is done, before the digitization, since pile-up particles can share the same cells as signal particles, which needs to be considered during digitization and clusterization.

3.1.1 Acts integration into FCCSW

In FCCSW the Acts tracking toolkit is not only used for track fitting but has various applications. For instance the magnetic field service of FCCSW is based on the Acts implementation. Its integration is described in detail in section 3.1.3. Since for the FCC-hh conceptual design study phase, no specific detector technologies have been selected yet, Acts is used to perform geometric digitization (see section 3.1.4). Additionaly, it is planned to integrate Acts-FATRAS (see section 3.2.4) as a fast simulation option into FCCSW, to offer a possibility to produce high statistic samples in reasonable time. Especially for the FCC-hh conditions, with its many particles being produced due to the high pile-up (see chapter 4), this is of interest. As soon as track reconstruction and track fitting is fully functional, it will be integrated into FCCSW as well. In fig. 3.3 the FCCSW-simulation-tracking chain is shown. The orange frame indicates, where Acts is, or will be used within FCCSW.

The Gaudi components, namely services, tools and algorithms are used to interface to Acts. They either use provided functionality directly or act as wrapper, internally holding an instance of the Acts Object. Using the python job options of Gaudi, the Acts tools can be configured (using their configuration structs) by the user at runtime, as demonstrated in fig. 3.4. The Gaudi wrappers handle the communication from and to the FCC event data model.

3.1.2 FCCSW geometry

In FCCSW one common geometry input for all types of simulation and reconstruction is used, to guarantee overall consistency. The geometry package used to describe the FCC geometry is DD4hep [104], described in more detail in section 3.1.2.1.
For the FCC-hh scenario the baseline tracking detector as described in section 2.3 was designed using a special detector design tool, the *tkLayout* software tool [67]. The flat layout design was then exported from tkLayout to XML and transcribed into DD4hep detector description. As illustrated in fig. 3.5, a Gaudi service builds the DD4hep geometry and allows to access it during simulation. For track reconstruction and digitization, which uses the Acts package, a track reconstruction geometry service was established, which calls the conversion function

[3] Geant4 uses a production cut in range, which can be translated to a production cut in energy. If a particle has an expected range smaller than the given cut, it will not be considered during simulation.

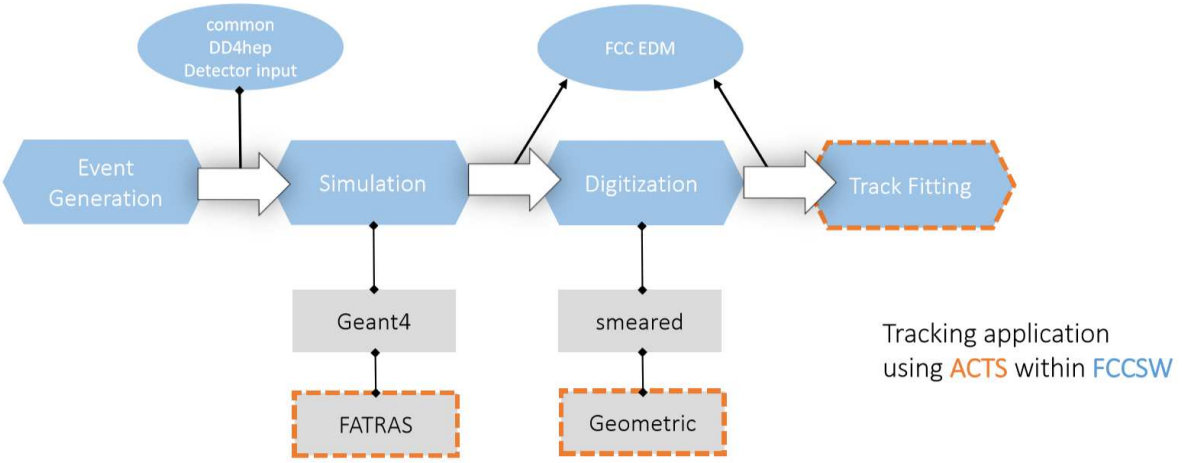

fig. 3.3: Acts integration into FCCSW. The boxes in blue show the FCCSW full simulation-track reconstruction-chain, which needs geometry input and write and read from/to the FCC event data model. The white arrows indicate the program flow. The grey boxes show different options of one step, e.g. digitization can either be done by smearing a hit or using a geometric approach. The orange bordered boxes show where Acts is/will be used internally.

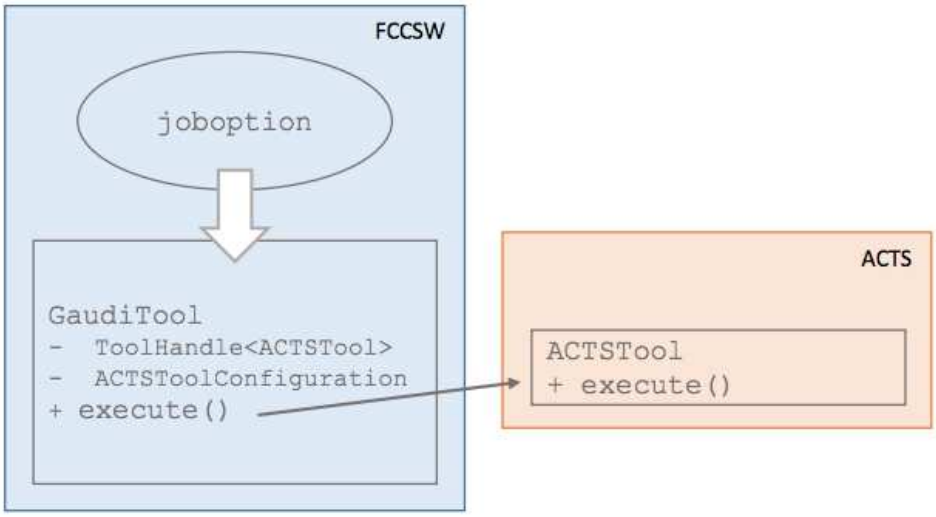

fig. 3.4: Display of how the Gaudi components (services, algorithms, tools) are instantiated and configured by python job options. The Gaudi component internally uses the Acts tool.

of the Acts `DD4hepPlugin` (see section 3.2.1.3) and returns a pointer to the Acts tracking geometry. Since the material description of the current FCC-hh tracking detector is still relatively simple at this stage, it was sufficient to use the material averaging within the Acts-extension of the `DD4hepPlugin`, described in section 3.2.2.1.

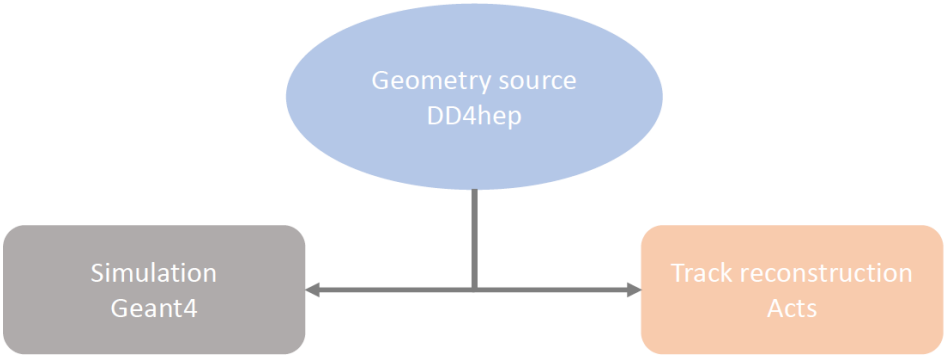

fig. 3.5: Diagram illustrating the consistent geometry building chain within FCCSW. Both, the simulation geometry of Geant4 and the track reconstruction geometry of Acts are built automatically from the common DD4hep geometry source.

3.1.2.1 DD4hep - Detector Description for high energy physics

Within the FCC software package, a detector description package developed by the AIDA [105] (*Advanced European Infrastructures for Detectors and Accelerators*) community is used. DD4hep [104] stands for *Detector Description for high energy physics* and is a generic detector description toolkit, which is an in-memory model based on C++ objects.
It internally uses the, in the high energy physics community widely used, *ROOT* [97] geometry package *TGeo* [106]. The ROOT geometry package is based on volumes, their relationship to one another and the overall world volume. Each volume can be placed several times within another volume. Hence, a TGeo volume does not represent a unique entity. Due to this fact and because TGeo is a pure geometrical description, lacking any detector relevant information, DD4hep implemented detector elements. These are implemented on top of TGeo and can for instance describe the detection techniques, readout information, alignment, calibration or conditions data. The detector element is realized as a unique `DetElement` class object and is the heart of the DD4hep detector description. Each detector consists of a tree of these `DetElements`. The tree of detector elements is parallel to the geometry tree, with each detector element having a link to its corresponding geometrical object but not vice versa. For example, not each cable or support structure needs detector relevant information, nevertheless needs to be described in the full geometry description to correctly account for the material. Each detector element is only placed once in the detector tree and thus, represents an exclusive entity and can be uniquely identified, which is crucial for simulation and reconstruction.
DD4hep implemented an extension-mechanism which can be used to extend the functionality of the `DetElement`. For this purpose any C++ class object can be created and added to the `DetElement`.
To build a geometry in DD4hep two ingredients are of need: an XML-description, stating all relevant detector parameters and corresponding constructors in C++, which build the detector in-memory and receive the needed parameters from the XML-description. The compact detector description is flexible, allowing to change detector parameters as e.g. the dimensions or the

number of layers at runtime without the need to go through the more time consuming process of recompiling the program. A high energy physics detector at an accelerator consists of different detectors: the tracker, the calorimeter, the muon-system etc., these usually consist of subdetectors. For the FCC-hh case the tracker has different subdetectors: the pixel tracker, the macro-pixel tracker and strip tracker, which will also be called hierarchies in the context of geometry building. As illustrated in fig. 3.14 these subdetectors have different parts: the barrel region, with usually plane rectangular modules, arranged on a cylindrical layer (the modules are also often tilted for better η-coverage for future experiments) and trapezoidal modules, arranged on a disc layer in the negative and positive end-cap region. Since these regions are very different, they require different detector constructors. These are usually written in a generic way. This allows the constructor to be reused by several XML-descriptions, which specify the constructor to use. For example in the FCCSW description one C++ constructor is used for all inner and outer barrel parts, as well as one for all inner, outer and forward endcap parts. The exact design of the constructors, as well as the XML format is very flexible and can be designed by the user. The DD4hep parsers do not require a fixed XML schema. Thus, new attributes can be easily introduced. This makes the tool powerful, since there are basically no limits on how the geometry is built. However, since there is no general rule of how to build a DD4hep geometry, the C++ detector constructors need to be provided by the user's side, which requires additional expertise.
To build a subdetector (e.g. the inner tracking detector) usually consisting of a barrel and two endcaps, DD4hep provides a possibility to group these parts, to form a subdetector just using a *subdetector assembly*-constructor in the XML-description. Finally the whole detector, grouped in subdetectors can be accessed and managed by a singleton entity the `LCDD`.

3.1.3 FCCSW Magnetic field implementation

To avoid code duplication, FCCSW uses the already present magnetic field implementation of Acts, described in section 3.2.3. Since the magnetic field needs to be accessible by simulation and reconstruction, it was implemented as Gaudi service. Following the Gaudi concept, an abstract interface class `IBFieldService` was implemented providing a `getField()` and `getFieldGradient()` method, returning the 3D magnetic field and gradient value at a position given as function parameter. Two implementations of the `IBFieldService` exist:

- `ConstantBFieldSvc` - describing a constant magnetic field implementation, returning the same magnetic field value for any given position
- `InterpolatedBFieldSvc` - it interpolates (using a linear approach) the magnetic field value from field values given in a magnetic field map file

The FCCSW implementations internally use the Acts implementations `Acts::ConstantBField` and `Acts::InterpolatedBFieldMap`. As soon, as the interface methods to access the magnetic field or gradient are called, the call is forwarded to the Acts object, as for example shown for the interpolated field service in fig. 3.6.

These FCCSW services can be configured at runtime using the Gaudi job options. In case of the constant magnetic field implementation, the magnetic field value can be configured. For the interpolated field implementation the magnetic field map can be provided, either in `txt/csv` or `root` file format. An example of the configuration of the `InterpolatedBFieldSvc` in the python job-options is shown in fig. 3.7, where the FCC-hh magnetic field map is given in cylinder coordinates and `root` file format.

In order to use the FCC magnetic field service during Geant4 simulation a wrapper `bFieldG4`, inheriting from the Geant4 interface class `G4MagneticField` was implemented. It internally calls

```
fcc::Vector3D InterpolatedBFieldSvc::getField(const fcc::Vector3D& position) const {
  return m_actsBField->getField(position);
}

Acts::concept::AnyFieldCell<> InterpolatedBFieldSvc::getFieldCell(const fcc::Vector3D& position) const {
  return m_actsBField->getFieldCell(position);
}
```

fig. 3.6: Implementation of the `getField()` and `getFieldGradient()` methods to access the magnetic field in the `InterpolatedBFieldSvc` of FCCSW, by forwarding the call to the Acts instance held by the service.

```
from Configurables import InterpolatedBFieldSvc
bFieldSvc = InterpolatedBFieldSvc("BFieldSvc", fieldMap = '/eos/experiment/fcc/hh/simulation/MagneticField/FCChhBField_rz.root',
    treeName= 'bField', lengthScalor=1., bFieldScalor= 1., cylinderCoordinates = TRUE, firstOctant=TRUE, OutputLevel = VERBOSE)
```

fig. 3.7: Configuration of the `InterpolatedBFieldSvc`, with the FCC-hh magnetic field map as input, within FCCSW, using Gaudi python job-options. A field map in *root* file format is provided in cylinder coordinates. Only the first octant is given by the map. The service will automatically extend the map to the other octants.

a magnetic field service following the `IBFieldSvc` interface. To allow to configure which magnetic field service implementation should be used, a configurable Gaudi tool `SimG4BFieldTool` was implemented. This tool sets up the magnetic field in Geant4 with a given magnetic field service. The implementation is continuously tested and has been validated. The validation included consistency checks of the interpolated field value with the given magnetic field map, the automatic symmetric extension of the map, as well as the the implementation within Geant4. It was found, that using the interpolated field service instead of the constant field service, approximately slowed the simulation of single muon events down by a third. The magnetic field value can also be visualized within FCCSW (see fig. 3.32).

3.1.4 Digitization and Clusterization

The process of emulating the detector response in simulation is referred to as *digitization*. *Clusterization* clusters neighbouring readout channels to form a measurement. The spatial position of clusters, represent space-points, which serve as input to pattern recognition. Clusterization is the first part of reconstruction and also needs to be applied to actual detector output.
The output obtained from Geant4 full simulation (see appendix A.3) are steps, consisting of a pre and a post step position of a particle trajectory with a corresponding energy deposition along the step length in the sensitive volume. Similar to full simulation, the pure simulation output of the FATRAS (see section 3.2.4) fast simulation gives the intersection point and direction of the particle path with the surface, representing the detector module. Both simulation outputs do not describe the actual measurements as obtained from a physical detector. The measurement of the path of charged particles is usually translated into a charge measurement, utilizing the fact that a charged particle ionizes along its path (see appendix A.4.1). Hence, the charge deposition in a suitable sensitive material (with high yield, as e.g. Silicon for ATLAS and CMS) is recorded by the detector. The actual design of the readout as well as the choice of material are detector specific. For high energy physics experiments, the readout is usually segmented, into small readout cells to allow an accurate determination of the position, where a particle passed a detector module. Therefore, the granularity of the readout grid determines (apart from other effects) the position and consequently the momentum and vertexing resolution of the tracking

detector. In addition, also the capability of resolving close by tracks in dense environments depends on the readout granularity.
This section describes the implemented digitization and clusterization, used for the studies of this thesis. Because the specific detector technologies which will be used for FCC-hh are not known yet, only geometry aspects for the clusterization are considered. For more details of the implementation within Acts, please see section 3.2.5.
The first required step of digitization within FCCSW is to build a `Acts::DigitizationModule`-class object for each sensitive detector module. This module contains all the relevant information, needed for digitization and clusterization. Within the geometry translation from DD4hep to Acts, the option of directly translating the given DD4hep readout segmentation to the information needed within Acts, is provided. For memory optimization reasons, also the possibility to build the class once for several detector elements (having the same readout), is provided (see section 3.2.1.3). Every detector element inside Acts holds a pointer to the defined `DigitizationModule`.

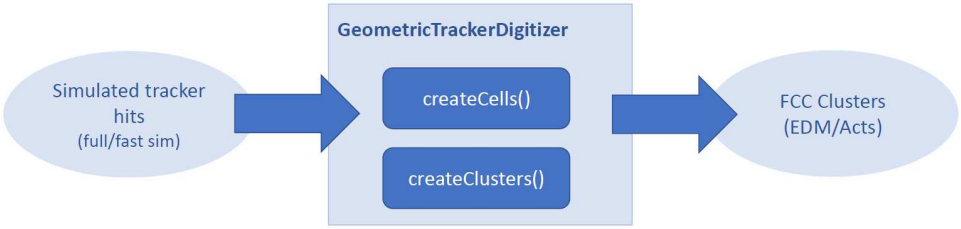

fig. 3.8: Program flow of the `GeometricDigitizer` within FCCSW. Given simulated tracker hits, it first digitizes the hits, using the `createCells()`-method and then clusterizes the cell `createClusters()`. The output are clusters.

Inside FCCSW a configurable digitization algorithm, the `GeometricTrackerDigitizer`, has been established to perform the digitization and clusterization. The program flow is illustrated in fig. 3.8. Simulated tracker hits in FCC EDM format are the input to the algorithm, either created by full or fast simulation. First, the hits are digitized using the subroutine `createCells()`, by determining the number of activated cells, given the hit information, and creating cell objects. These cell objects serve as input for clusterization, which is invoked by `createClusters()`. The algorithm allows to apply an energy threshold, which must be reached by each cell to be activated, configurable at runtime. It can be chosen, if cells sharing a common edge or cells sharing a common corner should be merged into the same cluster. The latter was taken as default and used for the studies in this document. Other configurable parameters are a weight for gaussian smearing applied to the step length and a lorentz angle, which determines the deviation of the charge carriers within the silicon, due to the applied magnetic field.
Two different cluster outputs can be created. Firstly, output in FCC EDM format, written to the FCC event store. It possibly consists of time, energy and position information, the track IDs and hits contributing to each cluster. Secondly, an internally created `FCCPlanarCluster` object can be created, holding the same information as the first option. The second option has been created due to memory related issues within the FCC EDM at the time of the implementation[4], which becomes a serious issue for the FCC-hh data amounts. The issue is under investigation.
Depending on the readout type, which is set during configuration, the cluster position is calculated. In case of digital readout the cluster position is the mean of the cell positions. If the detector uses analogue readout the cell positions are weighted according to their energy deposition. By

[4] Just after reading in the hits for one event at $\langle \mu \rangle = 1000$ the memory consumption exceeded 6 GB. For creating the output clusters another 3 GB were needed. However, theoretically the simple EDM structs should not exceed 1 GB.

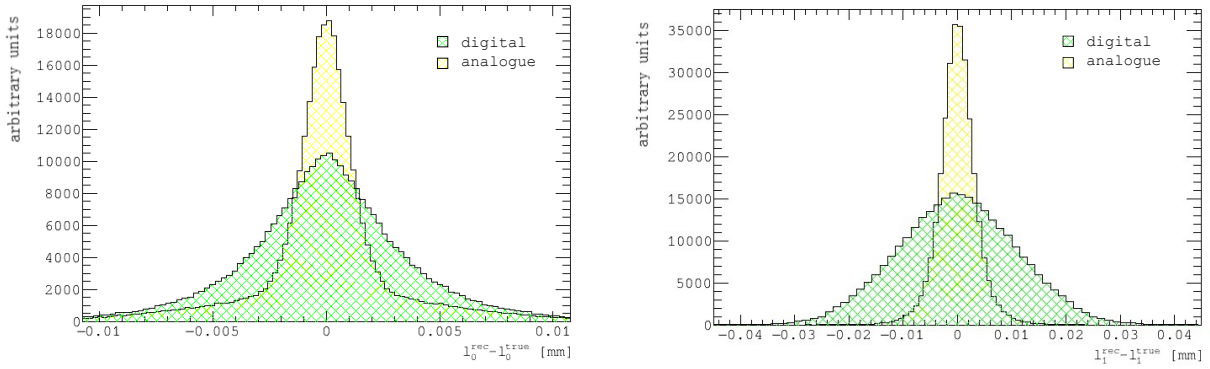

(a) Cluster position resolution for 25 µm pixel width in local x, global r/φ.

(b) Cluster position resolution for 50 µm pixel length in local y, global z.

fig. 3.9: Two figures showing the resolutions for the first tracker layer, as obtained from fast simulation and geometric digitization, for analogue and digital readout, in the two different readout directions.

calculating the difference between the cluster position and the corresponding hit positions, a realistic resolution estimate can be obtained. For FCC-hh granularities, the obtained resolutions for the first layer are shown in fig. 3.9, using Acts fast simulation.

In fig. 3.10 a possible configuration of the `GeometricTrackerDigitizer` is shown. The weight of the gaussian smearing of the path length within a cell is set to 0.1 per default and a default energy threshold to activate a cell of 3.6 keV (producing 1000 electron-hole pairs) is applied, which is a typical value for current silicon detectors. Due to not known technologies, the impact of the lorentz force to the charge carriers, hit inefficiency, cuts in incident angle or traversed length have not been applied.

```
from Configurables import GeometricTrackerDigitizer
digitizer = GeometricTrackerDigitizer()
digitizer.digiTrackHitAssociation.Path="digiHits"
digitizer.trackClusters.Path="trackClusters"
digitizer.clusterTrackHits.Path="clusterTrackHits"
digitizer.analogReadout=FALSE
```

fig. 3.10: Example for runtime configuration of the `GeometricTrackerDigitizer`, using the Gaudi job-options. The digitizer reads in hits (`digiTrackHitAssociation`) produced by FCC full simulation and writes out `trackClusters` to the FCC event store. Digital readout is used, by setting the analog readout option to 'false'.

3.1.4.1 Simulation output and truth handling

The first step of the FCCSW simulation chain, creates simulated hits, which are written to files using the EDM output format. In a second step, the hits are overlaid with pile-up and stored to another file, before being digitized and clusterized. The conditions at an FCC-hh collider of $\sqrt{s} = 100\,\text{TeV}$ with $\langle\mu\rangle = 1000$ create unprecedented amounts of data during simulation, compared to LHC-experiments. This leads to new memory related issues. For instance, when overlaid with pile-up, at the moment only one event can be stored per file. In addition, it is currently not possible to store both, tracker and calorimeter simulated hit information into the

same file, because the file size would exceed 1 GB. Even if the already mentioned memory related issues of the FCC EDM can be resolved, the produced outputs will still be high.

To reduce the total number of simulated tracker hits produced by Geant4 a dedicated `G4SensitiveDetector`, which is a Geant4 module responsible for creating and storing Geant4 hits, has been created. It merges all steps done by Geant4 from the same particle within the same sensitive detector volume. This reduces the total number of produced hits before digitization by nearly a factor of two. In addition it also speeds up the digitization process, since less hits need to be processed. For the majority of cases, hit merging produces the same result (cells hit after digitization) as without hit merging, because the scattering within the thin silicon sensors is very small. Rare cases where e.g. a low momentum secondary electron is strongly deflected and would activate additional cells occur only occasionally.

For the studies presented in the following, special information as e.g. truth simulation information was of need. All particles created within the detector material are registered by Geant4. Special caution is required, when storing the particle history, because for the FCC-hh case, with its high pile-up conditions, millions of particles are produced. This can lead to a memory consumption in the range of tens of GB. For this reason a possibility to flag only those particles which created a registered (above threshold) hit within the simulation was introduced. This allows to register the truth information and keep the memory at a reasonable level. This flag can be set at runtime using the job-options.
Using these two options, the file size still amounts to $\sim 300 - 400$ MB, just storing the simulated tracker hits of one event. Therefore, in future more improvements, including structural changes to the simulation-chain and rethinking of the event-based processing, need to be done.
To write out dedicated cluster information for the truth studies, the `GeometricTrackerDigitizer` allows to plugin dedicated cluster writers using the cluster information. For full simulation studies special writers to save the cluster information and the corresponding truth information of all particles taking part in the simulation, including generated particles as well as the particles produced within the detector, have been created.

3.2 A Common Tracking Software - Acts

The track reconstruction software of the ATLAS experiment [107] was established during the preparation of the technical proposals and technical design reports in the late 1990s and evolved until its deployment in 2008. The software, originally written in FORTRAN [108] language, has undergone a major optimisation for Run-2 in 2012 [109], to deal with the increased hit density due to the increased luminosity.
After years of development and usage, the ATLAS track reconstruction software is very well tested and has proven excellent performance (see [110–112]) in a complex magnetic field environment and within diverse tracking detector systems of ATLAS: the pixel and strip detectors, the transition radiation tracker and the muon tracking system and is equipped with a dedicated transport model through dense calorimeter material [113].
For the operation of the High-Luminosity LHC (HL-LHC) [44, 45], expected in the mid-half of 2026, the Phase-II upgrade of the ATLAS detector [53] is planned, which includes a significant update of both, hardware and software components. Especially dealing with the expected 200 simultaneous proton-proton collisions per bunch crossing will further complicate the track finding. This requires to prepare the software for changes on the computing hardware landscape, possibly exploiting modern CPU, GPU or FPGA architectures. Threadsafety is of particular interest, to enable multithreaded applications while maximizing the physics potential.
On these grounds the Acts package [114, 115] has been established as an experiment independent

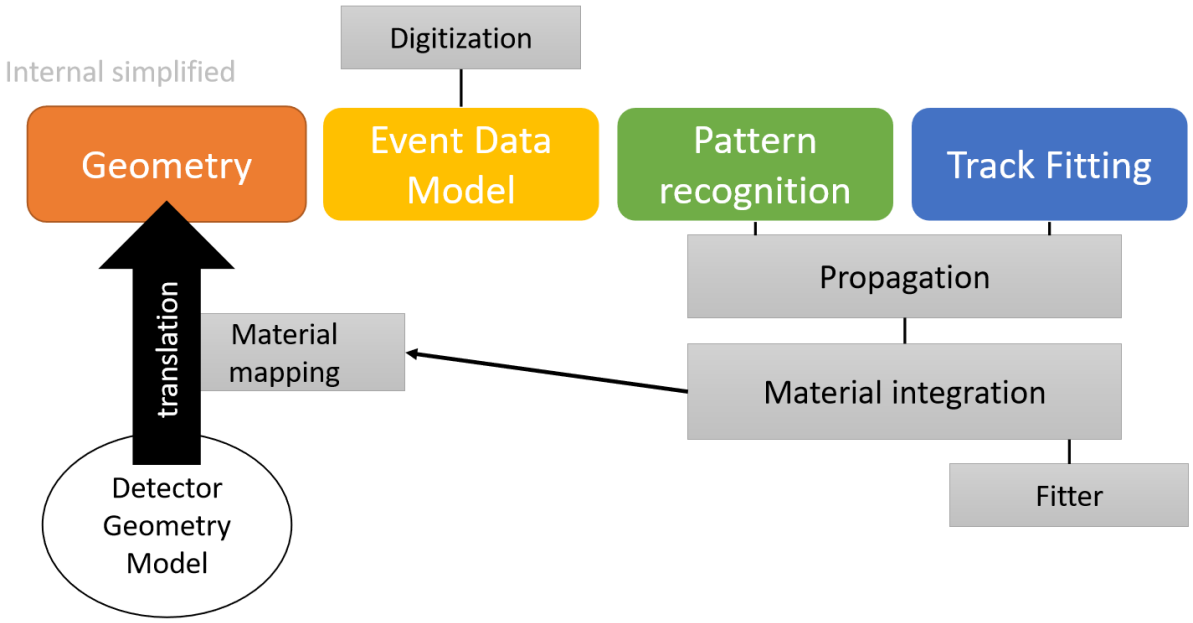

fig. 3.11: Overview of the provided components of the Acts track reconstruction package. This includes an internal and simplified geometry description, an internally used event data model, pattern recognition and track finding algorithms. In addition, digitization and clusterization tools are provided. The geometry can be automatically translated from the respective experimental detector model, using plugins.

track reconstruction package based on ATLAS track reconstruction software. The package however, should not be exclusive for the ATLAS upgrade but is designed as a general toolkit, usable for other experiments or future scenarios as e.g. the FCC design study.

Below, an overview of the Acts tracking package functionality and its components is given. The main building blocks of the Acts package include a tracking geometry description, a bare event data model for track parametrization, high performance and flexible algorithms for track propagation and fitting, and basic track finding algorithms, as shown in fig. 3.11. For track fitting and finding an internal propagation of the particle's parameters (track parameters), described by the internal event data model, through the tracking geometry is needed. This is realized by a propagator, which takes the magnetic field and the change of the particle's trajectory due to material effects into account. Highly templated code ensures experiment independence of the tracking algorithms. To directly interface to external software, as for instance needed for geometry translation, the code can be extended by writing plugins. In this way, the core-package of Acts, is independent of the experimental choices for geometry or magnetic field description and kept at minimal dependencies, namely *Eigen*[116], as an underlying math library[5], and *boost* [117]. If required for the experimental setup, building of certain provided plugins can be enabled. For additional features, the plugin library can be extended.

The templated design of Acts allows to plug in different algorithms for e.g. track finding and fitting. In this way the usage of different algorithms optimized for the specific experimental setups and research and development of fast algorithms for future scenarios is supported.

As a general platform for testing and developing algorithms, independent of any experimental event-processing framework, a simple test-framework was introduced. To test the algorithms

[5] As chosen for the ATLAS Track Reconstruction Software after testing various packages [109]

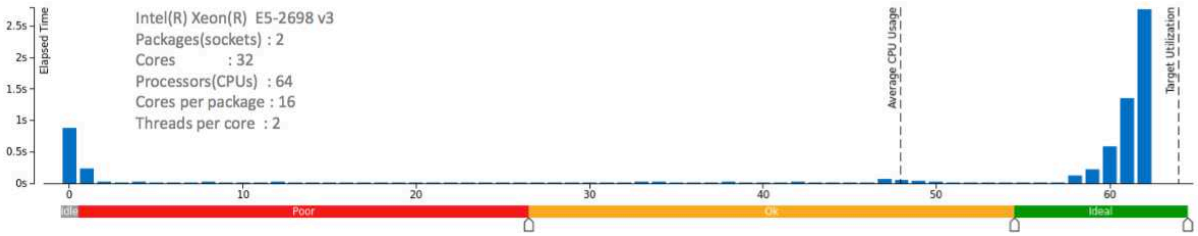

fig. 3.12: CPU-usage histogram for extrapolating track parameters through a generic tracking detector using the Acts test framework on a Xeon machine with 4 cores and 8 threads. The histogram displays the percentage of wall time the specific number of CPUs were running simultaneously. Spin and overhead time add to the Idle CPU usage value. The measurement and the resulting graphics have been done using Intel® VTune™ Amplifier XE [118].

of the Acts core package on thread safety and exploitation of parallelism, the test framework allows multi-threaded event processing. Figure 3.12 shows, for instance, the percentage of time the specific CPUs were running simultaneously when extrapolating track parameters through a generic detector, using Acts, on a 64 CPU machine. During initialization (e.g. geometry building, configuration of algorithms) only one processor is used, while during the main execution of the program, the handling is optimal, using the full capacity of available processors.

In section 3.2.1 and section 3.2.2 the general geometry and material description inside Acts as well as translation plugins from external software are described in further detail. Section 3.2.3 shows how magnetic field support for experiments is realized within the package. In section 3.2.4, a fast simulation application using Acts is introduced and section 3.2.5 shows how the detector response can be emulated in simulation by using geometric digitization and clusterization within Acts.

Since a software package evolves, especially in its early development, and is constantly updated and further enhanced, some of the implemented functionality described in the following (section 3.2.2 and section 3.2.4) was extended, especially with the shortly introduced update of the propagation. However, the underlying work-flow of the implementation still remain the same. In the following sections the software, as it was implemented, is described.

3.2.1 Tracking Geometry

In order to perform track reconstruction, a geometrical representation of the experiment is essential. For accurate full simulation, a detailed description of the detector, as close as possible to reality is required, to correctly emulate the particle's passage through the detector and its interaction with material. For track reconstruction, a simplified view of the detector is sufficient, but is also required to guarantee adequate runtime and CPU-consumption. However, the model should not be oversimplified. The sensitive detector modules, where the particle creates a measurement, as well as the material, which affects the particle's trajectory, need to be described accurately.

The final output of track reconstruction is a global 3D track, spreading over many layers of the detector consisting of several local 2D measurements on detector modules. This track structure, consisting of local measurements, is reflected in the tracking geometry by using surfaces, representing the detector modules. When intersected, the surfaces yield a local measurement and allow local to global transformations of measurement points. As in the physical detector, the surfaces representing the detector modules, are placed into layers. The layers are embedded

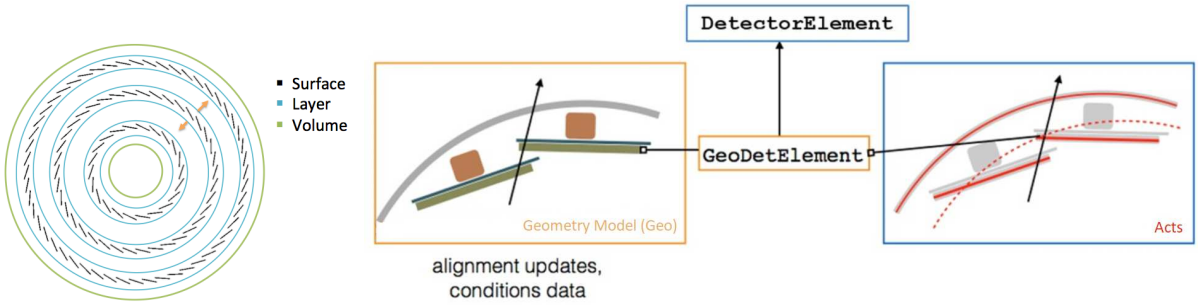

(a) The Acts geometry is described by volumes containing layers, which have a link (realized as a pointer) to their previous and next layer within the volume and surfaces, which describe the sensitive detector modules.

(b) Illustrations of the full and detailed geometry description on the left, versus the simplified, surface-based geometry description within the tracking geometry. Within Acts, a detector module is described by the class object `DetectorElement`, which internally holds a pointer to the original geometry object in the respective geometry description of the experiment. This link allows automated updates of the geometry, needed for alignment or conditions data. Figure by A.Salzburger.

fig. 3.13: Illustration, showing the basic geometry concepts of Acts. On the left, the possible geometry structure of barrel layers of a tracking detector consisting of volumes, layers and modules is shown in transverse plane. The right side shows the description of the sensitive detector modules within Acts.

in volumes, composing the tracking detector, as illustrated in fig. 3.13a. This gives a realistic geometry description of the sensitive detector components, enables localization of the surfaces within the detector and allows track following in the global 3D frame.
The surface concept is an integral part of the Acts tracking geometry because all other geometrical objects can be build from surfaces. In addition, they allow simple intersection. Surfaces are used to describe the sensitive detector parts and also the layer concept consists of a surface representing the layer and two boundary surfaces. A volume is described by its boundary surfaces.
In Acts the surfaces are a pure geometrical concept, which can have different boundary shapes (e.g. rectangle, cylindrical, trapezoidal) and allow intersection. To describe the physical detector module in software and to emulate a particle's interactions with material, more parameters are of need. These include the thickness of the detector module and also a identifier. It also contains information needed for digitization, as for example the readout information and conditions data (e.g. temperature, voltage). Therefore each surface representing a sensitive detector module has a C++ pointer to a `DetectorElement` carrying this information, as illustrated in fig. 3.13b.

For efficient and rapid track reconstruction, a central concept of the tracking geometry is its embedded navigation, which allows fast access to the sensitive surfaces for the propagation of the particle parameters through the tracking detector. This is realized using a bottom-up approach: the surfaces representing the detector modules are binned into a grid within the layers. These layers are binned into volumes representing different detector parts and hierarchies e.g. barrel and endcap, pixel and strip region. The volumes are nested into each other from the inside to the outside of the detector, as illustrated in fig. 3.14. The binning allows fast intersection with a surface or a layer, since only one surface at the intersection estimate and its neighbours need to be checked for possible intersection. Furthermore, layers and volumes have pointers to their neighbours, which allows fast navigation in-between the geometry objects.

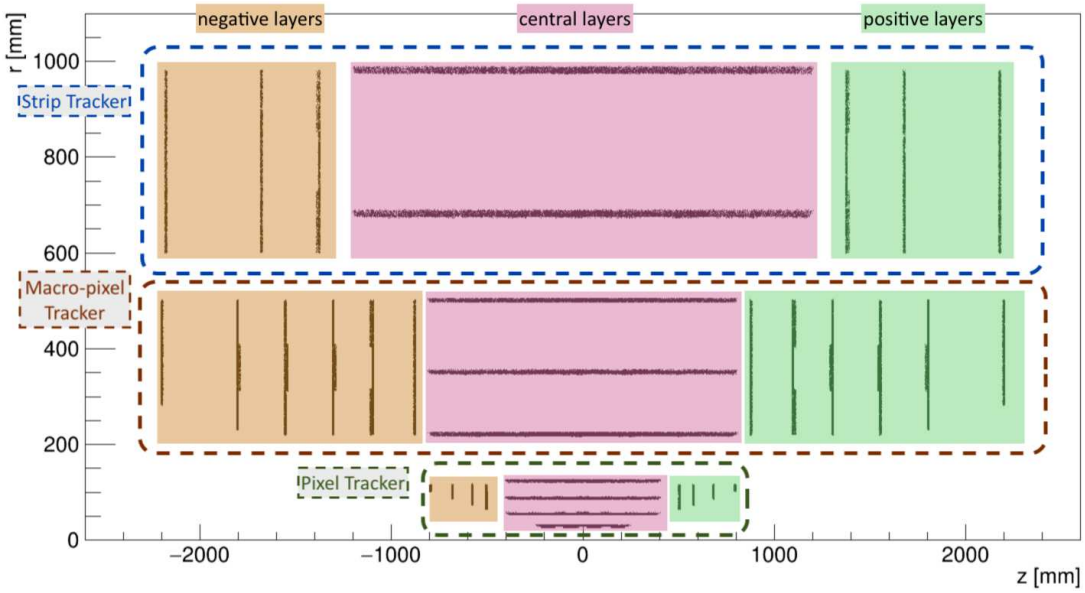

fig. 3.14: Example for a typical barrel-endcap like tracker structure having different subdetectors: *pixel*, *macro-pixel* and *strip* tracker, which are different hierarchies in the Acts geometry consisting of the endcap disc layers on the *negative* and *positive* side, as well as the *central* barrel layers.

Special configurable geometry builders create the tracking geometry from bottom to top, beginning with the lowest hierarchy, which is the subdetector closest to the beam pipe (e.g. the pixel detector) to the the outer parts of the sub detector (e.g. the strip detector). The builders ensure the correct binning and setting of pointers needed for navigation.
As summarized in fig. 3.15 the first step of geometry building is done by a layer builder. It builds all layers of a volume and possibly invokes the building of all contained sensitive surfaces. In case no surfaces are present, the layer is treated like a passive material layer. The surfaces are automatically binned, either in φ/z for the barrel region or in φ/r direction in the disc region. Building the binned array of surfaces is done by a dedicated `SurfaceArrayBuilder`. It automatically determines the bin boundaries using the geometrical extension of the surfaces and bins the surfaces either equidistant or arbitrary, as configured. Surfaces at the same bin position are identified and placed within the same bin to allow for special detector geometries as for instance double sided modules, composed of two single sided sensors. The dimensions of the layer can either be automatically adapted to the geometrical extension of the contained sensitive surfaces or can be set during configuration of the `LayerBuilder`. After all layers of a sub-volume (e.g. the barrel or the endcaps) of the pixel detector are built, the `VolumeBuilder` builds all subvolumes of one hierarchy and wraps this newly built volume around a potential inner volume. Hierarchy is in the following referred to as the hierarchy of sub-volumes in a cylindrical barrel-endcap-like structure, for instance an inner or outer tracking detector. Each geometric hierarchy is either decomposed of a barrel or two endcaps or a barrel and its corresponding endcaps. Similar to the other builders, the dimensions of the volumes can either be specified through configuration (important for translation) or be automatically estimated by the builder from the contained layer dimensions. Finally a high level `GeometryBuilder` steers the whole geometry building, by receiving all relevant volume builders via configuration and builds one final world volume. It returns a handle to the tracking geometry.

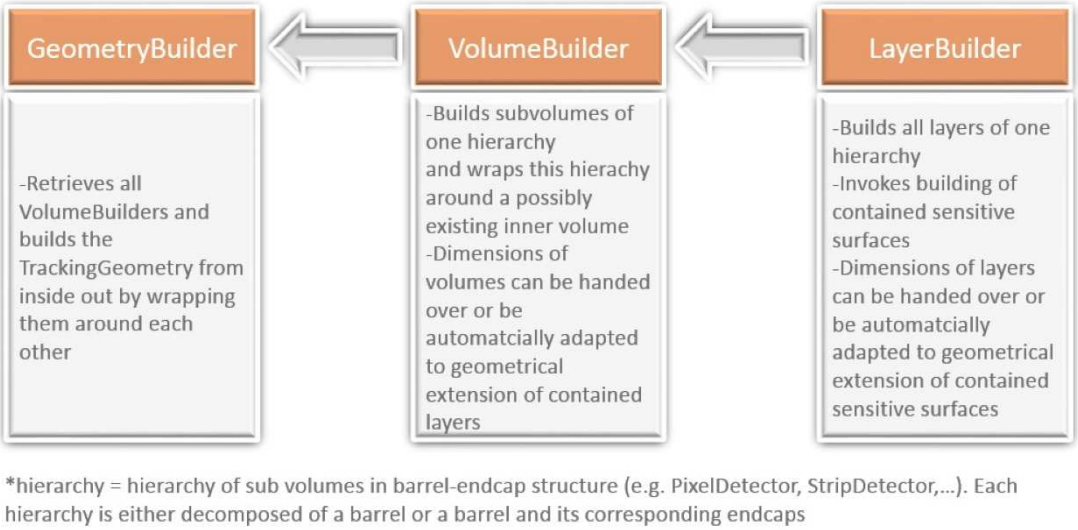

fig. 3.15: Summary of the geometry building process, using geometry builders within Acts.

The possibility to configure the geometry building tools is fundamental to offer a flexible geometry building process for various applications. All geometry builders follow a dedicated interface. The volume builder is currently designed for typical cylinder geometry setups (e.g. ATLAS, CMS or the FCC-hh reference design). It can be easily replaced by another volume builder designed for other (e.g. box-like) detector geometries. During geometry configuration, the dedicated geometry building tools can be selected by specifying which tools should be used.

3.2.1.1 General geometry plugin structure

For an experimental software setup a single in-depth detector description input is recommended, which can be translated into the different representations needed by other software packages. This ensures consistency in case of detector geometry changes during the design phase or adaption to real positions of an installed experiment. During runtime of an experiment, relative movements of the detector components, due to conditions change e.g. temperature, voltage, magnets power cycling, etc. can occur. To determine the exact position, the experiments use a procedure called *alignment* [119, 120]. Hence, an automatic translation procedure from the full and detailed geometry description used for full simulation into the simplified tracking geometry is essential. There are several different geometry modelers that are used in HEP experiments. Therefore, the plugin-mechanism should be used to ensure the geometry translation for an experiment.

As mentioned in section 3.2.1, each surface representing a sensitive detector element is linked to a detector element class, containing detector relevant information, as illustrated in fig. 3.13b. An experiment specific detector element inheriting from the `DetectorElementBase` class provides detector relevant information directly to Acts. The mechanism allows the user to directly use the information provided by the full geometry, by internally using the full geometry object in the Acts-representation of the detector element. Via the direct link any aspect of alignment is automatically taken into account.
After the definition of the specific Acts detector element, using the underlying geometry model, these detector elements need an automatic build mechanism integrated into the Acts geometry building chain, to ensure that the internal navigation is built correctly. A natural entry point is to inherit from the given geometry building tool interfaces, as for instance the `IVolumeBuilder`,

```cpp
/// Interface class for ILayerBuilders in a typical
/// | EC- | Central | EC+ |
/// detector setup.
///
class ILayerBuilder
{
public:
  /// Virtual destructor
  virtual ~ILayerBuilder() = default;
  /// LayerBuilder interface method
  /// @return  the layers at negative side
  virtual const LayerVector
  negativeLayers() const = 0;

  /// LayerBuilder interface method
  /// @return the layers at the central sector
  virtual const LayerVector
  centralLayers() const = 0;

  /// LayerBuilder interface method
  /// @return  the layers at positive side
  virtual const LayerVector
  positiveLayers() const = 0;

  /// Name identification
  /// @return the string based identification
  virtual const std::string&
  identification() const = 0;
};
```

fig. 3.16: The layer builder interface `ILayerBuilder` within Acts. A natural entry point to be used for geometry translations for cylindrical geometries. Each layer builder implementation needs to implement the above functions to build the layers for the different regions.

the `ILayerBuilder` or the `ISurfaceBuilder`. Acts provides automatic geometry building for a few standard detector geometries i.e. plane (possibly also inclined or double sided) modules arranged in cylindrical and barrel-endcap like structures symmetric around the interaction point as e.g. CMS, ATLAS or illustrated in an example tracker in fig. 3.14. In most cases it is sufficient to simply implement a layer builder inheriting from the `ILayerBuilder` interface (see fig. 3.16). The layer builder invokes building of the specific detector elements for the different regions: negative, central, positive (see fig. 3.14) and builds the layers using the tools. The binning of the detector elements and layers as well as the layer and volume building is then automatically done by the provided geometry builder and helper tools.
To summarize, an implementation of the detector element and a layer builder are in most cases the needed components of a geometry plugin in Acts. Since FCC uses DD4hep (see section 3.1.2.1) as underlying geometry package, the support of DD4hep needed to be ensured as a plugin, described in the following, within Acts.

3.2.1.2 The Acts TGeoPlugin

As described in section 3.1.2.1 the DD4hep detector description uses ROOT TGeo [106] as an underlying geometry model. ROOT [97] is widely used in the high energy physics community and also a translation from Geant4 [102] into the ROOT geometry exists. Hence, it was decided to split the pure geometry from the detector description and build a separate `TGeoPlugin` as a first

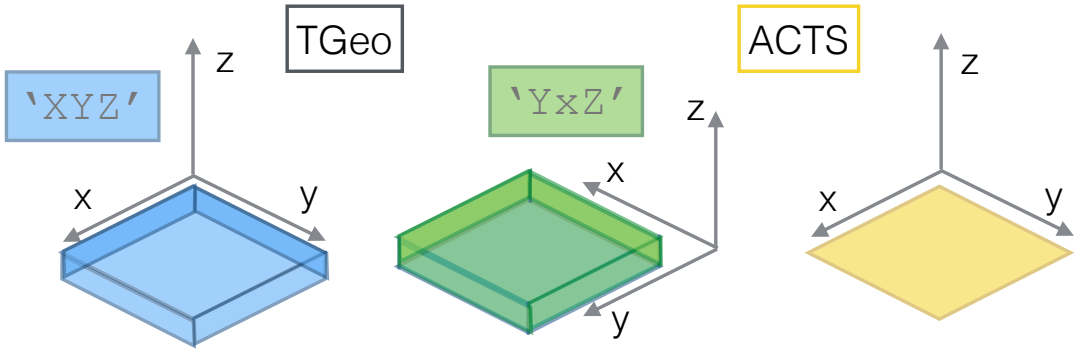

fig. 3.17: The default axis orientation during translation `'XYZ'` meaning that the x-,y-,z-axis of the volume in TGeo should be translated as the x-,y-,z-axis of the surface in Acts is displayed on the left. If, for example, the coordinate system is rotated by 90° around the z-axis, as displayed in the middle, the string should be `'YxZ'`.

step. This allows to also translate standalone `TGeo` geometries into Acts. Since the `TGeoPlugin` requires an additional dependency, namely ROOT, it is only build upon request.
The `TGeoPlugin` introduces a `TGeoDetectorElement` and a `TGeoLayerBuilder`, as generally needed by a geometry plugin in Acts (see section 3.2.1.1). The `TGeoDetectorElement` holds a direct link to the underlying ROOT geometry by having a C++ pointer to a `TGeoNode` object [121] as a private class member, which is set during the object construction, by providing the `TGeoNode` as a function parameter to the class constructor. A `TGeoNode` represents a positioned volume, in the TGeo geometry, that includes the placement and rotation matrix, given as a 4-dimensional transformation matrix, of a volume and its dimensions. In ROOT, the transformation matrix of a node is always given with respect to the volume the node is placed in (the mother-volume). The mother-volume itself (and its mothers) can be placed in other volumes. The global (with respect to the detector) transformation matrix from local to global coordinates can not just be obtained from the node and thus, can be provided as an additional argument during construction. The global transformation matrix is obtained automatically during translation in the layer builder.
The ROOT geometry model does not incorporate any detector relevant information. For this reason, detector relevant information as for instance the digitization information (provided by an Acts `DigitizationModule` see section 3.2.5) or the detector module identification need to be known at construction. The material of the module and a scale factor, which should be applied to all dimensions to translate from TGeo to Acts are additional parameters. In this way, all relevant parameters are provided to internally build the Acts detector element with its associated surface, which holds the boundary, rotation and position information.

Special attention needs to be paid to the fact that the translation of the bounds is not unambigous, because a 3D volume is translated into a 2D surface and the user's choice of axis orientation can be arbitrary. The distinction which axis orientation was chosen, is done by string-identification. This means that the user needs to pass a string, identifying the local coordinate system of the module. `'XYZ'` is the default configuration which means that the local x-,y-,z-axis of the volume in TGeo should be the local x-,y-,z-axis of the surface in Acts, as illustrated in fig. 3.17 on the left. In the middle a system rotated by 90° around the z-axis is displayed. The string for this orientation is `'YxZ'`, which means, that the local y-axis of the TGeo volume should be translated as the local x-axis of the Acts surface and the local x-axis of TGeo should be translated as the negative local y-axis of Acts. An upper case letter indicates that the axis should be translated with positive sign, while a lower case letter indicates that the

```
Acts::ActsExtension::Config layConfig;
layConfig.isLayer               = true;
layConfig.axes                  = "XZy";
layConfig.materialBins1         = 50;
layConfig.materialBins2             = 100;
layConfig.layerMaterialPosition = Acts::LayerMaterialPos::inner

Acts::ActsExtension* layerExtension = new Acts::ActsExtension(layConfig);
layer_detElement.addExtension<Acts::IActsExtension>(layerExtension);
```

fig. 3.18: Example configuration of the `ActsExtension` configuration struct for a layer. Specifying the axis orientation string of the contained modules and information needed for material mapping.

axis should be translated with negative sign. In case the coordinate system is oriented differently the rotation matrix is also translated accordingly, by switching the columns and adapting the sign, if needed. All sorts of configurations are possible, not forcing the first coordinate system to be right handed.
Apart from the detector element implementation the `TGeoPlugin` also contains a configurable layer builder, which scans through the ROOT geometry tree and finds the detector elements as indicated by the user in the configuration.

3.2.1.3 The Acts DD4hepPlugin

The `DD4hepPlugin` automatically converts a given DD4hep tracker into Acts reconstruction geometry. The plugin is build upon request only, because it requires a dependency on DD4hep and on ROOT. Furthermore, it also depends on the `TGeoPlugin`, as explained in section 3.2.1.2. The `DD4hepPlugin` implements the two required components to translate and plug in an external geometry into Acts (see section 3.2.1.1): a detector element implementation and a layer builder. The `DD4hepDetectorElement` in Acts inherits from the `TGeoDetectorElement` and specifies all relevant geometrical information and detector characteristic information e.g. the module identifier, to have identification consistent with the original geometry. Similar as for the TGeo detector element in section 3.2.1.2 an axis configuration string, as well as a unit scale factor can be set at construction. The material is either translated directly from DD4hep or is mapped. Information for digitization, as described later in this section, can be taken directly from DD4hep or be defined.

DD4hep (see section 3.1.2.1) provides a special extension mechanism for its `DetElement` which allows to add custom features or append needed user information. In Acts this functionality is used for the conversion from DD4hep into Acts. The extensions are used to indicate certain detector parts, e.g. if a `dd4hep::DetElement` is the beam pipe or if it is a layer carrying the sensitive modules, because this information can not be known just from the geometrical description. For instance a cylindrical layer is described as a tube in DD4hep, but also the volume containing all layers is described as a tube, hence this additional distinction is needed. The extensions are also used to distinguish if a subdetector is a barrel or an endcap (which is described as a disc volume in Acts) but both described with the underlying TGeo class `TGeoConeSegment` in DD4hep. Furthermore, the extensions are used to provide specific information needed for tracking, e.g. parameters for material mapping or digitization, as well as the axis orientation string. One extension object named `ActsExtension` was created, following an interface `IActsExtension` (as required by the DD4hep implementation). The extension was created in a way to be configurable at runtime. An example for its usage within the detector constructor for a layer specifying material mapping information and axis orientation is shown in fig. 3.18.
In addition the `DD4hepLayerBuilder` inheriting from the `ILayerBuilder`-interface in fig. 3.16 was introduced. As most Acts builders, it uses a configuration struct to configure how the

```
std::unique_ptr<const TrackingGeometry>
convertDD4hepDetector(
    dd4hep::DetElement worldDetElement,
    Logging::Level     loggingLevel          = Logging::Level::INFO,
    BinningType        bTypePhi              = equidistant,
    BinningType        bTypeR                = equidistant,
    BinningType        bTypeZ                = equidistant,
    double             layerEnvelopeR        = 1. * units::_mm,
    double             layerEnvelopeZ        = 1. * units::_mm,
    double             defaultLayerThickness = 10e-10 * units::_mm,
    const std::function<void(std::vector<dd4hep::DetElement>& detectors)>&
        sortSubDetectors
    = sortDetElementsByID);
```

fig. 3.19: Interface of the global DD4hep to Acts translation function. Given the world DD4hep-detector element it returns a unique pointer to the Acts tracking geometry.

detector elements should be binned on the layers, namely if they should be binned equidistant or arbitrary. In both cases the borders are automatically determined by the `SurfaceArrayCreator`. If possible, the use of equidistant binning is recommend, because it is faster. The potential `dd4hep::DetElements` of the negative, central and positive layers, to be translated into Acts, can be configured. The `DD4hepLayerBuilder` then parses the layer `dd4hep::DetElements` and searches recursively for the sensitive modules. Those can be nested in the `dd4hep::DetElement` tree. This means that the sensitive module components do not need to be direct children of the layer. The detector module itself is usually made of several components of material: a sensitive part and additional parts needed for support, readout or cooling. During translation the sensitive part of the module is represented as a surface with a corresponding `DD4hepDetectorElement` in Acts. Material assigned to the sensitive parts in the DD4hep description can be automatically translated into Acts. The corresponding module material can either be mapped (see section 3.2.2) or be directly set via the `ActsExtension`. The desired mapping surface of the layer as well as the binning of the material maps of the layer can be set, as for example done in fig. 3.18. If a list of DD4hep materials is given, an averaged homogeneous material is created, following the averaging mechanism described in eq. (3.1).
The `DD4hepLayerBuilder` extracts and converts all relevant geometric information and transformation from DD4hep to Acts.

A global translation function `convertDD4hepDetector()` (see fig. 3.19) was introduced. Given the world detector element as an input parameter, it translates the whole DD4hep detector. A unique pointer to the fully translated Acts `TrackingGeometry`-object is returned, transferring ownership to the caller. Optional parameters include the log level message output, possibly needed for debugging, the binning option for the modules in the different directions, which can be either *equidistant* or *arbitrary* and a sorting-function to be potentially given by the user. This is needed to sort the subdetectors from bottom to top, to ensure that the Acts geometry is build correctly, by wrapping outer volumes around inner volumes. The default uses the IDs of the detectors and assumes ascending ID-number. The translation allows to take the volume and layer bounds directly from DD4hep, for consistency with the full geometry. For the FCC-hh tracker, the layer and volume dimensions are directly taken from DD4hep. In case the layers and volumes are assemblies in the DD4hep construction (i.e. they are virtual, without any physical shape) the user can specify that Acts automatically builds the layer and volume envelopes according to the contained geometry objects plus a specified tolerance. In case a material layer is an assembly in DD4hep description, a default adaptable default thickness is used. This needs to be done to ensure, that layers are not overlapping. In any case the real thickness of the material is taken to

```
<include ref="PixelTracker.xml"/>
<detectors>
  <detector id="1" name="PixelTracker" type="DD4hep_SubdetectorAssembly"
   vis="BlueVisTrans">
    <shape name="PixelEnvelope" type="Tube" rmin="Env0_rmin"
     rmax="Env0_rmax" dz="Env0_dz" material="Air"/>
      <composite name="Barrel0"/>
      <composite name="nEndCap0"/>
      <composite name="pEndCap0"/>
  </detector>
</detectors>
```

fig. 3.20: Usage of the DD4hep assembly, which only needs to be delared in the XML-description. Where the `Barrel0`, the `nEndcap0` and the `pEndcap0` are the subdetectors of the pixel tracker defined in the file `PixelTracker.xml`

account for material effects, not the default thickness. The flow of the conversion algorithm is described in more detail below, after the use-conditions.

DD4hep is flexible and allows to build any kind of geometry in any way chosen by the user, as described in section 3.1.2.1. To ensure internal navigation in Acts, the detector needs to be build in a certain way: the different volume hierarchies need to be distinctive and grouped together; the detector modules belonging to one layer should be grouped and identifiable as well as the layers belonging to one volume; the detector needs to be build from bottom to top with volume wrapping of the different volume hierarchies. Consequently, there is no completely general automatic translation from DD4hep to Acts for any potential detector description. Hence, the current implementation is restricted on cylindrical symmetrical detectors, which applies for a typical multipurpose high energy detector at a particle collider. In case additional functionality is required, the plugin can be extended. To guarantee a working translation from DD4hep input to Acts geometry the following conditions are summarized below:

- The detector needs to have a barrel-endcap structure: Every hierarchy of subdetectors (e.g. pixel detector, strip detector,..) needs to be composed of either a single barrel or of a barrel and two endcaps (see fig. 3.14).
- If a hierarchy is composed by more than one volume e.g. a barrel and its corresponding endcaps, this needs to be mirrored in the geometry. The volumes can be grouped using the `DD4hep_SubdetectorAssembly` constructor which is provided by DD4hep (see example of usage in fig. 3.20) or by merging those volumes into a volume of "compound"-type.
- Since the translation scans trough the `dd4hep::DetElement` tree, the tree needs to be correctly build and the following objects need to be declared as a DD4hep `dd4hep::DetElement` [6]
  - the subvolumes e.g. barrel, endcap, beampipe[7]
  - layers, containing sensitive material and/or material layers (which will be mapped on the layer if indicated).
  - sensitive detector modules
- The `ActsExtensions` need to be used during the detector construction, indicating if a `DetElement` is:
  - a barrel

[6] The scanning was implemented in way, that the relevant objects do not need to be direct children and can be nested in substructures.

[7] They are usually build with different DD4hep constructors and are `dd4hep::DetElements` per default.

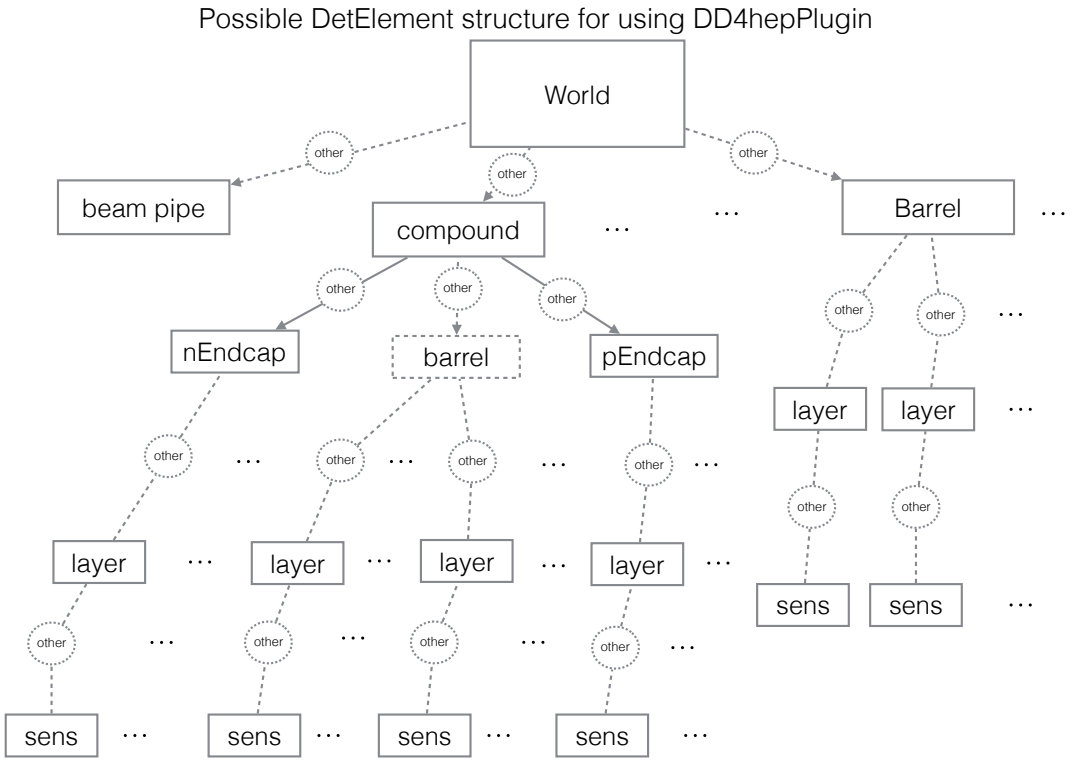

fig. 3.21: Possible DD4hep `DetElement`-structure to be used for translation with the Acts `DD4hepPlugin`. Options are displayed or surrounded with dashed lines and "other" indicates, that any other objects could be in-between.

- an endcap
- the beampipe
- a layer

The possible `dd4hep::DetElement`-tree structure which can be translated by `convertDD4hepDetector()` is displayed in fig. 3.21.

The main conversion function `Acts::convertDD4hepDetector()` is compact, making use of several sub-routines, as displayed in the program-flow in fig. 3.22.

The translation starts with the top DD4hep `DetElement`, the world. It finds possible subdetectors consisting of a barrel and endcaps or endcaps only (e.g. forward part of the tracker) in the `DetElement`-tree. It identifies these detector parts by their `ActsExtension`. The main function configures a volume builder for each of the subdetectors.

The function, creating the Acts `CylinderVolumeBuilders`, does the main part of the translation. It translates possible volume material and calls a sub-routine which collects the possible layers the volumes consist of. The `DD4hepLayerBuilder` and `SurfaceArrayCreator` are automatically configured, using information provided by DD4hep. Finally the Acts geometry building chain is invoked, using the volume builder input and returning an instance of the tracking geometry.

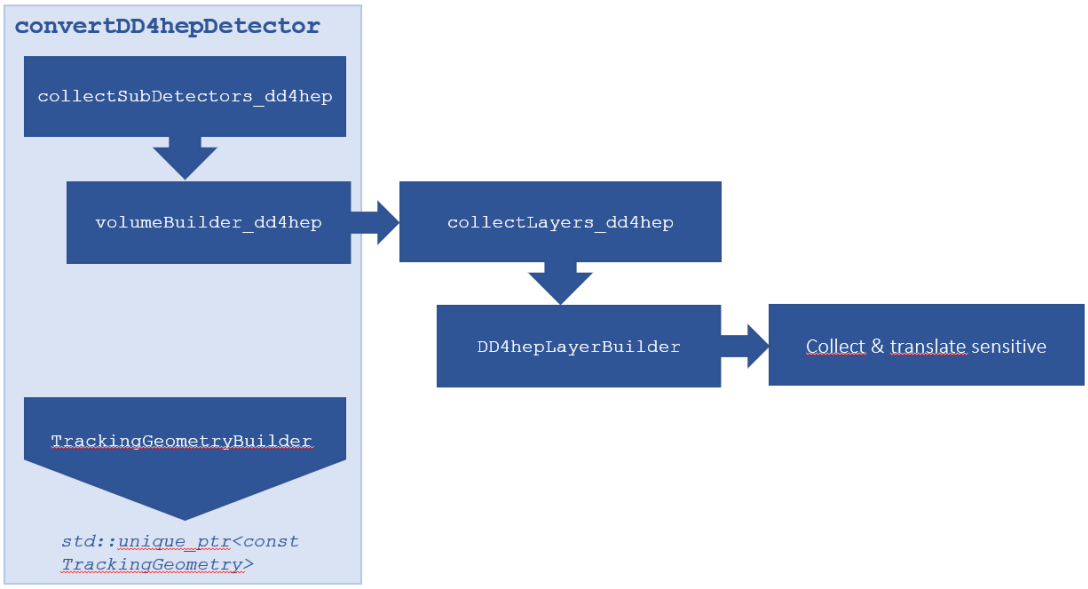

fig. 3.22: Program-flow of the conversion function `convertDD4hepDetector()`, implemented in the `DD4hepPlugin`. First, all possible volumes are found and volume builders are created, which then invoke building of the possibly contained layers. For each layer, the layer builder searches for contained detector modules and translates them to Acts detector elements.

3.2.1.4 DD4hepPlugin validation and tests

The `DD4hepPlugin` was tested with several different tracker setups, which are shown in appendix A.1. The plugin is used for the FCC setup. In fig. 3.23 on the left side the DD4hep geometry input for the FCC-hh scenario using the ROOT *geoDisplay* is shown, while on the right side the translated Acts geometry is displayed using an `obj` file format [122]. In addition to the FCC-hh tracking detector, the simplified version of the electromagnetic and hadronic calorimeter (being described by layers of equivalent material) and the barrel of the FCC-hh muon chambers are build in DD4hep and successfully translated. The full detector description, including the calorimeter material and the muon chambers, is necessary to allow the extension of track reconstruction to the muon detector and to correctly account for the material effects caused by the calorimeters for the extrapolation of the particle track. In Acts representation such an extrapolation of four different muon tracks is shown in red, with the magnetic field switched on, which can be seen in the slight bend of the muon tracks.
This first tests showed that the pure geometry translation is working correctly. The internal navigation within the tracking geometry was tested in a second step, making sure all links between volumes and layers are assigned correctly. Hence, to check that the sensitive volumes are positioned and linked correctly, a propagation test using the acts-test-framework was performed. The test uses a particle gun as input, which randomly produces muons (flat in η and φ) in a given η-range starting from the center of the detector. The muons are propagated through the detector, using the Acts embedded propagator, taking the magnetic field (see section 3.2.3) and material effects (see section 3.2.4) into account. The hit positions in the sensitive material are displayed. If the number of produced muons is sufficiently high, this test should give an image of the tracking detector. Figure 3.24 shows the hit map of this test for 1 M muons produced within $|\eta| < 4$. It agrees with the FCC-hh baseline tracker description in fig. 2.7. For a cross-check, the

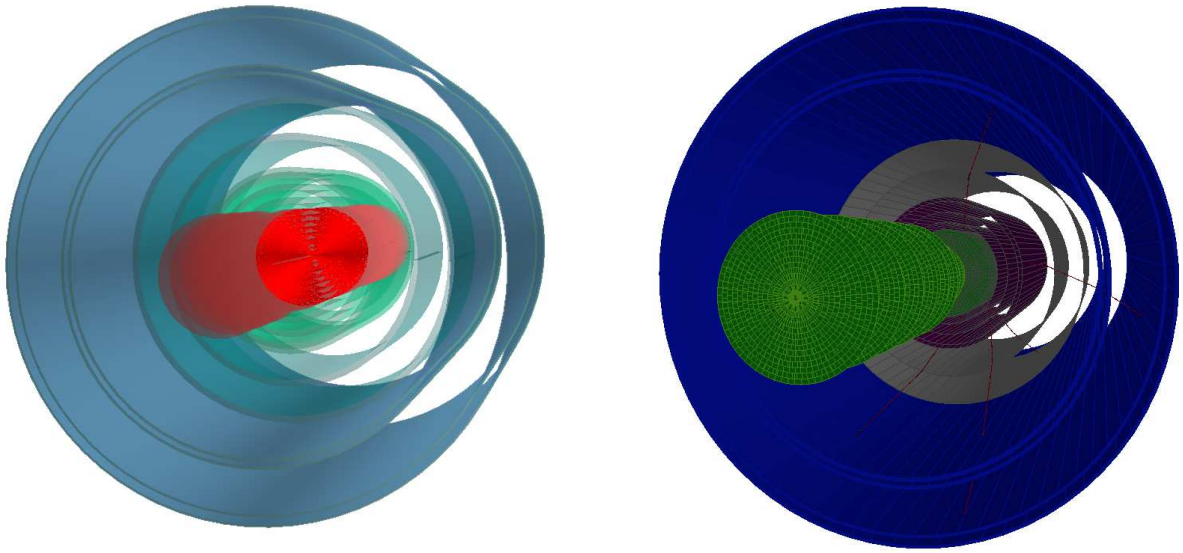

(a) DD4hep geometry displayed with `geoDisplay`.

(b) Tranlated Acts geometry displayed using an *obj* viewer.

fig. 3.23: Comparison showing the working translation from DD4hep geometry (left) input to the translated Acts (right) geometry of the FCC-hh tracker, simplified calorimeters and muons system barrels.

same was done using FCC full simulation (see section 3.1) in fig. 3.25, which conforms to the Acts description.

3.2.2 Material description and translation in Acts

Apart from the geometrical shapes and module positions, the detector material needs to be considered during the propagation of particle track parameters through the detector. Interactions of the particle with the material as for instance multiple scattering or ionization can change the particle track. As described in section 3.2.1, a simplified few of the material of the reconstruction geometry is sufficient but also necessary. For the ATLAS tracking geometry [123] an approach of mapping the detailed material used in the full geometry description onto the layers of the tracking geometry is in use and has proven good performance. Hence, the same strategy is followed for the Acts material description. In the following, the implementation is described.
The material is mapped onto layers of the tracking geometry which are marked to carry support material. This marking is done during the geometry building process, by using a newly introduced `SurfaceMaterialProxy`-class. This class inherits from the general `SurfaceMaterial`-class. In this way, it is treated as any other material during propagation. Information, as for instance how the material description should be binned, in case the material is not homogeneous, can be configured via the proxy.
Since an Acts layer object consists of several surfaces, the material can be mapped onto either, the inner, the outer boundary surface or the middle (representing) surface of the layer. Although the material is assigned to a surface object, the thickness of the material is correctly taken into account. The material is described on a two dimensional grid for each layer. The corresponding C++ class object is named `BinnedSurfaceMaterial`. The user defines the granularity of the grid during the geometry building process.
The material mapping is agnostic to any file format and software, used to create or store the

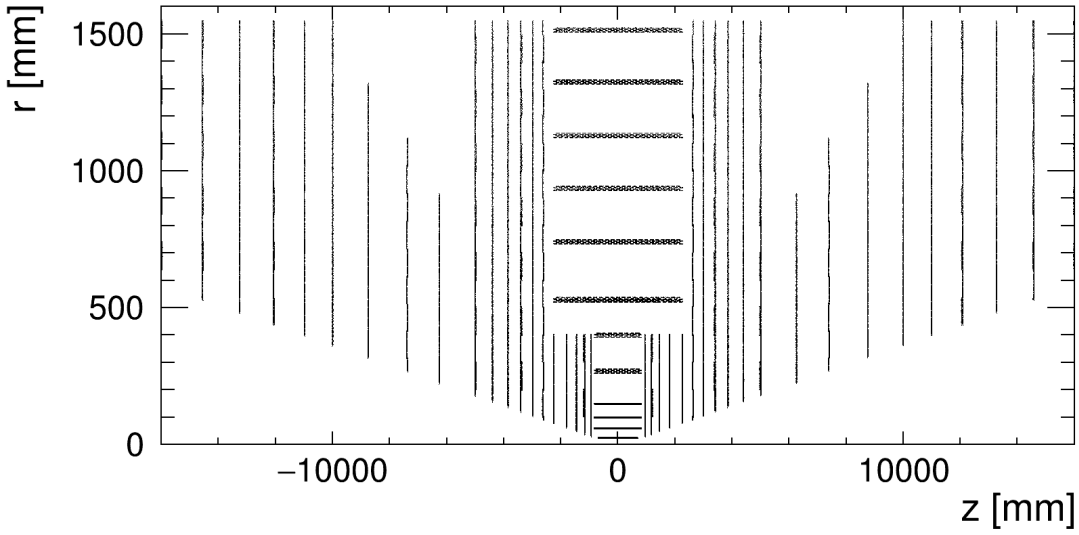

fig. 3.24: Fast simulation ouput, showing the sensitive hits of Acts propagation through the FCC-hh tracking detector, automatically translated from DD4hep using the `DD4hepPlugin`.

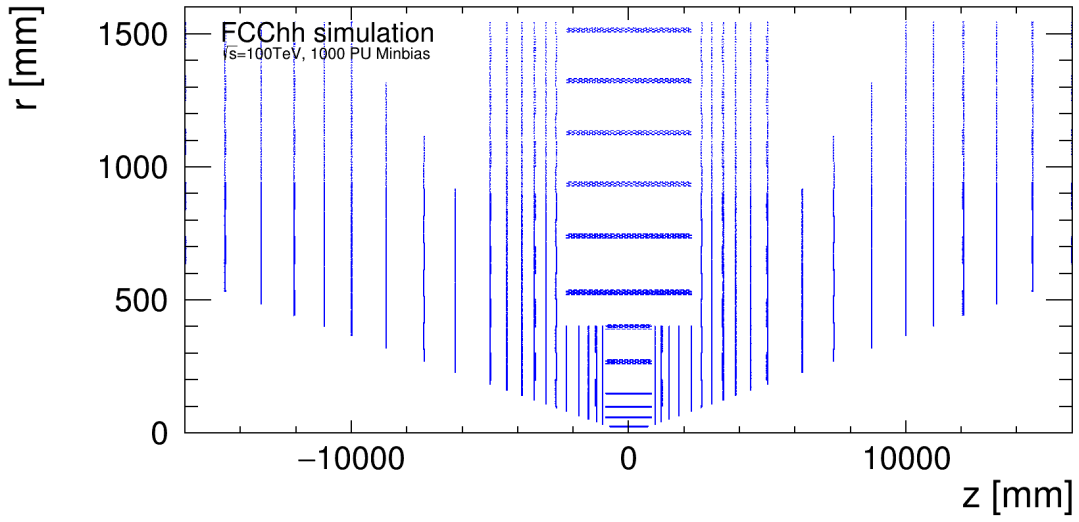

fig. 3.25: Full simulation output, using Geant4, showing the sensitive hits of FCCSW full simulation through the FCC-hh tracking detector described in DD4hep.

material maps. Since it is no key feature of track reconstruction itself, but is rather needed for geometry translation, it is implemented as a plugin and is only build upon request.
To create material maps from the detailed geometry input, the material should be stored in instances of the C++ class object `MaterialTrack`. This material track record class represents a track, starting from a certain position, in a certain direction, described by φ and ϑ and contains the full material record along this track. The material along the material track record is stored as a container of `MaterialStep` instances. Each material step contains the material and its thickness at a certain position. In Acts, the material is described by five parameters (for more detailed definitions see [124]):

- X_0 (radiation length) - material specific constant, which is an important characteristic for electromagnetic particle interactions with material, as for instance multiple scattering, energy loss of charged particles, due to radiation and the mean free path of photons
- L_0 (nuclear interaction length) - material specific constant, describing the mean free path of a hadron before hadronic interaction
- A (atomic mass number) - total number of protons and neutrons in the atomic nucleus
- Z (atomic number) - number of protons in the atomic nucleus
- ρ - the density of the material

Due to material averaging, these parameters are effective values and can be non-physical.
The material mapping process can be split into two sub-processes: the *material assignment* and the *material averaging*. To steer these processes a `MaterialMapping` class was introduced, which offers both functionalities.
During the material assignment process, the decision onto which layer each material step will be assigned, is done. This is illustrated in fig. 3.26, where a layer segment is represented in transverse plane by its three surfaces: *inner*, *representing* and *outer*. It contains detector modules (orange boxes), placed on support material (grey cylinder segment). In this example the material is mapped onto the inner layer surface, which is displayed in green. The inner surface of the next neighbouring layer is represented by a red line. During the material assignment process, the function `mapMaterial()`, uses a `MaterialTrackRecord` (dotted blue line), consisting of a starting point, a direction and different material steps, represented by crosses in the illustration, as input. The three green colored steps are mapped onto the first green layer, while the red colored material step is assigned to the next red layer.

The detailed program flow of the function `mapMaterial()` is described in the following. Given the starting point and direction of the material track, the Acts internal propagation is used to collect all layers marked to carry support material during the geometry building process, by using a proxy. The corresponding hit positions and layers are stored in a map. This map is used to assign each material step to the closest layer hit position. When assigning the material step to a layer, a geometrical projection from the track direction to the layer orientation has to be done. The accumulated material is recorded in a dedicated cache object, the `LayerMaterialRecord`. The `LayerMaterialRecord` stores the gathered material of a certain layer in a matrix, possibly binned, with granularities given by the user. In addition, it stores a collection of all added material steps per track, which can be used to write out material maps per single layer for debugging and validation. The `MaterialMapping` class uses this class to add material (during the mapping process) at a certain position on the layer, which is transformed into the corresponding bin of the grid. When adding material to the same bin, each material parameter is averaged. There are two types of averaging: the *qualitative averaging* of the material along the same track

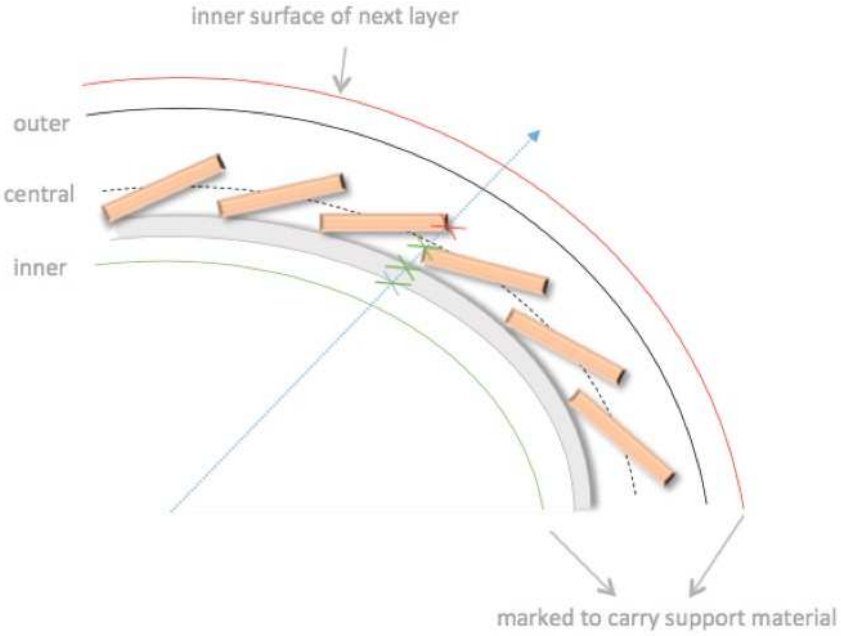

fig. 3.26: Example of material assignment onto the inner boundary surface of the layers. The green points are assigned to the current inner layer, the red points to the next inner layer.

and the *statistical averaging*, in case a bin is hit by several material tracks. The qualitative averaging is needed to correctly describe the material and its total thickness at a certain point. This is usually a mixture of different material components and is done immediately when the steps of a material track are added to a bin. It can be described by the following averaging formulas for the different material parameters:

$$\begin{aligned} \rho &= \frac{\sum_{i=1}^{n} t_i \rho_i}{\sum_{i=1}^{n} t_i} \\ \frac{t}{X_0} &= \sum_{i=1}^{N} \frac{t_i}{X_{0i}} & A &= \frac{\sum_{i=1}^{n} \rho_i A_i}{\sum_{i=1}^{n} \rho_i} \\ \frac{t}{L_0} &= \sum_{i=1}^{N} \frac{t_i}{L_{0i}} & Z &= \frac{\sum_{i=1}^{n} \rho_i Z_i}{\sum_{i=1}^{n} \rho_i} \end{aligned} \tag{3.1}$$

t...thickness, ρ...density, X_0...radiation length, L_0...nuclear interaction length, A...mass number, Z...atomic number

The radiation length, the nuclear interaction length and the density of the material are averaged according to the length of the given material step, while the atomic numbers are averaged according to the density of the material.
In case different material tracks hit the same layer bin, the statistical averaging is done, by first summing up the contributions for each material parameter and finally dividing by the total number of entries of the bin. The statistical averaging is not unambiguous. To stay flexible, on how the material tracks have been obtained, the averaging is only done upon request, by calling the function `averageMaterial()` of the `MaterialMapping`-class.

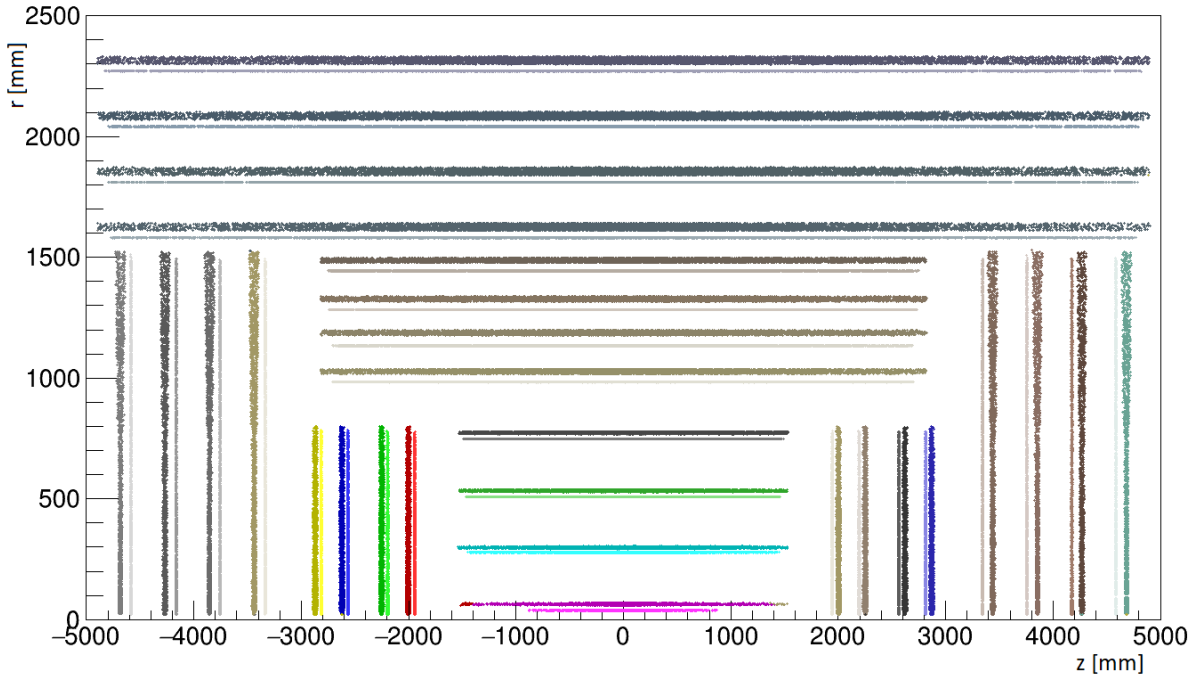

fig. 3.27: Material assignment test for a test tracker (see fig. A.1) with simple modules consisting of silicon only, without support structure. The material was assigned to the inner surface of the tracking geometry. Each layer is shown in a different color. While the darker color shade shows the real material position of the detector modules in the full geometry description, the same color with a lighter shade shows the assigned position in the Acts tracking geometry.

3.2.2.1 Materialmapping support for DD4hepPlugin

As mentioned in the above section, the layers which should carry support material need to be marked during geometry creation. This and the granularity of the layer material can be configured using the `ActsExtension`, as shown in fig. 3.18. For simpler geometries, no projected mapping is needed and the option of a direct translation from DD4hep can be chosen. For composite modules, consisting of different material layers, the `ActsExtension` allows to provide a vector of DD4hep materials. During the translation an averaged material is created for the whole module, using eq. (3.1).

3.2.2.2 Material mapping validation and tests

After the implementation of the above described material mapping algorithm, both, the material assignment and the averaging have been tested and validated. The material maps of the full and detailed geometry are produced using the *Geant4* [102] (see appendix A.3) package. Geant4 offers to track particles that are excluded from any interaction with the detector. For the tests, these so-called *geantinos* have been produced randomly for different directions. The Geant4 simulation was configured in a way to access the passed material at each simulation step and store the map of `MaterialTrackRecord` objects. A dedicated material mapping algorithm reads the material track records and initiates mapping of the material onto the layers of the tracking geometry by using the functionality provided by the `MaterialMapping`-class (as described previously in this section). It calls the statistical averaging function once per run.

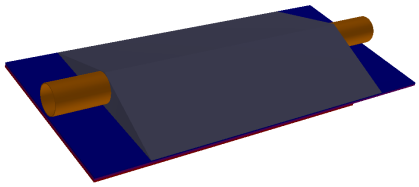

(a) Realistic detector module, used for the material mapping tests. The ATLAS IBL-Module [125] was used as a prototype. It consists of the sensitive Silicon, additional layers needed for readout made of: Silicon, Aluminium and Carbon, and a cooling pipe made of Titan embedded in a Carbon support component.

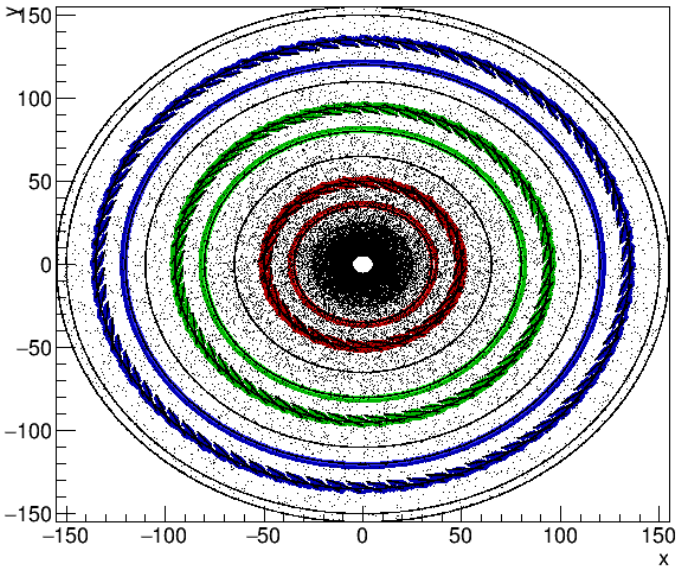

(b) Material assignment test for a test tracker with realistic modules, consisting of different components, placed onto a support layer. The material was assigned to the inner surface of the tracking geometry. Each layer is shown in a different color. While the darker color shade shows the real material position of the detector modules in the full geometry description, the same color with a lighter shade shows the assigned position in the Acts tracking geometry. The sensitive and passive material as seen by Acts propagation is overlaid in black.

fig. 3.28: Material assignment test (right) with test-tracker using more realistic modules (left).

To validate the assignment mechanism, the actual and assigned material positions have been compared. Figure 3.27 shows the comparison of a simple test tracker, consisting of modules made of silicon (see fig. A.1). Each material layer of the Acts geometry is displayed in a different color. Every assigned Geant4 material step is shown in the same coloring but in a slightly darker shading, to show if the material assignment was done correctly.
After the assignment process was found to be correct for this simple model, the same test was done with a more realistic detector setup, consisting of additional readout material and cooling components, as displayed in fig. 3.28a. This more realistic tracker considers support layers for module placement, as shown in the DD4hep input of fig. A.6 and fig. A.7. The result of the material assignment test is shown in fig. 3.28b. The sensitive and passive material seen by Acts propagation is overlaid in black.
To test, if the material on each layer is averaged correctly, the binned 2D material maps are compared to the Geant4 material, assigned to each layer. This comparison is shown for the thickness in units of nuclear interaction length (denoted as $\frac{t}{L_0}$) for the "IBL-like" test tracker in fig. 3.29. When comparing the material map of the Acts with the Geant4 description, the simplification of the averaged Acts material can be seen.

To test the full material seen by a particle along its path, a procedure similar to creating the full material maps is done. Instead of using the full Geant4 geometry, the tracking geometry on whose layers the material was just mapped on, is used. This test scans through the tracking

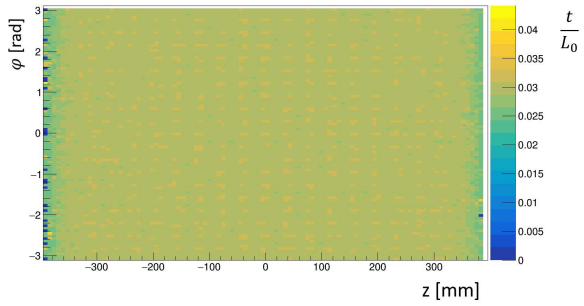

(a) Print-out showing the 2D material map assigned to this layer in Acts description using a binning of 100 × 100.

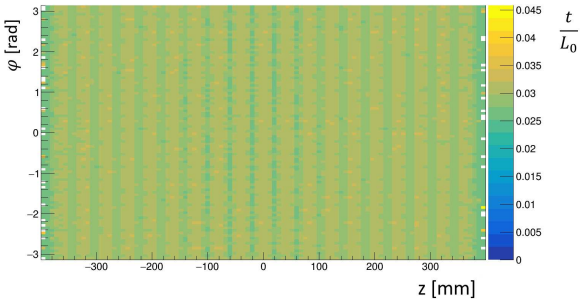

(b) Two-dimensional map showing the Geant4 assigned material at each point of the layer.

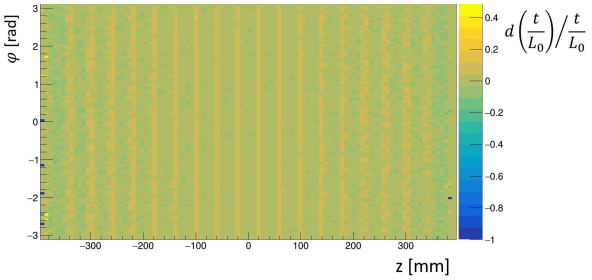

(c) Relative error of the thickness in units of nuclear interaction length for each point on barrel layer 3 of the IBL-like test tracker, between the Acts and the Geant4 material, assigned to that layer.

fig. 3.29: Comparison of thickness (t) in units of nuclear interaction length (L_0) between the full Geant4 material assigned to the third layer and the mapped material in Acts description using 1M single muon Events.

geometry, by extrapolating particles in random directions through the Acts detector and writing out `MaterialTrackRecords`. In this way, the full material a particle sees during propagation through the simplified reconstruction geometry, can be compared to the detailed description in Geant4. The outcome for the thickness in units of radiation length, using the "IBL-like" test tracker is shown in fig. 3.30. The average relative error is below 1%, only at very high η, where the particle passes a big amount of material due to the high incident angle, the error is increased.

3.2.3 Magnetic field integration into Acts

To determine the momentum and the sign of the electric charge of charged particles in a tracking detector, the whole tracking region is embedded in a magnetic field. The strength and shape of the magnetic field depends on the experiment. For instance, the FCC-hh baseline design foresees a 4 T solenoid (see section 2.2), while the ATLAS experiment uses a 2 T hybrid system consisting of a solenoid for the inner tracking system and toroid for the muon system and endcap region [126]. The bending of charged particles within the tracker, due to the magnetic field, needs to be correctly taken into account during simulation and track reconstruction. For this purpose the magnetic field needs to be accessed at any possible point of the detector during propagation. Among others, Acts provides two C++ classes for possible magnetic field implementations: `ConstantBField` and `InterpolatedBFieldMap`. Both classes have the same interface, returning the three-dimensional magnetic field value at a given position. This allows

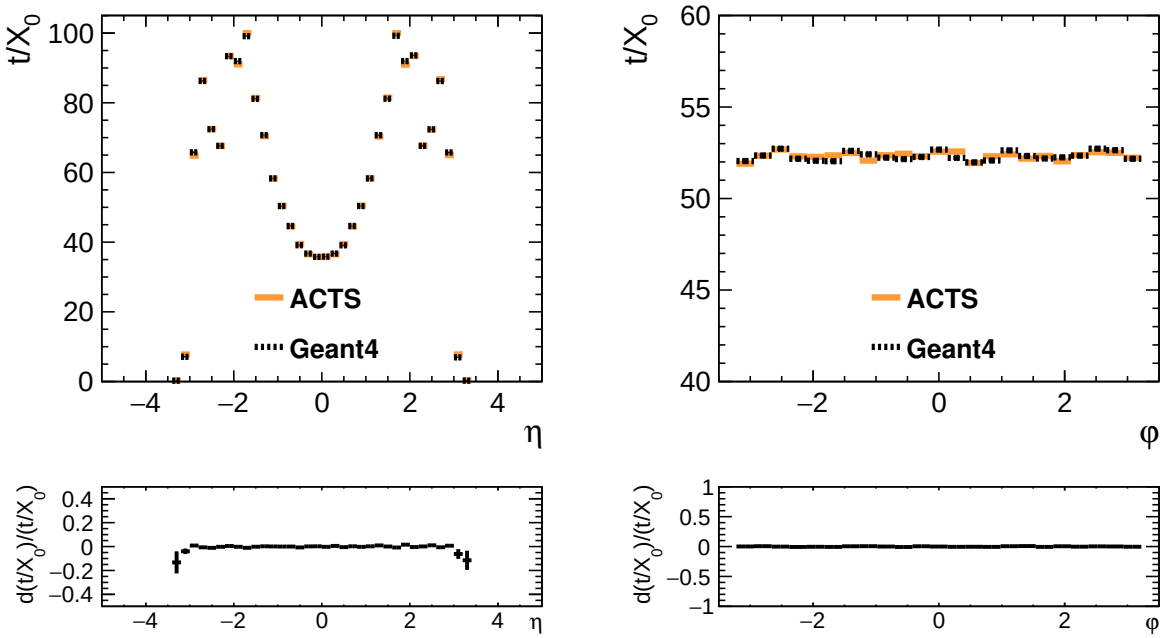

fig. 3.30: Comparison of the full thickness in units of radiation length, seen by a particle along its path, drawn against the pseudorapidity η on the left and against φ on the right, with the corresponding errors. The material was averaged using 1M single muon events. The material seen in full simulation using Geant4 is displayed in black, while the material seen during propagation through the Acts tracking geometry is displayed in orange.

consistent and straightforward replacement of the magnetic field description, by avoiding virtual function calls, since the Acts `Propagator` is templated on the magnetic field type. The constant magnetic field class returns the same value, given by configuration, at each point. The second implementation linearly interpolates the field value at a point, given a magnetic field map. The constant implementation can be sufficient to approximately describe the field of a solenoid. For a realistic description of an experiment, a magnetic field map describing the measured (or simulated) magnetic field is essential. Therefore, a mechanism to automatically create an `InterpolatedBFieldMap`-object from a given field map was implemented.
Functions (see interfaces in fig. A.8) allow to set up the interpolated field mapper in Acts with magnetic field values at positions, either given in Cartesian coordinates `xyz` or in rotational symmetric cylindrical coordinates *rz*. The functions use STL vectors to create the magnetic field map, in order to stay independent of any file format.

The functions have been tested with the ATLAS (given in cartesian coordinates) and FCC-hh (first quadrant in cylinder coordinates given) magnetic field maps. To test that both, reading in as well as the interpolation works correctly, interpolation through a given map at any point can be done. fig. 3.31 and fig. 3.32 show examples for these tests.

3.2.4 Material effects implementation and fast track simulation (FATRAS) using the Acts package

When a charged particle passes through matter, different effects, depending on the particle type and attributes as well as on the material properties, can occur. Those include interactions of

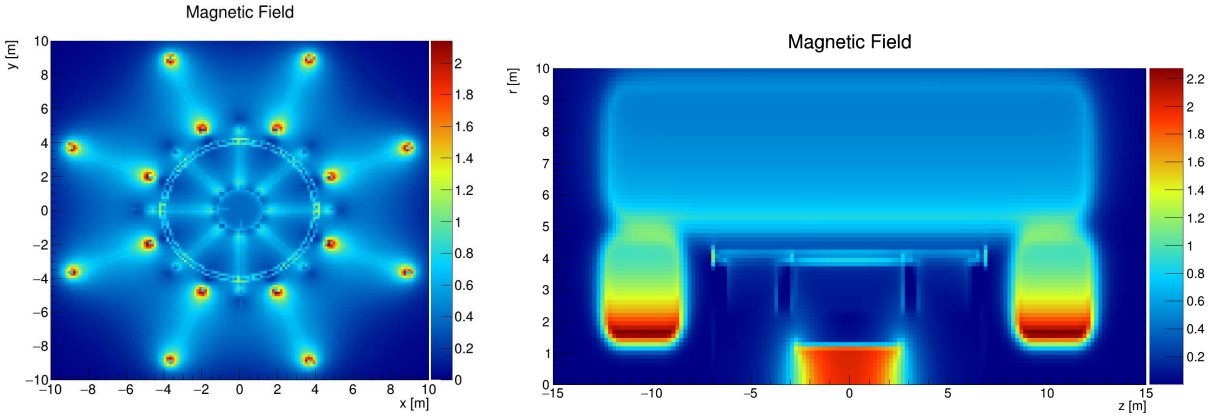

fig. 3.31: Display of magnetic field value at any point of the ATLAS detector map, obtained by reading in the ATLAS magnetic field map and using the interpolated field mapper. This test illustrates the correct magnetic field functionality in Acts for using the ATLAS magnetic field map given in `xyz` format.

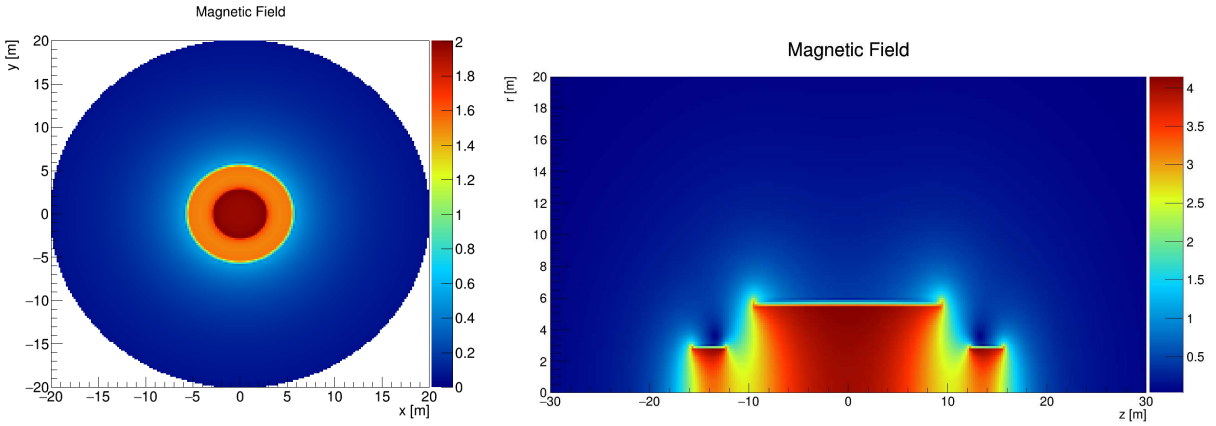

fig. 3.32: Display of magnetic field value at any point of the FCC-hh baseline detector map, obtained by reading in the FCC-hh magnetic field map and using the interpolated field mapper. This test illustrates the correct magnetic field functionality in Acts for using the FCC-hh field map given in `rz` format for the first octant.

the charged particle with the electronic shell of the absorber material, as for instance multiple scattering or energy loss due to ionization and radiation, and less frequently occuring hadronic interactions, for strongly interacting particles. For a detailed description of the passage of particles through matter and related effects please see [124]. Material interactions can deflect the particle (as in Coulomb Scattering), lead to the decrease of the particle's momentum or to the destruction of the particle. Simulation and reconstruction need to take these effects into account. This section is dedicated to a first integration and validation of the most relevant material interaction effects into an Acts fast simulation package *acts-fatras*.

There are different types of fast simulation. From a pure parametric smearing of the particle parameters to emulate a measurement, to simulation types producing the same type of output as full simulation, but using other approximations. The fast simulation type described in the following, uses the latter approach. For the ATLAS experiment using a fast simulation based on its track reconstruction software, named FATRAS [127], has proven to be a useful tool for producing large statistics of event samples in reasonable time. Due to its simplified geometry (with embedded navigation) but adequate material description, the simulation is significantly faster but in good agreement with the detailed full simulation [128].

The same strategy is followed for the Acts track reconstruction package, resulting in an additional package *acts-fatras* [129] which builds on the acts-core package. It provides tools which steer the simulation and the particle interactions with the material. Similar as for the acts-core package, the ATLAS code of FATRAS was used as a starting point. For the first implementation of FATRAS into Acts, only the most frequently occuring effects, namely multiple scattering and energy loss due to ionization, have been taken into account. The acts-fatras package uses the standard Acts propagator used for reconstruction. Since the material effects integration differs for reconstruction and simulation, different material interaction modules can be plugged into the propagator. For the reconstruction a default material effects engine is provided within the core package, taking average multiple scattering and energy loss effects into account. Simulation, however, needs a probabilistic approach following Monte Carlo techniques, which try to emulate small fluctuations in the outcome of an experiment by introducing a certain degree of randomness. In the FATRAS code, the different material effects are described by different samplers, i.e. one sampler for energy loss and another sampler for multiple scattering was implemented. The necessary samplers can be specified at runtime. Both samplers do surface-based updates, i.e. update the track parameters once after traversing a given material surface. This approach is accurate for the tracker, since the material is layered. For volume-based material simulation as it is the case for e.g. the calorimeters, steps within the material need to be done. Both samplers need to draw random numbers, following different distributions. During the simulation process, dedicated care is taken in order to allow for reproducible pseudo-random generators[8]

The energy loss sampler describes, when a moderately relativistic, charged, heavy particle passes

[8]Since the FATRAS repository provides tools to apply material interactions but does not steer the execution of the event loop, a reliable random generator needs to be provided by the respective experimental framework. In this way Acts follows the use of `C++11 Standard Template Library(STL)`-random number generators: with the source of randomness (in form of a random generator/engine/service) being decoupled from the particular distribution the random number should follow. The random generator needs to satisfy the STL-*UniformRandomBitGenerators* [130] generator concept, producing a uniformly distributed random number of specified type, in given bounds. The random distribution then uses the generator as input to produce a random number according to a specified distribution. Since each experiment will use a dedicated implementation of a random number generator, the samplers as well as the material interaction engine have been templated onto the random generator. To ensure thread safety, one random generator needs to be specified for each execution as a function parameter. The random number distributions are provided by acts-fatras, using the the following `C++ STL` distributions: normal, uniform, gamma and poisson. Additionally a Landau distribution is provided using quantiles provided by CERNLIB G110 [131].

through matter and undergoes inelastic scatters with the shell electrons of the material. This leads to excitation or ionization of those electrons. Hence, the particle loses kinetic energy along its path, which leads to a change of path of the particle within the magnetic field, due to momentum loss. This contribution to the energy loss will be referred to in the following as *ionization energy loss* and denoted as $\langle -\frac{\mathrm{dE}}{\mathrm{dx}} \rangle_{\mathrm{ionization}}$. For track reconstruction, the mean value of the energy loss due to ionization (described accurately by the Bethe-Bloch formula, see appendix A.4.1) is used and the resulting standard deviation is needed for the track parameter's covariance transport. For FATRAS, the energy loss is simulated by first calculating the most probable (MOP) energy loss (see appendix A.4.3) and then adding a landau distributed fluctuation:

$$\frac{\mathrm{dE}}{\mathrm{dx}}^{\mathrm{simulated}}_{\mathrm{ionization}} = \frac{\mathrm{dE}}{\mathrm{dx}}^{\mathrm{MOP}}_{\mathrm{ionization}} * \mathrm{scalor}_{\mathrm{eLoss}} + \sigma_{\mathrm{Landau}} \mathrm{rn}_{\mathrm{landau}} * \mathrm{scalor}_{\sigma} \tag{3.2}$$

$\mathrm{rn}_{\mathrm{landau}}$...random number following the landau distribution, $\mathrm{scalor}_{\mathrm{eLoss}}$, scalor_{σ}...possible scalors to be applied

The energy loss is sampled according to the traversed material represented by the current surface and material properties.
Additional fast samplers based on Gaussian mixture or non-Gaussian tail sampling to account for multiple elastic scatters of the charged particle with the atomic nuclei of the absorber material are also available. The mean scattering angle is calculated using the Highland parameterization, as stated in appendix A.4.4

3.2.4.1 FATRAS Validation

After the implementation of the above described material effects into FATRAS, they have been validated against the full simulation package Geant4 (see appendix A.3). To assure the same geometry is used by both, DD4hep was used as a common geometry input, since the needed translations to Acts and Geant4 have already been provided (see section 3.2.1.3) or integrated. For the validation, a simple cylindrical silicon layer, with a thickness of 320 µm has been implemented in DD4hep with 10 mm radius. A second sensitive layer, without material, was placed at 1 m radius to measure the differences in energy and momentum direction. To provide particle input to the Acts extrapolation, using the FATRAS material effects, a configurable particle gun was implemented into the acts-framework which creates particles of given type with random momentum and direction (flat in η and φ) in given ranges.
The energy loss validation was done for muons produced centrally in radial direction $(1, 0, 0)$ with a transverse momentum of 1 GeV, varying the thickness of the cylinder: 100 µm, 320 µm and 1 mm. After a first comparison of the energy loss between Acts and Geant4, it was found, that the most probable value was slightly shifted towards higher values in Acts and that the variance was too broad. Hence, scalors to both, the most probable value and the standard deviation have been introduced. Figure 3.33a shows the validation using scalors, as explained in appendix A.5.

For the multiple scattering validation, the muon transverse momentum was varied using: 1 GeV, 10 GeV and 100 GeV. For this case the Acts and the Geant4 simulation have been in good agreement without the need of parameterization, see fig. 3.33b.

3.2.5 Digitization and Clusterization

The digitization and clusterization methods described in the following are used for FCC-hh tracker performance studies: for obtaining the channel occupancy and data rates (see chapter 4) and double track resolution in b-jets, as described in chapter 5.
When a particle passes the sensitive region of a detector module, with a certain incident angle

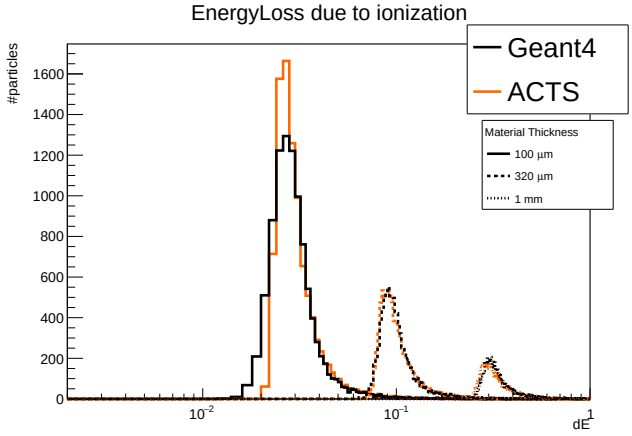

(a) Comparison of energy loss due to ionization of Acts fast simulation (orange) compared to Geant4 simulation (black), for different material thicknesses. The difference in energy is shown.

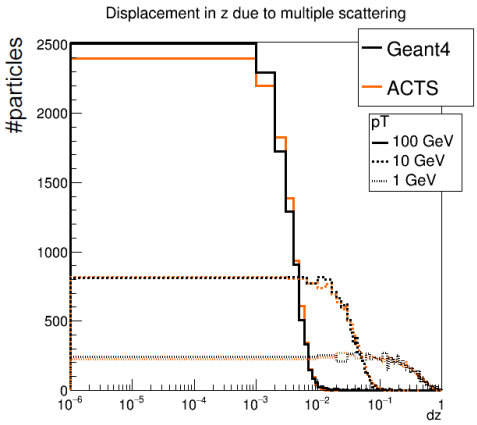

(b) Comparison of the deviation of the particle track due multiple scattering effects of Acts fast simulation (orange) compared to Geant4 simulation (black), for different particle transverse momenta.

fig. 3.33: Validation of Acts FATRAS material effects against Geant4, using single muons.

with respect to the module, it will traverse one or more readout cells and deposit charge in those cells, as illustrated in fig. 3.34. As soon as the generated charge exceeds a detector specific threshold, those cells will be registered by the readout to be *activated* and the detector signal will be processed further. Digitization strongly depends on the specific detector type and is usually implemented within the experimental framework. For design studies of future tracking detectors (as e.g. FCC-hh) the particular detector technologies are not defined yet. Therefore a geometric approach to digitization, which can be used as a good approximation of existing detector technologies is provided by Acts. This section describes the geometric digitization in Acts and the introduction of a clusterization process using the cells obtained by digitization. The clusterization is generic and can as well be applied to other (more realistic) digitization models. A general introduction to digitization and clusterization, as well as its usage within FCCSW was given in section 3.1.4.

The readout granularity determines how many cells are traversed by the particle, which determines the cluster shape and size. Hence, the readout granularity and other readout relevant information, e.g. energy threshold or the readout type (digital/analogue) are implemented to be configurable. The configuration is done during geometry construction, by creating a `DigitizationModule` (C++) class object, which is held by the detector element class of Acts. The `DigitizationModule` calculates all sensitive cells (implemented as `DigitizationCell` objects) which are hit during a simulation step, as shown in fig. 3.34. The `DigitizationCell` is a simple C++ struct, holding the identification of possibly up to two channels, for one- or two-dimensional segmentation of the readout chip e.g. silicon strip or pixel. To emulate *digital* readout, this information is sufficient. Additionally, the cell can store the deposited energy or other readout data in case of *analogue* readout.

For clusterization the exact cluster sizes and shapes are not known in advance. Thus, all combinations of cells need to be considered. This problem is commonly known in pattern recognition and can be solved using a *connected component labelling* approach. It is realized as a function, finding all neighbouring cells on a detector module and bundling them into simple STL

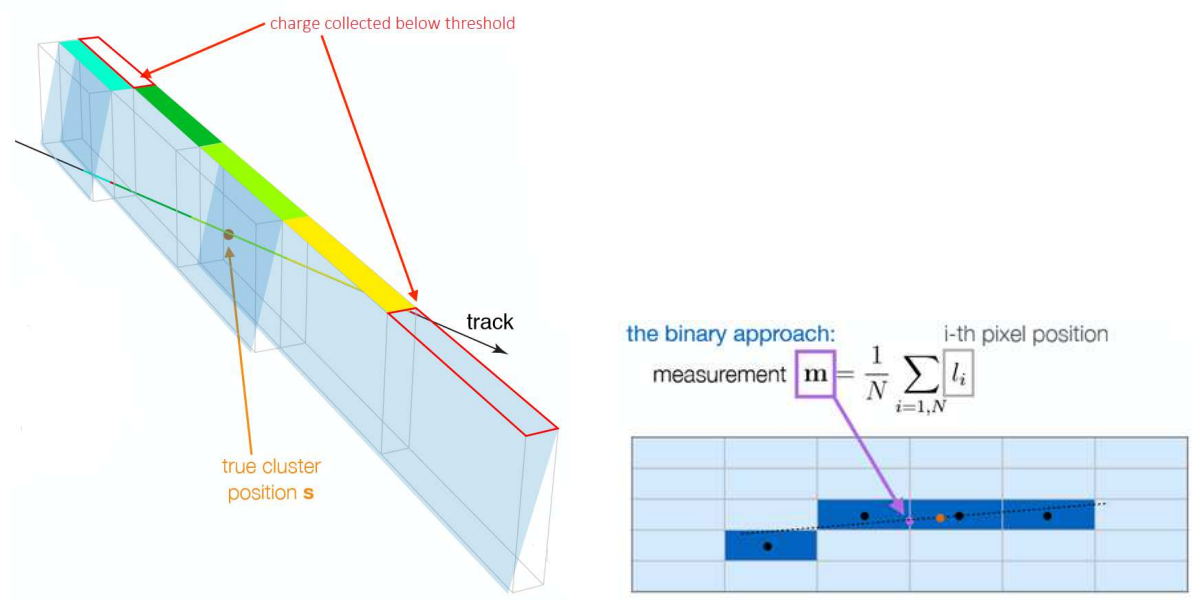

fig. 3.34: Two illustrations showing the digitization and clusterization process. The figure on the left shows cells being activated by one track, in 3D. If the energy deposited within the cell is below threshold, the cell will not be activated. On the right, the calculation of the cluster position for the digital case is shown in 2D. Figures by A. Salzburger.

```
template <typename cell_t>
std::vector<std::vector<cell_t>>
createClusters(std::unordered_map<size_t, std::pair<cell_t, bool>>& cellMap,
               size_t nBins0,
               bool   commonCorner = true,
               double energyCut    = 0.);
```

fig. 3.35: The function definition of the clusterization method, implemented in Acts. It receives the digitization cells of one detector module and bundles the neighbouring cells to create clusters. An energy cut (excluding cells which fall below threshold) can be applied. The function is templated on the digitization cell type to allow users to use their own implementation of `Acts::DigitizationCell`.

vectors, to stay independent of the particular cluster type, to be used in an experiment. The definition of the function, which can be used in an algorithm within an experimental framework, is shown in fig. 3.35. The function is templated onto the digitization cell to allow other or inherited cell implementations, which carry additional information. It is required, that the cell provides channel identification to find the neighbouring channels, as shown in fig. 3.36a in orange and green. The cells are stored in a hashmap[9], which use a global index for each cell per module. Planar modules with 2D readout are assumed. If cells sharing a common corner or a common edge should be merged into one cluster, can be configured.
Clusterization is applied for all cells of one module. Since same cells can be hit by different particles of the same event, clusterization needs to be done after all cells have been collected for one event. In case another particle hits the same cell, the cell information needs to be merged for analogue readout. For this purpose the function `addCell()` of the `DigitizationCell`, summing up all energy deposits, was implemented.
Since in general (even at $\langle\mu\rangle = 1000$) the activated cells are rather sparsely distributed on one detector module, which can have up to tens of thousands of pitches in total, a *sparse matrix* approach is used. For this approach only the activated cells are filled into the above described hashmap for each module. The map also contains information, if a cell was already assigned to a cluster.
The workflow of the implemented clustering algorithm is described in the following. The algorithm starts by filling the first cell into the first cluster container. Then all activated and not used neighbours of this cell are also put into this cluster container. As soon as a cell is assigned to a cluster the cell will be marked as 'used', so that it will not be used for creation of any other cluster. After all neighbours of a cluster are found, the same procedure is repeated with the next cells, which have not already been assigned to a cluster. In this way, one cluster is filled completely at a time before filling the next cluster. The global grid index, starts at the top left corner of the grid and then continues to the right for each line, as displayed in fig. 3.36a. Because only one global index is used, also the total number of possible bins in one row needs to be given to calculate the neighbouring indices.

For the FCC-hh case with $\langle\mu\rangle = 1000$ it was found that on average $\sim 54\,\text{M}$ cells on more than 49 000 modules are created per event. The runtime can become an issue and the clustering algorithm needs to be fast and use an optimized data model. Therefore, the algorithm has been optimized. Before arriving at the presented more efficient implementation, different data models have been used. This included using 2D cell identification, 2D cell identification using bit-shifting (using one identifier only), using pointers to cells instead of copying cells, et cetera. Instead of using a `std::unordered_map`, with an amortized look-up time in the order of O(1), also a `std::map` (O(log(n))) was tested, which was found to be 50 % slower. An alternative approach using a look-up window with arrays, checking for neighbours to the right and stopping as soon as no neighbour is found, repeating the same procedure to the left, was tested. The number of activated cells is rather dense, so that this variation took more than double the time of the hash-map solution. The final implementation was tested for different pile-up scenarios and found to scale linearly with pile-up, as shown in fig. 3.36b.

The validation of the Acts digitization and clusterization tools using muons and pions within FCCSW is shown in appendix A.6.

[9] Realized by using a `std::unordered_map` of the C++ standard library [132].

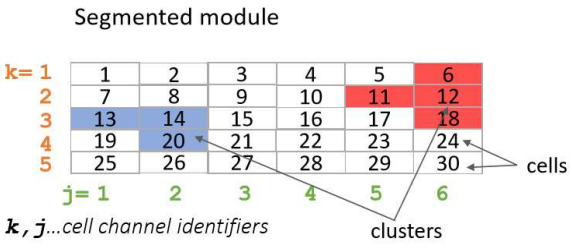

(a) Illustration of the readout-module, segmented into cells. The indices j and k in green and orange show the channel numbers in each direction for 2D binning. Only one global bin is used for clusterization. It starts at the upper left corner and continues to the right and down.

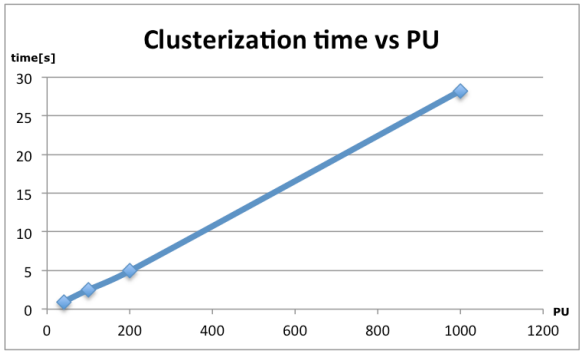

(b) The time spend in the `createClusters()` method (see fig. 3.35), using merged minimum bias events at 100 TeV for different pile-up scenarios: no-pile-up (just one minimum bias event), $\langle\mu\rangle = 40$, $\langle\mu\rangle = 200$ and $\langle\mu\rangle = 1000$. The clusterization scales linearly with the pile-up and needs approximately 30 s to cluster ~ 54 M cells.

fig. 3.36: Definition of the cell identifiers (left) and time needed for clusterization versus pile-up (right).

Chapter 4

Occupancy and data rates of the FCC-hh baseline tracker

The high pile up environment, as described in chapter 2 of the FCC-hh scenario is expected to be a major challenge for pattern recognition of particle tracks. At an average pile-up rate $\langle\mu\rangle$ of 1000 the density of measurements will be highly increased, which will significantly raise the number of possible hit combination and finally further complicate pattern recognition.
Therefore, studying the cluster occupancy (density of measurements) as well as the channel occupancy is important to predict the tracker performance. The channel occupancy also allows for a first estimate of the expected full data rates at first trigger level. The data rates together with the needed radiation tolerances will set the requirements on suitable readout technologies.
To obtain the channel occupancy, full simulation (details in section 3.1) of 100 TeV proton-proton collisions have to be performed. The energy deposits of the ionizing particles are modeled by Geant4 and used as input for a geometric digitization, which is followed by clusterization, as described in detail in section 3.1.4. The particle spectrum at 100 TeV is explored in section 4.1. In section 4.2, the measurements obtained after clusterization, are studied in detail. The channel occupancy also depends on the size of the cluster (= number of channels contributing to one cluster), which is examined in section 4.3. Section 4.4 and section 4.5 summarize the findings on the channel occupancy and data rates to be expected at the FCC-hh for $\langle\mu\rangle = 1000$.

4.1 Charged particle spectra at 100 TeV

When colliding protons, two possible scattering processes may occur: *elastic*, where the particle's kinetic energy is conserved and both protons stay intact, and *inelastic*. Inelastic scattering is further divided into three distinct processes: *single* and *double diffractive scattering* (one or both protons are excited) and *non-diffractive scattering* including all other possible processes, which can have hard (high transverse momentum) and soft (low transverse momentum) components[1].
As shown in fig. 2.2, the proton-proton cross section is dominated by soft background events, only a small fraction will undergo a hard scatter among the proton's constituents. Some of them will produce jets and particles of high transverse momentum. The *hard scatter event* is accompanied by the so-called *underlying event*, which is a term used to describe the soft remanent of the collision. This term is distinct from the *minimum bias event*, which in general describes all inelastic events, without a hard scatter process, recorded with as little trigger bias as possible.
The pertubative QCD [133] (Quantum Chromodynamics) can not be used for describing the low momentum minimum bias interaction. Consequently phenomenological models in Monte Carlo generators (e.g. PYTHIA8 [98]) with tunable parameters are used [134].
Minimum bias events are used to model pile-up in simulation by merging minimum bias events

[1] The choice of hard and soft processes is an arbitrary one, but mainly motivated by perturbative and non-perturbative calculation at the underlying processes.

as described in section 3.1.
The accuracy of the Monte Carlo generators used to simulate minimum bias events depends, amongst other parameters, on the model and the tuning of the generator. The model accuracy depends on how well the parton distribution functions[2] and the kinematics at a given center-of-mass-energy are understood. For LHC collisions, with a center-of-mass-energy of 13 TeV the simulation can be compared with data and the parameters (tuning) be adapted to fit the data (see [136, 137]). For the FCC-hh regime with an unprecedented center-of-mass energy of 100 TeV, some uncertainties remain, since the tuning consistent with the most recent LHC-data is extrapolated to the higher energies.
For the FCCSW simulations (as described in section 3.1) PYTHIA8 is used for event generation, using the tuned parameters (Monash 2013 tune see [99]) of LHC simulation. More detailed information on the expected kinematics and event generation at a 100 TeV proton-proton collider, including a comparison of different event generators, can be found in *chapter 1, sections 2 and 3* of [56].
To simulate the pile-up for a FCC-hh experiment with $\langle\mu\rangle = 1000$, 1000 minimum bias events are merged during detector simulation into one event. The averaged charged particle multiplicity of minimum bias events at 100 TeV can be seen in fig. 4.1a. No p_T-cut has been applied. The shape of the distribution looks very similar to ATLAS [136] and CMS [137]. The only slight difference, is that the two maxima lie at higher pseudorapidity, which is most likely due to the higher boost of the particles. In the forward region, the distribution drops, because the kinematics are different than in the central region. The p_T-spectrum of the transverse momentum of the generated particles is shown in fig. 4.1b. The particle spectrum in forward region (blue), with $\eta > 2.5$ has lower transverse momentum than the spectrum in the central region with $\eta \leq 2.5$ (green). Table 4.1 compares selected generated particle parameters of the LHC, the HL-LHC and the FCC-hh scenario. While the raise of the total cross section is only about 50 %, the inelastic cross section rises only by ~ 25 %. This means, that many hard-scatter event cross sections increase more strongly, which leaves FCC-hh with great discovery potential. The total number of charged particles per event is increased strongly, when considering pile-up: for LHC it is of $\mathcal{O}(3)$, which is raised by one order of magnitude for the HL-LHC and by two orders of magnitude for the FCC-hh. The average p_T of the produced particle is rather low and only raised slightly for the FCC-hh case.

Parameter	LHC	HL-LHC	FCC-hh
σ_{inel}[mb] [57]	80	80	103
σ_{tot}[mb] [57]	108	108	150
$\langle\mu\rangle$	40	200	1000
Charged tracks per collision (N_{ch}) [57]	70	85	122
$\langle p_T\rangle$ [57] [GeV/c]	0.56	0.6	0.7

tab. 4.1: Comparison of LHC, HL-LHC and FCC-hh particle properties produced at the collision. With σ_{inel} and σ_{tot} being the total and inelastic cross sections. The average number of pile-up is denoted with $\langle\mu\rangle$. Source: [52], *table 7.1.*

[2]The parton distribution function (PDF) is denoted as $f_i(x, Q^2)$ and describes the probability of finding a parton of flavour i (quarks or gluon) with a fraction x of the proton's momentum. Q denotes the energy scale of the hard interaction. Cross sections are calculated by convoluting the parton level cross section with the PDFs [135].

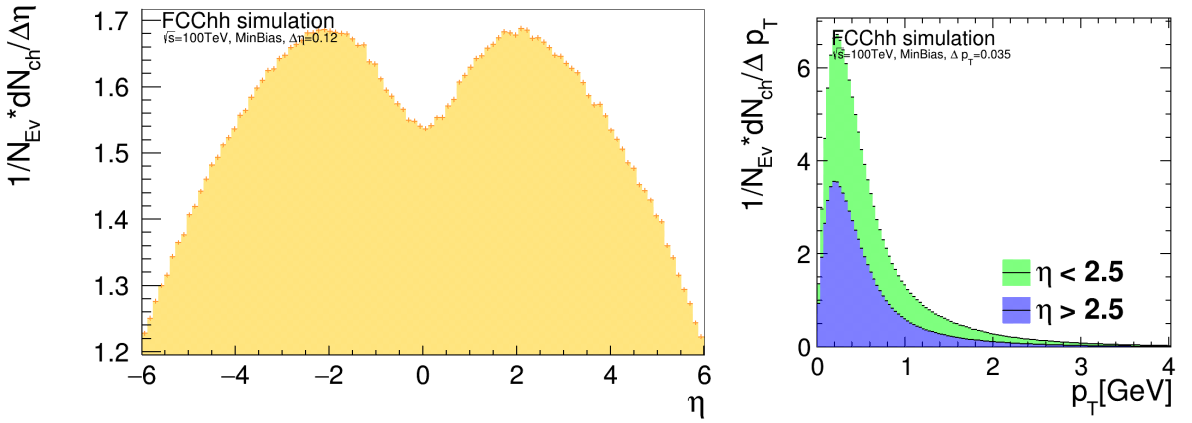

(a) Generated charged particle multiplicity over η. No p_T-cut is applied to the generated output.

(b) The p_T-spectrum of generated particles for $\eta < 2.5$ (green) and $\eta > 2.5$ blue.

fig. 4.1: The generated charged particle multiplicity (left) and p_T-spectrum (right) of one minimum bias event over η, without including pile-up. FCCSW event generation and simulation at 100 TeV have been used.

During full simulation which propagates the generated particles through the detector, the magnetic field in longitudinal direction in the tracker will bend the path of these particles in the transverse plane, according to the lorentz force [61]. Consequently, depending on their transverse momentum, not all of the input particles will reach the tracker. Assuming the particle will be forced onto a circular track by the lorentz force, one can equate the centripetal force and the lorentz force to calculate the curvature of the particle trajectory:

$$\frac{m \cdot v^2}{r} = e \cdot v \cdot B \tag{4.1}$$

By substituting the momentum with $p = m \cdot v$, the following identity is obtained:

$$p = e \cdot r \cdot B \tag{4.2}$$

In high energy physics natural units [138] are used for convenience and [GeV/c] is usually used as unit for momentum. Hence, a unit conversion needs to be done:

$$1\frac{GeV}{c} = \frac{10^9 \cdot e \cdot V}{3 \cdot 10^8 \frac{m}{s}} p[\frac{GeV}{c}] = \frac{3 \cdot 10^8 \frac{m}{s}}{10^9 \cdot e \cdot V} \cdot r \cdot B = 0.3 \cdot r \cdot B$$

Finally, the radius of particle track in transverse plane can be obtained:

$$r[m] = \frac{p[\frac{GeV}{c}]}{0.3 \cdot B[T]} \tag{4.3}$$

Using this simple equation, a prediction, on the radial reach of each particle, with a certain transverse momentum can be done. The maximum distance a particle can travel in the transverse plane of the detector, when starting from the origin, is the diameter of the above circle. Figure 4.2a shows the generated charged particle p_T-spectrum overlaid with colored lines, each marking the minimum transverse momentum a particle must have, to arrive at a certain barrel layer. This is

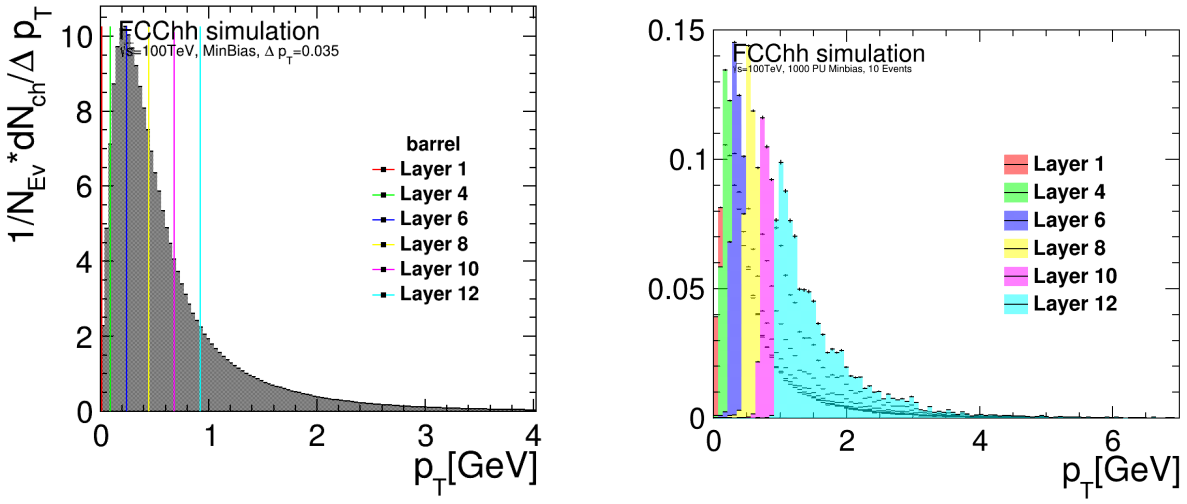

(a) (b)

fig. 4.2: On the left, the generated charged particle p_T-spectrum is displayed. The lines indicate which particles (right from the line) can possibly arrive at which layers due to bending in the magnetic field. On the right, a cross-check with simulation is shown, by assigning the hits at the layers to their generated particles.

only an estimation. Small differences may occur due to interactions of the particles with the detector material, thus the particle track will not be a perfect circle or the particle could be absorbed in the material. In addition the magnetic field may not be perfectly homogeneous. In fig. 4.2b the calculation is tested, displaying the p_T-spectrum of all generated particles arriving at the different layers. The observed p_T-spectrum fits very well the expected behaviour.

4.2 Reconstructed clusters of the FCC-hh environment

As a first step towards studying the occupancy for a high pile-up environment, the tracker response has been studied for different simulation configurations. The number of particles coming from the interaction region is expected to be roughly constant over η (see fig. 4.1a). As a consequence, the number of measurements should be proportional to the η-coverage of a given detector layer as well as to the overlap of that given layer, e.g. see fig. 4.3 for the η-coverage and the overlap of the barrel layers.

In fig. 4.4a the number of clusters for each barrel layer is displayed against the radial position for four different options in order to understand the different contributions.
The light green squares show the number of clusters per layer, produced by generated particles only and magnetic field turned off. This case follows very well the expected value (combination of η-coverage and overlap), which is scaled to the first value for this case and displayed with black dots. Only a slight difference in the last layers is observed, because less particles are arriving at the last layers due to hadronic interactions and decays. When the magnetic field is turned on (dark green triangles), the particles are bent due to the magnetic field which increases the number of clusters by $\sim 10-20\,\%$. For this option only higher momentum particles reach the last layers (see fig. 4.2b), which leads to a noticeable decrease in the number of clusters in those layers. When including measurements stemming from secondary particles, (blue squares and triangles) created within the detector, the number of clusters rises by 70 %. In the layer closest to

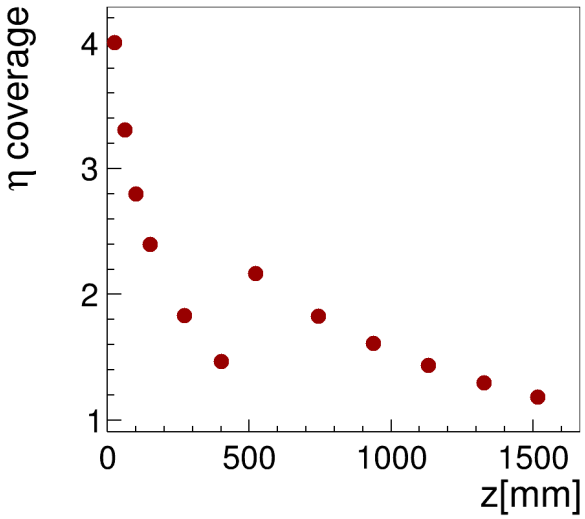

(a) Each point displays the η-coverage of a barrel layer, plotted against the radius of that layer.

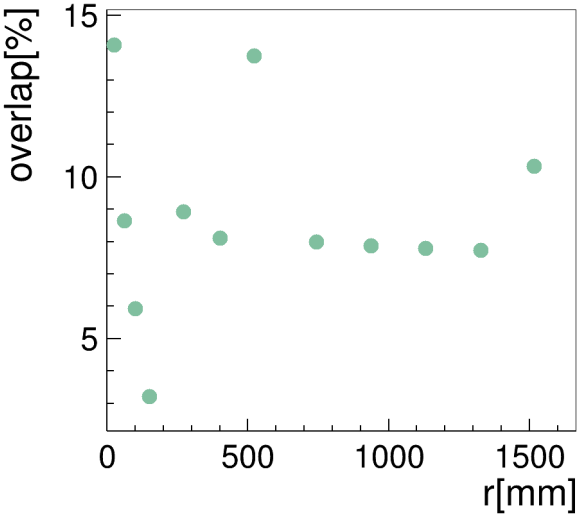

(b) The percentage of overlap, compared to a cylinder, of the detector modules of each barrel layer is shown versus the radius of that layer.

fig. 4.3: Pseudo-rapdidity (η) coverage and overlap of the barrel layers.

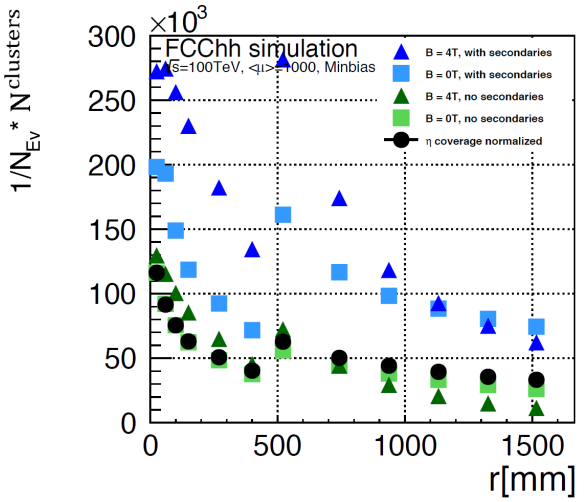

(a)

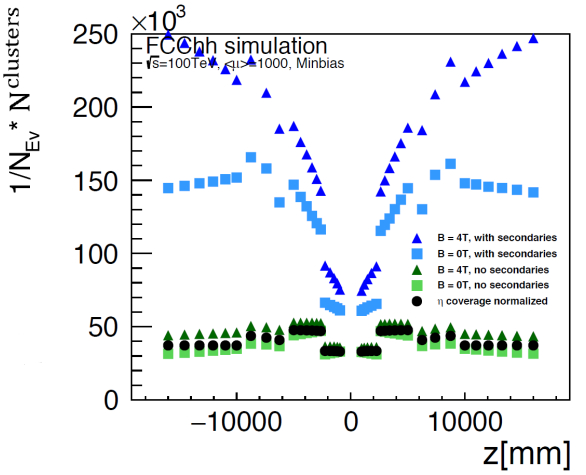

(b)

fig. 4.4: Number of clusters for generated particles only (green), with (squares) and without (triangles) magnetic field and including hits from all particles (blue) for the barrel layers fig. 4.4a and the endcap discs fig. 4.4b. The black points display the expected value due to η-coverage corrected to the overlap.

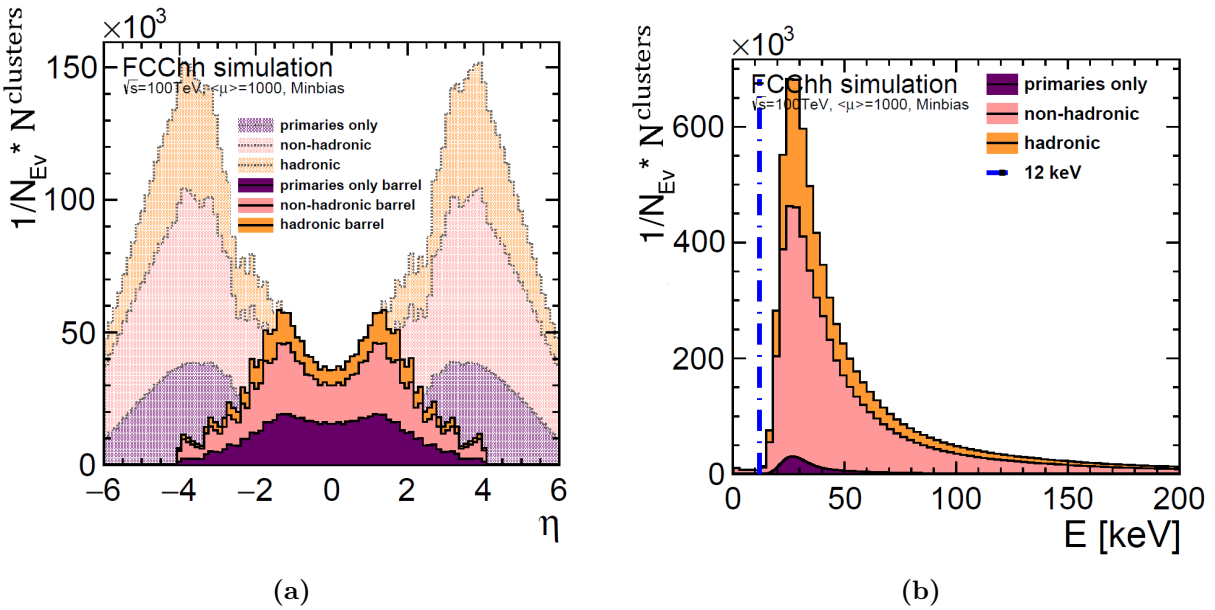

f

fig. 4.5: Composition of clusters regarding particle and interaction type (*primary* particle, *hadronic* and *non-hadronic*) over η (left) with barrel contribution overlaid and over deposited energy (right).

the interaction point the particle tracks are more dense, which can lead to more shared clusters (more than one particle contributing to the same cluster) and decreased total number of clusters. Two effects lead to an increasing number of clusters in the outer endcap discs (see fig. 4.4b). The first is, that particles which are bend due to the magnetic field aggregate in the forward part. This effect becomes particularly strong when including secondary-particles created in the detector (blue), which in general have a softer p_T spectrum, thus experiencing stronger deviation in the magnetic field. The second effect is due to the increased secondary particle production in the forward region of the beampipe, since more material is passed.
Figure 4.5a shows the number of clusters versus the pseudorapidity. The clusters are classified according to their particle type as either being *primary*, i.e. coming from the particle generation, *hadronic* interacting or *non-hadronic* interacting. In case more than one particle contributes to the same cluster, it is classified as a primary particle, as soon as one of them is a primary particle. In case various non-primary particles produced within the detector material contribute to the same cluster, it is classified hadronic, if a hadronic interacting particle belonged to the same cluster. For distinction of the barrel and the endcap region, the full distribution for the whole tracker is overlaid with the contributions of the barrel only. Non-hadronic contributions are most dominant and more secondaries are produced for higher incident angle due to higher material budget and thus higher probability of ionization and hadronic interactions.

In fig. 4.5b the energy depositions of those measurements is plotted for the different contributions. Below the blue line at 12 keV only non-hadronic components, most likely low energy secondary electrons, are dominant. These are produced through ionization within the material and due to their low energy will not leave the silicon. For track reconstruction only signals stemming from particles which have enough energy to leave the material and form tracks are of interest. Low energy contributions can be excluded by applying an energy threshold.

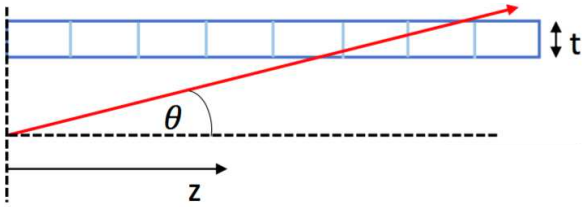

(a) For a barrel layer, the incident angle ϑ as well as the readout granularity and the detector thickness t determine the cluster size in global z-direction.

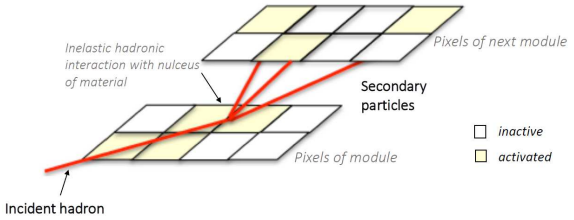

(b) Hadronic interaction can cause more, smaller clusters.

fig. 4.6

4.3 Study of cluster sizes

The cluster size is the number of activated cells/channels a cluster consists of. This is of particular interest, because it has a strong impact on the channel occupancy: the bigger the cluster size, the higher the occupancy.

The cluster size depends on the incident angles of the particle tracks to the detector module in the readout directions, as well as on the readout granularity and the detector thickness. Finer readout granularity and thicker sensitive silicon substrate can increase the cluster size.
The cluster size in local y-direction of the module, which is parallel to the beam line should follow

$$\frac{\mathrm{t}}{\tan\vartheta * \mathrm{p}} \qquad \text{p...pitch size} \tag{4.4}$$

for the barrel (see fig. 4.6a) and

$$\frac{\mathrm{t} * \tan\vartheta}{\mathrm{p}} \qquad \text{p...pitch size} \tag{4.5}$$

for the endcap. For the cluster size in local x-direction (global r/φ-direction) the situation is more complicated and depends on the geometry as well as on the bending of the particle trajectory within the magnetic field, which depends on the particle $\mathrm{p_T}$.
To understand the sensitivity of the cluster size on the particle interactions the cluster sizes have been studied separately as a function of local x, y and the layer. The first barrel layer, a middle barrel layer (layer number 7) and the outermost barrel layer have been chosen for representation. The cluster sizes are displayed in fig. 4.8 and fig. 4.9 including measurements created by generated particles only (green), including also secondary particles created in the detector (blue), both with (line) and without (dashed line) magnetic field.
To understand the different contributions the cluster size in local x-direction, where a uniform distribution is expected (see first column of fig. 4.8), is displayed first. Excluding secondary particle contributions, the cluster size in local x-direction is close to one for all layers, which is the minimal cluster size. Switching on the magnetic field of 4 T during simulation, the cluster size increases, due to the bending of the particles in transverse plane. This effect is more pronounced at outer radii, since less straight tracks are left going outwards. When including the contribution of secondaries, primarily the cluster size rises, especially for low momentum secondaries. However, when particles are passing more material the occurence of hadronic interaction is more probable, which can lead to smaller cluster sizes, as illustrated in fig. 4.6b. This effects can be seen without the magnetic field (light blue dashed lines) as the cluster size increases approximately by a factor of two for the first layer and then the cluster size decreases for the outer layers, after

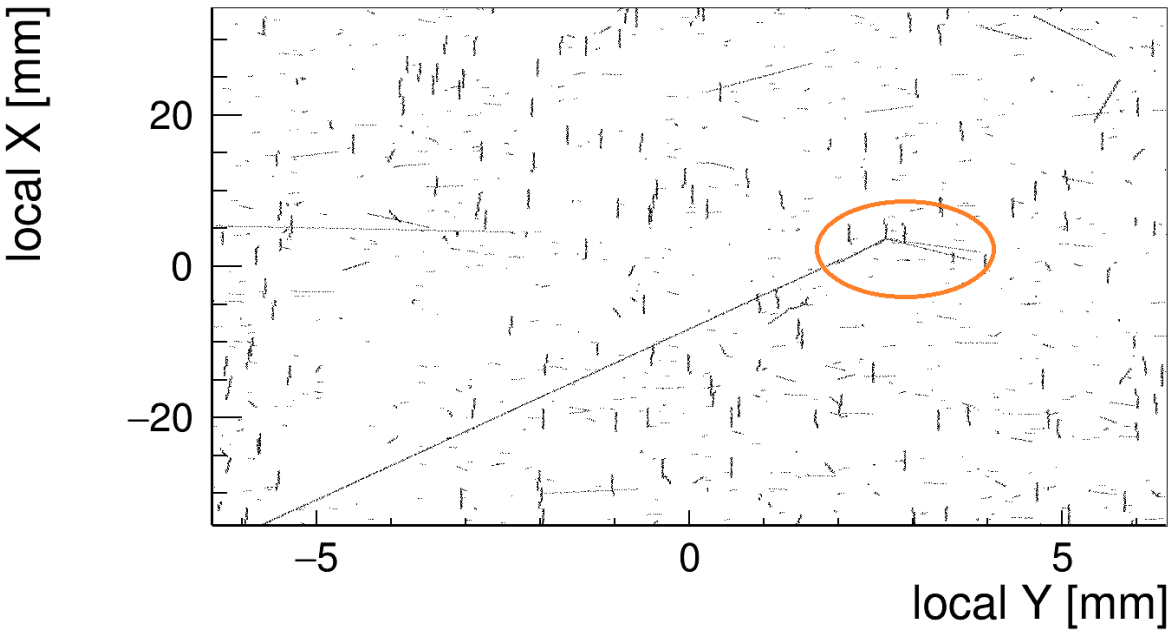

fig. 4.7: Activated cells in a module in the outermost ring of the first barrel layer at 100 TeV and $\langle\mu\rangle = 1000$. The orange ellipse highlights a hadronic interaction occuring in the sensitive detector module, after a particle traversed a significant amount of material.

more material has been passed. Turning on the magnetic field, strongly increases the cluster size due to the bending of the particles, however decreases the broadening due to low momentum secondaries, because they get deflected.

In fig. 4.7 the activity within a module in the last barrel ring is shown as an example. The activated cell positions of a detector module as obtained by simulation are plotted. This example shows the particle tracks of particles passing through the module and their contribution to the average cluster size, with a hadronic interaction occuring, marked by an orange ellipse.

In the following the distributions of the cluster sizes in local x-direction over η are studied (see fig. 4.8 second column). As expected, a uniform distribution equal to the value seen along φ, excluding secondaries and switched off magnetic field (light green dashed line) can be seen. When turning on the magnetic field (dark green line), as seen along φ before, the cluster size increases due to curling of the particles. The distribution is now no longer uniform over η. This effect occurs due to two reasons: firstly the generated particle p_T-spectrum is softer in forward direction, which can bee observed in fig. 4.1b and secondly, low momentum looping particles are accumulated in forward direction. When including secondary particle measurements the probability of δ-electrons [17] and low momentum secondary particle production grows with the passed material and therefore with η. For the outer layers the same effects as described above can be observed. Furthermore the distribution becomes flatter going outwards, even when considering the smaller η-coverage of the outer layers, which is again due to the fact that less straight tracks arrive at the last layers.

In fig. 4.9 the cluster sizes for the different layers in longitudinal direction (local y) are shown along η. Excluding effects of secondaries and magnetic field, the longitudinal cluster size is expected to follow $\tan\vartheta$ (see fig. 4.6a) and therefore with increasing η bigger clusters are expected. When the magnetic field is turned on, the particles are bent in transverse direction and therefore create smaller cluster sizes along longitudinal direction. When secondaries are included, smaller cluster sizes are expected due to hadronic interaction (see. fig. 4.6b), especially in forward

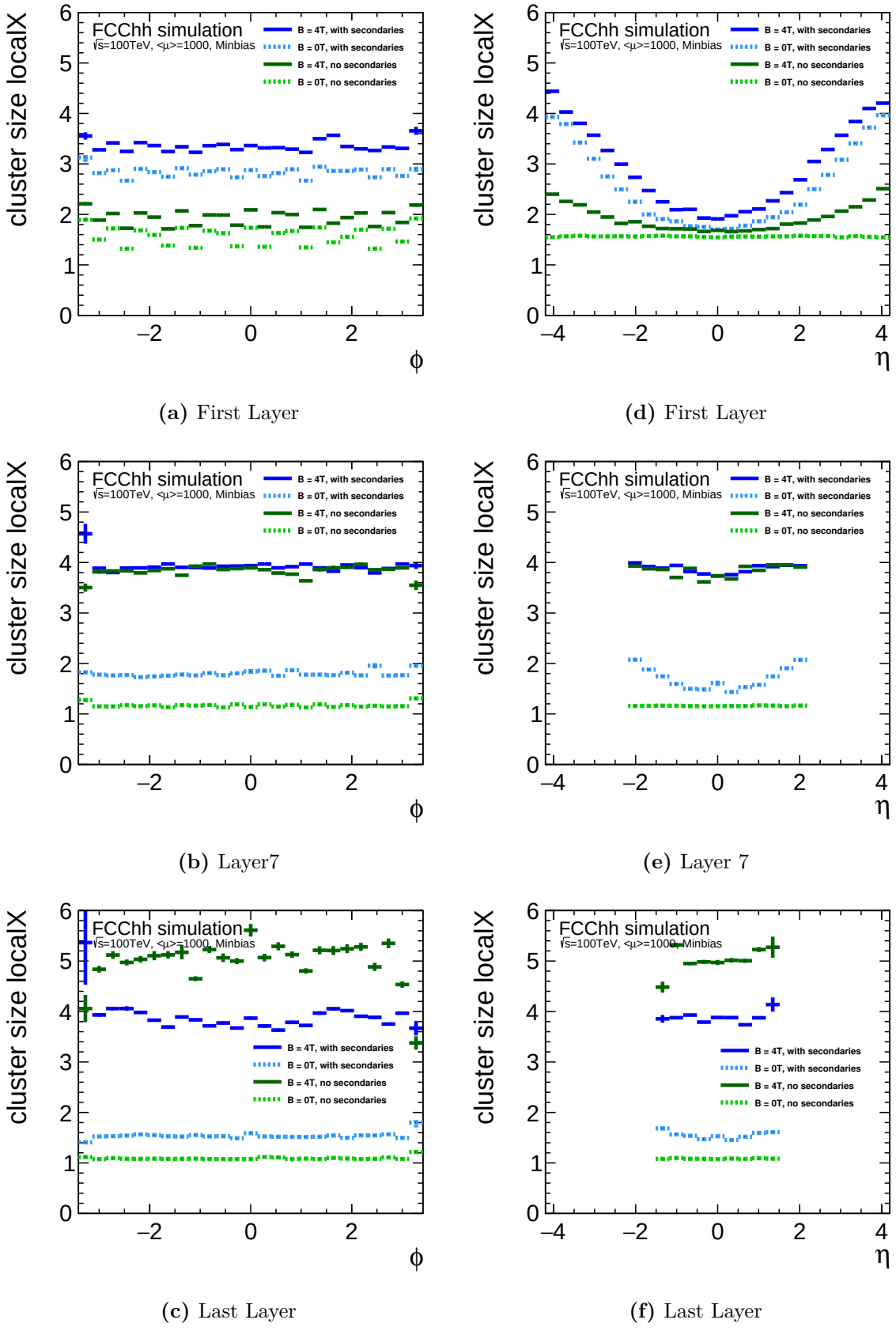

(a) First Layer

(d) First Layer

(b) Layer7

(e) Layer 7

(c) Last Layer

(f) Last Layer

fig. 4.8: Cluster size in local-x-direction (global r/φ-direction) plotted against the φ (left) and η (right) -position of the cluster.

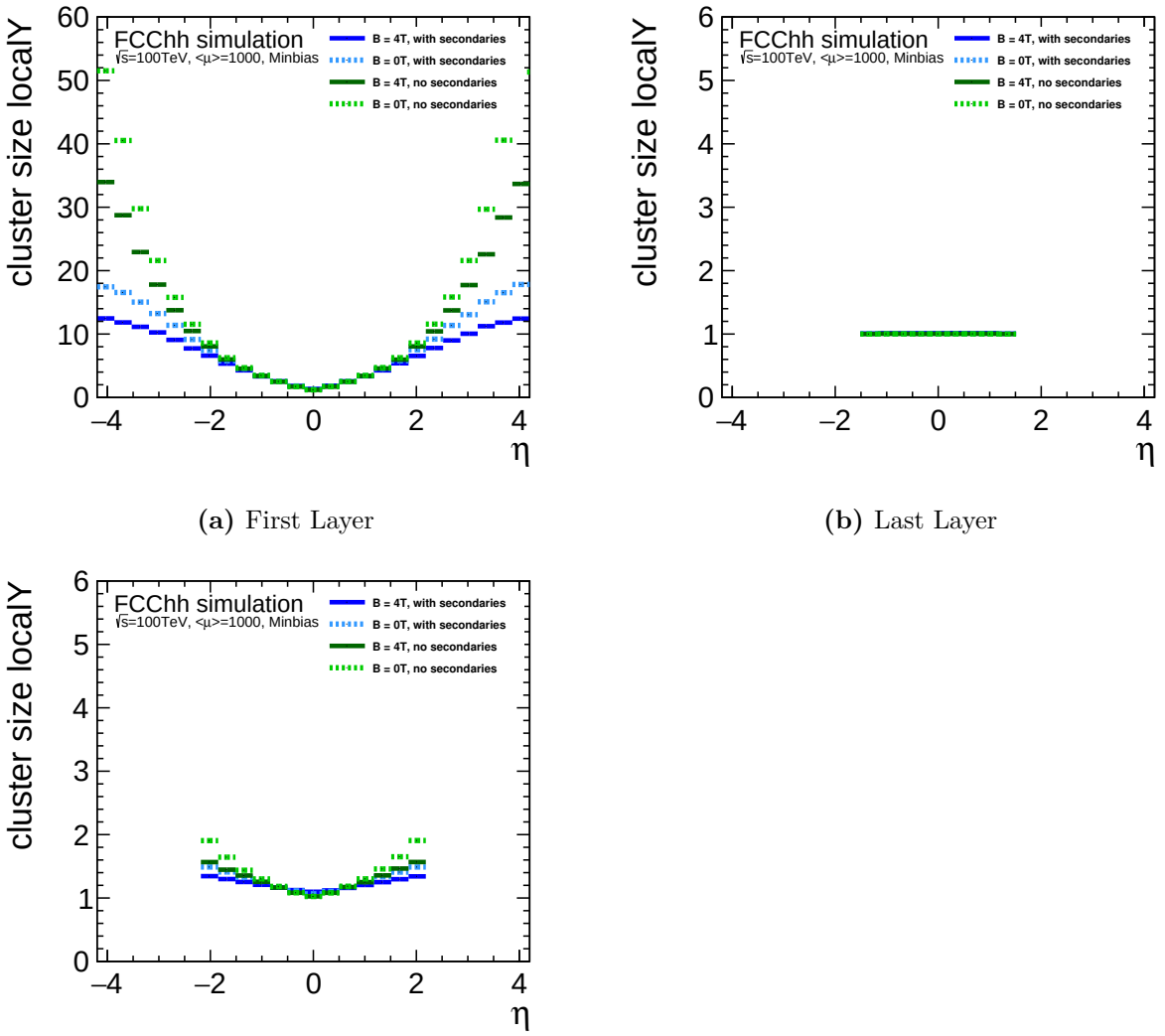

(a) First Layer

(b) Last Layer

(c) Layer 7

fig. 4.9: Cluster size in local-y-direction (global z-direction) plotted against the η (right)-position of the cluster.

direction, when more material is passed. This effect can be well observed for the first layer with a pitch size of 50 µm. For layer 7 which has macro pixels with a pitch size of 400 µm, the increase of pitch size accounts for a reduction of cluster size $\propto$ 4.5. However, also the effect of hadronic interaction (due to increased material) and magnetic field is more pronounced. The last layer lies in the strip region with a pitch size of 50 mm, this reduces the cluster size by approximately a factor of 4 (compared to having 50 µm) and the cluster sizes approach their minimum of one.

4.4 Assessment of channel occupancy for the FCC-hh scenario

The channel occupancy of a module is calculated by dividing the number of activated channels by the total number of channels of this module:

$$\text{occupancy}[\%] = \frac{\textit{activated cells per module}}{\textit{total number of cells per module}} * 100 \tag{4.6}$$

The channel occupancy depends on the density of measurements - the *cluster occupancy* ($N^{clusters}/mm^2$). An increased number of clusters will lead to more activated channels, thus increasing the channel occupancy. However, also the cluster size plays an important role (see section 4.3). The number of activated channels is linearly proportional to the cluster size. Hence, the channel occupancy is raised for bigger clusters. If the readout granularity is chosen to be finer, the total number of channels is increased, reducing occupancy despite large cluster sizes.

These different contributions as well as the channel occupancy are displayed along z in fig. 4.10 and fig. 4.11 and have been determined as average of minimum bias events with $\langle\mu\rangle = 1000$. Each point displays the average for a ring of modules at its specific z-position for the barrel layers. In the endcap region each point gives the average of a region with different granularity (*pixel, macro pixel, strip*) and displays the position of a disc in z. The first five points belong to the inner endcaps, then the outer endcaps follow and finally, the discs of the forward tracker beginning with three intermediate discs continue.

The total *cluster size*, determined by the interplay of cluster size in φ and cluster size in z, which was studied in detail in section 4.3 is displayed in the first row of figs. 4.10 and 4.11. For the pixel layers (first column of fig. 4.10) the cluster size increases with z from a minimum value of 4 in the central region to a maximum of 17 in the outer parts. This is firstly due to the increased incident angle with growing z (see fig. 4.6a) which increases the cluster size along z. Secondly, the cluster size along φ is increased due to aggregation of looping particles in the outer parts. The passage of more material with growing z leads to low momentum secondary production and increases the cluster size. Due to a smaller η-coverage (smaller incident angle in z), increased hadronic activity in the outer layers (fig. 4.10 right column and fig. 4.11 left column) and decreased granularity in z in the outer barrel layers, the distribution is dominated by the cluster size in φ-direction and stays roughly constant along z at a value of 4. For the endcap discs (fig. 4.11 right column) the incident angle reaches its maximum in the outer rings, where the cluster size has a value of 4 and then decreases with growing z. The strip region and the endcap macro pixel region have a bigger cluster size than the pixel region, because they occupy the outer rings and decrease along z. However, the difference between the minimum and maximum cluster size is smaller than in the barrel, because of the coarser granularity in the outer rings.

The *cluster density* is roughly constant over η in the central region. Since the barrel modules cover equidistant space in z, each consecutive module covers less space in η (see fig. 4.4a). Thus, the cluster occupancy (see second row) decreases slightly with z for the first four layers and stays roughly constant for the following layers. The cluster occupancy has its highest value of nearly 1.2 clusters per mm^2 in the central region of the innermost layer. In the endcap region

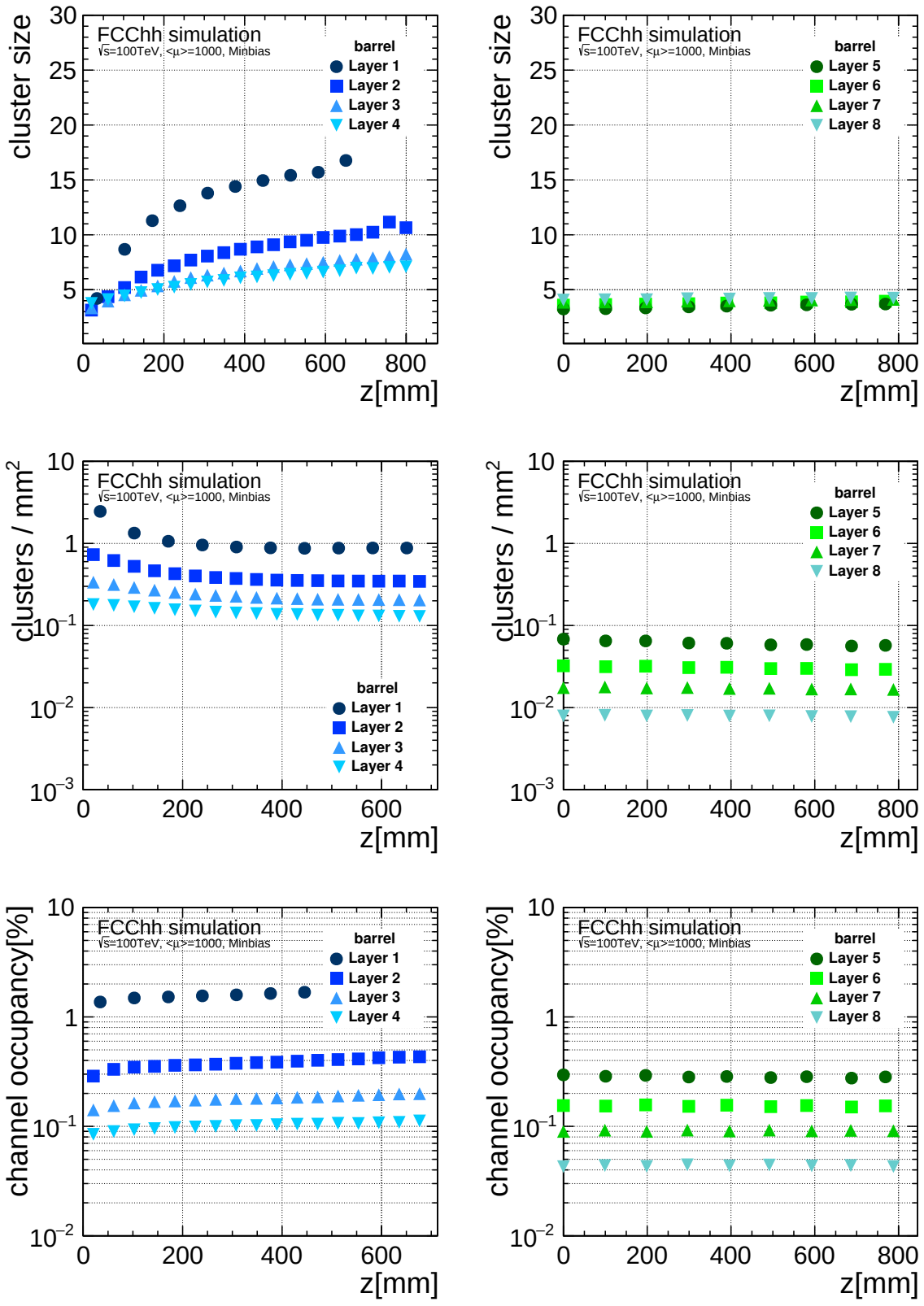

fig. 4.10: Cluster size, cluster occupancy and channel occupancy for the different barrel layers along z. Each point displays a ring of modules in z. The results for the pixel layers are displayed on the left in blue colors and for the the macro pixel region on the right in green colors.

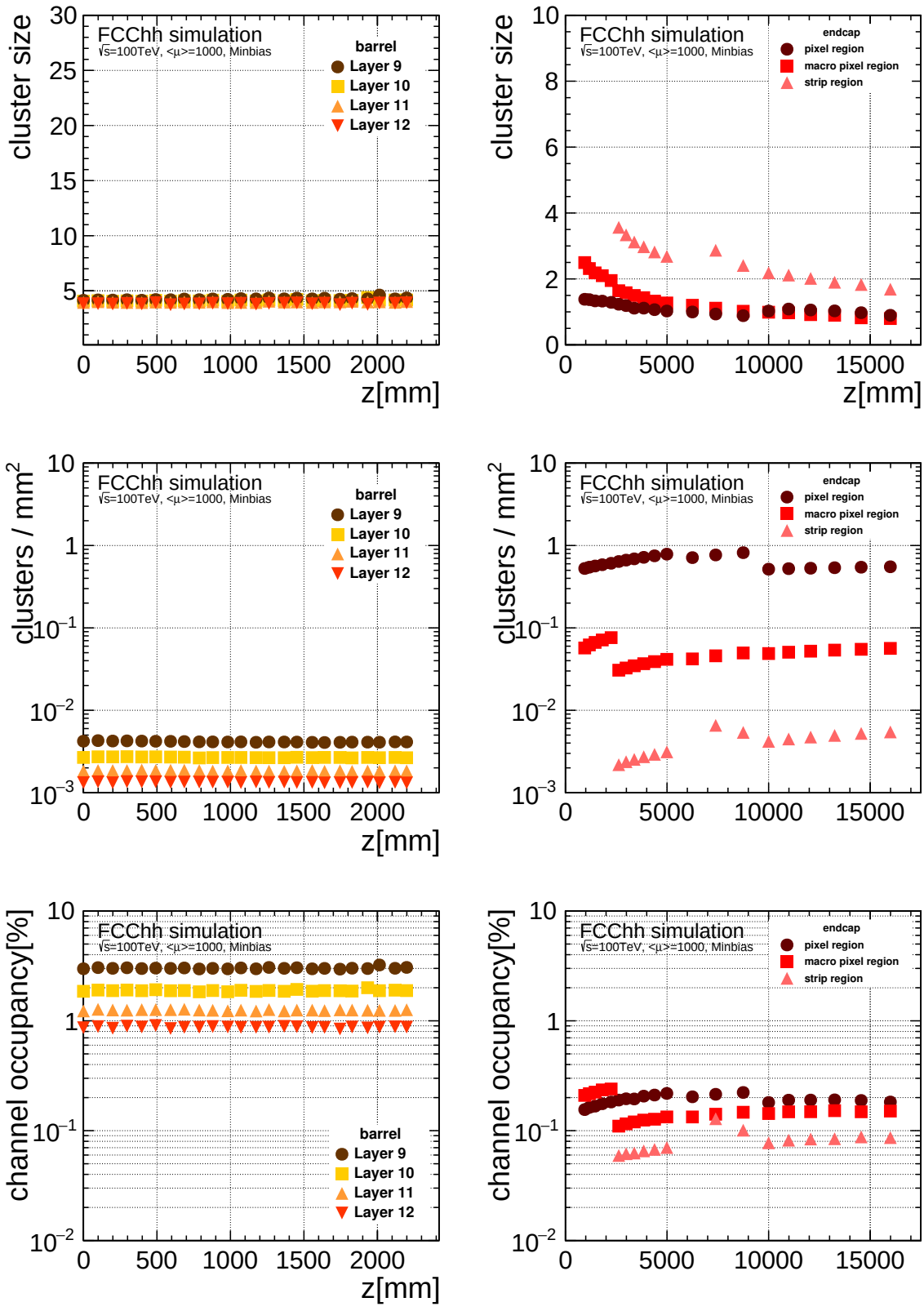

fig. 4.11: Cluster size, cluster occupancy and channel occupancy for the different barrel layers of the strip region as well as for the endcap regions along z. Each point displays a ring of modules in z. The results for the strip layers are displayed on the left in orange colors and for the endcap region on the right in red colors.

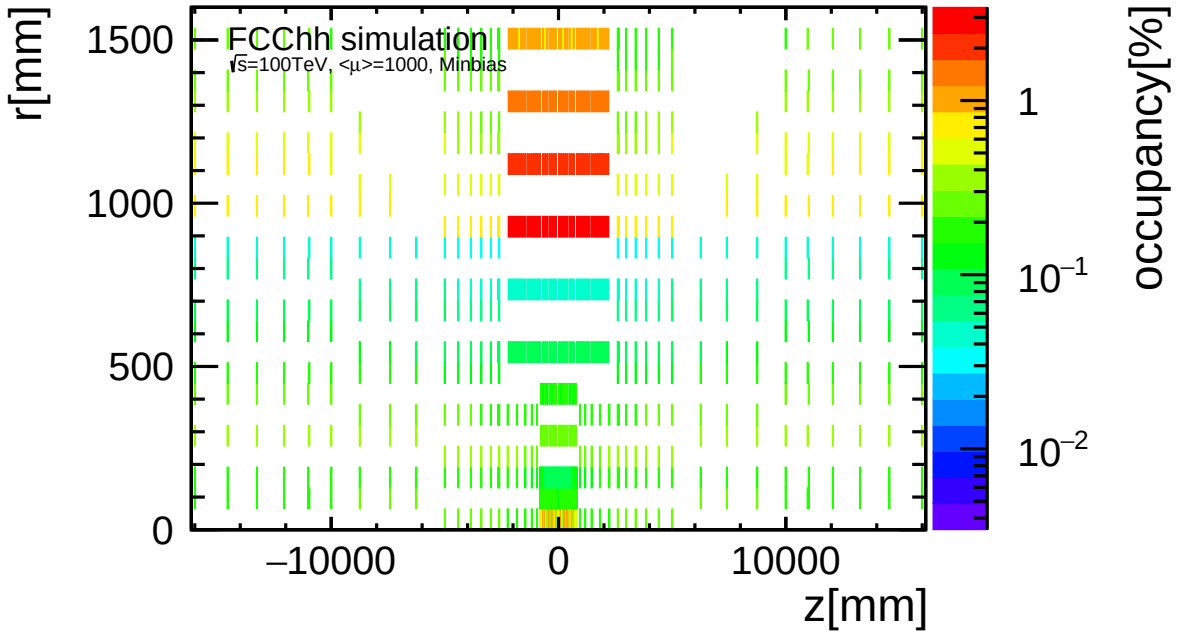

fig. 4.12: Channel occupancy map at $\langle\mu\rangle = 1000$, showing the average channel occupancy of each module of the whole tracker.

the cluster density slightly rises along z which is due to an increased number of clusters along z, as observed in fig. 4.4b).

The *channel occupancy* is displayed in the last row of figs. 4.10 and 4.11. For the layer closest to the beam line a channel occupancy of 1.6 % is observed, for all subsequent pixel and macro-pixel layers the occupancy is decreased. In the strip layers the highest channel occupancy values are observed, it reaches 3 % in the first strip layer. In the endcaps the occupancy stays below 1 %.

The full occupancy map for $\langle\mu\rangle = 1000$ is shown in fig. 4.12, displaying the averaged occupancy for each module of the tracker. Especially the first layer as well as the strip barrel layers have a high channel occupancy $> 1\,\%$[3]. This can lead to highly complex pattern recognition as well as mismatches and to increased dead-times of the detector modules. In table 4.2 the averaged channel occupancy for each barrel layer is shown.

For track reconstruction, only particles creating hits in subsequent layers are of interest. Low momentum electrons, which do not leave the detector can disturb the signal. Thus, an energy threshold is applied which needs to be reached in order to activate a pixel/strip. The specific energy threshold depends on the sensor technology and the experimental design. Because the technologies are not known at this stage, a typical energy threshold per readout cell for a silicon detector of 3600 eV (the production of 1000 electron-hole-pairs in Silicon), was applied to account for the possible impact of an energy threshold. Applying such an energy threshold reduces the channel occupancy by 6-13 % (see second column of table 4.2). Another possibility to reduce the channel occupancy can be to increase the granularity. However, this would lead to enhanced data rates. To estimate the effect of an increased granularity, the third column shows the occupancy, using the granularities of the inclined layout, which has a decreased strip size of 1.5 mm instead of 50 mm in layers 9-11. For that case the channel occupancy is below 1 % despite for the first

[3]Part of this could be mitigated by smart readout schemas, which would go beyond the scope of this study.

tab. 4.2: Averaged channel occupancy expected at $\langle\mu\rangle = 1000$ for each barrel layer for three different scenarios.

Layer n°	No threshold	$E_{thr} = 3.6\,keV$	inclined granularities, no threshold
1	1.629 ± 0.042	1.491 ± 0.040	1.634 ± 0.045
2	0.391 ± 0.010	0.348 ± 0.009	0.392 ± 0.011
3	0.182 ± 0.005	0.160 ± 0.004	0.183 ± 0.005
4	0.103 ± 0.003	0.089 ± 0.002	0.103 ± 0.003
5	0.284 ± 0.008	0.262 ± 0.007	0.285 ± 0.008
6	0.154 ± 0.005	0.141 ± 0.005	0.154 ± 0.005
7	0.093 ± 0.003	0.086 ± 0.003	0.093 ± 0.003
8	0.044 ± 0.001	0.041 ± 0.001	0.044 ± 0.001
9	3.018 ± 0.093	2.810 ± 0.089	0.155 ± 0.368
10	1.887 ± 0.060	1.753 ± 0.060	0.097 ± 0.230
11	1.252 ± 0.051	1.164 ± 0.051	0.064 ± 0.152
12	0.875 ± 0.035	0.812 ± 0.037	0.880 ± 0.042

layer. However, the data rates increase, which will be further discussed in the following section.

4.5 Estimated data rates for the FCC-hh baseline tracker using binary readout

Binary readout is assumed for the whole tracker, hence only 1 bit is accounted for each activated readout channel. In case more information e.g. timing or energy is needed, more than one bit needs to be considered.
The data rates are calculated by multiplying the number of activated bits per module N_i^{bits} with the number of bits needed to address each readout channel. The last factor generally depends on the module's arrangement, i.e. the number of readout channels in r/φ and z for a given type of detector module. It can be evaluated as:

$$N_i^{bits} = \log_2(N_i^{rows}) + \log_2(N_i^{columns}) \tag{4.7}$$

The number of bits per event is given as an integral over all modules in each region.
To obtain an upper limit of the data rates for digital readout at the first trigger level and 40 MHz bunch crossing rate, the obtained data amount must be multiplied by the event rate of 40 MHz. The obtained integrated data rates for each region are summarized in table 4.3. The first column states the plain data rates. Applying an energy threshold of 3.6 keV (second column) to activate a pixel/strip, the data rate drops by 10 %. When using the inclined granularities, although the occupancy decreases, the data rates increase, because of the increased number of channels to be addressed.

In table 4.4 the data rates per layer, as well as the data rate density, which is a geometry independent measure, for 40 MHz and 1 MHz event rate are shown.

Data rates [TB/s]	Flat layout	With threshold	inclined granularities
Pixels (inner)	1054.3 + 379.6	944.5 + 337.9	1056.3 + 380.2
Macro-pixels (middle)	559.2 + 423.1	515.4 + 391.4	560.3 + 423.8
Striplets/Macro-pixels (outer)	127.8 + 192.8	118.8 + 179.1	165.4 + 242.4
	2737 TB/s	**2487 TB/s**	**2828 TB/s**

tab. 4.3: Summary of total data rates, as estimated for the three tracker regions: *pixels* (inner tracker), *macro-pixels* (middle tracker) and *striplets/macro-pixels* (outer tracker), as well as for different scenarios: with/without energy threshold and inclined granularities (smaller strip size). Each number is shown as a sum of respective numbers of the central and forward tracker.

Barrel layer:	**1**	**2**	**3**	**4**	**5**	**6**
Average radius [mm]	25	60	100	150	260	380
Data rate [Tb/s]	2263.1	1506.4	1140.3	938.5	438.0	348.6
Data rate @ 40 MHz [Gb/s/cm^{-2}]	944.0	229.6	107.0	60.2	14.8	8.0
Data rate @ 1 MHz [Gb/s/cm^{-2}]	23.6	5.7	2.7	1.5	0.4	0.2

7	**8**	**9**	**10**	**11**	**12**
530	742	937	1132	1327	1540
835.5	537.8	331.3	249.0	192.8	109.5
5.1	2.4	1.2	0.7	0.5	0.2
0.1	...				

tab. 4.4: Summary of maximum fluence [cm^{-2}], module occupancy and data rates [Gb/s/cm^{-2}] as estimated for the nominal FCC-hh pile-up of $\langle\mu\rangle = 1000$ and tracker flat geometry.

4.6 Conclusion and outlook

The FCC-hh environment will be challenging in terms of track reconstruction with, on average, $\sim 30\,\mathrm{M}$ activated Pixels and $\sim 9-10\,\mathrm{M}$ clusters per event, assuming pile-up of $\langle\mu\rangle = 1000$. For the flat baseline layout, the channel occupancy exceeds the general goal of 1 % (as stated in section 2.3) in the first layer and the strip region. Moreover, the immense data rate densities per cm^2, with a maximum of $944\,\mathrm{Gb/s/cm}^{-2}$, are of particular concern in the innermost vertex detector layers and rings. Possible improvements as well as the tilted layout need to be studied in detail. The tilted layout with inclined modules is expected to reach higher cluster occupancy but smaller channel occupancy rates, because a reduction of cluster size can be achieved. This is shown for the ATLAS upgrade in [86] (*chapter 3.4*) or [139] (*chapter 2.2.4*) as well as for the CMS upgrade in [68] in (chapter 6.2.2.)
When considering the deviation of charge carriers, due to the lorentz force, inside the silicon, while drifting to the readout electrodes, the cluster sizes in r/φ-direction can be reduced, by optimizing the rotation angle of the modules.
In addition to the high channel occupancy and data rates, by taking into account an unprecedented limit on radiation tolerance within these layers/rings and that a limited power supply can be used to keep the material budget of the vertex detector sufficiently low, there is no technology available for these purposes so far. However, there is ongoing research by the *CERN RD50* collaboration, which investigates radiation hard silicon sensors for high luminosity detectors [140, 141]. Thin monolithic silicon sensors, with a thickness of $\mathcal{O}(2)$ µm, can be studied as a potential technology. This would keep the cluster size lower, because the sensitive material is thinner and the technology promises also good radiation hardness, as studied by *RD53* for the ATLAS and CMS upgrades [142]. A dedicated R&D programme needs to be setup in the future to address all these issues.

Chapter 5

Double track resolution in b-jets for a 100 TeV pp-collider at extreme pile-up conditions

At all scales, the hard scattering process in proton collisions is dominated by hard collisions among the proton constituents (=*partons*) [56] (*chapter 9*). Subsequently emitted high energetic quarks or gluons [143] will not be seen as such in the detector. Due to color confinement [144] they *hadronize* [145] into color-neutral hadrons, which are finally observed as particle *jets* in the detector [146]. A jet describes the dense region of hadrons and associated particles produced during the hadronization process.
In order to determine the properties of the event and underlying physics process, e.g. whether light quarks or b-, c- or t-quarks were produced, the internal structure of a jet needs to be resolved by reconstructing its constituents. This requires that the readout granularity of the tracking system is fine enough to separate the tracks originating from the different particles. Otherwise, multiple particles will contribute to the same measurements and subsequently lead to confusion in the track reconstruction algorithms. This and especially multiple overlaps can lead to the loss of tracks. For Run2 of the LHC with its center-of-mass-energy of 13 TeV, the average separation between highly collimated charged particles is comparable to the readout granularity of the sensors of the inner tracking detector [110] of the ATLAS experiment. For the FCC-hh, at 100 TeV center-of-mass energy, the situation is expected to be even more challenging, due to the production of jets with higher transverse momenta (see [56], *figure 100*), which leads to smaller angular separation. In addition, the high pile-up environment of $\langle\mu\rangle = 1000$ can lead to contamination of the jet signals.

For illustration, the cluster position in the transverse view of the barrel part of the tracking detector of a 10 TeV b-jet event are displayed in fig. 5.1. The clusters, which represent measurements and later serve as input for pattern recognition as space points, are shown without pile-up on the left side and overlaid with the expected pile-up on the right side. While on the left side, the location of the two jets of that event can be guessed by eye, the high pile-up environment completely occupies the tracker and the jets are not visible any longer. Already in this simple and high-level representation, the difficulties for FCC-hh are easily spotted: a high density of clusters within jets and strong contamination of the signal by pile-up.
In the following, the impact of these two problems is studied in detail. After a general introduction to the bottom-quark in section 5.1 and the definition of a jet in section 5.2, the Monte Carlo samples used for the study are described in section 5.3. In section 5.4 the capability of double track resolution in highly energetic b-jets for the FCC-hh, with and without pile-up, is investigated. The capability to reconstruct close-by tracks is limited in the presence of pile-up. Section 5.5 specifically investigates to what extend the events are pile-up dominated. In section 5.6 the effect on tracking efficiency considering shared clusters along the track and its possible improvement using neural network identification is estimated. Finally the presented results are summarized in section 5.7 and their impact on track reconstruction performance is discussed.

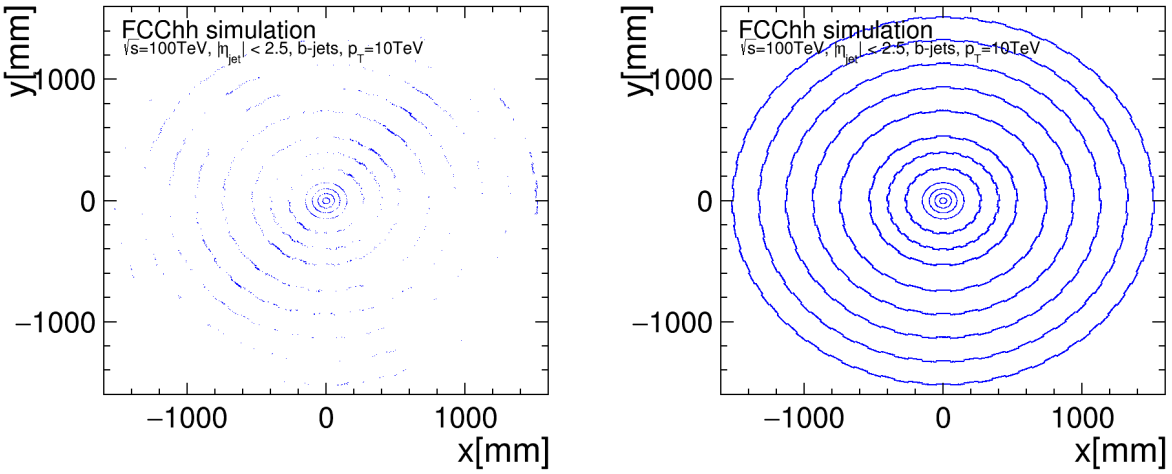

fig. 5.1: Cluster positions of the barrel only in the transverse plane of the tracking detector for a 10 TeV b-jet event without (left) and overlaid with pile-up at $\langle\mu\rangle = 1000$ (right).

5.1 The bottom-quark

For this study the charged-particle separation is studied using jets originating from a *bottom quark*, which belongs to the third generation of quarks and is relatively heavy with 4.18 GeV/c [147]. At hadron-colliders the bottom quark is created together with its anti-partner $\bar{b}$. Each of the $b\bar{b}$-pairs will form a separate jet, while hadronizing into a b-flavored hadron, which has a finite lifetime [148]. The decay length of a b-hadron depends on its type and momentum and follows $v\gamma\tau$, with γ being the relativistic lorentz factor due to time dilatation [149], which depends on the particle's momentum, v its velocity and τ standing for the B-hadrons lifetime in its rest frame. The b-quark is the heaviest quark creating hadrons and has a relatively long lifetime of $\mathcal{O}(10^{-12})$ s. At the LHC, with its center-of-mass-energy of 13 TeV, the B-hadron usually decays after a centimeter [148]. This feature is often used for distinction of the b-jet to other jet-types, e.g. by identifying the displaced secondary vertex, to *tag* the jet at the ATLAS and CMS experiment (see [150]).
For highly boosted B-hadrons, which are expected at a 100 TeV hadron collider, the B-hadron can travel longer distances and even decay within the detection volume. See [151] for a simulation study, investigating a b-tagging algorithm based on the increased hit multiplicity between the tracker layers, due to the B-hadron decay. In this context the radial decay vertices of B-hadrons with different transverse momenta were studied and show that a large fraction of highly energetic B-hadrons with $500\,\text{GeV} \leq p_T \leq 5000\,\text{GeV}$ decay within the FCC-hh tracker. For B-hadrons with $p_T = 5000$ GeV only 22 % decay before reaching the first layer and a small fraction can even pass the tracker without decaying.
Due to the characteristic that the B-hadron travels a certain distance before it decays, excellent track separation within the jet is needed for it to be reconstructed. This is illustrated in fig. 5.2a, where the substructure of a b-jet compared to a light jet (jet produced by light quarks, i.e. up-, down- or strange-quark) is illustrated: the B-hadron decays after a certain distance, thus, the particle tracks are closer to each other than, when coming from a single vertex. Since the B-hadron can even decay within the tracker, the b-jet can give an upper bound for the smallest track distances.

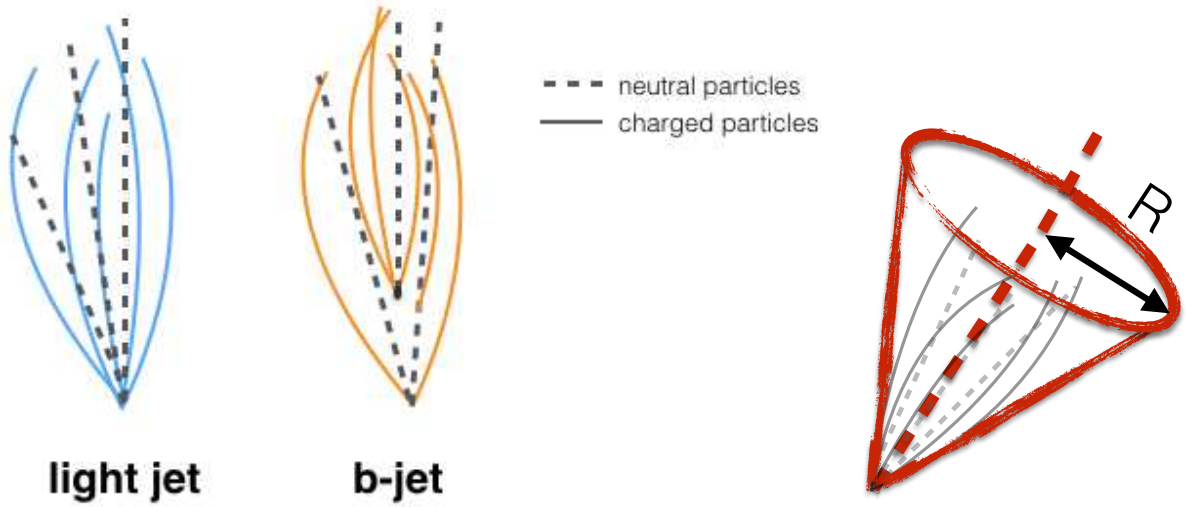

(a) Scematic comparison of the jet substructure of jets stemming from light (left) quarks and b-quarks (right). The resulting B-hadron has a finite lifetime and decays within the jet.

(b) Definition of a jet by its axis and extension $R = \sqrt{\eta^2 + \varphi^2}$ in the pseudorapidity-azimuthal-angle plane.

fig. 5.2

Apart from being a suitable candidate to study double track resolution, identifying that a jet originates from a b-quark, and measuring its properties is crucial for various physics scenarios. These include searches for new physics, as well as probing the standard model. For instance, the decay of the Higgs-boson into a pair of a bottom quarks and its anti-partner is the boson's most frequent decay (see fig. 2.2) and can directly probe the bottom-Yukawa coupling. This decay was recently observed by ATLAS and CMS [33, 152]. Furthermore, the measurement of b-jets play an important role for studying the top-quark, due to the top quark's most prominent decay into a W-boson and a b-quark [153, 154].
In addition, the detection of highly energetic b-quarks can also play a central role for interesting beyond the standard model (BSM) physics searches. An example are heavy resonances, which are predicted in many BSM-models addressing the hierarchy problem. These heavy particles preferably decay into pairs of the heaviest quarks, the third generation quarks e.g. $Z' \rightarrow t\bar{t}$, $Z'- \rightarrow b\bar{b}$, (see [155, 156] for recent searches at ATLAS and CMS and [157] for an outlook for the FCC-hh scenario). Moreover Higgs pair production and its subsequent decay to $HH \rightarrow b\bar{b}b\bar{b}$ are important signatures which could give hints to new physics [158].
Furthermore, the B-hadron and its decay can also be used to study the strong interaction. The decay of B-hadron results in generation-changing processes, due to the fact that the b-quark is the lighter particle of the third-generation quark doublet, b-physics offers a possibility to study CP-violation [148].

5.2 Jet definition and clustering

A jet describes a region of a collimated bunch of particles stemming from the hadronization process and can be observed as a concentrated high energy deposition in the calorimeter or dense particle tracks in the tracking detector. Jet reconstruction is an important part of full event reconstruction. This means, connecting the detector-signals induced by hadrons and their

by-products to the initially produced particles at parton level.
To geometrically determine the jet, the particles are bundled together using specific algorithms. Hence, the exact jet definition and location strongly depends on the underlying algorithm, defining which particles will be combined into the same jet. In the following, the geometrical jet-definition as illustrated in fig. 5.2b is used. It is defined by its jet axis and its radius R in the pseudorapidity-azimuthal-angle plane. Different solutions for the so-called *jet-clustering* exist, based on different assumptions and qualities depending on the application. A general overview of jet definitions and jet-clustering algorithms can be found in [159].
At the LHC-experiments prevalently the *anti-*k_T*-algorithm* finds application to cluster jets, which applies a bottom-up approach. The algorithm starts with calculating all distances of each particle to the beam and between the particles using eq. (5.1). Then it clusters the particles with $d_{ij} < d_{iB}$ into the same jet and creates a new jet with a particle if $d_{iB} < d_{ij}$, with each particle being only assigned once to a jet. This routine is reiterated until all particles are assigned to a jet.

$$d_{ij} = \min\left(\frac{1}{k_{Ti}^2}, \frac{1}{k_{Tj}^2}\right)\frac{\Delta R_{ij}^2}{R^2}, \qquad d_{iB} = \frac{1}{k_{Ti}^2}, \tag{5.1}$$

$$\text{with } \Delta R_{ij}^2 = \Delta\eta_{ij}^2 + \Delta\varphi_{ij}^2, \qquad \Delta\eta_{ij}^2 = \eta_i - \eta_j, \qquad \Delta\varphi_{ij}^2 = \varphi_i - \varphi_j \tag{5.2}$$

i, j...particle indices, d_{ij}...distance between particles, k_T...transverse momentum,
R...jet radius parameter, d_{iB}...distance of particle i to beam,
η...pseudorapidity, φ...azimuth angle, [159, 160].

The special feature of the anti-k_T-algorithm compared to other implementations is, that it starts with the particles of highest transverse momentum and collects nearby particles until none is found within a given radius R. Therefore, the jets have the shape of cones and are circular in the η/φ-plane.
During simulation the true information of the particles (see chapter 3) is known. Hence, to find jets, the generated particles can be clustered using the above information. These, in the following called *truth jets*, describe the true location and spread of the jet most accurately.
In a particle detector experiment the same objects measured by different sub-detectors can be used to cluster jets e.g. calorimeter clusters and reconstructed particle tracks. For higher efficiency usually a combination of the detected information received from the different sub-systems is used [161, 162]. The efficiency of the jet reconstruction depends on the detector setup and calibration, as well as on the reconstruction algorithms. It can be determined in simulation, by matching the reconstructed jets with the truth jets.

5.3 Monte Carlo samples and jet generation

For this study the b-jet samples have been produced using the *FCChhSimJobs*-framework [163], centrally producing full simulation hadron collisions for FCC-hh, at a center-of-mass of 100 TeV. For the b-jet samples, pairs of bottom quarks, flat in given p_T and $|\eta| \leq 1.6$ are produced back-to-back in LHE file format [164]. Monte Carlo samples for five different p_T-values have been created: 500 GeV, 1 TeV, 2 TeV, 5 TeV and 10 TeV. The parton-level LHE-events are then showered using the Pythia8 [98] event generator version 8.230 with Monash 2013 tune [99]. The vertex of the generated particles is smeared at generator level with $\sigma_{x/y} = 0.5\,\text{mm}$ and $\sigma_z = 40\,\text{mm}$. After the generation process, the particles are simulated, digitized and clusterized as

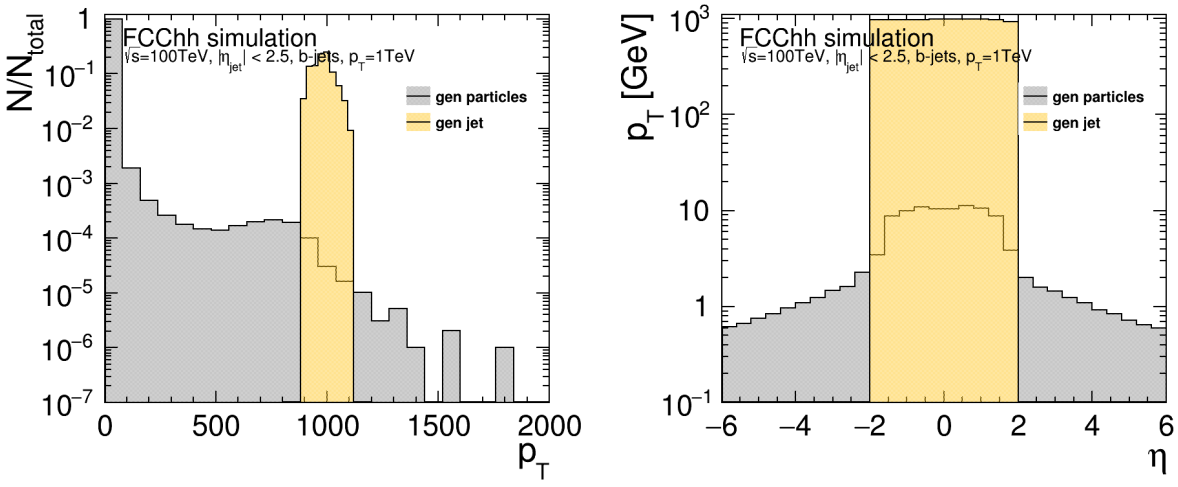

fig. 5.3: The p_T-spectrum (left) and the p_T-spectrum versus the pseudorapidity (right) of the generated particles from the b-jets samples at 1 TeV, used for this study in grey, overlaid with the found jet-properties in yellow.

described in detail in section 3.1.4. In the following, only tracker information is considered. Here, a threshold of 1000 electron-hole pairs produced in the sensitive Silicon substrate is considered by applying an energy threshold of 3.6 keV per readout pad.
Using the generated particles, truth jets (definition in section 5.2) are created, using an anti-k_T-algorithm of the FastJet library [160] version 3.3.0, with R = 0.4 and $|\eta| < 2.5$. It was decided to use truth jets for this study to receive accurate results and stay independent of any detector response or reconstruction algorithm.
The jet-clustering algorithm produces several jets, using all generated particles with the above selection cuts. To use the jets, which actually stem from the two b-quarks, the two jets with the highest p_T are selected. Because the distinction between jets of different p_T is an integral part of this study, the resulting jets are only selected if they lie within certain bounds of $|\,(p_T - p_{T,true})\,| \leq 100\,\text{GeV}$ with $p_{T,true} = \{500\,\text{GeV},\ 1\,\text{TeV},\ 3\,\text{TeV},\ 5\,\text{TeV},\ 10\,\text{TeV}\}$.

In fig. 5.3 the charged particle multiplicity of the generated particles in dependence of their transverse momentum and their p_T-spectrum for b-jet events of 1 TeV is displayed in grey, with the properties of the jets found with the anti-k_T-algorithm overlaid in dark yellow. The soft underlying event can be distinguished in the p_T-spectrum, with the bulk of particles in the lower transverse momentum region of $p_T < 100\,\text{GeV}$. Only a small fraction of particles - belonging to the jet - has higher transverse momentum. The p_T of the found jets is ranging between the above cuts, with a peak at 1 TeV. On the right side of fig. 5.3, the p_T of the generated particles and the found jets is plotted against their pseudorapidity. The jets and their constituting generated particles lie within $|\,\eta\,| \leq 2$, while in forward region a soft particle spectrum is observed.

During the jet creation also the primary vertex of the jet is determined. To determine the vertex of the jet, the vertices of the participating particles are weighted according to the transverse momentum. The vertex with the highest transverse momentum is assigned to the jet.
The b-jet events are studied stand-alone and overlaid with the expected pile-up of 1000, by merging 1000 minimum bias events as described in section 3.1. The particle spectra, clusters and densities of the pile-up events at 100 TeV are studied in detail in section 4.1.

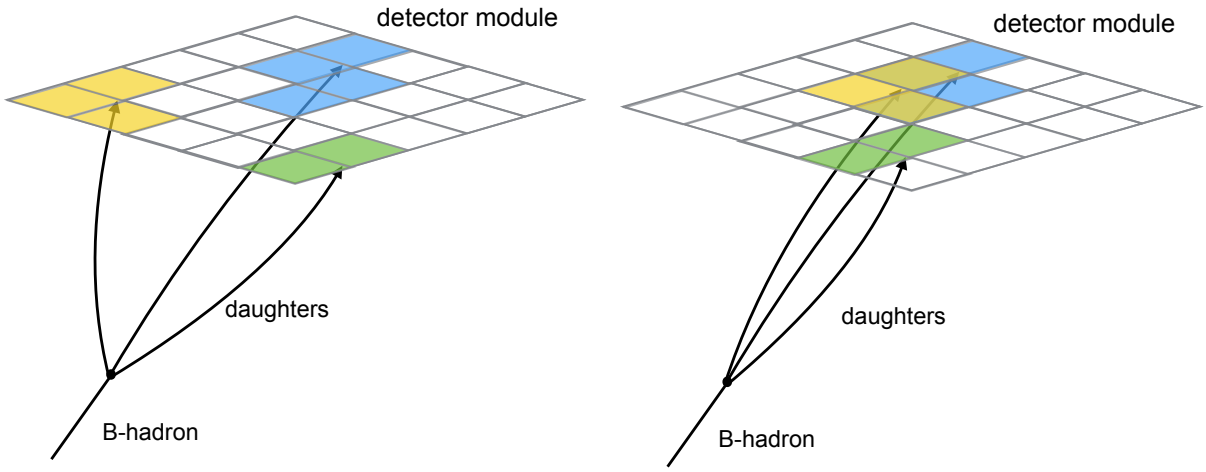

(a) Definition of single-particle clusters.

(b) Definition of multi-particle clusters.

fig. 5.4: Illustrations for cluster definitions. On the left, three single particle clusters, created by daughters of the B-hadron are displayed in different colors. On the right, those clusters are merged and are hence part of a multi-particle cluster.

5.4 Characteristics of b-jets in the high energy regime and the problem of cluster merging

At a 100 TeV hadron collider a new regime of phase-space can be explored. This includes the production of highly boosted objects, e.g. b-jets with transverse momenta at a scale of several TeV. Those jets will be strongly collimated, i.e. the particles forming the jets will be close together and possibly difficult to separate. Whether close-by tracks can be resolved in the tracker, strongly depends on how finely segmented the readout-grid of the silicon detector module is. The separation of tracks within a jet plays a crucial role in track reconstruction, which is needed to identify from which particle the jet originated and thus is required to determine the underlying physics event.

Figure 5.4 illustrates how collimation can lead to multi-particle clusters: three daughters of a recently decayed B-hadron reach a detector module. The module's readout structure are segmented pixels, which are displayed as a grey-framed grid in the figure. The pixels are activated due to the passage of particles. The activated pixels are displayed in separate colors, to indicate which signal is created by which particle. Neighbouring pixels form a cluster of which, each, is readout as a measurement in the tracking detector. On the left side of the sketch, the daughter particle tracks are sufficiently distant to form separate clusters on the detector module, while on the right the three daughters are more collimated creating only one big cluster. In the following these clusters will be referred to as *multi-particle clusters*, whereas clusters generated by a single particle will be called *single-particle clusters*.

Clusters, whose position represent the input to track finding and track fitting (see chapter 3), can lead to ambiguities, if created by more than one particle. A single miss-match of space-points belonging to a track can lead to decreased track reconstruction efficiency and can worsen the impact parameter resolution. This in turn is essential for identifying b-jets.

This section takes a closer look on the occurence of multi-particle clusters within jets. The identification of such clusters is non-trivial and requires a precise definition. As described in detail in section 3.1.4.1, the information written out per cluster also includes which particles participate to each cluster. A simplified definition would classify each cluster, which is made of

more than one particle as a multi-particle cluster. However, in track reconstruction not each of these particles may be of interest. Examples are secondary electrons which are created and stay contained within the detection layer and therefore will not create a particle track of their own. On these grounds, a particle cut needs to be applied, identifying particles which have enough energy to leave the detector module, they are created in.
Therefore, a transverse momentum of at least 15 MeV was chosen as a minimum requirement for a particle to be accounted for. This corresponds to a particle being able to travel at least 25 mm in the 4T magnetic field, following eq. (4.3). Within the tracking detector, that is the smallest occuring distance between layers. To apply a cut in transverse momentum and not in e.g. energy, also eliminates highly energetic delta electrons. As a second approach, counting only particles which appeared on at least two layers was considered and gave very similar results. However, the latter was too computing intensive to be used with a high number of clusters. Thus, the first approach was chosen to identify multi-particle clusters. In addition to the requirement of a minimum transverse momentum, the particle should not be produced within the sensitive silicon of the particular cluster.
Using this definition the ratio of multi-particle clusters to the total number of clusters within each jet can be determined. In this way geometrical effects or effects due to the charged-particle multiplicity of the underlying event or pile-up are accounted for, which would not be the case when simply displaying the quantity of multi-particle clusters. To evaluate the clusters independently of the chosen jet radius, the rate is plotted versus the angular-distance ΔR (see eq. (5.2)) of each cluster to the jet axis. To account for a jet-vertex that is not at the beam-spot, the cluster positions have been corrected for the possible longitudinal shift.

The multi-particle cluster rate at a certain distance from the jet radius was statistically evaluated and is displayed in fig. 5.5 for the total tracker and its different sensor regions *pixel*, *macro-pixel* and *strip* as introduced in section 2.3. The dashed lines display the values of jet-events without pile-up for the different jet-p_T values, while the filled histograms include pile-up at $\langle\mu\rangle = 1000$.
Predictably, as it appears from fig. 5.5 the multi-particle cluster rate reaches its maximum close to the jet core within $\Delta R \leq 0.02$ and then falls steeply until it reaches a plateau, which reflects the pedestal of the general event activity. The rate increases with higher transverse momentum of the jet, because the tracks of high p_T-jets are more collimated and reaches maximum values between 4.8 % for 10 TeV-jets and 0.84 % for jets with 500 GeV transverse momentum. The background-plateau outside the jet is below 0.2 %.
When pile-up is included, a higher background-plateau of about 1.6 %, is observed. This means that the contribution from pile-up creates similarly dense conditions as observed in the core of a 2 TeV-jet. Due to the increased cluster rate for $\langle\mu\rangle = 1000$, the relative fraction of multi-particle clusters in the jet cores is smaller than without pile-up. Including pile-up, the maxima are ranging from 1.74% to 4.4% for the different p_T-values.
In the pixel region the number of multi-particle clusters is increased and reaches 9.5 % without and 7 % with pile-up within $\Delta R \leq 0.02$ for 10 TeV jets and respectively 1.2 % or 1.5 % at 500 GeV. Also the plateau without pile-up has a slightly higher value of 0.4 %. The reason for the increased rates in the pixel region is due to the fact that the pixel region is the area closest to the interaction point. For the outer parts of the detector, the particle trajectories are less dense. This effect is further enhanced by the magnetic field, which bends the trajectories apart when the particles move outwards. Hence, the rate of multi-particle clusters, without pile-up, decreases in the macro pixel and strip region and lies between at most 2.8 % or 3.1 % for 10 TeV and 0.46 % or 0.96 % at 500 GeV. Including pile-up the ratio of multi-particle clusters increases dramatically in the strip region and even exceeds the numbers without pile-up. The background-plateau for the strip region is stable at a high value of approximately 3.8 % and reaches 5.3 % in the core of

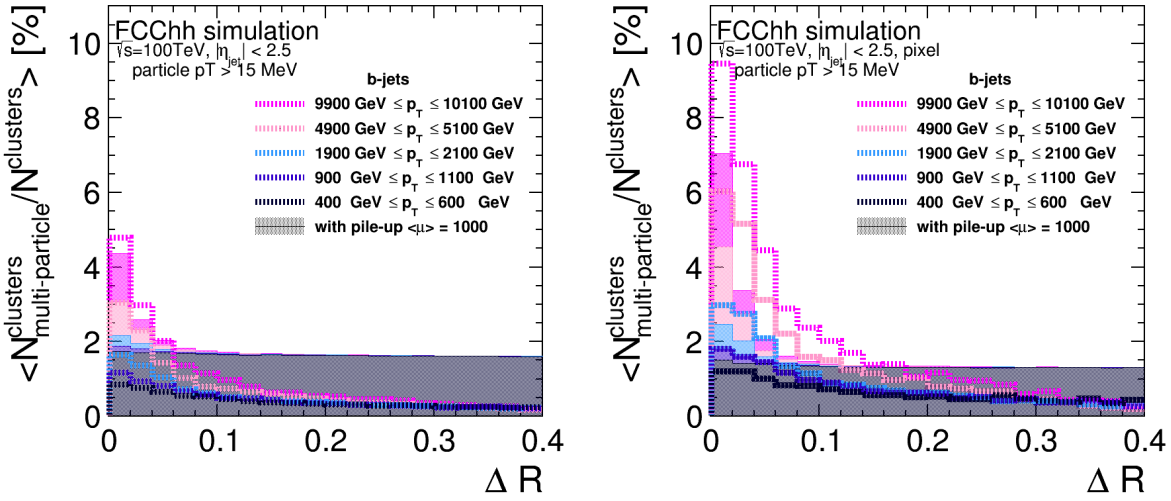

(a) all regions

(c) pixel region

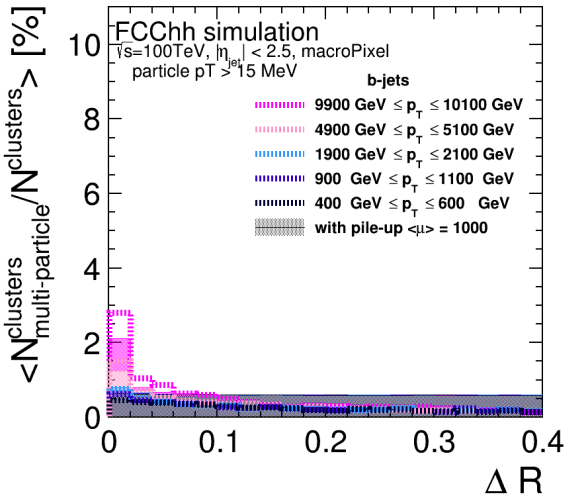

(b) macro pixel region

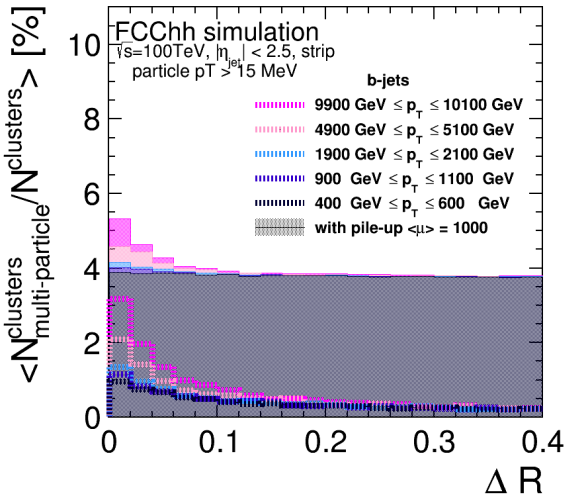

(d) strip region

fig. 5.5: Multi-particle cluster rate in [%] versus angular distance ΔR of the cluster to the jet axis for the whole tracker and separate, for the three different tracker regions: *pixel*, *macro pixel* and *strip*.

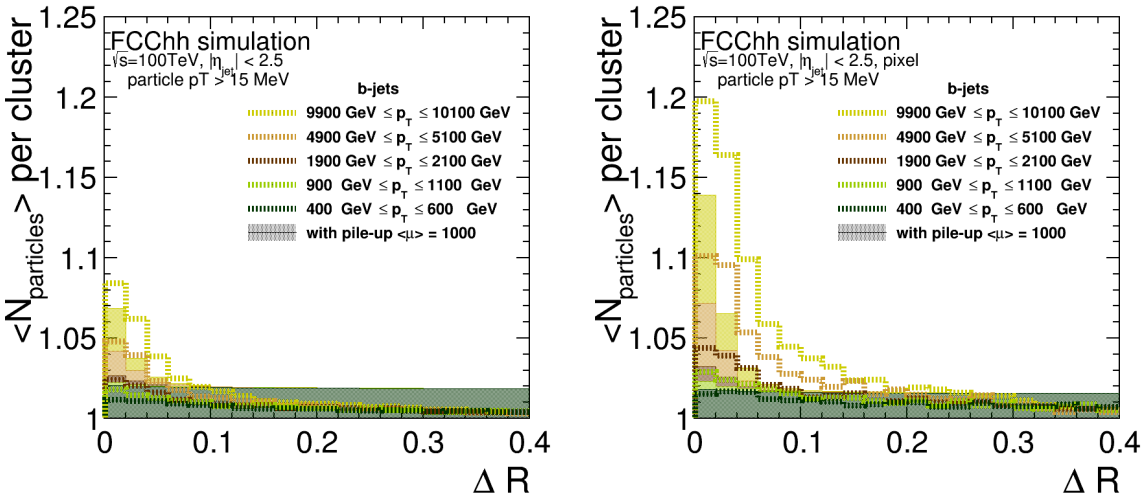

(a) all regions

(c) pixel region

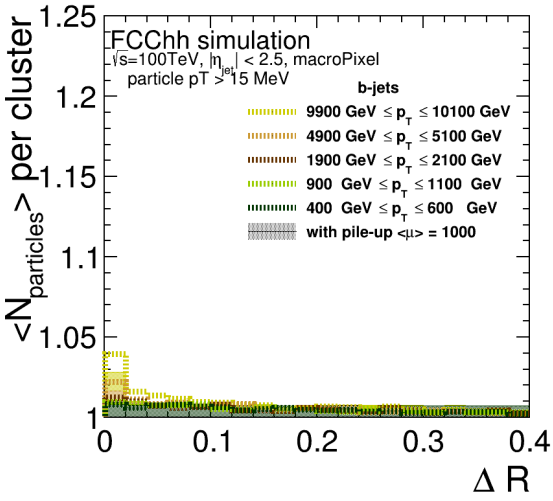

(b) macro pixel region

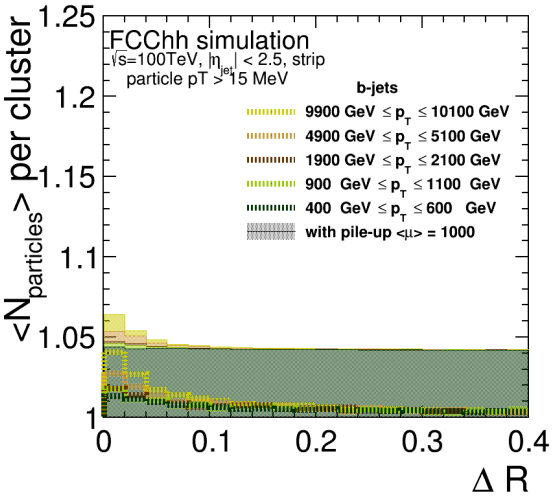

(d) strip region

fig. 5.6: Average number of particles within the same cluster versus angular distance ΔR of the cluster to the jet axis for the whole tracker and separate, for the three different tracker regions: *pixel*, *macro pixel* and *strip*.

10 TeV-jets. The reason for the highly increased rate when including pile-up is the high channel occupancy in the strip region, due to the coarser readout segmentation, as studied in detail in section 4.4.

Since a cluster is counted to be a multi-particle cluster as soon as more than one particle participated in its creation, the above obtained rate does not provide information, if a cluster could be even shared by more than two particles. For this reason, the average number of particles participating to a cluster, in dependence of the angular distance to the jet axis, is obtained and respectively displayed for the different regions and jet energies in fig. 5.6.
Because the multi-particle cluster rate and the number of particles per cluster correlate, the distributions look similar. It reaches a maximum ranging from 1.01 for 500 GeV-jets and approximately 1.09 for a 10 TeV-jet close to the jet axis and falls until it reaches the minimum

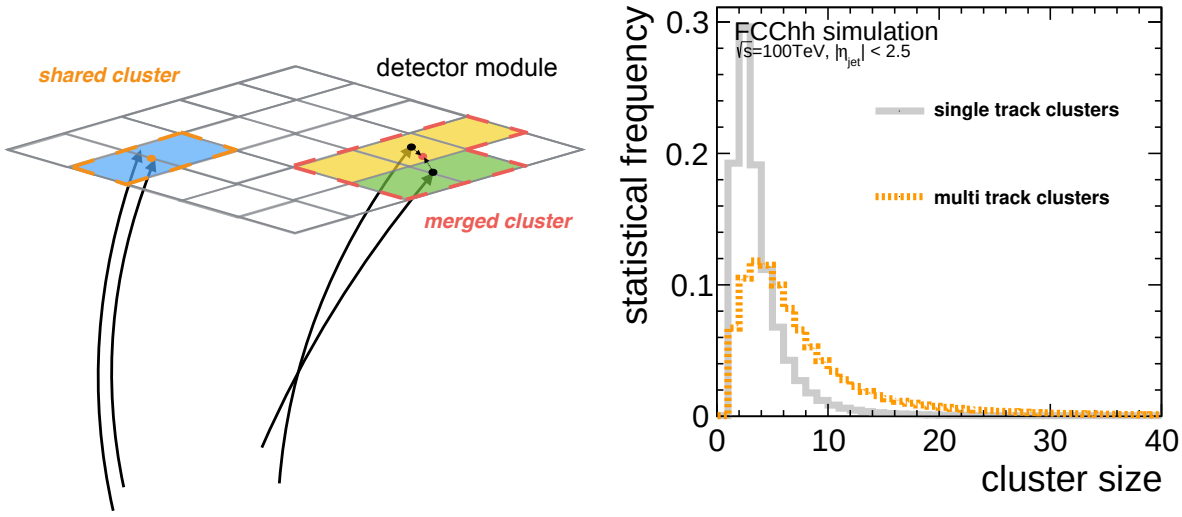

(a) Sketch, showing the difference between a shared and a merged cluster.

(b) Comparison of the cluster sizes for single- and multi-particle clusters.

fig. 5.7

of one particle creating the cluster. The numbers are increased for the pixel region, where a jet with transverse momentum of 10 TeV has on average nearly 1.2 particles participating to a cluster within $\Delta R \leq 0.02$. This means that, if all merged clusters would only be two-particle clusters, one out of five clusters would need to be merged. Since the merged cluster rate for this energy and bin is not 20 %, but lower at around 9.5 %, the multi-particle clusters need to be in many cases created by more than two particles for 10 TeV-jets, in the pixel region. The possibility that a merged cluster is created by more than two particles is similarly high for a 5 TeV-jet, but declines with decreasing p_T of the jet in the pixel region. In the macro-pixel and strip region the probability that a multi-particle cluster is on average made by two particles, is in good agreement with the observed multi-particle cluster rate. When including pile-up, the background-plateau is increased as from one to 1.02 and as before higher in the strip region at 1.04 number of particles on average per cluster.

The merging of clusters does not only put constraints on track finding but can also have serious impact on track fitting and hence, on the track parameter's accuracy. This can worsen the reconstructed momentum, impact parameter and vertex resolution, due to shifted cluster positions. The resolution can degrade in case a cluster is not only shared by multiple particles, but if multiple close-by clusters are merged, as for example illustrated in fig. 5.7a. The merging of clusters leads to a bigger cluster size and a change of the original position of the measurement, which can have an impact on both, track finding and track fitting. Especially if merging occurs in the inner detector layers, the impact parameter resolution is strongly affected. If there is an effect, due to cluster merging, can be estimated by comparing the cluster sizes of single-particle clusters with multi-particle clusters as done in fig. 5.7b.

The cluster sizes for multi-particle clusters are significantly increased with a mean value of 8.5 and a peak value of 4.4, compared to clusters formed from a single particle with a respective mean value of 3.5 and a peak value of 2.5. This means that instead of particles just sharing a cluster, cluster-merging happens frequently.

5.5 The b-jet signals and the high pile-up environment

As illustrated in fig. 5.1, both, the dense environment within the jet-cone as well as the high pile-up background are of concern for the track reconstruction. In the previous section, the focus was on the occurence of multi-particle clusters within the jet-cone with and without pile-up. In the following, the relative difference $(N_{signal+PU} - N_{PU}) \setminus N_{signal+PU}$ of the number of clusters and hits (number of activated channels) of signal mixed with pile-up, compared to the case when only pile-up would be present is evaluated within the jet-core. This shows, if the signal can be distinguished from the high background or if the event is completely dominated by pile-up. To be independent of the chosen angular jet radius, the relative difference was calculated as a function of ΔR. The number of hits and clusters was evaluated separately.

The results for both, hits and clusters are shown in fig. 5.8, for different jet momenta. Close to the jet core a significant increase in both, the number of clusters and the number of hits is observed while in the outer parts of the jet the relative increase for all jet energies is below 0.55 %. The increase close to the jet-axis depends on the transverse momentum of the jet and is strongly enhanced for jets with higher p_T. For example the number for clusters within an angular distance of $\Delta R = 0.01$ from the jet axis is increased by 7.5 % for a 500 GeV-jet and even by 70 % for a 10 TeV-jet. The increase of the number of hits is less pronounced but still strong, ranging from 4% to 55 % for the different jet-energies. The reason might lie in the more collimated character of the jets, which produce more clusters with smaller clusters sizes and therefore statistically activate less channels.
Due to the finer readout granularity in the pixel region, the relative difference of the number of hits is much closer to the number of clusters compared to the macro-pixel and strip region e.g. it reaches 68 % for a 10 TeV-jet close to the jet core, while the same quantity for the number of clusters is at 70 %.

As observed, the number of hits increases significantly in the angular region close to the jet core. This could possibly increase the channel occupancy, which can lead to problems not only in pattern recognition, but also when transferring the data from the module. To investigate the possible increase in channel occupancy of single modules in b-jet events compared to minimum-bias events with $\langle\mu\rangle = 1000$, as studied in detail in chapter 4, the channel occupancy per module is shown in fig. 5.9. The channel occupancy for the b-jet events, overlaid with pile-up is shown in blue. On top, the channel occupancy of pile-up events only, without signal, is plotted in black. The figure shows, that for most modules the channel occupancy is below 5 %. However it can reach high values, for example one out of 1000 modules (with in total 49 114 modules in the tracker, see chapter 2) can have a channel occupancy of more than 5 % and even two out of 10^7 modules can reach occupancies of more than 20 %. When adding the b-jet events on top of the pile-up, the distribution looks very similar, except that even higher values, up to 24 % can be reached in one out of $10^7 - 10^8$ cases. This means that the main contribution to channel occupancy originates from pile-up. In the same figure, the channel occupancy just from the pixel and the macro pixel area are plotted on top of the distribution in orange and in magenta. For these two regions the channel occupancy stays below 3 %. This shows that the extremely high values appear in the strip region, but also in the pixel region, high occupancy values above 1 % are found. High local occupancies are not only problematic from a pattern recognition perspective but can also overload the readout structures. In this way the signal on those modules can be completely lost.

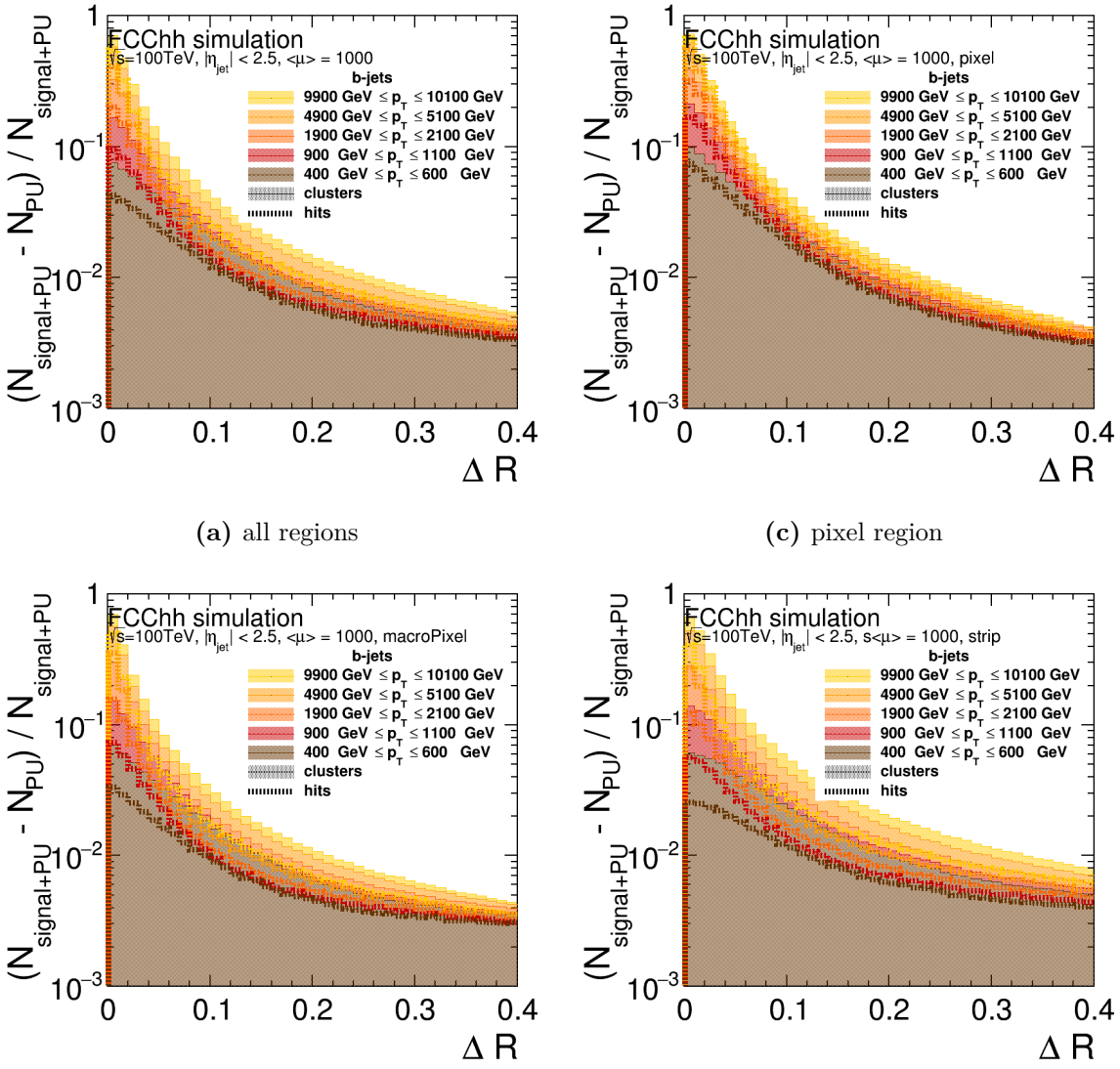

(a) all regions

(c) pixel region

(b) macro pixel region

(d) strip region

fig. 5.8: To illsutrate whether the signal is completely swallowed by the pile-up, the number of clusters (filled) and the number of hits (dotted line) for different jet-p_T's versus the angular distance from the jet-axis ΔR is shown. The different figures show the results for all regions and the different granular regions of the detector separately.

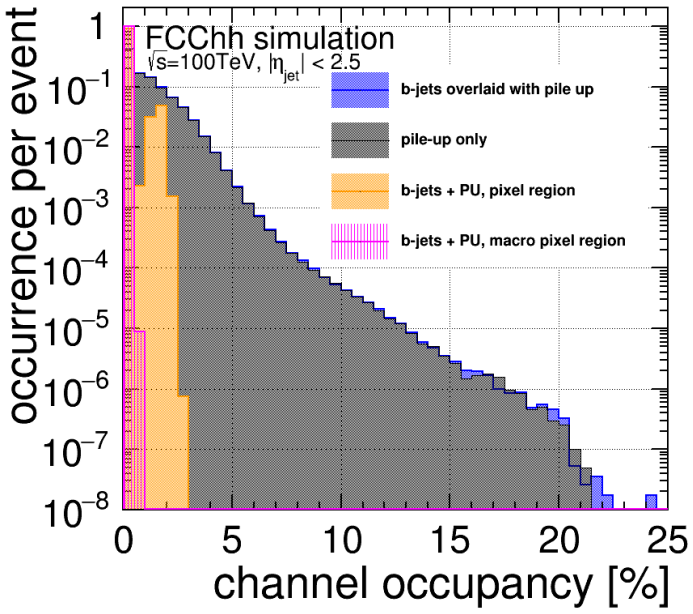

fig. 5.9: Module channel occupancy for b-jet events overlaid with pile-up (blue) and pile-up only (grey), with contribution of *pixel* region only (yellow) and *macro pixel* region only (pink) plotted on top.

5.6 Shared clusters along the track and projected tracking efficiency

Shared or merged clusters, commonly referred to as *shared* in the following, can lead to the creation of track duplicates during pattern recognition. This will impede the distinction to fake tracks. Hence, the number of shared clusters along the track is crucial for the feasibility of reconstructing a track. To suppress low momentum secondary particles and to keep the fake rate at a reasonable level the requirement of at least eight hits on different layers was found to be necessary for FCC-hh [165], without considering pile-up. For comparison, ATLAS uses a hit requirement of seven hits on different layers [110]. In the following a *track* or *reconstructable particle* is referred to as a particle fulfilling the track requirement of at least eight hits on different layers.

In fig. 5.10a the fraction of reconstructable particles to the total number of particles producing at least one sensitive hit (including secondaries) is plotted against the angular distance to the jet-core, using a bin size of 0.01, for different jet transverse momenta. Close to the jet-core the fraction reaches 70 % and falls off going outwards. This is due to the fact, that in the jet-core many high momentum particles are produced, while outside the jet-core most particles have lower momenta. The higher the jet-p_T, the more boosted are the particles within the core and the higher is the fraction of particles producing at least eight hits, which corresponds to a p_T of at least 445 MeV in the barrel region. When including pile-up, the total number of tracks with lower transverse momentum is increased, hence the fraction of particles being reconstructable is 10 % outside the jet-core. The increase close to the jet-core is more pronounced and reaches values between 11 – 32 % depending on the jet transverse momentum. The total number of tracks produced versus the jet-axis for different momenta, with and without pile-up is shown in fig. 5.10b, to set the track fractions in context. Including pile-up the total number tracks increases towards larger values of ΔR since the distribution of the pile-up particles increases

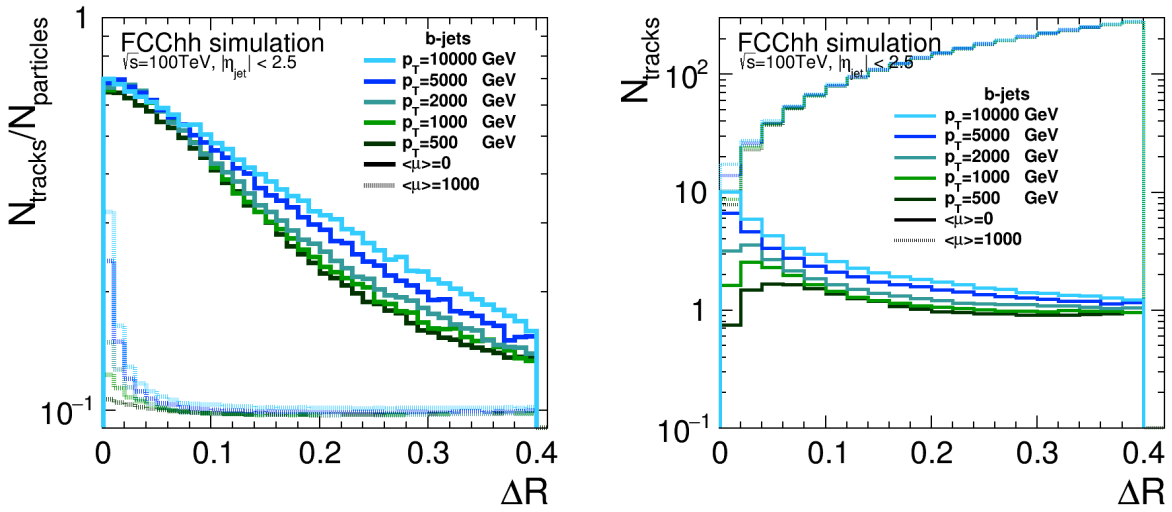

(a) Fraction of reconstructable particles (making at least eight hits on different layers) to the total number of particles, produced during simulation, which make at least one hit, against the distance from the jet core, for different jet p_T's. The dashed lines show the results including pile-up.

(b) Number of reconstructable particles over the angular distance of the jet-axis, for different jet transverse momenta.

fig. 5.10

towards higher η (see fig. 4.1a) and the jets are produced centrally.
In the following, only reconstructable particles, which require the minimum hit requirement on truth level are further considered.

The number of clusters along a track is shown in fig. 5.11 in blue and the number of different layers hit along the track is shown green. Both curves have a similar shape, starting at eight, due to the hit requirement and fall off rapidly after 21, since this is the maximum number of hits, if a particle passes half of the detector layers in forward direction (20 endcap discs and the first barrel layer). Since the numbers did not depend on the jet transverse momentum, the average for the events with different jet-p_T is shown. More than 96 % of the clusters are not shared (orange), however rarely 12 – 14 clusters along a track can be shared. When including pile-up the probability that all clusters along the track are shared clusters is increased and only more than 75 % of the clusters are not shared.

For track reconstruction, the number of shared clusters along the track plays a key role. In figs. 5.12a, 5.13a, 5.14a, 5.15a and 5.16a the rate of tracks with no shared clusters, zero to four shared clusters and more than four shared clusters along the track is plotted against the angular distance of the particle to the jet-core, for different transverse momenta. The rate is calculated relative to the total number of tracks following the above defined track requirements. Due to the collimated nature of the jet, the rate of tracks with shared-clusters increases close to the jet-core. Furthermore, the fractions depend on the transverse momentum of the jet samples. The higher the transverse momentum, the more the jets are boosted and their decay products are less separated.
Without considering pile-up, for jets with transverse momentum of 500 GeV, the rate of tracks with no shared clusters along the track is 83 %, within $\Delta R = 0.02$ and reaches 97 % at angular distances greater than 0.2 from the jet-core. The fraction of tracks with one shared cluster along

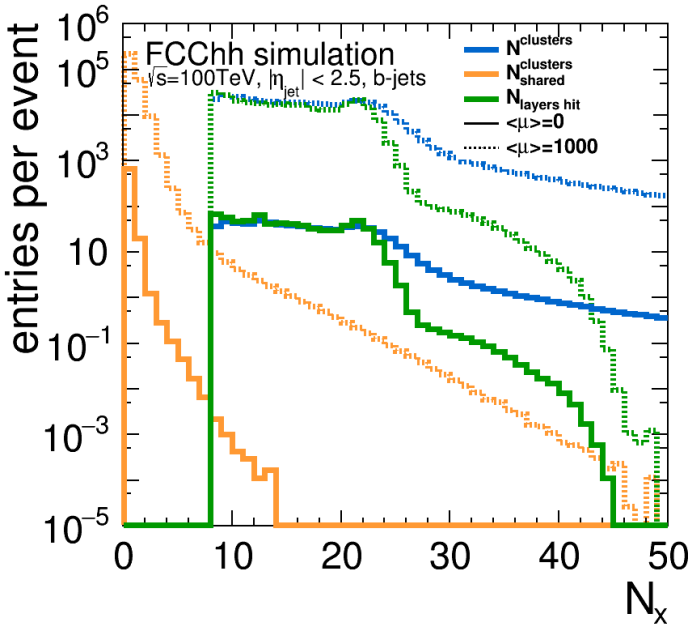

fig. 5.11: Number clusters (blue), different layers hit (green) and shared clusters (orange) along a track, with (dashed) and without pile-up. The average for events with different jet-p_T is shown.

the track reaches a maximum of 14 % in the jet-core and falls off to several percent going outside. Tracks with two shared clusters along the track are found to be at most a few percent, while all other rates are in the sub-percent range. For higher jet-momenta, the rates increase, as expected. Especially for jets with a transverse momentum of 10 TeV, the rates of tracks with shared clusters become high. For instance the fraction for clean tracks, consisting of non-shared clusters goes down to 43 % within an angular distance of 0.02 from the jet-core and all rates for tracks consisting of shared clusters go up to a few percent or tens of percent. Even tracks consisting of more than four shared clusters along the track have a fraction in the percent range. When pile-up of $\langle\mu\rangle = 1000$ is considered, outside the jet-core, the rates of tracks consisting of shared clusters remain high. For example nearly 30 % of all tracks have shared clusters, even outside the jet-core, and - as it is induced by pile-up - this is independent of the jet-p_T.
This can lead to confusion during track finding and in-efficiency in tagging of fake tracks. For instance, ATLAS currently allows at maximum two shared clusters along the track. Hence, shared clusters along the track are a serious issue for track reconstruction and can lead to the complete loss of the track.
In ATLAS, an artificial neural network [166] was trained to identify merged clusters, using the measured charge, which is proportional to the deposited energy, and its relative position of pixels in the cluster. It identifies clusters created by two particles with an efficiency of 90 % and clusters created by more than two particles with 85 %. The neural network can tag clusters into three different categories: to either be shared by one, two or more than two clusters. To estimate the tracking efficiency in dense environments at the FCC-hh, a projected tracking efficiency is determined. The efficiency is calculated by dividing the number of tracks, which can be reconstructed, by the total number of tracks fulfilling the track requirement. Since truth information is used, this method provides an upper limit of an ideal pattern recognition. In case shared clusters are found along the track, they are assumed to be lost and not reconstructable.

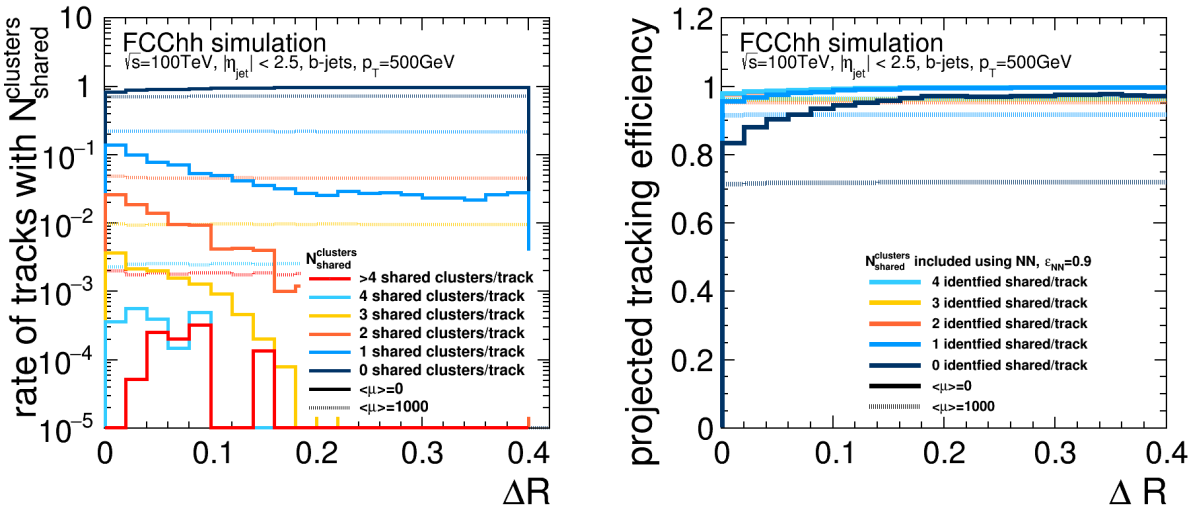

(a) Rate of tracks with the given number of shared clusters along the track, shown in different colors.

(b) Projected tracking efficiency, assuming a perfect pattern recognition. The different colors indicate the distributions of tracks with a given number of shared cluster along the track, presuming an efficiency of a neural network identifying these shared clusters with an efficiency of ε_{NN} of 90 %.

fig. 5.12: Track rate (left) and projected tracking efficiency (right) for b-jets with $400 < p_T < 600$ GeV, plotted against the angular distance ΔR of the respective track to the jet-core. The solid lines show the rates without including pile-up, while the dashed lines include pile-up of $\langle\mu\rangle = 1000$.

This efficiency is shown in dependence of the angular distance to the jet-core in figs. 5.12b, 5.13b, 5.14b, 5.15b and 5.16b for the different jet transverse momenta. The dark blue curve represents the reverse of the established rate of tracks with no shared clusters to the left of each efficiency plot. In the center of the jet-core, within an angular distance of $\Delta R = 0.02$, the efficiency drops to 41 – 83 % depending on the transverse momentum of the jet. Towards the outside of the jet-core a maximum of 97 % can be reached not considering pile-up, which is lowered to 72 % at $\langle\mu\rangle = 1000$.
To estimate the tracking efficiency in case shared clusters can be identified, the following formula was used

$$\varepsilon^{\text{projected}}_{\text{tracking}} = \frac{\sum_{i=0}^{N^{\text{clusters}}_{\text{shared}}} N^{\text{tracks}}_{i} \varepsilon^{i}_{NN}}{N^{\text{tracks}}}, \tag{5.3}$$

with $N^{\text{clusters}}_{\text{shared}}$ being the number of shared clusters along the track. N^{tracks} is the total number of tracks and ε_{NN} is the efficiency of the neural network (NN). To show the projected tracking efficiency, a neural network efficiency of 90 % was assumed, following the example of ATLAS and up to four shared hits along the track have been considered which is highlighted by different colors in figs. 5.12b, 5.13b, 5.14b, 5.15b and 5.16b. The drawback of this approach, is that this would require the possibility to readout the charge deposition. This means more information needs to be stored in terms of bits. Currently, ATLAS uses an eight bit readout, which will be reduced to four bits at the HL-LHC. However the FCC-hh tracker is currently assuming binary readout, which already results in high data rates, as shown in section 4.5. The projected tracking

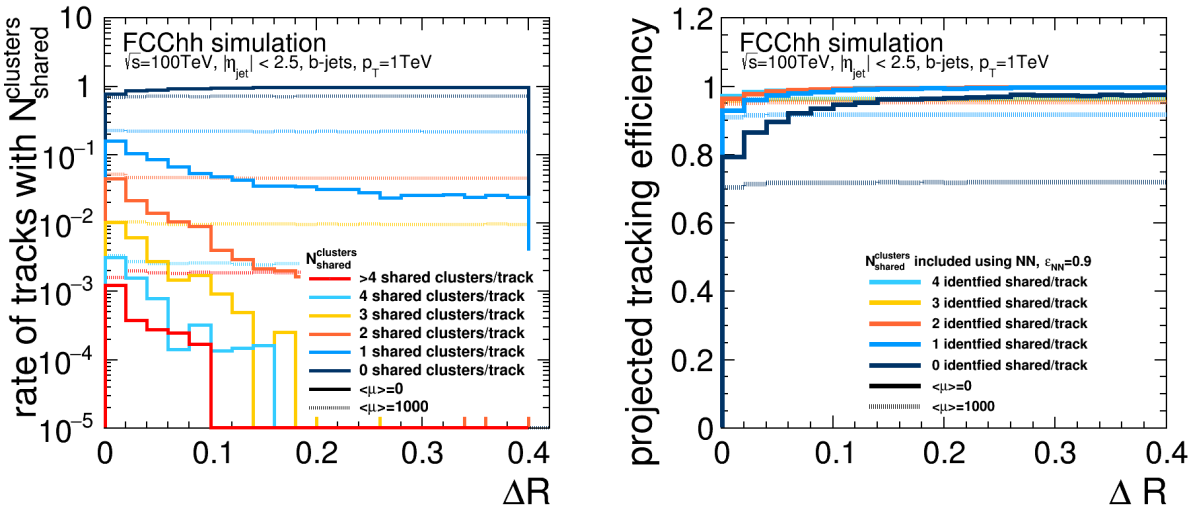

(a) Rate of tracks with the given number of shared clusters along the track, shown in different colors.

(b) Projected tracking efficiency, assuming a perfect pattern recognition. The different colors indicate the distributions of tracks with a given number of shared cluster along the track, presuming an efficiency of a neural network identifying these shared clusters with an efficiency of ε_{NN} of 90 %.

fig. 5.13: Track rate (left) and projected tracking efficiency (right) for b-jets with $900 < p_T < 1100\,\text{GeV}$, plotted against the angular distance ΔR of the respective track to the jet-core. The solid lines show the rates without including pile-up, while the dashed lines include pile-up of $\langle\mu\rangle = 1000$.

efficiency without using neural network identification is the inverse of figs. 5.12a, 5.13a, 5.14a, 5.15a and 5.16a. When the shared clusters can be identified, the projected tracking efficiency improves strongly and allows to nearly converge to 100 % outside the jet-core, even with pile-up included. Although the tracking efficiency can be strongly recovered within the jet-core and values between 85 – 98 % can be achieved, track reconstruction in those dense environments still remains challenging.

5.7 Conclusion and discussion of results

While the high-p_T jets create a signal that is distinguishable from the pile-up background close to the jet-core, the main contribution to the channel occupancy at the FCC-hh tracking system comes from pile-up. With values smaller than 1 % in the macro-pixel region, up to 3 % in the pixel region and up to 21 % in the strip region. High peak values up to 24 % can be reached due to the signal contributions in the strip region.
Cluster merging close to the jet axis happens frequently, especially close to the beamline in the pixel region, where the multi-particle cluster rate reaches a maximum of 11 % without and 6 % with pile-up for 10 TeV-jets. Often these multi-particle clusters in the pixel region originate from more than two particles. In the strip region, due to the coarser granularity, the pile-up particles have a big impact on the cluster merging and the detector is highly occupied in that region. The occurence of multi-particle clusters is in many cases due to cluster merging, which worsens the

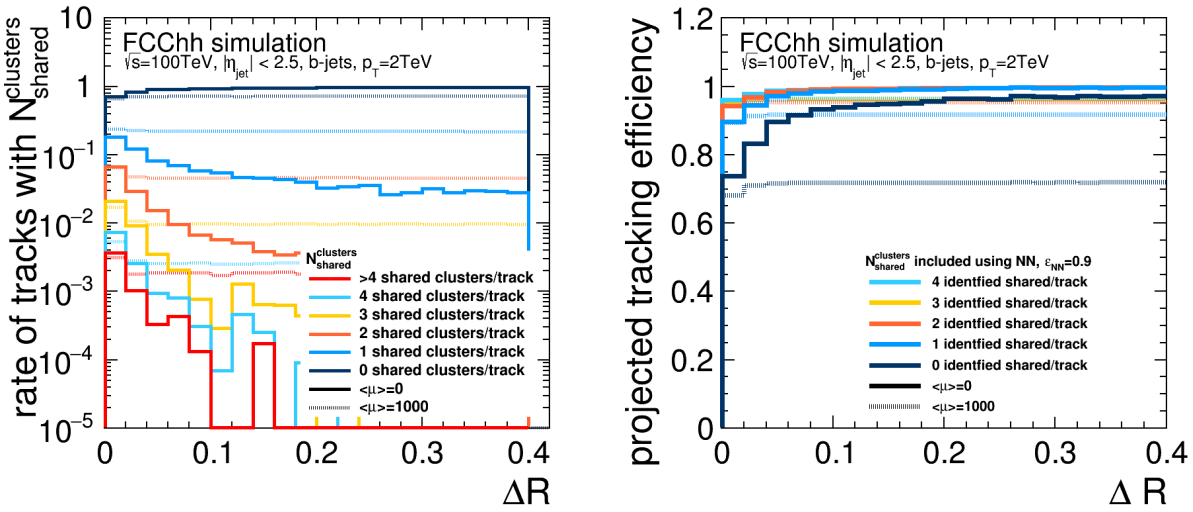

(a) Rate of tracks with the given number of shared clusters along the track, shown in different colors.

(b) Projected tracking efficiency, assuming a perfect pattern recognition. The different colors indicate the distributions of tracks with a given number of shared cluster along the track, presuming an efficiency of a neural network identifying these shared clusters with an efficiency of ε_{NN} of 90 %.

fig. 5.14: Track rate (left) and projected tracking efficiency (right) for b-jets with $1900 < p_T < 2100$ GeV, plotted against the angular distance ΔR of the respective track to the jet-core. The solid lines show the rates without including pile-up, while the dashed lines include pile-up of $\langle\mu\rangle = 1000$.

track parameters' resolution.

As found for the ATLAS experiment, the merging of clusters significantly degrades the track reconstruction capability in the cores of jets and leads to 6.1 – 9.3 % lost tracks for jets with $p_T = 200 - 1600$ GeV [110].

From the findings of this study and the results provided by ATLAS, it can be concluded that the merging of clusters due to highly collimated jets and the pile-up environment put significant constraints on track reconstruction performance for the FCC-hh.

Especially for jets with higher transverse momentum, a decrease in efficiency, due to higher cluster merging rate is expected. For 10 TeV jets, the projected tracking efficiency drops down to 43 % within an angular distance of 0.02 from the jet-axis and increases with decreasing jet-p_T up to 83 % for a 500 GeV jet. Even outside the jet-core the tracking efficiency does not reach 100 % but 97 % due to cluster merging. When pile-up is considered, it further drops to 72 %. Just from pile-up, the number of tracks with shared clusters in raised to 30 %.

A possibility to deal with cluster merging could be a similar approach as done in ATLAS, using neural networks. Such a neural network allows to identify shared clusters and possibly increase the tracking efficiency up to 85 – 98 % depending on the jet p_T. To identify shared clusters, additional readout information would be of need, which would further increase the data rates (see section 4.5).

Future studies including the exact degradation in the track reconstruction performance, due to the merging of clusters need to be done to quantify the presented degradation, once the full simulation track reconstruction chain is established for FCC-hh.

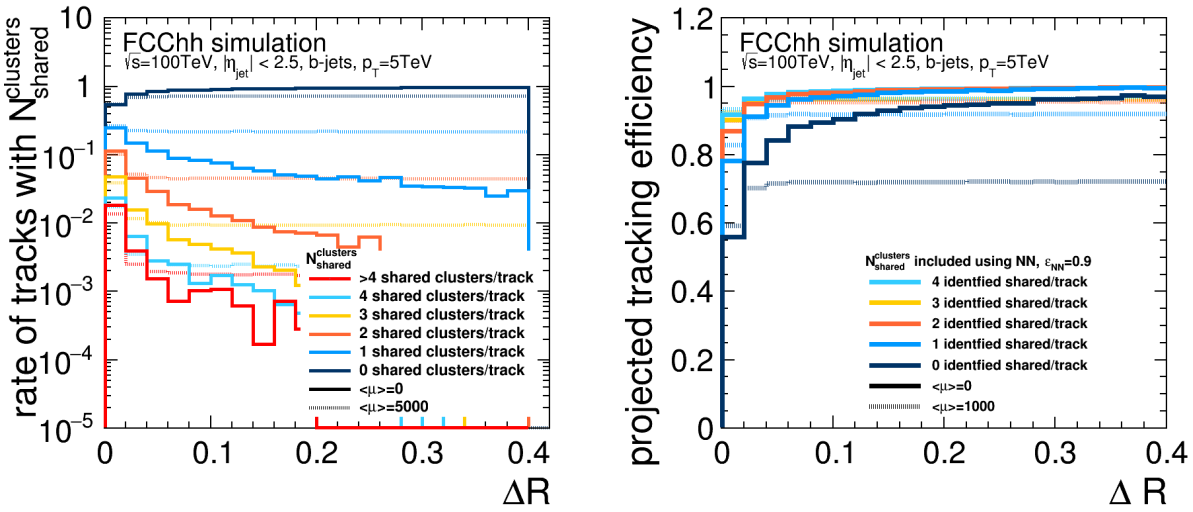

(a) Rate of tracks with the given number of shared clusters along the track, shown in different colors.

(b) Projected tracking efficiency, assuming a perfect pattern recognition. The different colors indicate the distributions of tracks with a given number of shared cluster along the track, presuming an efficiency of a neural network identifying these shared clusters with an efficiency of $\varepsilon_{\mathrm{NN}}$ of 90 %.

fig. 5.15: Track rate (left) and projected tracking efficiency (right) for b-jets with $4900 < p_T < 5100\,\mathrm{GeV}$, plotted against the angular distance ΔR of the respective track to the jet-core. The solid lines show the rates without including pile-up, while the dashed lines include pile-up of $\langle\mu\rangle = 1000$.

As discussed in section 4.6 the tilted layout and a finer segmentation in the strip region would help to reduce the impact of pile-up and the high channel occupancy. For the *HL-LHC* [44] with pile-up of 200, the inclined ATLAS *ITk layout* [167] was found to improve tracking efficiency in dense environments, independent of the jet-p_T and distance of the jet-axis (see [168]). The improvement is due to the better pixel granularity, the larger number of layers and the larger leverarm. Hence, with the inclined modules of the tilted layout, a decreased rate of merged clusters is expected.

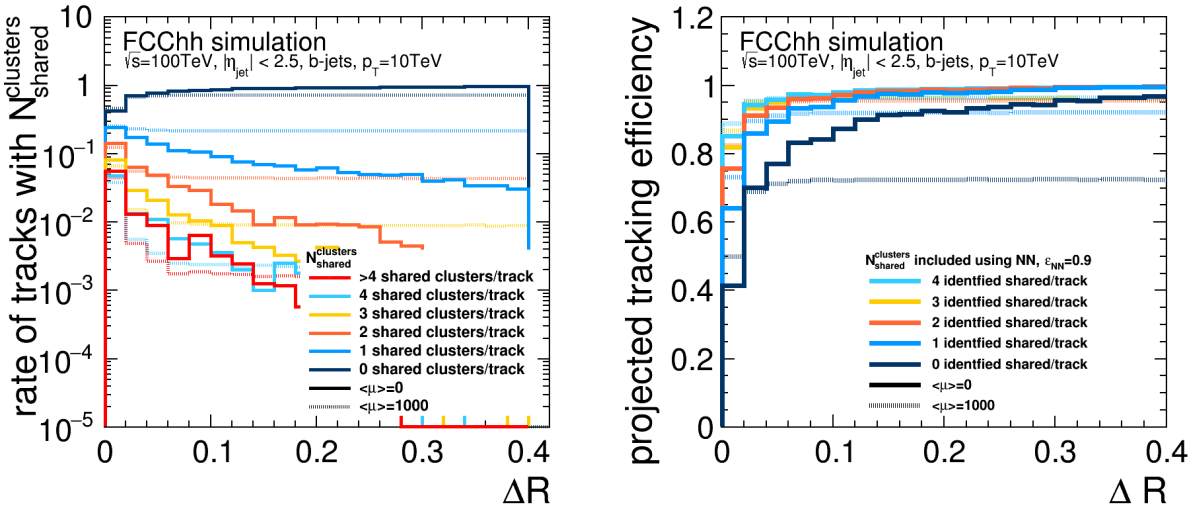

(a) Rate of tracks with the given number of shared clusters along the track, shown in different colors.

(b) Projected tracking efficiency, assuming a perfect pattern recognition. The different colors indicate the distributions of tracks with a given number of shared cluster along the track, presuming an efficiency of a neural network identifying these shared clusters with an efficiency of $\varepsilon_{\mathrm{NN}}$ of 90 %.

fig. 5.16: Track rate (left) and projected tracking efficiency (right) for b-jets with $9900 < p_T < 10\,100$ GeV, plotted against the angular distance ΔR of the respective track to the jet-core. The solid lines show the rates without including pile-up, while the dashed lines include pile-up of $\langle\mu\rangle = 1000$.

Chapter 6

Prospects for search of long-lived wino with disappearing track signature at FCC-hh

One of the big open question in physics concerns dark matter: despite the clear evidence for its existence at this point, the nature of dark matter is still unknown [169]. Astrophysical observations, including the exploration of the large-scale structure of the universe [170] and galaxies [171, 172] demonstrate its existence. Furthermore, it also suggests that dark matter dominates the matter content of the universe.
Possible non-baryonic dark matter candidates, including WIMPs (weakly interacting massive particles), axions, sterile neutrinos or primordial black holes, must not interact or interact very weakly with electromagnetic radiation. In addition, they have to conform with the astronomical observations and they need to be stable on cosmological time scales, otherwise they must have decayed already [37].
One prominent candidate for dark matter are supersymmetric partners of the known particles described by the standard model. Theoretical supersymmetric models (SUSY) [173] extend the standard model by introducing a new space-time symmetry between fermions (spin $\frac{1}{2}$) and bosons (spin 1). SUSY provides a potential WIMP dark matter candidate: a neutralino, which is the lightest supersymmetric particle (LSP) in many SUSY models [40].
In SUSY, the higgsino and the gaugino are the superpartners of the higgs boson and the gauge bosons (W^+, W^-, Z^0) mediating the electroweak force. As a result of SU(2) × U(1) breaking effects, the gaugino and higgsino degrees of freedom can mix and lead to new physical particles: *charginos* (electrically charged mass eigenstate) and *neutralinos*, which are majorana fermions without electric charge. The chargino states are denoted as $\widetilde{\chi}_1^{\pm}$ and $\widetilde{\chi}_2^{\pm}$. The lightest neutralino is denoted as $\widetilde{\chi}_1^0$ [40]. Charginos and neutralinos are often referred to as electroweakinos.
Minimal supersymmetric extensions of the standard model (MSSM) impose the so-called *R-parity*: a discrete symmetry assigning all SM particles a value of +1, while supersymmetric particles acquire a value of –1. In case R-parity is conserved, this has important consequences on scattering and decay processes. For instance, an initial state, which involves the known standard model particles (even R-parity) e.g. a proton-proton collision at a particle collider, supersymmetric particles (odd R-parity) can only be produced in pairs, which decay relatively fast due to their high mass. The final decay products can be SM particles and/or the LSP, which due to R-parity conservation can not decay further and thus remains stable. Hence, the lightest neutralino, which only interacts weakly, is a good dark matter candidate [40, 174].
The wino (supersymmetric partner of the W boson) or higgsino are assumed to be the lightest gaugino states in many SUSY models, which succeed in providing a dark matter candidate, as for example the anomaly-mediated supersymmetry breaking (AMSB) [175, 176]. In that case, the charged SU(2)-multiplet partner of the neutral wino (higgsino) LSP, which is the lightest chargino, is close-by in mass to the LSP. This is due to the approximate custodial symmetry [177], which forbids mass splitting at tree-level and only allows radiative corrections which are calculated to be approximately 160 MeV for the wino case (at two-loop level) [178] and 350 MeV [179] for the

higgsino LSP scenario.
The consequence of the small mass difference is, that the chargino decays mainly to the neutralino and a soft pion (see fig. 6.1b). This also leads to a relatively long-lived chargino with a decay length of $c\tau = O(1-10)\,cm$ [178] and a possibility to detect the chargino in the detector. The neutralino passes through the tracker without interaction and the pion, due to its low transverse momentum will not be reconstructed in the tracker. Hence, the chargino signature can be observed by searching for a *disappearing track* in the tracker. For the small radiative corrections to the mass difference, the calculated wino (higgsino) lifetimes are of approximately 0.2 (0.023) ns (see [54], *figure 4*).
When assuming that the neutralino is dark matter, which was produced in thermal processes, there is an upper limit of the WIMP mass. This upper limit can be calculated from the observed relic density of dark matter and is 3 TeV for the wino case (see [180], *figure 2*) and 1 TeV for the higgsino case (see [180], *figure 5*). Hence, it could be discovered at 100 TeV center-of-mass collisions at FCC-hh.
The latest disappearing track searches performed by the ATLAS experiment using data of $\sqrt{s} = 13\,TeV$ exclude wino masses below 460 GeV with a lifetime of 0.2 ns at 95 % CL [181].

6.1 Event topology and kinematics

This study probes charginos and neutralinos produced in pairs: $\tilde{\chi}_1^{\pm}\tilde{\chi}_1^{\mp}$, $\tilde{\chi}_1^{\pm}\tilde{\chi}_1^{0}$ for the wino case[1]. In order to trigger (see section 2.4) and select events as being possible chargino-neutralino candidates, selection cuts which distinguish these events from others need to be applied. These selection cuts usually use criteria based on charged lepton detection, detection of jets (see section 5.2) or missing transverse energy[2] (E_T^{miss}) (see [69, 184, 185]).
The signature of the probed events is characterized by the presence of one or two charginos, which possibly create short track signatures in the detector due to their decay and a neutralino, which leaves the detector undetected. Since the $\tilde{\chi}_1^{\pm}\tilde{\chi}_1^{\mp}$- or $\tilde{\chi}_1^{\pm}\tilde{\chi}_1^{0}$-pairs produced in the proton collision are mass degenerate for the pure chargino case and nearly mass degenerate for the mixed chargino-neutralino case, the particles will be produced at rest (in the transverse plane) and the transverse momenta will cancel each other out leaving small to no E_T^{miss}. In that case, the event can not be triggered or selected and hence, will not be registered by the experiment. However, in presence of a hard QCD-jet due to initial state radiation[3], the electroweakino-pair will recoil against the jet. As a consequence the produced SUSY particles are boosted, which allows to detect missing transverse energy. In most SM searches ISR is a nuisance, which can contaminate the final states. As for this case and also other SUSY searches, ISR is of big advantage and mandatory for being able to select this signal [186]. The corresponding Feynman diagram is shown in fig. 6.1a. Figure 6.1b shows an event display (jet is omitted) of the production of a chargino-pair and the subsequent decay of one of the charginos within the FCC-hh tracking detector. Since the neutralino-mass is nearly mass degenerate with the chargino,

[1] In general the lower indices indicate the mass ordering, i.e. $M_{\tilde{\chi}_1} < M_{\tilde{\chi}_2}$

[2] The total energy and initial momentum of the colliding partons (the hypothetical consituents of a proton, see [182]) along the beam-axis is unknown. According to the laws of momentum and energy conservation, the total sum of energy of particles produced in the transverse plane to the beam-axis must be zero. Hence, if particles are invisible to detection because they are only interacting weakly (as it is the case for neutrinos or the dark matter candidate neutralinos), this can be observed by missing transverse energy, which is equal to the negative net transverse momentum: $E_T^{miss} = -\sum_i p_T$ [183].

[3] The constituents of the proton, namely gluons and quarks are continuously splitting apart and recombining. This activity can be disturbed in case the protons are scattered, which can leave individual quarks and gluons in an uncombined state, resulting in jet-signatures and is called initial state radiation (ISR) [186].

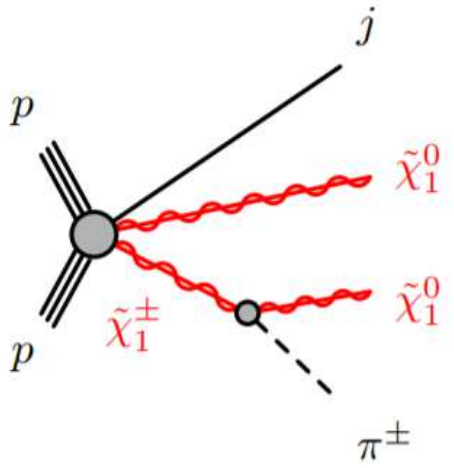

(a) Feynman graph, illustrating the production mechanism of a chargino-neutralino-pair $pp \to \tilde{\chi}_1^\pm \tilde{\chi}_1^0 + j$ and the subsequent decay of the chargino to a neutralino and a pion $\tilde{\chi}_1^\pm \to \tilde{\chi}_1^0 + \pi^\pm$. Source of figure: [187].

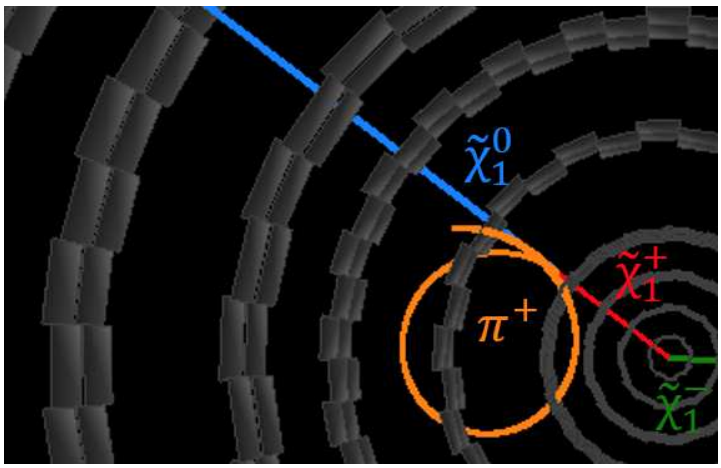

(b) Event display (using Acts fast simulation within the FCC-hh tracker, with $m_{\tilde{\chi}_1^\pm} = 1600.33\,\text{GeV}$ and $m_{\tilde{\chi}_1^0} = 1600.17\,\text{GeV}$) of the production of a $\tilde{\chi}_1^+\tilde{\chi}_1^-$-pair and the decay of the $\tilde{\chi}_1^+$ after the fourth layer of the tracking detector.

fig. 6.1

it is boosted in the same direction as its mother. The pion is emitted very softly and hence, is strongly curled within the FCC-hh magnetic field of 4T (for details of the decay kinematics, please see appendix A.7).

6.2 Event Generation

Monte Carlo (MC) event samples are used [188] (section *Simulation Samples*), assuming the minimum AMSB model for the wino. The configuration is chosen in a way to account for the observed Higgs boson mass at 125 GeV, without maximal mixing ($\tan\beta = 5$ and $m_0 = 20\,\text{TeV}$). Only pure wino LSP scenarios are taken into account. The kinematic distributions have been simulated using `MAD-GRAPH5_aMC@NLO` 2.3.3 [189] with the output of event generation files in LHE-file-format [164].

6.3 Simulation

The parton-level LHE-events are showered using the Pythia8 [98] event generator version 8.230 with Monash 2013 tune [99]. The vertex of the generated particles is smeared at generator level with $\sigma_{x/y} = 0.5\,\text{mm}$ and $\sigma_z = 40\,\text{mm}$. After the generation process, the particles are input to FCCSW simulation (see section 3.1) using Geant4 [102]. The simulation was configured in a way to force the chargino to decay into a neutralino and a charged pion. The decay time of the charginos can be configured at runtime to allow the simulation of different scenarios. Details on the implementation of the chargino simulation can be found in appendix A.9. To account for the pile-up, the chargino events have been overlaid with minimum bias events as explained in section 3.1. After the particle interactions within the detector have been simulated, the output of Geant4 is digitized and clusterized as described in detail in section 3.1.4. A minimum energy deposition of 3.6 eV for a particle to be registered, was applied during simulation and an

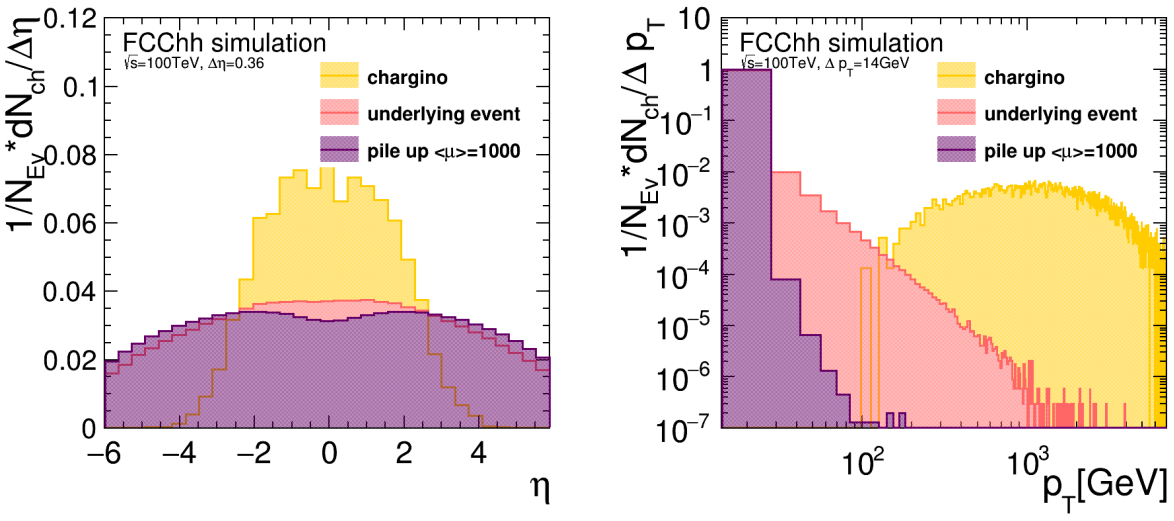

(a) The averaged charged particle multiplicities for each event normalized to 1, over η, displayed for the different contributions.

(b) The averaged charged particle multiplicities for each event normalized to 1, versus the particle's p_T, displayed for the different contributions

fig. 6.2: Pseudorapidity (η) and transverse momentum (p_T) distributions, separately displayed for the pile-up noise in magenta ($\sim$ 1000 overlaid minimum bias events), the underlying event is displayed in coral, while the chargino distribution is displayed in yellow. Only primary charged particles have been used, which represent all generated particles reaching the detector.

additional threshold of 3.6 keV (production of 1000 electron-hole-pairs in Silicon) was applied to activate a readout cell during digitization.

6.4 Charged particle spectra and decay vertices

The η and p_T-spectra of the primary simulated particles are displayed in fig. 6.2a and fig. 6.2b. Both figures display three different distributions, showing the contributions of pile-up with $\langle\mu\rangle = 1000$ in magenta, the underlying event[4] in coral and the chargino particles in yellow. The bulk of the charginos are produced within the central region with $|\eta| \leq 2$, while both, the underlying event and the pile-up noise are produced rather flat in η, with a slight decrease in the forward region. In contrast to the pure pile-up contribution, the underlying event has an increased activity in the central region. When comparing the transverse momentum distribution of those three different cases, apparently the p_T-spectra of the pile-up particles and the charginos are well separated. While the contributing particles from pile-up have a relatively soft p_T-spectrum, with the bulk being below 10 GeV, the charginos are produced at high p_T only, with the majority ranging from 100 – 7000 GeV. The underlying event is similar to the pile-up, with the majority of particles within the soft region, but with a stronger tail reaching towards $\mathcal{O}(1000)$ GeV, which presumably comes from additional particles being produced in the hard scatter, apart from the chargino, as for instance the ISR-jet.

[4]For definition of the underlying event and kinematics at 100 TeV, please see section 4.1.

6.5 Hit requirement selection

The minimum number of space-points to reconstruct a particle trajectory within a magnetic field is three. Given the extremely high number of clusters in the first layers (see fig. 4.4a), the number of fake tracks[5] will be increased for a small number of hits required to build tracks. In addition, the track parameters resolution will be rather poor for this case. Hence, requiring a higher number of hits on different detector layers will increase the track quality and decrease the fake-background. On the other hand, the signal acceptance (which decreases when requiring more number of hits due to the short lifetime of the wino) needs to be maximized. To find the optimal hit requirement, balancing those competing demands, the fake background, as well as the momentum resolution and signal strength need to assessed.
To set first limits on the possible requirement of hits on different layers, the fraction of particles surviving at each layer is shown in fig. 6.3, for the wino-signature, against the radial position of the layer. The underlying event and the pile-up are shown separately. For this first check, only tracks fully contained within the barrel region have been considered. This choice was taken because it was found that out of 10 000 wino-events only 872 contained wino-tracks with four hits and only 19 out of these had at least one hit in the endcap region. The radial position of each layer is drawn with a vertical grey dashed line. At $r = 0$ all charged particles produced in the interaction, of which many do not even reach the first layer, are displayed and are scaled to be 100%. Each subsequent entry is relative, scaled to this first number. Absolutely, there are on average 1.6 winos, 410 charged particles from the underlying event and 202 690 charged particles from the pile-up contribution produced per event. From fig. 6.3 it can be seen that after the 4th layer, the percentage of wino-tracks surviving decreases rapidly in order of magnitudes from 4.45 % down to 8.4 ‰ at the 5th layer and 2 ‰ at the 6th layer. The background from underlying event and pile-up decreases smoothly. However, a reduction of 0.1 of the pile-up tracks corresponds to roughly 20 000 less number of tracks. Hence, it was chosen to study more closely tracklets with 4, 5 and 6 hits on different layers.

6.6 Event selection and background estimation

The chargino is expected to have high transverse momentum (see fig. 6.2b). Due to its decay to a neutralino, large missing energy (E_T^{miss}) contribution is expected. A jet with high transverse momentum from initial state radiation together with the missing energy requirement will allow to trigger the chargino event candidates. Further selection can be based on the occurrence of a high-p_T tracklet.
In general, the background can be divided into two categories: physical and unphysical background. The physical background from Standard Model events arises due to tracklets which fulfill the event selection criteria. Other physical background contributions may arise, as soon as the event candidate is selected. These include tracklets from pile-up and the underlying event. The third category is unphysical background from fake tracks, emerging from random combinations of space points. Especially in the high pile-up environment of FCC-hh, the number of fake tracklets is expected to be high.
There are three different background contributions, which can complicate finding the possible chargino tracklet:

1. physical background from SM events
2. physical background from pile-up and underlying event

[5] Fake tracks are tracks which are formed from random combination of space-points.

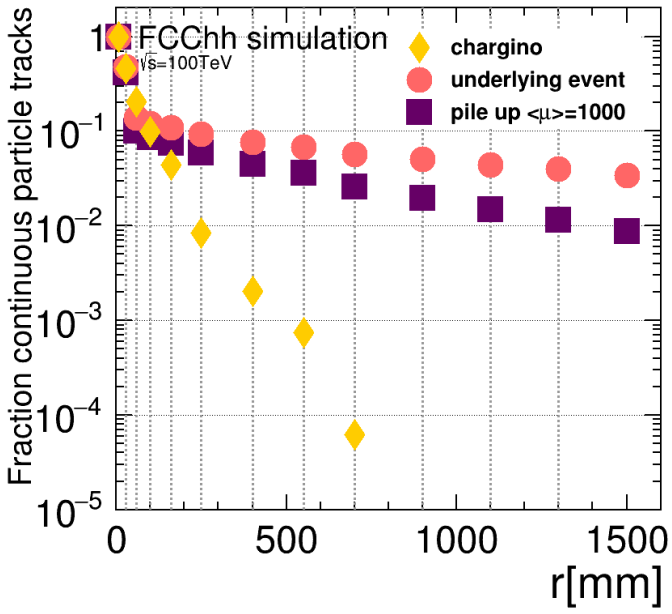

fig. 6.3: Fraction of tracks surviving at each layer, for the chargino wino signature with $\tau = 0.2\,\text{ns}$, the underlying event and the tracks coming from pile-up. Each vertical grey dashed line displays the radial position of a layer. The first entry display the total number of generated particles

3. unphysical combinatorial background from pile-up and underlying event

All backgrounds are estimated and described in more detail in the following subsections. Mainly for simplicity reasons, only the barrel region was studied in detail. Nevertheless, studying only the barrel region enhances the signal to background ratio for tracklets stemming from pile-up. Due to their high p_T the charginos are mainly produced in central regions, while a big fraction of background is expected in the more forward regions, as shown in section 6.6.1. To keep the signal rate sufficiently high, tracklets fully contained in the barrel region, for the different hit requirements have been considered, which correspond to an η-coverage of 2.4, 1.8 and 1.46.

6.6.1 Tracklets stemming from pile-up and underlying event

To estimate the tracklet-candidates within pile-up of $\langle\mu\rangle = 1000$ and underlying event, all particles creating only 4, 5 or 6 measurements on different layers are considered. Electrons are treated in a special manner, since those can loose considerable amounts of energy through radiation. This can lead to a change in their curvature and hence lead to reconstruction as a tracklet. As soon as an electron has lost 90 % of its initial energy, the subsequent produced clusters are not counted to belong to the same track. In the following, the characteristics of all tracklets are studied in detail.

Figure 6.4a shows the distribution of the tracklets versus the pseudorapidity η from pile-up and underlying event. The plot is stacked and shows the composition of particle types of the tracklets. On average 7040 tracklets are produced per event with the main contribution being pions (83 %) followed by kaons (12 %) and protons (3 %). Electrons have a relatively small share of (0.7 %). The composition of the underlying event without including pile-up is very similar to the composition with $\langle\mu\rangle = 1000$, see fig. 6.5a. The contribution of the underlying event is very

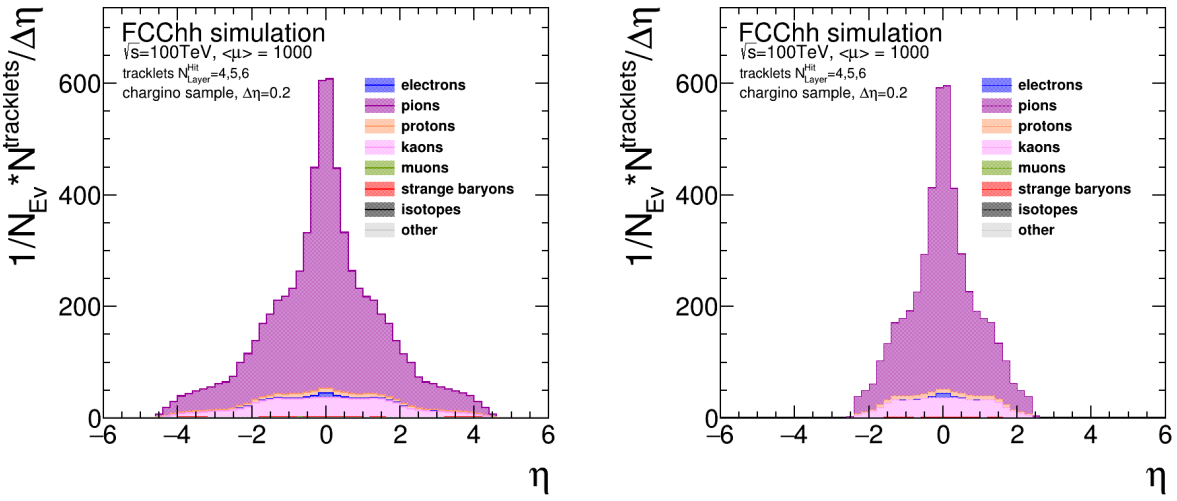

(a) All primary tracklets included.

(b) Only primary tracklets, fully contained in the barrel region, included.

fig. 6.4: Charged particle multiplicity and composition of primary tracklets of the underlying event and pile-up. The average number of tracklets, which could be mistaken for a wino disappearing track signature expected per events is shown, versus the pseudorapidity η. The different colors indicate the contributions of the different particle types.

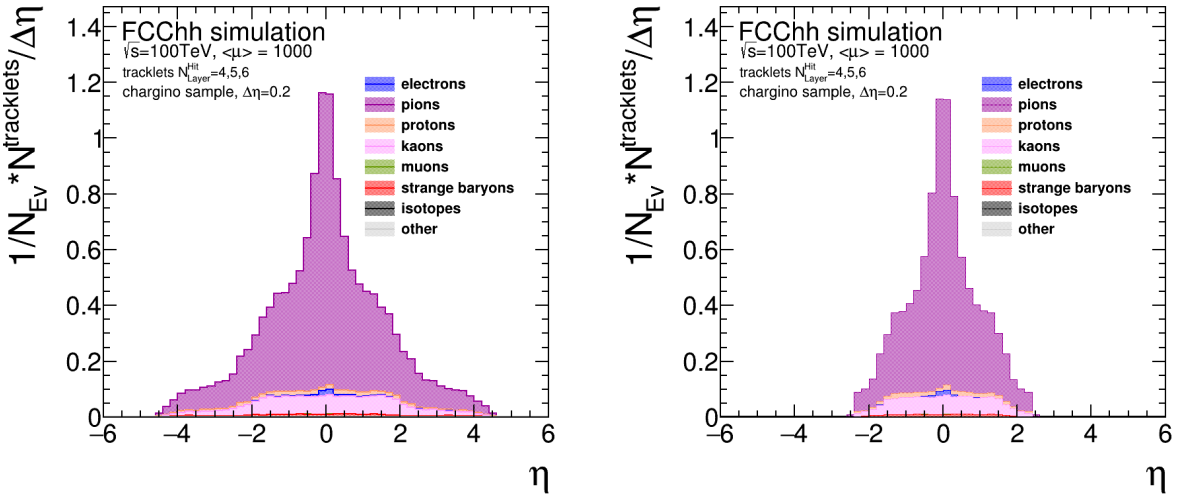

(a) All primary tracklets of underlying event included.

(b) Only primary tracklets of the underlying event, fully contained in the barrel region, included.

fig. 6.5: Charged particle multiplicity and composition of primary tracklets of the underlying event. The average number of tracklets, which could be mistaken for a wino disappearing track signature expected per events is shown, versus the pseudorapidity η. The different colors indicate the contributions of the different particle types.

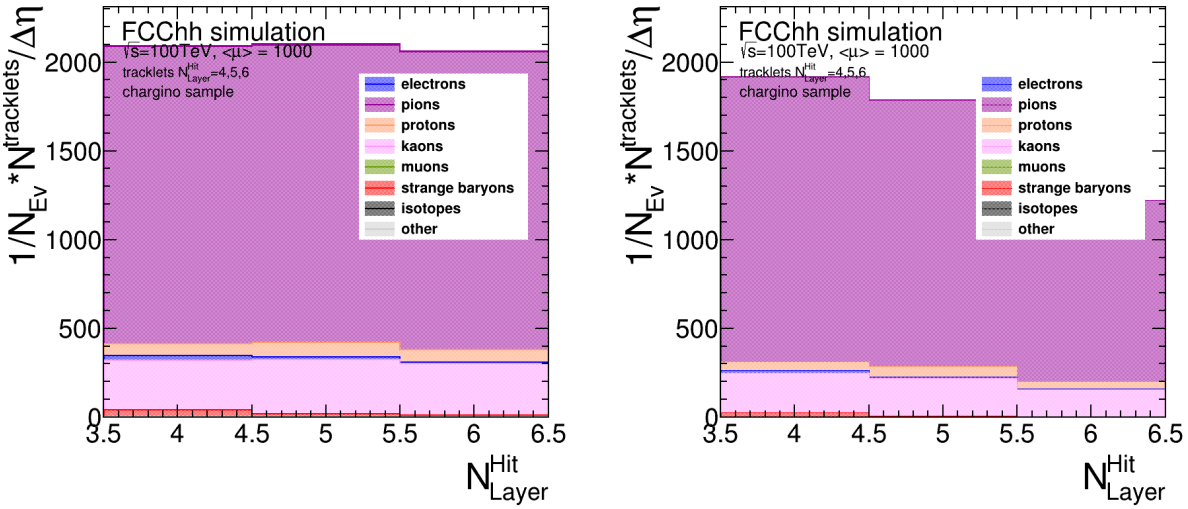

(a) All primary tracklets included.

(b) Only primary tracklets, fully contained in the barrel region, included.

fig. 6.6: Number of different layers hit by primary tracklets of the underlying event and pile-up. The plot is stacked and shows the composition of tracklets.

small, since on average only ~ 14 tracklets are caused by it per event.
Studying only the barrel region reduces the possible background tracklets, as shown in Figure 6.4b and Figure 6.5b. In total 4932 tracklets are produced per event on average at $\langle\mu\rangle = 1000$, which is a reduction of $\sim 30\,\%$. The particle composition is very similar when including the endcaps.

So far, no differentiation of tracklets made of 4, 5 or 6 hits was made. Figure 6.6 shows the composition in dependence of the number of different layers. Including the endcaps the number is roughly the same, for all three cases. When considering barrel only, in total 1919 tracklets are on average expected when requiring four hits on different layers, which is lowered to 1790 requiring five hits and 1223 tracklet for six hits.

Whether a tracklet could be mistaken for a disappearing track, strongly depends on the transverse momentum of the particle. In fig. 6.7 the truth p_T-distribution of all tracklets (left) and tracklets in the barrel region only (right) is shown. The charginos have very high transverse momentum in the range of 30 to 10 000 GeV, while the background tracklets are mostly in the low momentum region. In the barrel region only one tracklet (1.5 including endcaps) per event has a transverse momentum higher than 10 GeV, on average.

Figure 6.8 shows that while the highest momentum charginos are produced very central, the background tracklet momenta increase with increasing η. This is most likely because the probability for hadronic interaction and hence, for a particle to create a tracklet, is increased, when more material is passed.

The background and the chargino tracklets are kinematically very well separated on truth level. However, after reconstruction this does not need to be the case. To test for this case a simple fit method based on the *Riemann fit*, more closely described in appendix A.8, has been applied, to fit a track through all measurements belonging to the same tracklet. The used Riemann fit method is just a simple approximation. It does not take any effects due to multiple scattering into account and hence performs worse than other more complex methods. Since for the charginos high momentum tracks are expected, effects due to multiple scattering should be small.

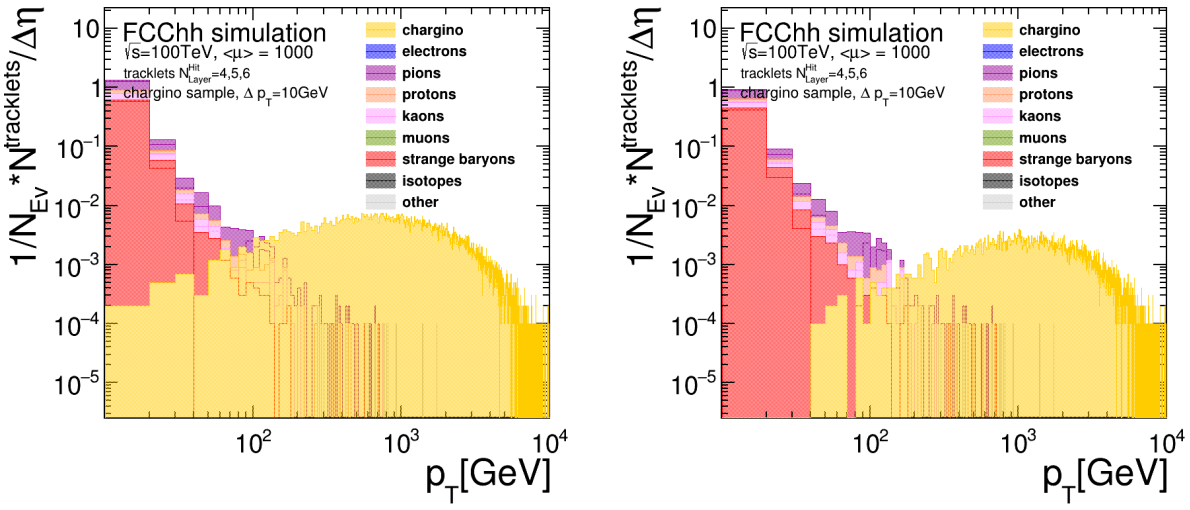

(a) All primary tracklets included.

(b) Only primary tracklets, fully contained in the barrel region, included.

fig. 6.7: Truth transverse momentum distribution of tracklets. The plot is stacked and shows the particle composition. The p_T-distribution of the charginos is overlaid in yellow.

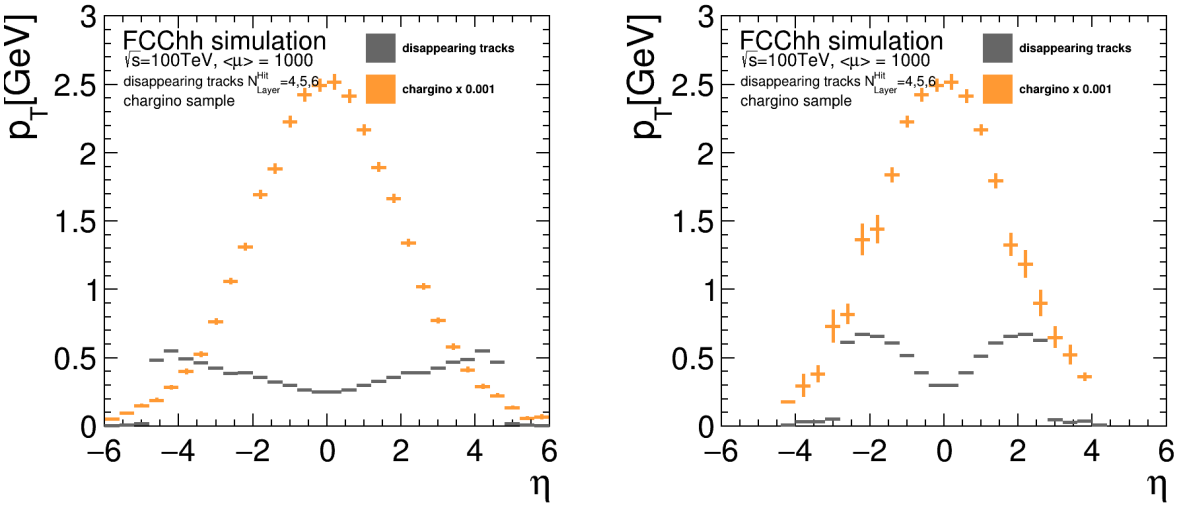

(a) All primary tracklets included.

(b) Only primary tracklets, fully contained in the barrel region, included.

fig. 6.8: Average transverse momentum of background tracklets (disappearing tracks, grey) and chargino (yellow) over η.

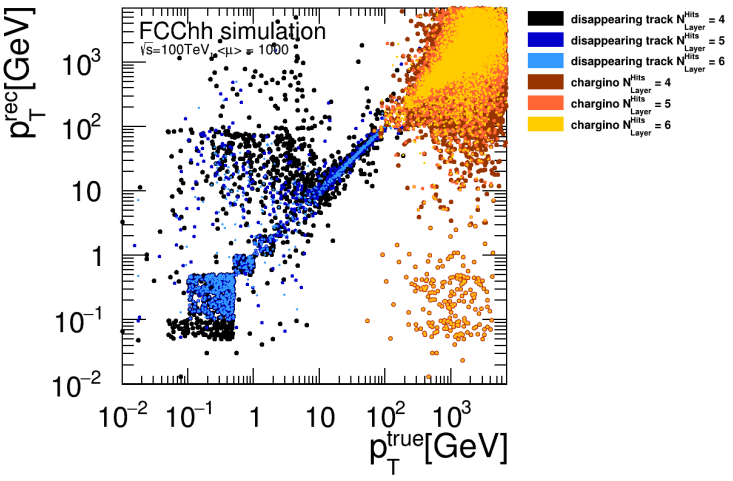

fig. 6.9: Reconstructed transverse momentum versus true transverse momentum of the tracklets from pile-up and the charginos for requiring four, five and six hits on sepatrate layers. The contributions for a different number of hits on different layers $N^{\text{Hits}}_{\text{Layer}}$ is shown in distinct colors.

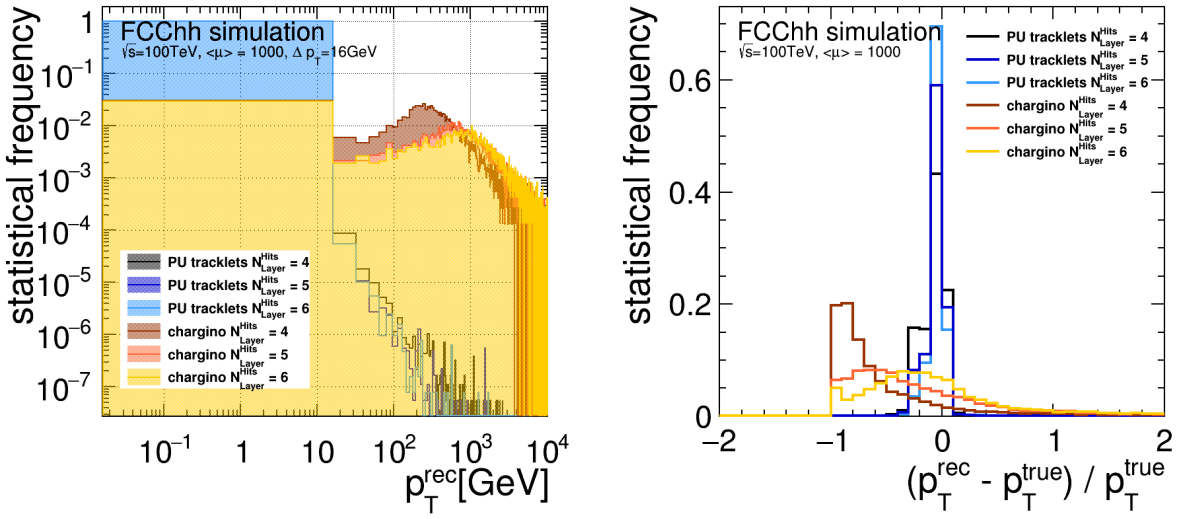

(a) Reconstruced transverse momentum of tracklets from background of pile-up and underlying event (PU tracklets) and chargino tracklets.

(b) Relative difference of reconstructed and true p_T of tracklets from background of pile-up and underlying event (PU tracklets) and chargino tracklets.

fig. 6.10: The contributions for a different number of hits on separate layers $N^{\text{Hits}}_{\text{Layer}}$ is shown in distinct colors. The distributions have been normalized. Hence, the y-axis shows the statistical frequency of each entry.

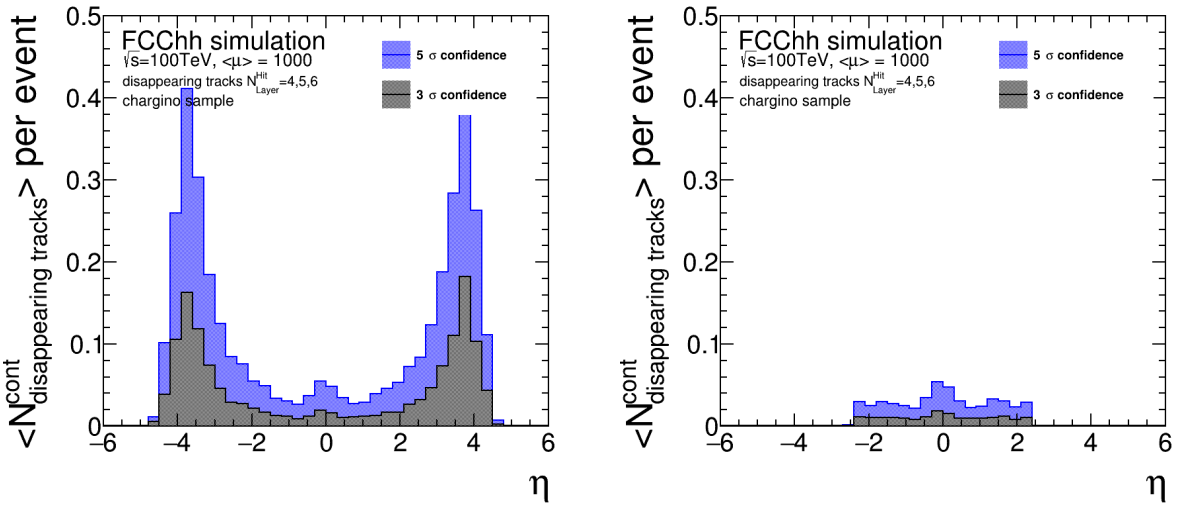

(a) All primary tracklets included.

(b) Only primary tracklets, fully contained in the barrel region, included.

fig. 6.11: Number of primary vertices of background tracklets contaminating the primary signal vertex, in dependence of η.

Figure 6.9 shows a scatter plot of the reconstructed transverse momentum (p_T^{rec}) versus the true transverse momentum (p_T^{true}) of both, the charginos and the background tracklets in the barrel region. Especially in the very low (due to material effects) and very high momentum region the fit performs worse. In the latter case it is because the tracklet is closer to a straight line, than to a circle. Hence, a fraction of low momentum tracklets from pile-up are reconstructed to have high p_T and a significant share of the high p_T chargino tracklets are reconstructed with lower transverse momentum as displayed in fig. 6.10a. The reconstructed momentum resolution is worse for requiring less number of hits for the tracklets [65] which is shown in fig. 6.10b.

Since the primary vertex of the chargino can be identified by the ISR-jet, only tracklets close to the signal vertex are potentially contaminating the signal. The primary vertex can only be identified with a certain resolution depending on the impact parameter resolutions. To obtain the number of tracklet vertices contaminating the signal vertex, the overlap of the two error ellipses of the signal vertex with each tracklet vertex was considered. The error ellipse is defined by the vertex, given from truth information, as the center and, depending on the confidence level, three or five times σ_{z_0} and σ_{d_0} as axes. The impact parameter resolutions have been interpolated in η from the profiles given in fig. 2.8, in dependence of the transverse momentum. Because the resolution is improved for higher p_T, the resolution corresponding to the lower p_T was used, as a conservative assumption. For instance, for a track with 4 GeV, the 2 GeV curve was used, while for a particle with ≥ 5 GeV, the 5 GeV curve was used to interpolate the resolution. In fig. 6.11 the η-distribution of vertices contaminating the signal vertex is shown with (left) and without (right) including the endcaps for 3σ and 5σ confidence level. Due to the worse impact parameter resolution at high η, resulting from multiple scattering effects, the contribution is much higher, when including endcaps, with in total 3.7 (5σ) and 1.4 (3σ) number of tracklets contaminating the primary vertex, per event. When only the barrel region is considered, in total only 0.49 (5σ) and 0.18 (3σ) number of tracklets are found to disturb the primary vertex, per event. In fig. 6.12 the transverse momentum distribution of the contaminating vertices is shown for the two confidence values, with and without endcaps. In total approximately only 4×10^{-4}

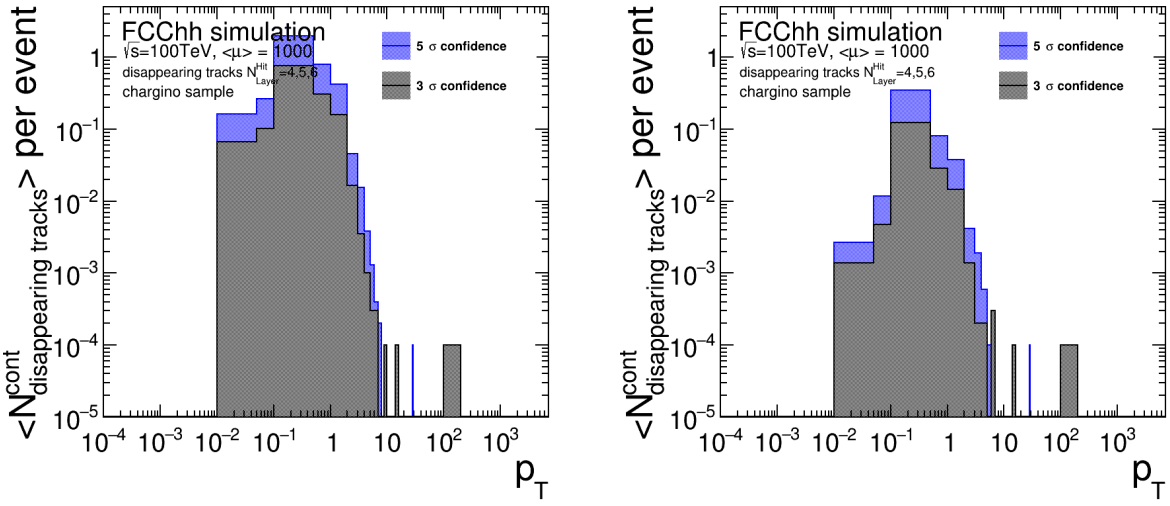

(a) All primary tracklets included.

(b) Only primary tracklets, fully contained in the barrel region, included.

fig. 6.12: Transverse momentum distribution of primary vertices of tracklets contaminating the primary signal vertex.

(5σ) and 3×10^{-4} (3σ) number of tracklets are found to contaminate the primary vertex and have a transverse momentum $> 10\,\text{GeV}$.

6.6.2 Combinatorial background estimation

Due to the extremely challenging pile-up conditions of 1000 simultaneous proton-proton collisions per bunch crossing expected at FCC-hh, the occupancy was estimated to be relatively high, up to the percent range as established in chapter 4. In these conditions, the fake background due to random combinations of hits is expected to be high. For an exact estimation of the fake background, full simulation followed by full event reconstruction including track finding, track fitting and ambiguity solving needs to be applied. Given the density of clusters on the different layers, the combinatorics can be estimated, as described in the following.

Tracklets creating 4, 5 and 6 hits on different barrel layers have been considered, which corresponds to an η-coverage of 2.4, 1.8 and 1.46 respectively. As a first step towards obtaining the combinatorial background arising due to the high pile-up, random hits have been generated in a small window in φ and z. The window is defined by the single point resolution of the tracking layers in z ($dz = 5 \cdot \sigma_i^z$) and a cone in phi denoted as $d\varphi$:

$$A_i^{\text{window}} = d\varphi \times dz \tag{6.1}$$

with the resolution given by the pitch size of the layer $\sigma_i^x = \frac{p_i}{\sqrt{12}}$. The cone is defined by the lowest p_T which should possibly be registered, as illustrated fig. 6.13b:

$$\Delta\varphi = 2 * \tan^{-1} \frac{R_L}{\sqrt{4R_T^2 - R_L^2}}. \tag{6.2}$$

Since the truth transverse momentum of all simulated charginos is above 90 GeV (see fig. 6.2b), 50 GeV have bin chosen as a lower limit to be sensitive to the chargino signature. In this way,

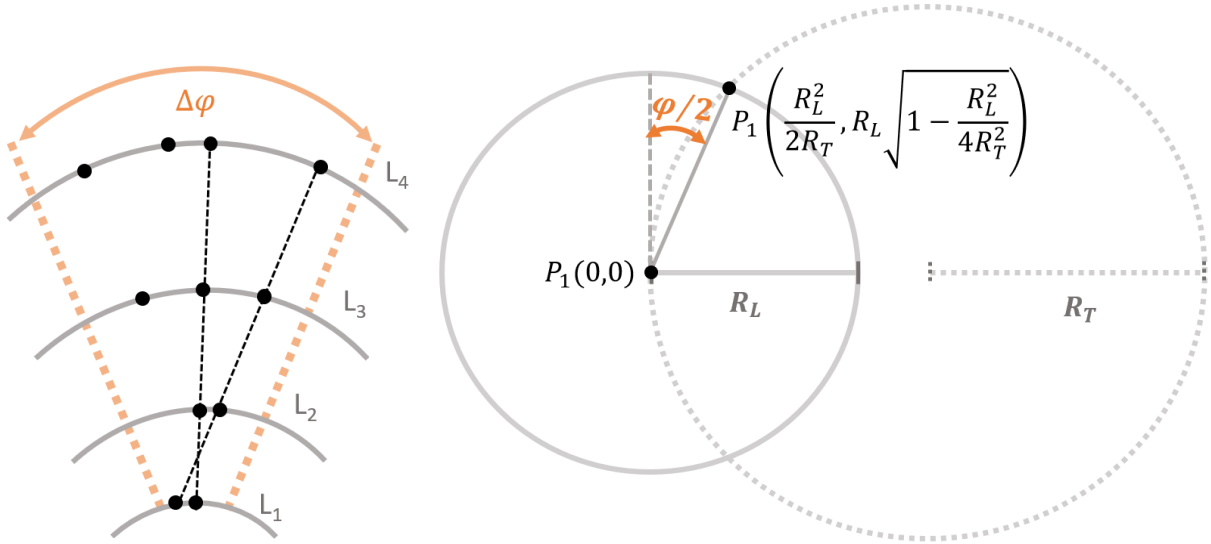

(a) Each cone segment displays a part of a barrel layer 'Lx' in transverse plane. The points illustrate hits on the layers. The sketch shows the possible combinations (black dashed) given a hit on the first with hits on the last layer, within a cone (orange dashed) defined by δφ.

(b) Sketch illustrating the calculation of the opening angle Δφ, defined by the radius of the trajectory in the transverse plane R_T and the radius of the barrel layer R_L.

fig. 6.13: Illustrations for the combinatorial background estimation.

the worse reconstruction performance due to the small number of hits is accounted for, but still a significant amount of fakes is excluded. To obtain an upper limit, the same window $d\varphi = 0.0096$, which corresponds to a 50 GeV-track reaching the sixth layer has been used, for all layers.
The randomly created hits are fitted using the Riemann method, shown in appendix A.8. After fitting, a quality cut on the fake tracks is applied using the χ^2-method, as explained in appendix A.11.1. In addition, only tracks with a reconstructed impact parameter $d_0 < 50\,\mu m$ pass the cut. In this way, the rate of fake tracklets with a good fit quality can be established, as summarized in table 6.1. The obtained p_T spectra are shown in fig. 6.14a.

Process	P passing χ^2 for $N^{Hit}_{Layer} = 4$	P passing χ^2 for $N^{Hit}_{Layer} = 6$	P passing χ^2 for $N^{Hit}_{Layer} = 5$
PU fakes	1.11×10^{-4}	7.50×10^{-5}	2.51×10^{-5}

tab. 6.1: Rate of fitted tracklets, for different number of layers hit, passing the goodness-of-fit-cut using the χ^2-method and the d_0-requirement.

To obtain the number of tracklets per event, consistent with above assumptions, maps denoted as $N^{Hits}_{Lx}(\eta)$ have been created. The maps store the average number of clusters per event

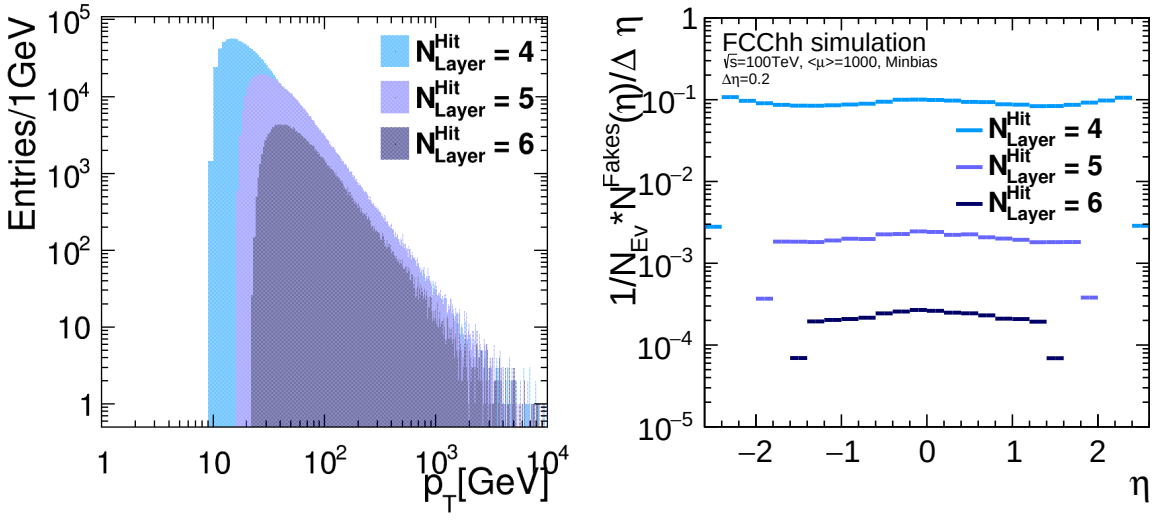

(a) Transverse momentum spectra of the fake tracklets used to estimate the combinatorial background for 4, 5 and 6 hits on different layers. The spectra have been produced by fitting tracks to randomly produced hits.

(b) Estimated number of fake tracklets with high $p_T \gtrsim 50\,\text{GeV}$ per event due to combinatorial background in the high pile-up environment of $\langle\mu\rangle = 1000$ for requiring 4, 5 and 6 hits on different layers in dependence of η.

fig. 6.14: Estimation of the combinatorial backhround.

with $\langle\mu\rangle = 1000$ for each barrel layer in dependence of η. The total number of possible fake combinations $N^{fakes}(\eta)$ along η can be estimated by the following formula:

$$N^{Fakes}(\eta) = \langle N^{Hits}_{L_1}\rangle \cdot N^{Combi}_{L_n}(\eta) \cdot \prod_{i=2}^{n-1} P_{L_i}(\eta), \tag{6.3}$$

where $\langle N^{Hits}_{L_1}\rangle = 14$ is the average number of hits per dz (defined in eq. (6.1)) on the first layer. This number is multiplied with each bin of the histogram $N^{Combi}_{L_n}(\eta)$, which is the number of possible combinations, given by the number of hits in a cone, as defined in fig. 6.13a, in the last layer (denoted with subscript 'n'):

$$N^{Combi}_{L_n}(\eta) = N^{Hits}_{L_n}(\eta) \cdot \frac{d\varphi}{2\pi} \tag{6.4}$$

This number is multiplied with the probability of finding a hit along the track on any layer in-between

$$P_{L_i}(\eta) = N^{Hits}_{L_i}(\eta)\frac{A_i^{window}}{2\pi r \Delta z(\eta)}. \tag{6.5}$$

The distribution of clusters is given over η and for the full cylinder. To account for the look-up window (see eq. (6.1)), which is defined for a small region in r/φ and z, the geometrical factor $1/2\pi r\Delta z(\eta)$ is applied for each η-bin j of $N^{Hits}_{L_i}(\eta)$, with $\Delta z(\eta) = | z_j - z_{j+1} | = | \sinh\eta_j - \sinh\eta_{j+1} |$.

The thereby obtained fake background in dependence of pseudorapidity requiring either 4, 5 or 6 hits on different layers is shown in fig. 6.14b. For requiring four hits on different layers the distribution reaches values between $0.08 - 0.11$ given an η bin width of 0.2 and in total 2.22 combinations. When requiring just one more hit the total number of fakes is reduced by two

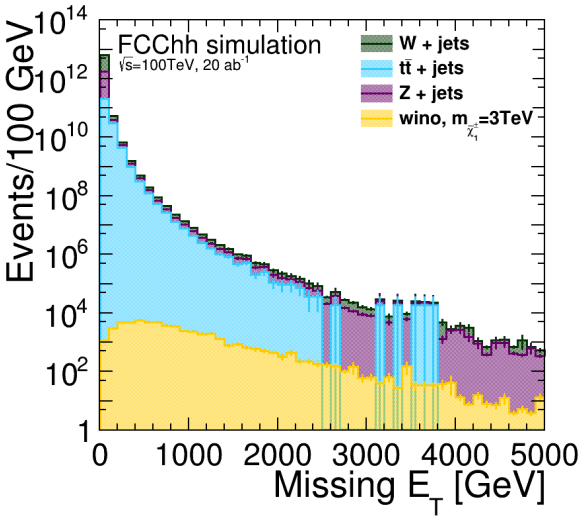

(a) Stacked SM background contributions, overlaid with the wino signal for $\tau_{\tilde{\chi}_1^\pm} = 0.2\,\text{ns}$ and $m_{\tilde{\chi}_1^\pm} = 3\,\text{TeV}$. Total number of expected events (for an integrated luminosity of $20\,\text{ab}^{-1}$) is plotted versus the missing transverse energy of the event.

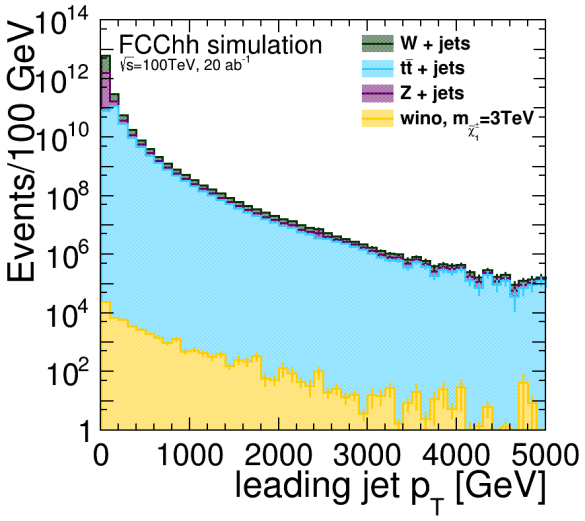

(b) Stacked SM background contributions, overlaid with the wino signal for $\tau_{\tilde{\chi}_1^\pm} = 0.2\,\text{ns}$ and $m_{\tilde{\chi}_1^\pm} = 3\,\text{TeV}$. Total number of expected events (for an integrated luminosity of $20\,\text{ab}^{-1}$) is plotted versus the leading jet transverse momentum of the event.

fig. 6.15

orders of magnitude to 3.67×10^{-2} with values ranging between $1.8 - 2.5 \times 10^{-3}$ along η. For six hits the number of fake combinations is reduced again by one order (reduction less strong due to coarser readout-granularity of layers 5 and 6) of magnitude to $1.9 - 2.7 \times 10^{-4}$ per η bin and 3.3×10^{-3} in total.

6.6.3 Physical background estimation

In the following, the number of SM background events and hence, their tracklet candidates, which pass the event selection are estimated. The SM background arises from SM processes with similar event characteristics as the chargino event: high amount of missing transverse energy and a high p_T jet. SM processes which fulfill those characteristics may be gauge boson production in association with jets or top-quark pair production. The W-boson fulfills the missing energy requirement if it is decaying to a lepton and a neutrino $W^\pm \to l^\pm\bar{\nu}/\nu$ [190]. In case the lepton is a tauon (τ) or an electron, there is a possibility that a tracklet arises. For the muon-case, rejection can be done by identification in the muon chambers. The Z-boson could produce sufficiently high missing energy in case of a decay to two neutrinos $Z \to$*invisible* [190]. In this case, there is no physical tracklet candidate. Only fake tracklets need to be considered. The top-pairs will be selected due to their subsequent decay into two W-bosons and two b-quarks producing jets $t\bar{t} \to W^+bW^-\bar{b}$ [191].
FCCSW DELPHES [192] simulation samples (see appendix A.9), generated with madgraph gridpacks [193], have been used for the estimation. The information about the missing energy of the event and generated jets is provided by DELPHES [85] simulation. The used simulation samples are listed in appendix A.9.

In fig. 6.15, the missing transverse energy and the p_T of the leading jet, of the possible SM backgrounds is shown. The SM backgrounds are stacked and overlaid with the distribution of the chargino event. The W and Z samples have been generated for different kinematical regions (see appendix A.9). Hence, the contributions of each sample has been weighted according to their cross section, before being merged to one histogram. The obtained distributions have been normalized to one, to represent the statistical occurrence per event. Finally the histograms are scaled by the total number of events expected N_X^{Events} at FCC-hh for the specific process. This is calculated by multiplying the expected integrated luminosity $L^{int} = 20\,ab^{-1}$ (see chapter 1) by the cross section of the process X, σ_X:

$$N_X^{Events} = \sigma_X * L \tag{6.6}$$

The cross sections and total number of expected number of events are summarized in table 6.2.

Process	σ	N^{Events} for $L=20\,ab^{-1}$
W	$1.3\,\mu b \pm 1\,\%$	2.6×10^{13}
tt	$34.81\,nb^{+2.9\,\%}_{-4.7\,\%}$	6.962×10^{11}
Z	$0.4\,\mu b \pm 1\,\%$	8×10^{12}
$\tilde{\chi}_1^{\pm}\tilde{\chi}_1^{\pm}$, wino, m = 3 TeV	8.640×10^{-04} pb	17 280
$\tilde{\chi}_1^{\pm}\tilde{\chi}_1^{0}$, wino, m = 3 TeV	1.7802×10^{-03} pb	35 604

tab. 6.2: Summary of cross sections and expected total number of events at FCC-hh for the different background processes and the signal, assuming a wino at the mass limit of 3 TeV. The total gauge boson cross sections are given at NNLO (precision $\mathcal{O}(\%)$), see [56] *chapter 4*. The total $t\bar{t}$ production cross section is calculated at NNLO, see [56] *chapter 11.2, tab.50*

Only a certain fraction of W-bosons will decay hadronically or into an electron and the corresponding neutrino. The same is valid for Z-bosons decaying into a pair of neutrinos. Hence, the distributions are also weighted by those rates, summarized in table 6.3.

The charginos have been produced for two different production processes in a mass-range of 700 – 4600 GeV. The missing transverse energy for the chargino sample is the transverse momentum of the chargino(s). To obtain the p_T of the leading jet, an anti-k_T-algorithm of the FastJet library [160] version 3.3.0, with R = 0.4 and $|\eta| < 2.5$, was used for jet-clustering (see section 5.2 for details). For this estimation study, truth jets have been used, by clustering the generated particles, excluding the chargino. To obtain the E_T^{miss} and leading jet-p_T distributions per event, the contribution of each event was weighted according to its cross section, given the mass and production process (see tables A.4 and A.5). Finally these distributions have been scaled by the number of expected wino events at the upper mass limit of 3 TeV. In total 17 280 events are expected for the $\tilde{\chi}_1^{\pm}\tilde{\chi}_1^{\mp}$-production and 35 604 for the $\tilde{\chi}_1^{\pm}\tilde{\chi}_1^{0}$-production process for $m_{\tilde{\chi}_1^{\pm}} = 3$ TeV and a total integrated luminosity of $20\,ab^{-1}$.

As a starting point, the same event selection as used for a disappearing track study for the ATLAS upgrade was used, described in [139], *chapter 3.3.6*. An event must fulfill the following kinematical requirements:

1. $E_T^{miss} > 450$ GeV

Process	rate[%]	N^{Events} for L=20 ab^{-1}
$W^{\pm} \to e^{\pm}\bar{\nu}_e/\nu_e$	10.71 ± 0.16	-
$W^{\pm} \to \tau^{\pm}\bar{\nu}_\tau/\nu_\tau$	11.38 ± 0.121	-
$\tau^{\pm} \to \pi^{\pm} + X + \bar{\nu}_X/\nu_X$	46.61 ± 0.31	-
$\tau^{\pm} \to e^{\pm}\bar{\nu}_e/\nu_e + X$	17.82 ± 0.04	-
total:		
$W^{\pm} \to e^{\pm}\bar{\nu}_e/\nu_e + X$	12.73 ± 0.41	3.3×10^{12}
$W^{\pm} \to \pi^{\pm} + X + \bar{\nu}_X/\nu_X$	5.3 ± 0.52	1.38×10^{12}
$t\bar{t} \to e^{\pm}\bar{\nu}_e/\nu_e + X$	$2 \times (12.73 \pm 0.41)$	1.77×10^{11}
$t\bar{t} \to \pi^{\pm} + X + \bar{\nu}_X/\nu_X$	$2 \times (5.3 \pm 0.52)$	7.38×10^{10}
$Z^0 \to$ invisible	20 ± 0.06	1.6×10^{12}

tab. 6.3: On top of the table an overview of the decay rates of the relevant processes is given. The second half of the table shows the finally obtained total rates and number of expected events after combining the different processes for an integrated luminosity of $20\,ab^{-1}$, as expected at FCC-hh.

2. at least one jet with $p_T > 300\,GeV$
3. $\min\Delta\Phi(jet_{ISR}, E_T^{miss}) > 1$ between leading four jets with $p_T > 50\,GeV$

The first criterion ensures the presence of high missing transverse energy. The second and third requirement guarantee the presence of an ISR-jet that boosts the $\tilde{\chi}_1^0$.

In addition to the selection cuts mentioned above, a more stringent event selection has been established, based on the E_T^{miss} and leading jet p_T distributions given in fig. 6.15. It was found that the significance, defined as the rate of the signal yield for a given cut, divided by the square root of the background yield, was at maximum for the following cuts: $E_T^{miss} > 1200\,GeV$ and $p_T > 800\,GeV$, as shown in fig. 6.16 in orange, with the corresponding axis labels on the right. The used significance definition, is the mean discovery significance and expresses how many standard deviations the signal exceeds the pure background, since the gaussian standard deviation of a poisson distribution is approximately the square root of the number of events. For consistency, the p-value for the background only hypothesis, is also shown fig. 6.16, in black, with axis values on the left. The lowest p-values are obtained for the highest significance values. For details of the definition of significance and p-value, please see appendix A.11.

In case the ATLAS selection is applied to the chargino event samples 94.51 % of events pass the E_T^{miss} requirement, 41.05 % pass the the second criterion and 63.28 % the third. In total 37.48 % of chargino events pass the selection. In fig. 6.17 the η and p_T distribution of the chargino samples passing the selection criteria is shown. A shift towards higher transverse momenta and more central production is observed.
Using the optimized event selection cuts, in total 15.11 % of the chargino samples pass the event selection, with 72.72 % passing the E_T^{miss} requirement, 19.32 % passing the leading jet-p_T and 43.93 % passing the third requirement.

Table 6.4 shows the rate of events passing the event selection. The gauge boson samples are given for different kinematical regions, with distinct probabilities of passing the event selection. The rate of passing the event selection has been evaluated separately for each sample and was then weighted according to its cross section. The chargino rate has also been evaluated separately

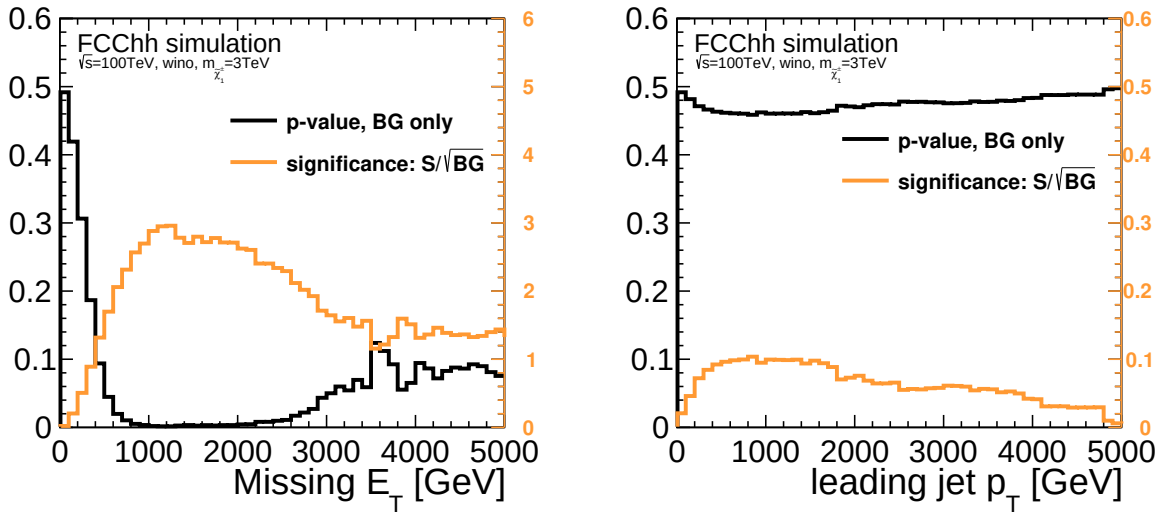

(a) (b)

fig. 6.16: Significance and p-value for the background only hypothesis in dependence of the missing transverse energy (left) and the leading jet transverse momentum (right). The plots are based on fig. 6.15a and fig. 6.15b, which assumes a total integrated luminosity of $20\,\mathrm{ab}^{-1}$ and wino signal at the mass limit of $m_{\tilde{\chi}_1^\pm} = 3\,\mathrm{TeV}$.

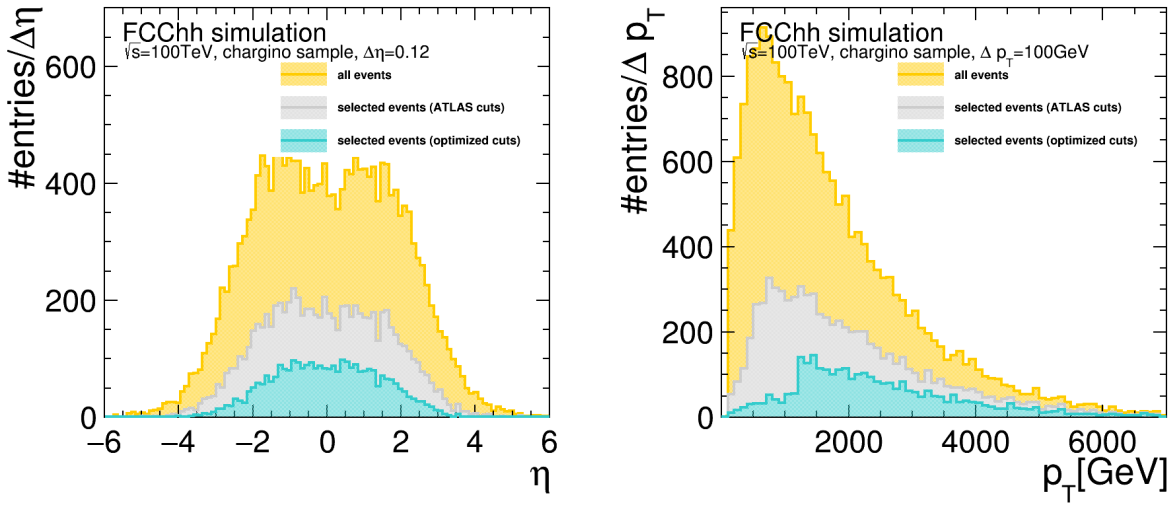

(a) Distribution of pseudorapidity of chargino events, which passed all selection criteria compared to all simulated chargino events.

(b) Distribution of transverse momentum of chargino events, which passed all selection criteria compared to all simulated chargino events.

fig. 6.17

for the two different production processes $\widetilde{\chi}_1^{\pm}\widetilde{\chi}_1^{\mp}$ and $\widetilde{\chi}_1^{\pm}\widetilde{\chi}_1^{0}$. The rates for the gauge bosons and wino are average rates.

Process	rate for $N_{Layer}^{Hit} = 4$	rate for $N_{Layer}^{Hit} = 5$	rate for $N_{Layer}^{Hit} = 6$
$W + \text{jets} \to e/\pi + \nu$	1.46×10^{-8}	1.20×10^{-8}	9.67×10^{-9}
$t\bar{t} \to e/\pi + \nu$	9.81×10^{-5}	8.25×10^{-5}	7.00×10^{-5}
$Z + \text{jets} \to \text{invisible}$	8.32×10^{-5}	8.32×10^{-5}	8.32×10^{-5}
$\widetilde{\chi}_1^{\pm}\widetilde{\chi}_1^{\mp}$, wino	0.3993	0.3993	0.3988
$\widetilde{\chi}_1^{\pm}\widetilde{\chi}_1^{0}$, wino	0.2812	0.2197	0.1785
new cuts:			
$W + \text{jets} \to e/\pi + \nu$	7.42×10^{-10}	6.64×10^{-10}	5.54×10^{-10}
$t\bar{t} \to e/\pi + \nu$	8.74×10^{-7}	8.74×10^{-7}	7.28×10^{-7}
$Z + \text{jets} \to \text{invisible}$	2.20×10^{-6}	2.20×10^{-6}	2.20×10^{-6}
$\widetilde{\chi}_1^{\pm}\widetilde{\chi}_1^{\mp}$, wino	0.1642	0.1642	0.1640
$\widetilde{\chi}_1^{\pm}\widetilde{\chi}_1^{0}$, wino	0.1106	0.0865	0.0703

tab. 6.4: Average rate $\langle \frac{dN^{Events}_{passed}}{dN^{Events}} \rangle$ of events passing the event selection cuts for L=20 ab^{-1}, for the different η-cuts ($\eta = 2.4,\ 1.8,\ 1.46$), due to the hit requirement on different layers. On top, the ATLAS event selection cuts are used, while on the bottom the optimized selection cuts are applied.

By combining the rates with the total number of events expected for the background processes, as summarized in table 6.3 and the total number of events expected for the wino, with a mass of $m_{\widetilde{\chi}_1^{\pm}} = 3\,\text{TeV}$, the total number of events passing the event selection can be obtained (see table 6.5).

6.7 Results

After the events are selected regarding missing energy and jets, the final selection is done on the tracklets. In the following, the total number of tracklet candidates for the background and wino events in dependence of p_T are evaluated. Finally, the possible exclusion limits depending on the wino mass and decay time are assessed.

6.7.1 Tracklet candidates

Possible tracklet candidates from the *W+jet* and $t\bar{t}$ events are the pions and electrons potentially produced during W-decay. To obtain the p_T-spectrum of those leptons, the leptons have been kinematically selected from the generated particles of the simulation samples. At maximum one lepton-neutrino pair is selected, which fulfills the requirement of conservation of the invariant mass [183] of the W-boson and whose charges match the charge of the mother W-boson. The truth p_T of the selected leptons is then smeared using the single pion and single electron resolutions (see appendix A.8) for using four, five and six hits on different layers, given for this p_T. Since those resolutions are only given up to $p_T = 100\,\text{GeV}$, the resolutions created using a toy-model (as explained in appendix A.8) are used for higher transverse momenta. During this procedure,

Process	$\langle N_{cut}^{Events} \rangle$ for $N_{Layer}^{Hit} = 4$	$\langle N_{cut}^{Events} \rangle$ for $N_{Layer}^{Hit} = 5$	$\langle N_{cut}^{Events} \rangle$ for $N_{Layer}^{Hit} = 5$
$W + jets \rightarrow e/\pi + \nu$	68 380	56 333.8	45 350.5
$tt \rightarrow e/\pi + \nu$	2.4635×10^7	2.0703×10^7	1.7575×10^7
$Z + jets \rightarrow$	1.33×10^8	1.33×10^8	1.33×10^8
wino, m = 3 TeV	16 911.9	14 723.4	13 247.5
total	1.5785×10^8	1.539×10^8	1.5077×10^8
new cuts:			
$W + jets \rightarrow e/\pi + \nu$	3 476.83	3 110.85	2 598.47
$tt \rightarrow e/\pi + \nu$	219 463	219 463	182 885
$Z + jets \rightarrow$	3.5142×10^6	3.5142×10^6	3.5142×10^6
wino, m = 3 TeV	6 777.43	5 916.52	5 335.76
total	$3,7439 \times 10^6$	$3,7427 \times 10^6$	3.7050×10^6

tab. 6.5: Total number of events after event selection for the different processes for L=20 ab^{-1}, for the different η-cuts ($\eta = 2.4,\ 1.8,\ 1.46$), due to the hit requirement on different layers. On top, the ATLAS event selection cuts are used, while on the bottom the optimized selection cuts are applied.

only tracks of selected events fully contained in the barrel region are considered. Since this first step is only needed to obtain the shape of the distribution, each truth p_T is smeared several times to obtain a smooth distribution. The acquired tracklet-p_T distributions have been normalized to one and then weighted according to their cross section and the rate passing the event selection, depending on their kinematical region. The electron-tracklet and pion-tracklet distributions have been merged to one distribution, representing the occurrence of each tracklet p_T per event. Finally the distributions are scaled separately by the total number of events expected for a W-boson or a pair of top-quarks decaying to a pion or an electron, given in table 6.3 and by the probability of an electron or a pion to produce a tracklet with 4, 5 or 6 hits on different layers (see table 6.6).

Process	P for $N_{Layer}^{Hit} = 4$	P for $N_{Layer}^{Hit} = 5$	P for $N_{Layer}^{Hit} = 6$
$e \rightarrow$ tracklet	1.72×10^{-3}	1.41×10^{-3}	1.25×10^{-3}
$\pi \rightarrow$ tracklet	4.67×10^{-3}	5.50×10^{-3}	5.35×10^{-3}
wino, $\tau = 0.2$ ns	38.54×10^{-3}	9.13×10^{-3}	2.21×10^{-3}

tab. 6.6: Probability of an electron or a pion creating a tracklet with 4, 5 or 6 hits on different layers obtained from single particle simulation. In the lower section the probability of the wino surviving until a certain layer is given (see also fig. 6.3).

As done for the physical standard model background tracklet p_T-distributions, the truth p_T of each wino passing the selection cut has been smeared several times using the toy-model resolutions. In this way, a smooth shape is obtained. Each event has bee weighted with its corresponding cross section. The distributions have been acquired separately for the two different

production processes and normalized to one, before being scaled by the number of particles passing the event selection and η-cut. This gives the tracklet-p_T distribution of the wino per event. To obtain the final number of winos for each tracklet p_T, the distributions are scaled by the total number of expected events for a given mass and production process and the rate of the wino creating tracklets (see table 6.6). This rate depends on the probability of the wino surviving until a given layer determined by the decay time, and the probability of the wino making more than the given number of hits. For this section, the upper WIMP mass limit for the wino of $m_{wino} = 3\,\text{TeV}$ and a decay time of $\tau = 0.2\,\text{ns}$ have been assumed.

The tracklet p_T distribution, arising from primary particles of the pile-up events, has been obtained by smearing the truth p_T of the tracklets in the barrel region with the single pion (in case of all particles but electrons) and single electron (used, in case of electrons) or toy (for truth-$p_T > 100\,\text{GeV}$) resolutions. This distribution is used to acquire the shape of the distribution and is therefore normalized to one. The distribution is then scaled by the number of particles expected per event summarized in table 6.7. This is the total average number of tracklets expected per event, with a certain number of hits on different layers, times the rate of those contaminating the primary vertex (see section 6.6.1). Due to the requirement that the ISR-jet needs to boost the tracklet, the possible tracklet φ-window is limited to $2\pi - 2$, which is consistent with the third event selection criterion. Since the distribution of particles will be flat in φ, the number of tracklets per event is scaled by a factor of $1 - \frac{1}{\pi}$.

Process	$\langle N^{tr}_{\text{per Event}} \rangle$ for $N^{Hit}_{Layer} = 4$	$\langle N^{tr}_{\text{per Event}} \rangle$ for $N^{Hit}_{Layer} = 5$	$\langle N^{tr}_{\text{per Event}} \rangle$ for $N^{Hit}_{Layer} = 5$
PU tracklets	0.19	0.18	0.12
PU fakes	2.23	3.67×10^{-2}	3.30×10^{-3}

tab. 6.7: Average number of tracklets of physical and combinatorial background from pile-up, expected per event.

Apart from the physical background, also the fake background due to pile-up needs to be considered. The expected number of fake tracklets per event for the different layers was estimated in section 6.6.2. As done for the physical background due to pile-up, this number is scaled by $1 - \frac{1}{\pi}$.
Both, tracklet p_T distributions obtained from physical and fake background of pile-up per event are scaled by the total number of events passing the selection cuts, which is given by table 6.5.

The finally obtained tracklet-p_T distributions for the different number of hits on different layers and the two different event selections can be observed in figs. 6.18 to 6.20. Although, the highest contribution in total number of tracklets comes from physical pile-up background, the signal can be well separated from that contribution, due to the significantly harder p_T spectrum of the signal. For requiring only a small number of hits, the fake pile-up background gives a substantial contribution to the background. The impact is reduced, by requiring more number of hits. Using the optimized cuts considerably enhances the signal to noise ratio. The SM background from W and $t\bar{t}$ is dominant for all cases and lies also in the kinematic region of the signal tracklet. For figs. 6.18 to 6.20 the rather conservative assumption, that all pions and electrons are a source of background has been made. However, although the pions and electrons begin to shower in the tracker, a certain fraction will be identified by the calorimeters and can be rejeceted. To take the rejection due to calorimeter identification of jets into account, energy resolutions, as obtained by FCC-hh full simulation studies have been used, to estimate the jet-reconstruction

Process	$\langle N^{tr} \rangle$ for $N^{Hit}_{Layer} = 4$	$\langle N^{tr} \rangle$ for $N^{Hit}_{Layer} = 6$	$\langle N^{tr} \rangle$ for $N^{Hit}_{Layer} = 5$
$W + jets \rightarrow e/\pi + \nu$	111 166	89 375	69 267.8
$tt \rightarrow e/\pi + \nu$	93 751.8	88 8956.2	72 821.9
PU tracklets	2.0527×10^7	1.8658×10^7	1.2509×10^7
PU fakes	26 579.3	288.8	8.5
wino, $m = 3\,TeV, \tau = 0.2\,ns$	805.9	149.3	29.2
new cuts:			
$W + jets \rightarrow e/\pi + \nu$	1713.7	1392.3	1006.8
$tt \rightarrow e/\pi + \nu$	835.2	943.0	757.8
PU tracklets	486 839	453 727	307 386
PU fakes	630.4	7.0	0.2
wino, $m = 3\,TeV, \tau = 0.2\,ns$	324.6	60.1	11.8
new cuts and calorimeter rejection:			
$W + jets \rightarrow e/\pi + \nu$	362.6	233.5	184.9
$tt \rightarrow e/\pi + \nu$	19.2	16.0	7.9
PU tracklets	486 839	453 727	307 386
PU fakes	630.4	7.0	0.2
wino, $m = 3\,TeV, \tau = 0.2\,ns$	324.6	60.1	11.8

tab. 6.8: Total average number of tracklets $\langle N^{tr} \rangle$ producing 4, 5 or 6 hits on different layers, expected for L=20 ab^{-1} and a tracklet p_T range of $0 < p_T \leq 10\,TeV$ of all the SM background contributions and the physical and combinatorial background from pile-up. The total number of wino tracklets is calculated for a mass of 3 TeV and a decay time of 0.2 ns.

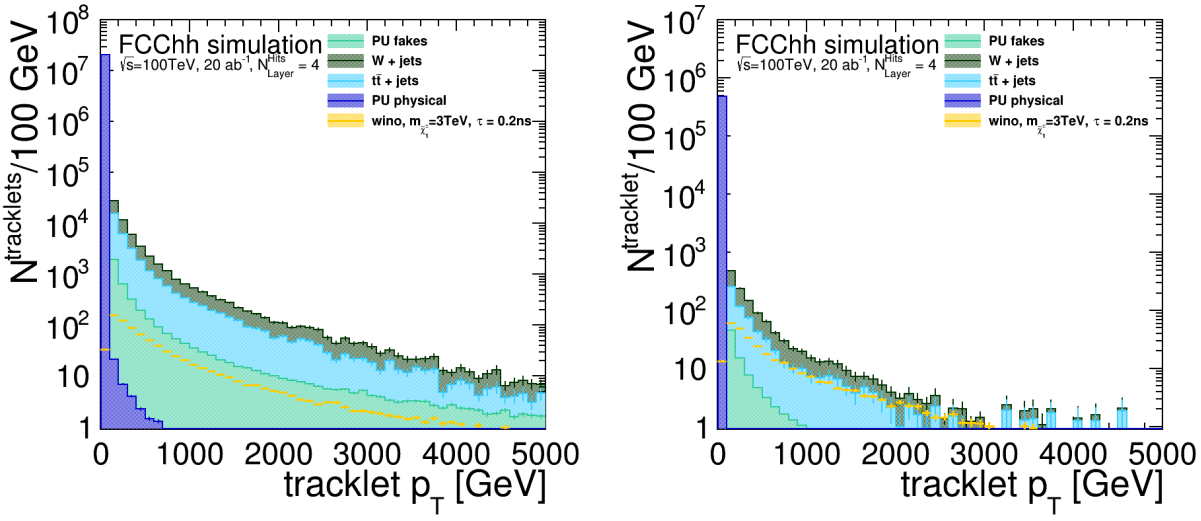

(a) Using ATLAS cuts. **(b)** Using optimized cuts.

fig. 6.18: Total number expected background tracklets with 4 hits on different layers, stacked versus tracklet p_T, overlaid with the total number of wino tracklets expected for $m_{\tilde{\chi}_1^\pm} = 3\,\text{TeV}$ and $\tau_{\tilde{\chi}_1^\pm} = 0.2\,\text{ns}$ and $L = 20\text{ab}^{-1}$.

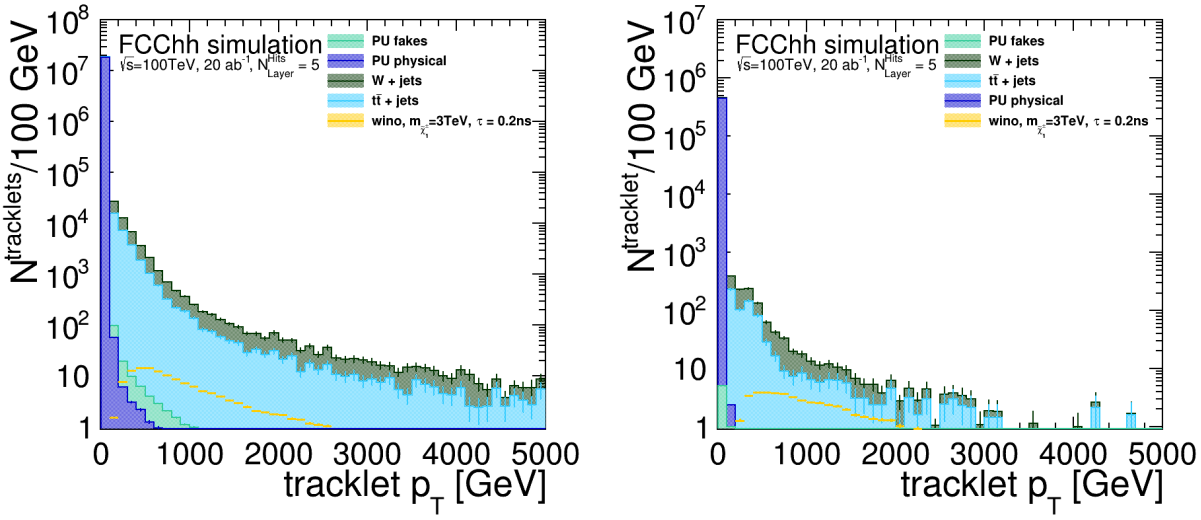

(a) Using ATLAS cuts. **(b)** Using optimized cuts.

fig. 6.19: Total number expected background tracklets with 5 hits on different layers stacked versus tracklet p_T, overlaid with the total number of wino tracklets expected for the upper mass limit with $m_{\tilde{\chi}_1^\pm} = 3\,\text{TeV}$, $\tau_{\tilde{\chi}_1^\pm} = 0.2\,\text{ns}$ and $L = 20\text{ab}^{-1}$.

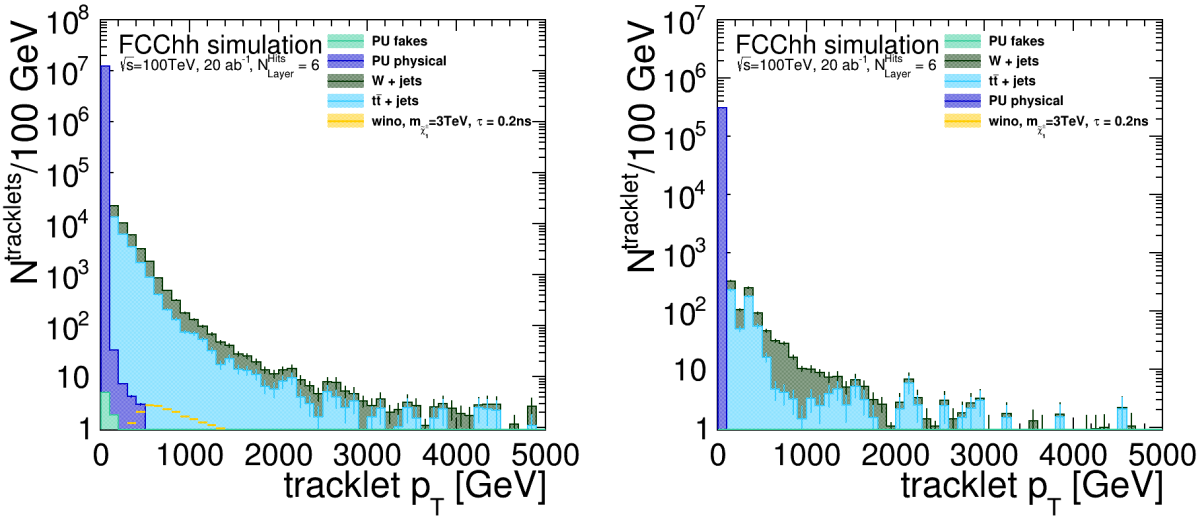

(a) Using ATLAS cuts. **(b)** Using optimized cuts.

fig. 6.20: Total number expected background tracklets with 6 hits on different layers stacked versus tracklet p_T, overlaid with the total number of wino tracklets expected for the upper mass limit with $m_{\tilde{\chi}_1^\pm} = 3\,\text{TeV}$, $\tau_{\tilde{\chi}_1^\pm} = 0.2\,\text{ns}$ and $L = 20\text{ab}^{-1}$.

efficiency. For the electromagnetic calorimeter, the energy resolution, as obtained for simulation including pile-up of $\langle\mu\rangle = 1000$ (see [52], *figure 7.17*) has been used:

$$\frac{\sigma_{E_{Rec}}}{\langle E_{Rec}\rangle} = \frac{10\,\%}{\sqrt{E}} \oplus 0.52\,\% \oplus \frac{1.31\,\text{GeV}}{E}. \tag{6.7}$$

For the hadronic calorimeter energy resolutions obtained after topo-clustering and using a deep neural network has been used (see [76, 77]):

$$\frac{\sigma_{E_{Rec}}}{\langle E_{Rec}\rangle} = \frac{46\,\%}{\sqrt{E}} \oplus 1.8\,\% \oplus \frac{3.1 + 2.15\,\text{GeV}}{E}. \tag{6.8}$$

The additional term of 2.15 GeV was estimated as electronics noise. Assuming the reconstructed energies are gaussian distributed, given the resolution for each energy, the probability of identifying a jet can be calculated. As a minimum jet energy 50 GeV has been chosen, which is consistent with the event selection. Applying this probability, most SM-background tracklets with high momenta are identified and hence are excluded, as it can be seen in fig. 6.21.

6.7.2 Exclusion limits

In the following the possible exclusion limits at 95 % CL for different decay times and masses of the wino are assessed. The limit is calculated by obtaining the p-value for the background only hypothesis. For this purpose a likelihood fit of the background tracklet-p_T-distributions, as obtained in section 6.7.1 to the background plus signal distribution was done, using the RooFit package (part of ROOT toolkit see [97]), maximizing the number of signal events. The obtained signal distribution changes, depending on the decay-time and the mass of the chargino. As explained in the previous section, two different tracklet-p_T distributions have been obtained for the two different production processes of the chargino and have been scaled to represent

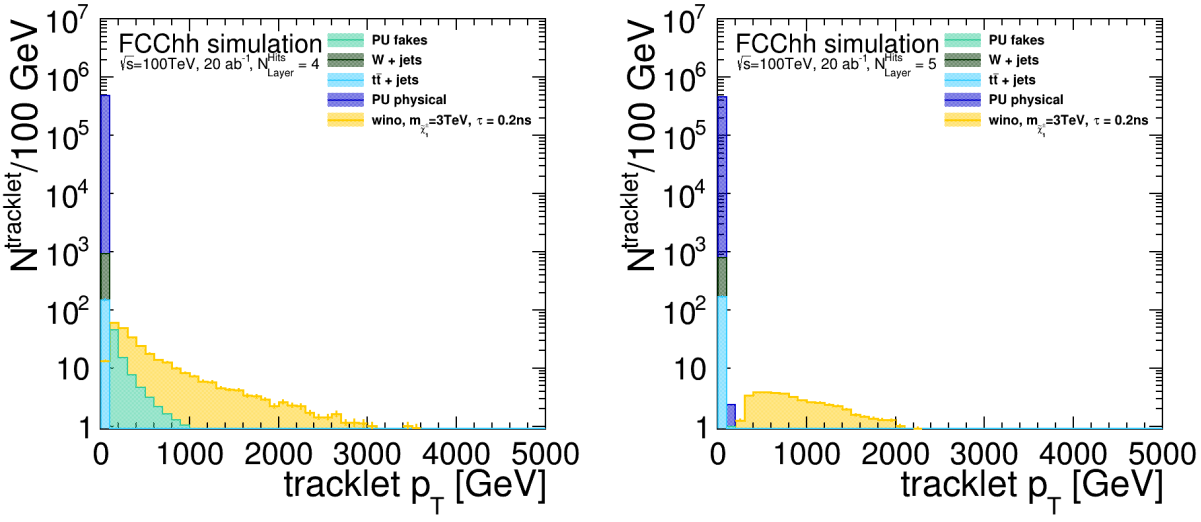

(a) Using optimized cuts and calorimeter rejection. **(b)** Using optimized cuts and calorimeter rejection.

fig. 6.21: Total number expected background tracklets with 4 and 5 hits on different layers stacked versus tracklet p_T, overlaid with the total number of wino tracklets expected for the upper mass limit with $m_{\tilde{\chi}_1^\pm} = 3\,\text{TeV}$, $\tau_{\tilde{\chi}_1^\pm} = 0.2\,\text{ns}$ and $L = 20\text{ab}^{-1}$. Using the calorimeter rejections leaves only signal tracklets at high p_T, since electrons and pions are assumed to be identified above a certain p_T.

the occurrence of tracklets per event. The final distribution is obtained by first scaling to the total number of expected events, which is given by the cross section for the specific mass, listed in tables A.4 and A.5. In a second step, the probability of a chargino creating a tracklet with 4, 5 or 6 hits on different layers needs to be considered. This probability depends on the rate of charginos surviving until the given layer and has an upper limit, due to the fraction of charginos creating more than the requested number of hits. The rates have been simulated with a toy model as described in appendix A.10.
The p-value and the confidence limits are calculated using the asymptotic formula with a profile-likelihood ratio as test statistic described in [194].

The results for the different cut options are shown in fig. 6.22. As expected, the best possible rejection could be obtained using the optimized cuts plus the calorimeter rejection. Here, most of the masses ($< 3600\,\text{GeV}$) could even be probed with very small wino decay times in the range of 0.1 ns and masses $< 4600\,\text{GeV}$, with decay times $< 0.2\,\text{ns}$. Although the rejection of fakes is higher, when requiring more hits on different layers, longer lifetimes would be required to place 95 % CL on a possible null hypothesis rejection. For requiring six hits on different layers, the total number of signal events is too small for all cut scenarios. Even without assuming calorimeter rejection, wino masses up to 4400 GeV could be probed, assuming a decay time $\leq 0.2\,\text{ns}$.

6.8 Conclusions and Outlook

Most recent ATLAS results set 95 % CL on exclusion of winos with $\tau_{\tilde{\chi}_1^\pm} = 0.2\,\text{ns}$ and masses up to 460 GeV [181]. At the HL-LHC exclusion up to 850 GeV is expected [195]. The sensitivity to the disappearing track search could be significantly improved in the FCC-hh scenario. Wino masses up to 3600 GeV can be accessed with lifetimes $\leq 0.1\,\text{ns}$. Even higher masses, up to 4600 GeV

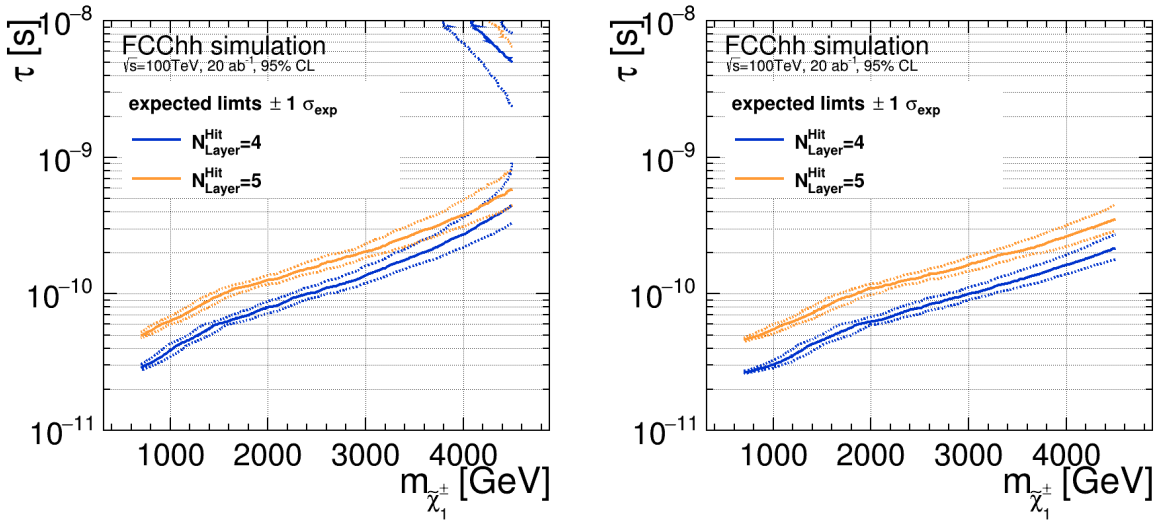

(a) ATLAS cuts

(b) Optimized cuts

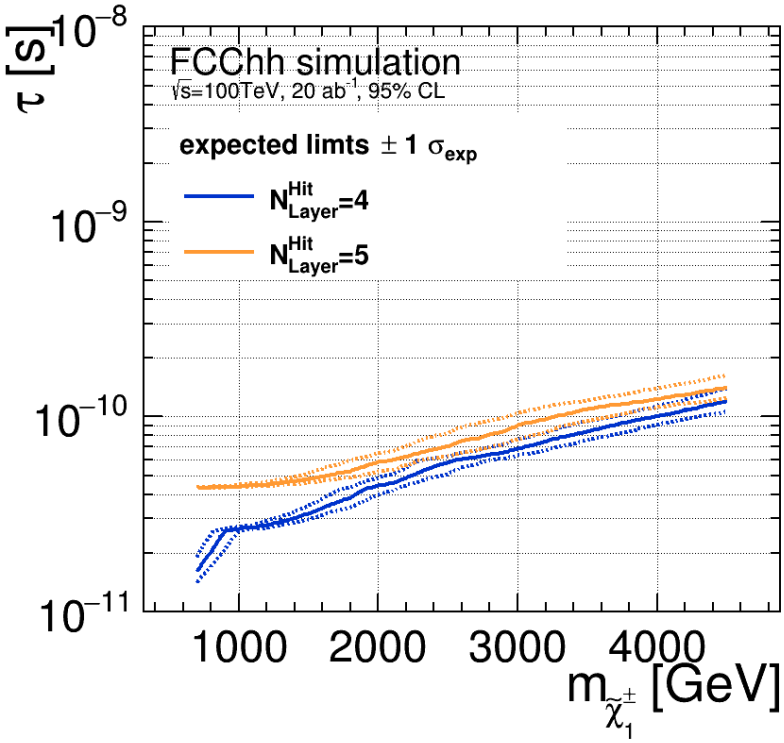

(c) Optimized cuts and calorimeter rejection.

fig. 6.22: Expected exclusion limits at 95 % confidence level, as a function of wino mass and lifetime, assuming an integrated luminosity of $L = 20\,ab^{-1}$. The dashed lines, show the 1σ region of the expected limits and the median is displayed as solid line. The limits are given for the different cuts and for assuming different number of layers hit.

could be accessed with lifetimes $\leq 0.2\,\text{ns}$. The FCC-hh gives a unique opportunity to possibly reject wino candidates at an unprecedented mass and lifetime scale. It would allow to access the wino signature at the upper mass limit of the LSP, given by the relic density of dark matter. The obtained results are independent of the decay mode since the pion and neutralino are not detected. However, further improvement could be reached, taking possible decay products into account and identifying the secondary vertex (see [196, 197]).
A source of systematic uncertainty in simulation, which was used to estimate the physical and combinatorial background, stems from the simplified tracker description of the FCC-hh baseline detector, assuming rather small material budget. Hence, especially the combinatorial background can increase, for a future more detailed tracker model. Additional systematic uncertainties are due to the uncertainties on the cross sections and the estimation methods.
A first estimation on the possibility to find a disappearing track of signature was done, showing great potential. As a next step, the discovery reach for a higgsino model as chargino, which has smaller lifetime than the wino, could be established in a similar manner. As soon as the full simulation-reconstruction chain is fully functioning for the FCC-hh case, more detailed studies can be done. As shown in [188], adding a 5th layer within the pixel region can significantly improve the sensitivity of the search. Timing will significantly reduce combinatorial BG.

Conclusion and Outlook

By the end of this year, after the comprehensive conceptual design volumes will be delivered, the first phase of the FCC design study will be completed. In the scope of this design phase, a first assessment of the FCC-hh baseline tracker performance was done. This allows to explore not only the FCC-hh potential but also to identify possible difficulties, where more research and development are of need.

With the collider's high luminosity combined with the increased detector granularity, a FCC-hh experiment would allow to study SM physics at unprecedented precision. Furthermore, the 100 TeV pp-collider would enable exploration of physics at a new mass-range. It would give a unique possibility to directly detect a wino dark matter candidate, leaving a disappearing track signature within the tracker. As shown in chapter 6, the sensitivity to reject the background only hypothesis is very promising. Masses up to and beyond the upper mass limit, calculated from the relic DM abundance of 3 TeV [180] could be probed at the expected lifetime of 0.2 ns [54], even considering pile-up with $\langle\mu\rangle = 1000$.

For tracking there are two main challenges expected: the high pile-up environment and the resolution of high p_T-jets. As shown in chapter 5, clusters are often created by more than one particle within high p_T-jets and hence are expected to lead to significant degradation of tracking performance in the core of jets. In the core of 10 TeV-jets, 57 % of all tracks have shared clusters along the track. For 500 GeV-jets 17 % of all tracks have shared clusters. Often multiple clusters along a track are shared, even by more than one other particle. Shared clusters can lead to the complete loss of the track during reconstruction. By using neural networks for identifying merged clusters, the tracking performance is expected to be greatly improved, but still only reaches values between 85 % and 98 %. Using the tilted layout, an improvement of double track resolution is expected.

The biggest obstacle is likely to arise due to the high pile-up conditions. Suitable technologies, withstanding the immense radiation in the inner tracking layers and being able to deal with the high data densities of 944 $Gb/s/cm^2$ (at first trigger level, assuming binary readout) have yet to be found. Using the current flat baseline tracker model, the high particle density leads to the activation of ~ 30 M pixels and the production of $9-10$ M clusters per event and $2-3$ TB/s data rate at first trigger level (see chapter 4). Pile-up significantly increases the probability of cluster merging. Due to pile-up, the rate of merged clusters reaches 1.6 %, which is as high as the rate in the core of a 2 TeV-jet. Almost 30 % of all tracks have shared clusters just from pile-up, even outside the jet-core. Furthermore, channel occupancies close to and exceeding 1 % per layer are expected in the innermost layers, which complicates pattern recognition and vertex reconstruction. Peak values of 3 % in the pixel region and even 24 % in the strip region are expected. A finer granularity would improve the channel occupancy, however, raise the data rates. The tilted layout, as well as dedicated tracker optimiziation are expected to give improvement. To deal with the pile-up in pattern recognition, timing might be necessary. Since this would require to readout additional information, this conflicts with the already high data rates.

The high pile-up environment is also critical for simulation and reconstruction, in terms of both, speed and memory. Currently only one event can be stored per file and the simulated hits of both, tracker and calorimeters can not be stored to the same file. The number of hits in the tracker per event is in the order of $\mathcal{O}(7)$. At the moment the smallest execution unit is an event. A

possible solution for FCC-hh would be to use a smaller execution unit. For instance, digitization and clusterization could run in parallel for each detector module. Another possibility would be to run the chain for different regions separately. Instead of storing the simulated hits, only the reconstructed clusters, for both, tracker and calorimeters could be stored, which also reduces the total number of objects stored.
Dedicated research projects will need to be established in the next design phase to find possible detector and readout technologies as well as suitable computing techniques to deal with the high pile-up environment.

Appendix A

Appendix

A.1 Validation and testing of the DD4hep-plugin

This section documents validation and tests of the DD4hep-plugin described in section 3.2.1.3. The plugin is an automated translation from DD4hep geometry into Acts reconstruction geometry. To assure a general translation for trackers at a collider experiment, different geometry scenarios have been tested. Two types of validation tests have been done: simple geometry building tests, checking the pure geometric translation and tests checking, if the embedded navigation of the Acts geometry (details see section 3.2.1) was built correctly. For the geometry building tests, the Acts geometry was visualized using `JSON` [198] or `OBJ` [122] file format. The navigation was checked, by making a fast simulation of muons through the detector and displaying the hits, which are given in ROOT file format [97].

First an "ATLAS-like" test tracking geometry, with modules tilted in transverse plane was tested, for which fig. A.1 compares the pure geometry translation. In fig. A.2, on the left side, the sensitive modules of the tracker barrel in DD4hep, displayed with the ROOT `geoDisplay` [106] can be seen. On the right side, the sensitive hits, as well as the (non-physical) layers and the bounding volume, obtained by extrapolating muons through the translated reconstruction geometry is displayed. The plot on the right side exhibits, how the sensitive modules are placed within layers, which are wrapped by volumes.

A similar test has been done for a "CMS-like" tracker, arranged flat in a circle around the beam pipe with alternating distances in radial direction, as displayed in fig. A.3.

The CLIC community [199, 200] provided a DD4hep description of a simple "CLIC-like" detector. This detector has double-sided modules which are staggered on top of each other in radial direction, within the same layer. Hence, this test tracker was an excellent candidate to proof the ability of translating, building and navigating to sensitive surfaces, residing in the same bin within a layer, as shown in fig. A.4.

Of prior importance is a working geometry translation for the FCC-hh case. In section 3.2.1.3 geometry comparisons for this case are shown. Figure A.5 complements these comparisons, showing the correctly working translation of the barrel modules in the transversal plane, in more detail.

Finally, a test tracker with a more realistic detector description was created in DD4hep. Similar as in a realistic experiment the modules are placed on a support tube made of Aluminium and consist of different components (using the ATLAS IBL-Module [125] as prototype): the sensitive Silicon, additional layers needed for readout made of Silicon, Aluminium and Carbon, and a cooling pipe made of Titan embedded in a Carbon support component (see fig. 3.28a). The resulting test tracker in DD4hep description and the succesfull translation are shown in fig. A.6 and fig. A.7.

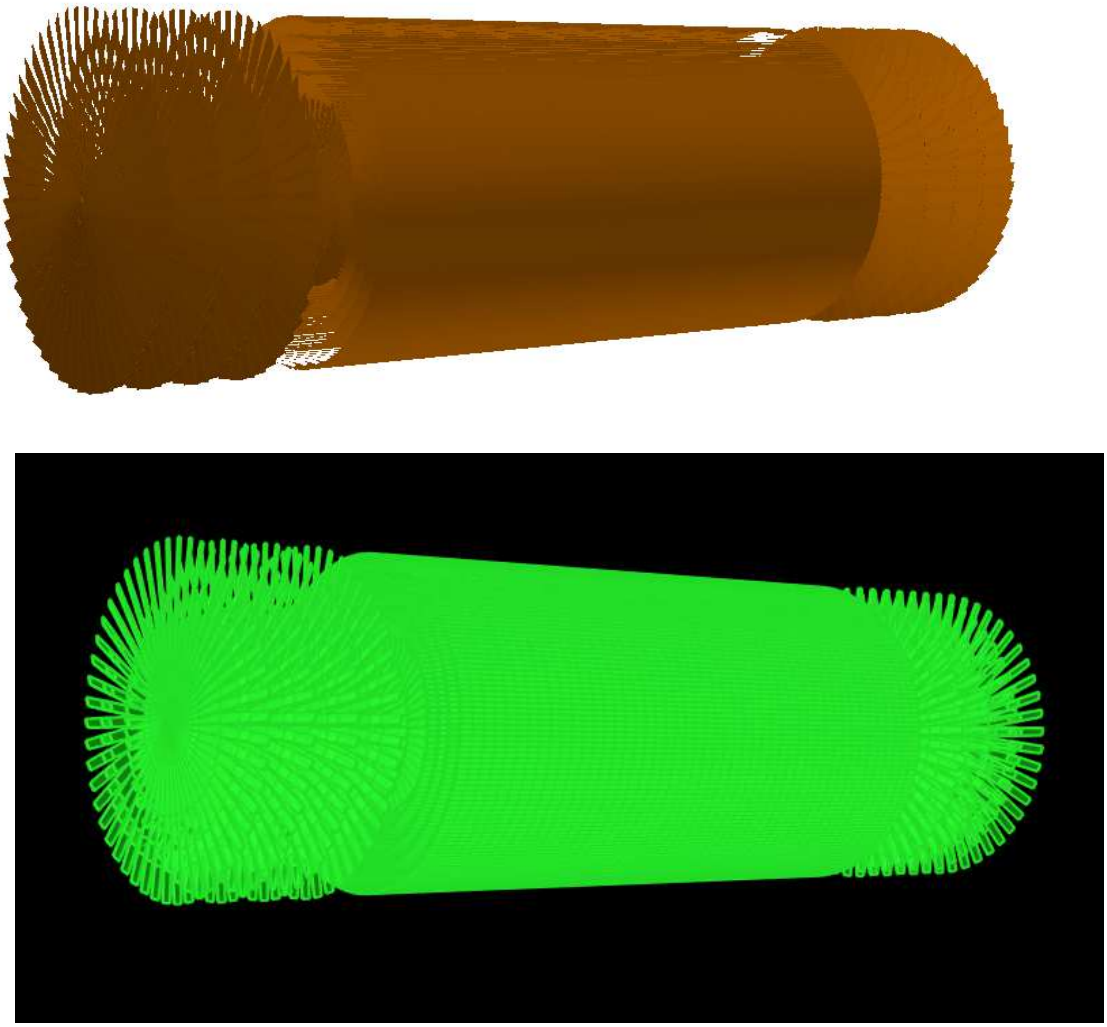

fig. A.1: On top, the DD4hep input of the sensitive modules of an "ATLAS-style" test tracker (with tilted silicon modules) is displayed. The bottom shows the translated surfaces in Acts, using `JSON` output of the Acts test framework, with an event display.

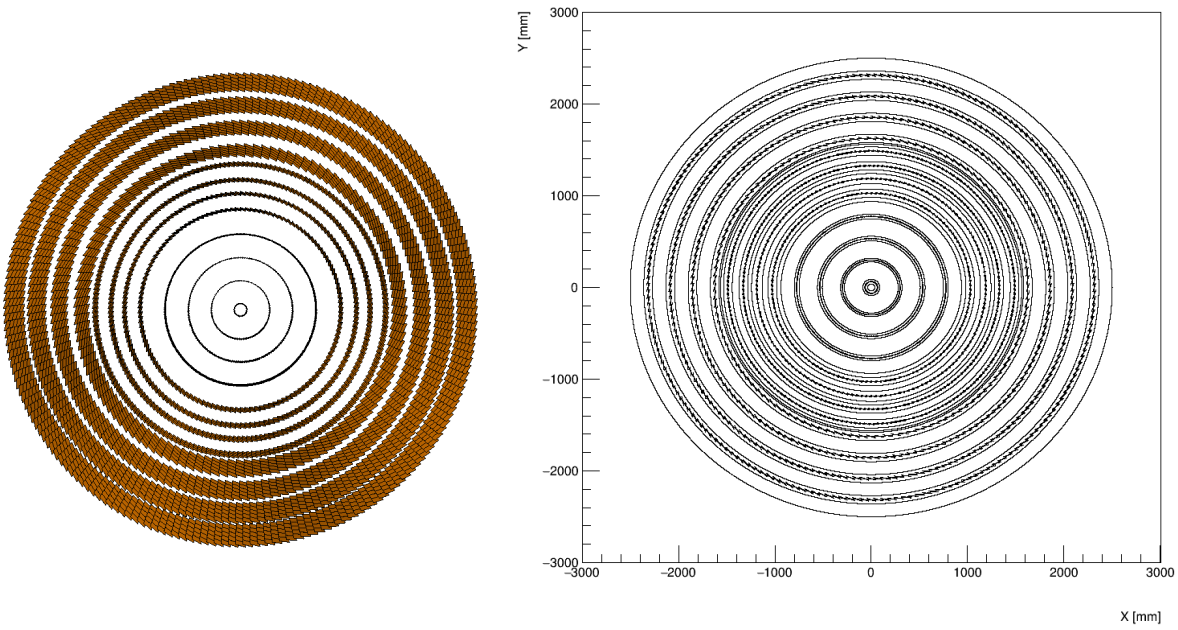

fig. A.2: Comparison of the sensitive modules of the DD4hep geometry input (left) to the obtained hits (sensitive, layers and volume) when extrapolating through the translated Acts geometry (right), of an "ATLAS-style" test tracker (with tilted silicon modules). The barrel region in transversal plane with respect to the beam-axis is shown.

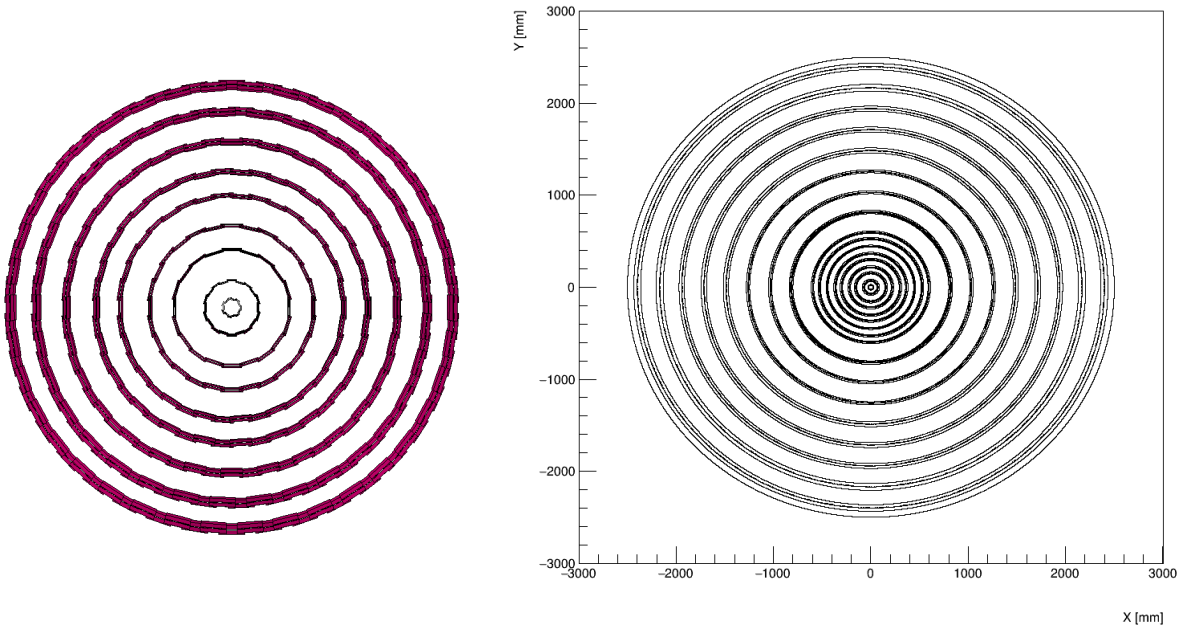

fig. A.3: Comparison of the sensitive modules of the DD4hep geometry input (left) to the obtained hits (sensitive, layers and volume) when extrapolating through the translated Acts geometry (right), of an "CMS-style" test tracker (flat modules). The barrel region in transversal plane with respect to the beam-axis is shown.

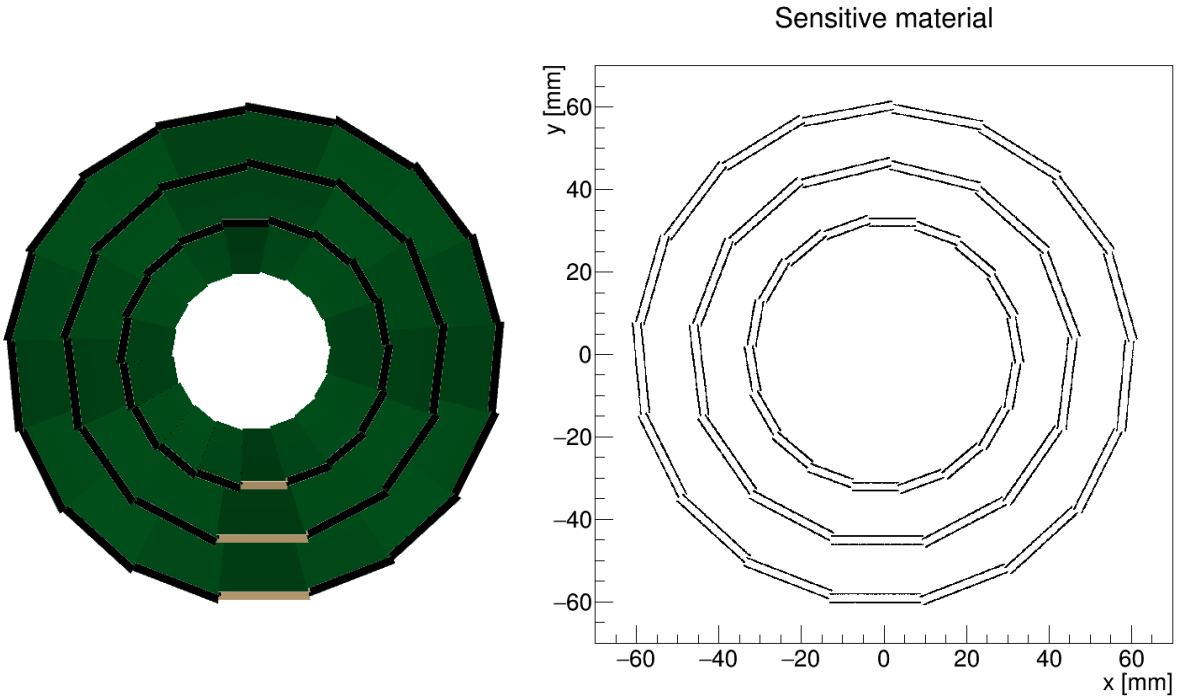

fig. A.4: Comparison of the sensitive modules of the DD4hep geometry input (left) to the obtained hits when extrapolating through the translated Acts geometry (right), of a "CLIC-style" test tracker (staggered modules). The barrel region in transversal plane with respect to the beam-axis is shown.

A.2 Magnetic field interface in Acts

Figure A.8 shows the interfaces to create a magnetic field mapper implemented in Acts, more closely described in section 3.2.3. Currently, there are two implementations, one for values given in rotational symmetric cylinder coordinates and a second one for Cartesian coordinates.

Reading in the field values and translating them to vectors is a task assigned to the specific experimental framework. To keep it flexible to any implementation, an additional input parameter is a mapping function, which provides how the local bins of the spatial coordinates are mapped to the global coordinates of the magnetic field input. To understand the need of this function, one should consider the following case in cylindrical coordinates: the spatial bin coordinates in r-direction have n number of entries, while the in z-direction m number of entries are given, hence, the m $\times$ n number of entries are needed of the magnetic field values to describe the field, at any given point. The function, to be provided by the user, tells how these values should be associated. The case that a magnetic field map is only given for the first quadrant or octant and should be symmetrically extended to all other quadrants/octants is enabled, if a flag is set by the user. The function then creates the grid of the magnetic field map, symmetrically expands, if needed, and finally return an interpolated field mapper.

For the acts-framework, the possibility to read in a magnetic field map from either `txt/csv` or `root`-file format, which internally uses the above described function to create the field mapper was introduced, allowing the user to just specify the magnetic field map file or the field values in case of a constant field, using boost program options (see [201]). Since this this functionality depends on external software, it was implemented as a plugin.

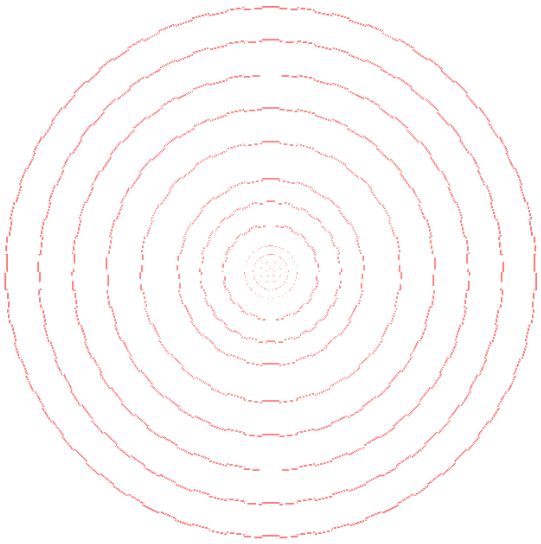

(a) Display of the DD4hep description of the FCC-hh barrel modules in the transversal plane.

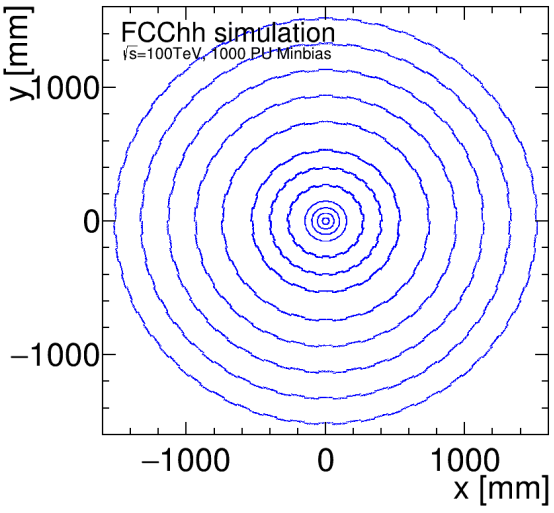

(b) Barrel hits, shown in transversal plane, as obtained from Geant4 full simulation using FCCSW, which gives an image of the barrel modules.

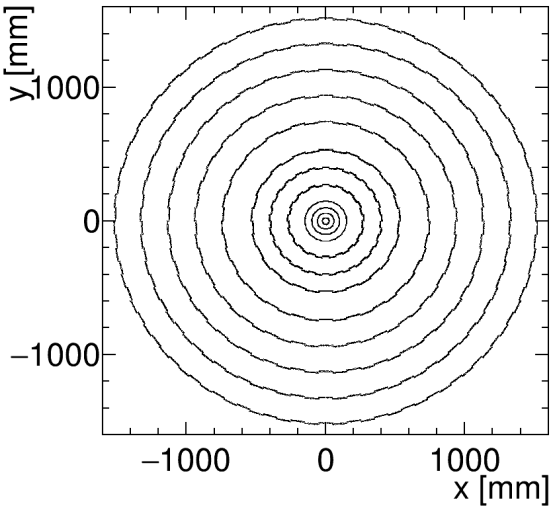

(c) Barrel hits, shown in transversal plane, as obtained from Acts fast simulation, which gives an image of the barrel modules.

fig. A.5: Comparison of the DD4hep geometry input, on top, to the sensitive hits obtained from full simulation (bottom left) versus the sensitive hits obtained from fast simulation using Acts (bottom right). The barrel region in transversal plane with respect to the beam-axis is shown. The plots show perfect agreement between the geometry description used for full simulation and the geometry description used for fast simulation and recosntruction.

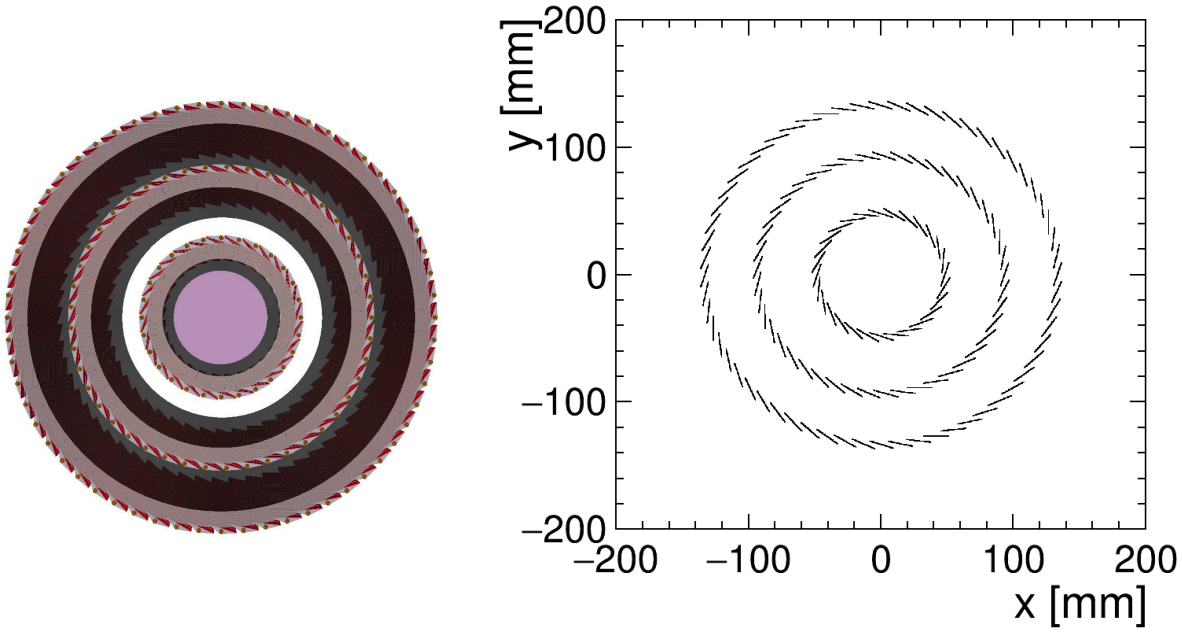

fig. A.6: Comparison of the DD4hep geometry input (left) to the obtained sensitive hits when extrapolating through the translated Acts geometry (right), of a more realistic test tracker using ATLAS "IBL-like" modules (see fig. 3.28a) consisting of different components needed for readout and cooling placed, on a support tube. The barrel region in transversal plane with respect to the beam-axis is shown.

A.3 The Geant4 simulation package - usage and interfacing

This section shortly describes the Geant4 [102] simulation package and complements the description of implemented software in chapter 3, which often requires interfacing to Geant4. For detailed information on Geant4, please see [202].

Geant4 performs simulation of runs, consisting of events with given particle input. It propagates each particle by stepping the particle properties through the detector, taking, magnetic field, volume boundaries, interactions and decay into account: any time a new volume boundary is reached, an interaction or a decay happens, a new step is created with the updated particle properties, taking the magnetic field into account. Particle interactions with the material are applied stochastically according to a physics list, where each particle type with its properties and its corresponding possible interactions are defined. Users can either use a physics list provided per default from Geant4 or implement their own physics list.

To specify which geometry should be used, a detector construction needs to be provided by the user. The Geant4 geometry can either be created directly in Geant4 or translated from ROOT `TGeo` [106] or `gdml` [203], which is provided by Geant4. DD4hep provides an automated mechanism for translating DD4hep into Geant4 geometry. In case of the acts-framework a plugin was introduced which invokes the translation and returns the Geant4 geometry given the DD4hep geometry. In FCCSW a service invokes the translation.

Geant4 simulation consists of different units, which allow the user to interface with the simulation during runtime, in case additional information needs to be accessed or special functionality applied. These are so-called "actions":

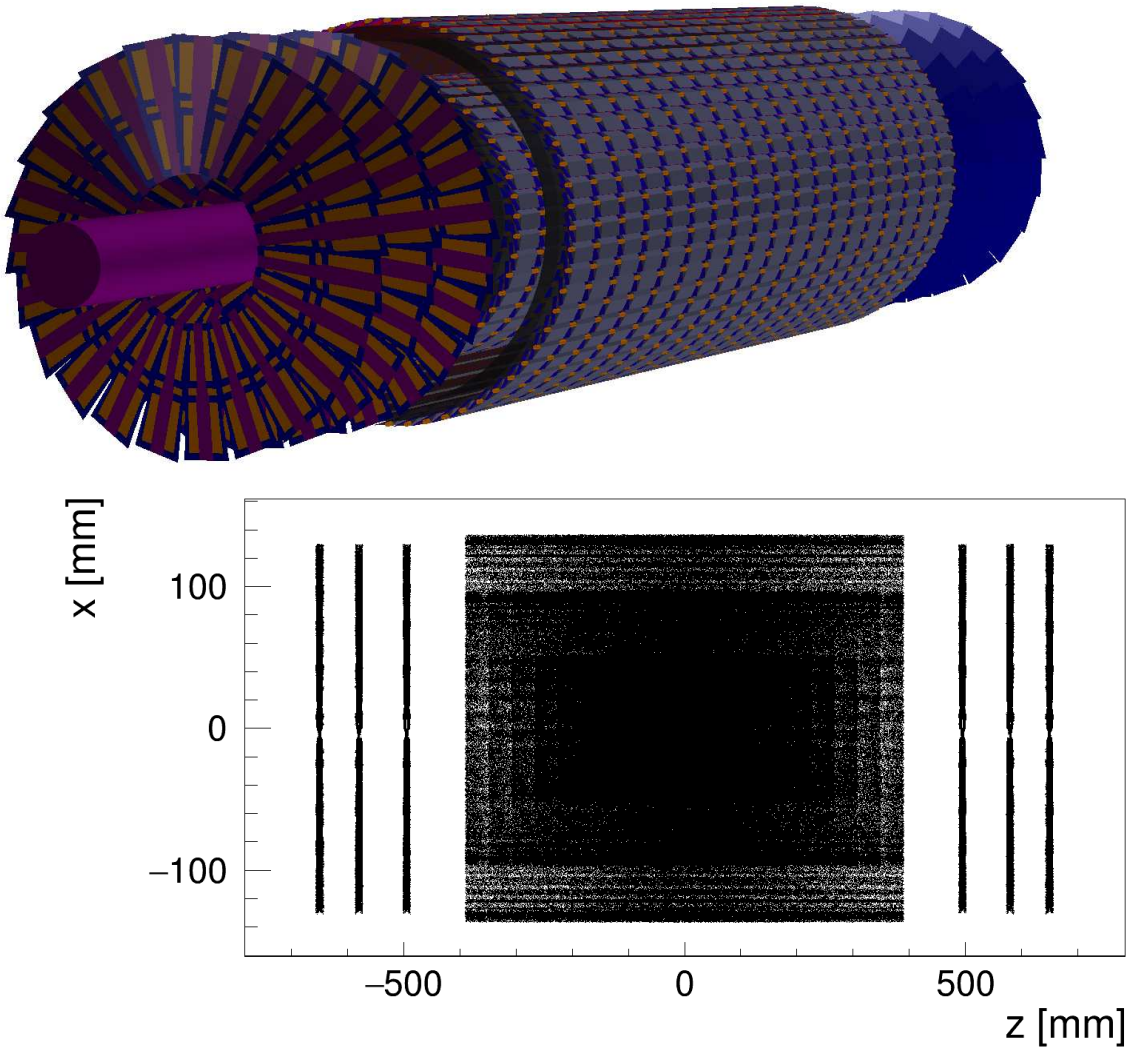

fig. A.7: On top, the DD4hep input of the sensitive modules of a test tracker to a more realistic material description. following the example of the ATLAS IBL-Module is displayed. The bottom shows the translated sensitive surfaces in Acts, as seen through fast simulation.

```
Acts::InterpolatedBFieldMap::FieldMapper<3, 3>
fieldMapperXYZ(const std::function<size_t(std::array<size_t, 3> binsXYZ,
                                          std::array<size_t, 3> nBinsXYZ)>&
                                           localToGlobalBin,
               std::vector<double>         xPos,
               std::vector<double>         yPos,
               std::vector<double>         zPos,
               std::vector<Acts::Vector3D> bField,
               double                      lengthUnit  = Acts::units::_mm,
               double                      BFieldUnit  = Acts::units::_T,
               bool                        firstOctant = false);
```

```
Acts::InterpolatedBFieldMap::FieldMapper<2, 2>
fieldMapperRZ(const std::function<size_t(std::array<size_t, 2> binsRZ,
                                         std::array<size_t, 2> nBinsRZ)>&
                                          localToGlobalBin,
              std::vector<double>         rPos,
              std::vector<double>         zPos,
              std::vector<Acts::Vector2D> bField,
              double                      lengthUnit    = Acts::units::_mm,
              double                      BFieldUnit    = Acts::units::_T,
              bool                        firstQuadrant = false);
```

fig. A.8: The interfaces for the implemented functions to create a field mapper in Acts, in Cartesian (left) and rotational symmetric cylinder (right) coordinates.

- *run action* (optional): steers the run; possibility for the user to interface at the beginning and the end of a run
- *primary generator* action (required): sets up the particle input for each event
- *event action* (optional): invokes an event; possibility for the user to interface at the begin and the end of an event
- *stepping action* (optional): possibility for the user to access and update the particle information at each step

Finally the Geant4 simulation is steered by a run manager, which the user needs to initialize with the wished physics lists, detector description and actions.

A.4 Implementation of particle interactions with matter in track reconstruction and FATRAS

This section describes in detail the underlying formulas implemented in Acts to describe the particle interactions with matter in section 3.2.4.
Table A.1 gives an overview of the symbols for the parameters and constants used in the following.

A.4.1 Mean energy loss due to ionization of heavy particles

The mean energy loss rate $\langle -\frac{dE}{dx}\rangle_{\text{ionization}}$ is well described by the Bethe-Bloch formula (see [124], *chapter 33.2.3* and [113]), with parameters and constants defined in table A.1:

$$\langle -\frac{dE}{dx}\rangle_{\text{ionization}} = Kz^2\frac{Z\rho}{A}\frac{1}{\beta^2}[\frac{1}{2}\ln\frac{2m_e c^2\beta^2\gamma^2 T_{\max}}{I^2} - \beta^2 - \frac{\delta(\beta\gamma)}{2}] \tag{A.1}$$

$$T_{\max} = \frac{2m_e\beta^2\gamma^2}{1 + 2\gamma m_e/m + (m_e/n)^2} \tag{A.2}$$

$$\frac{\delta}{2} = \ln(\frac{E_{\text{Plasma}}}{I} + \ln\beta\gamma - \frac{1}{2}) \tag{A.3}$$

$$I = K_{\text{Ionization}} Z^{0.9} \tag{A.4}$$

The mass stopping power eq. (A.1) is accurate up to a few percent in the region $0.1 \leq \beta\gamma \leq 1000$ for intermediate Z-materials (see [124] *figure 33.1*). The energy-loss is independent of the particle's mass, but depends on its velocity and the absorber material. At small energies the first contribution is dominant and the distribution falls with $\sim 1/\beta^2$, since slower particles feel the electric force of the shell electrons for a longer time, until it reaches its minimum at $3m_p c^2$ (with m_p being the mass of the penetrating particle). A particle with a mean energy loss rate close to the minimum is called minimum ionizing particle (MIP). After the minimum is reached, the distribution rises again for $\beta\gamma > 4$ with $\sim \ln(\beta^2\gamma^2)$, because the transverse electric field of the particle rises due to realistic effects. However, the just described increase is reduced because the medium gets polarized and shields the electrical field far from particle path. This is described by the density effect corrections (eq. (A.3)) [124].
For electrons the formula is slightly altered, see appendix A.4.2. In addition to energy loss due to ionization, also energy loss due to radiation needs to be considered. These contributions become more important than ionization at sufficiently high energies, especially for electrons `Bremsstrahlung` (see [124], *chapter 33.4*) becomes important at around 1 GeV and radiative effects for muons and pions become important at several hundred GeV (see [124], *chapter 33.6*).

Symbol	Definition	Value/Unit
K	$4\pi N_A r_e^2 m_e c^2$	$0.307075\,\mathrm{MeV mol^{-1} cm^2}$
Z	atomic number of absorber	
A	atomic mass number of absorber	g/mol
z charge of incident particle	density of absorber material	$\mathrm{g/cm^3}$
β	$v = p/E$	
γ	$1/\sqrt{1-\beta^2} = E/m$	
m_e	electron mass	$0.511\,\mathrm{MeV}$
r_e	classical electron radius	$e^2/4\pi\varepsilon_0 m_e c^2 ... 2.818\,\mathrm{fm}$
α	fine structure constant	$e^2/4\pi\varepsilon_0\hbar c = 1/137$
N_A	Avogadro constant	$6.022 \times 10^{23}\,\mathrm{mol^{-1}}$
T_{max}	maxmium kinetic energy transfer to an electron in a single collision	MeV
m	restmass of particle	MeV
E	particle energy $E = \sqrt{p^2 + m^2}$	MeV
I	mean excitation energy	MeV
δ	density effect correction	
E_{Plasma}	plasma energy	$\hbar\omega_p$ $= 28.816\,\mathrm{eV} * \sqrt{\rho Z/A}$
$K_{Ionization}$	ionization potential constant	$16\,\mathrm{eV}$

tab. A.1: Definition of the parameters and constants used in this section, as defined in [124]. Natural units [138] are assumed.

A.4.2 Mean ionization energy loss of electrons and positrons

For electrons and positrons the above formula must be slightly altered, due to the fact that the passing electron and the shell electrons have the same mass and in case of electrons are identical, indistinguishable particles. The detailed description and formulas can be found in *chapter 33.4* of [124]. In Acts, the same formula as for the ATLAS implementation is used as described in [113]:

$$\langle -\frac{dE}{dx}\rangle_{\text{ionization}}^{\text{electron}} = K\frac{Z\rho}{A}[\ln\frac{2m_e}{I} + 1.5\ln\gamma - 0.976] \tag{A.5}$$

A.4.3 The Landau distribution and the most probable energy loss due to ionization

For thin abosrbers, as it is the case for the tracker, the energy loss is described by the Landau-distribution, which resembles a gaussian distribution with a long tail [204]. Those high values stem from rare collisions with small impact parameter resulting in the production of highly energetic δ-*electrons* with energies in the keV-range [17]. The result is an asymmetric energy loss distribution function, whose most probable energy loss is at a smaller value than its mean energy loss. Within Acts the following formula is used to describe the most probable energy loss (see see [124], *chapter 33.2.9* and [113]):

$$\frac{dE}{dx}_{\text{ionization}}^{\text{MOP}} = \xi[\ln\frac{2mc^2\beta^2\gamma^2}{I} + \ln\frac{\xi x}{I} + j - \beta^2 - \delta(\beta\gamma)] \tag{A.6}$$

$$\xi = \frac{K}{2}\frac{Z}{A\beta^2} \tag{A.7}$$

The standard deviation of the landau distribution, needed for error propagation in track reconstruction and for emulating the landau distribution during simulation, can only be estimated because the distribution has no exactly defined moments due to its asymmetric tail.
The FWHM (full width at half maximum) is given by

$$\text{FHWM}_{\text{Landau}} = 4\xi \quad [124] \tag{A.8}$$

For a gaussian distribution the relation between the FWHM and the standard deviation σ writes as

$$\text{FHWM}_{\text{gaussian}} = 2\sqrt{2\ln 2}\sigma \tag{A.9}$$

Using the gaussian standard deviation definition together with the FHWM of the landau distribution results in

$$\text{sigma}_{\text{Landau}} \approx \frac{2}{\sqrt{2\ln 2}}\xi \tag{A.10}$$

A.4.4 Multiple scattering

During the passage of a charged particle through a medium, it scatters on the atomic nuclei of the material and will be deflected due to the coulomb force [205]. Single scatters can be described by the Rutherford cross section [206]. Following the central limit theorem, multiple small-angle scatters along the path lead to a gaussian distributed total deflection of the particle trajectory [124]. The width of the projected total scattering angle can be parameterized using the Highland scattering formula (see [113] *(17)*):

$$\sigma_M(\Theta_p) = \frac{13.6\text{MeV}}{\beta p}\sqrt{\frac{x}{X_0}}(1 + 0.038\ln\frac{x}{\beta^2 X_0}) \tag{A.11}$$

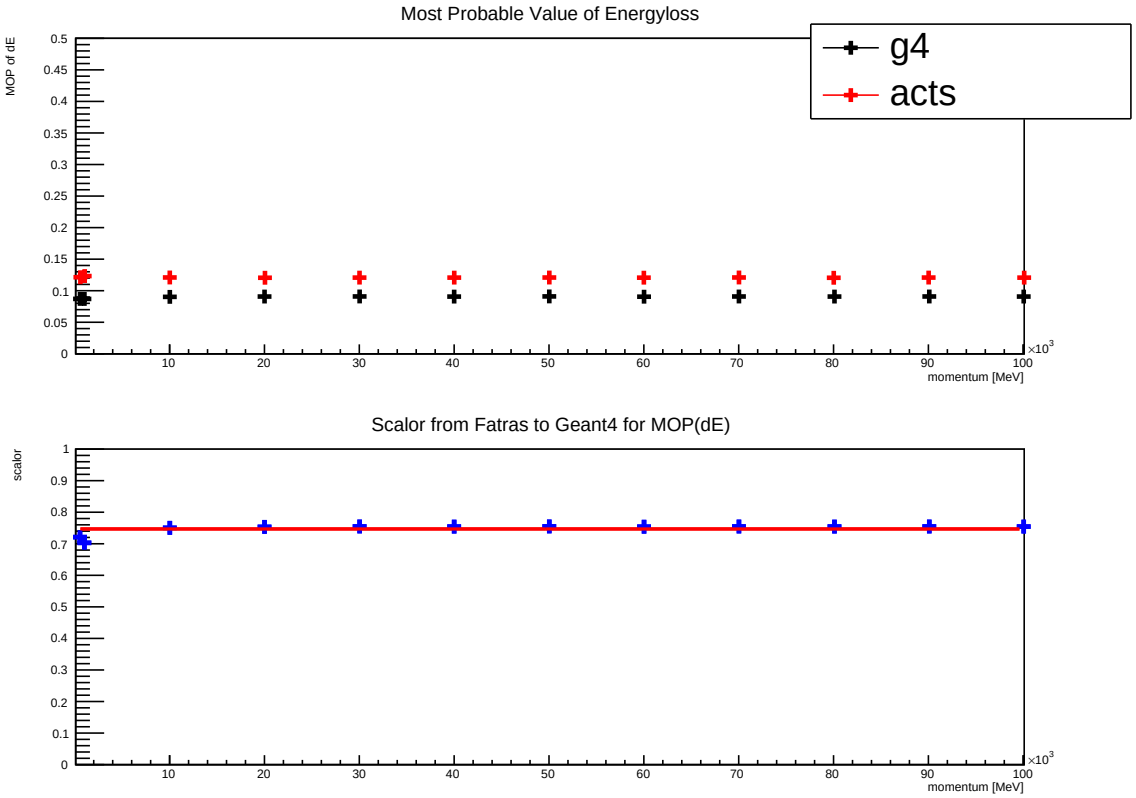

fig. A.9: On top, the difference of the most probable energy loss due to ionization within Acts and Geant4 simulation are shown. The bottom shows the evaluation of the scalors from Acts to Geant4.

where x/X_0 is the traversed distance in units of of radiation length, Θ_p is the projected scattering angle in the plane of the original direction.

A.5 Validation of material effects integration of FATRAS against Geant4

This section shows supplementary material to the FATRAS validation described in section 3.2.4.1. Since there have been discrepancies between the Acts, obtained from the formulas described before and Geant4 simulation, scaling parameters (scalors) have been obtained, as described in this section. To estimate the optimal value, which best fits the Geant4 reference, the most probable value and the standard deviation have been obtained, at different energies by fitting a landau-distribution using the ROOT [97] analysis framework. The obtained values for both Acts and Geant4 are then compared in figs. A.9 and A.10 to obtain the final scaling factors for the energy loss and standard deviation: $\text{scalor}_{\text{eLoss}} = 0.7452 \pm 0.0048$ and $\text{scalor}_{\sigma} = 0.6893 \pm 0.0058$. Using the obtained scalors, a good agreemnet between Acts and Geant4 is found, as shown in fig. 3.33a.

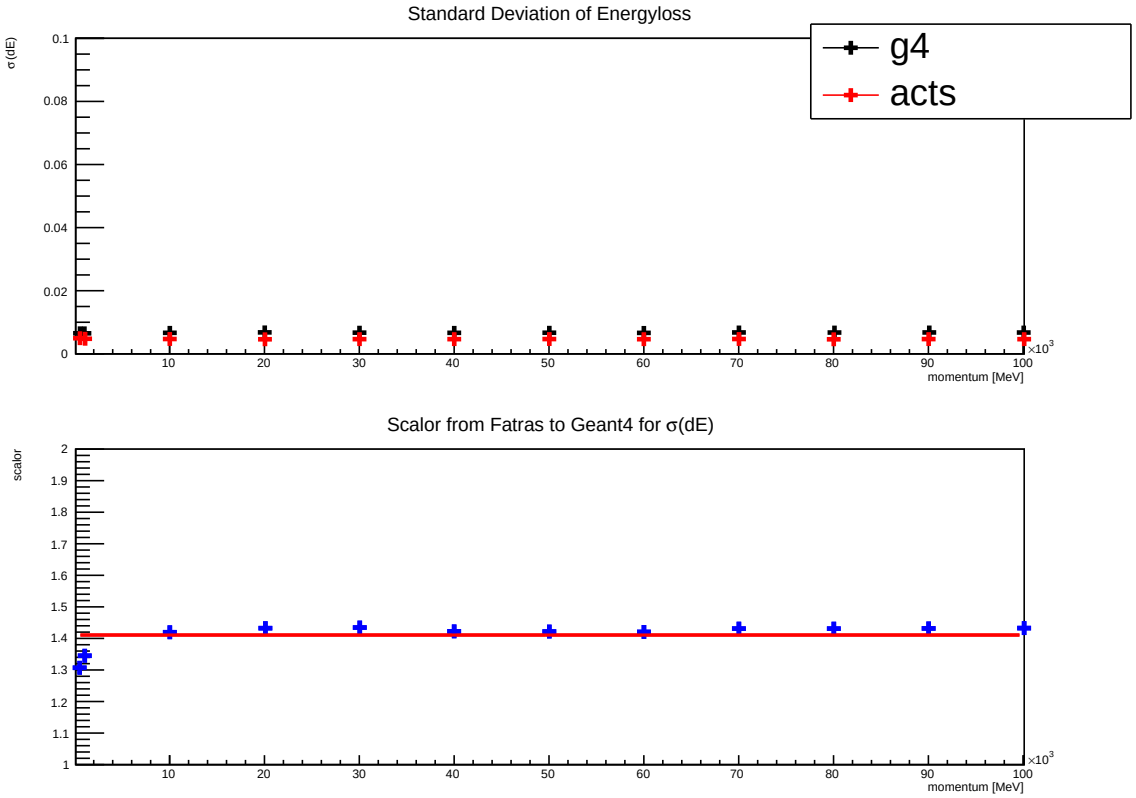

fig. A.10: On top, the difference of standard deviation of the most probable value of energy loss due to ionization within Acts and Geant4 simulation are shown. The bottom shows the evaluation of the scalors from Acts to Geant4.

A.6 Validation of digitization and clusterization

This chapter shows a step-by-step validation of the digitization and clusterization implemented in FCCSW section 3.1.4, which internally uses the Acts digitization and clusterization tools introduced in section 3.2.5. The valdiation uses the FCC-hh baseline tracker (see section 2.3). To be independent of any effects due to the change of pitch sizes, the same cell size of $25\,\mu m \times 50\,\mu m$ (which is the default granularity for the pixel region) is used for all barrel and endcap layers. Since muons penetrate the whole detector and only interact electromagnetically (mostly energy loss due to ionization and elastic multiple scattering as described in appendix A.4.1 and appendix A.4.4), muons are good test particles for validation. Hence, 100 000 muons, with a transverse momentum of 10 GeV, merged into one event, are used for the validation. To also account for effects due to hadronic interaction, 100 000 pions with a transverse momentum of 10 GeV, merged into one event, are tested as well. To understand the effect of magnetic field and secondary particles created in the detector, all muon plots are done for the following four cases:

1. no magnetic field, no secondaries
2. with magnetic field, no secondaries
3. no magnetic field, with secondaries
4. with magnetic field, with secondaries

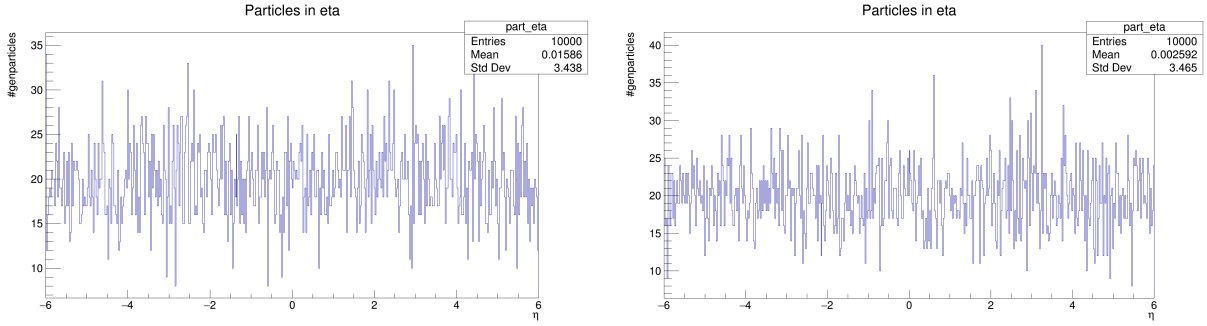

(a) Generated particle spectrum of 100 000 muons, with a transverse momentum of 10 GeV, merged into one event, plotted against pseudorapidity η.

(b) Generated particle spectrum of 100 000 pions, with a transverse momentum of 10 GeV, merged into one event, plotted against pseudorapidity η.

fig. A.11: Particle spectra of the muons (left) and the pions (right) over η, used for validation.

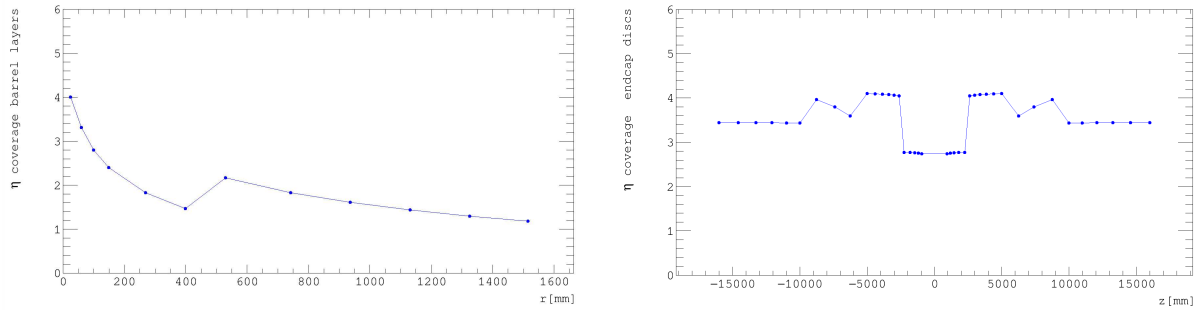

(a) Each point shows the η coverage of a barrel layer, plotted against its radial position.

(b) Each point shows the η coverage of an endcap disc layer, plotted against its position in z.

fig. A.12: Coverage of pseudorapidity region of barrel (left) and (endcap) layers.

With the magnetic field turned on or off just for the muon particles coming directly from the generated (*no secondaries*) and including secondary particle of the muons produced in the tracker (*with secondaries*). Since for pions the hadronic interaction and the subsequent production of secondary particles was of interest, only the last two of the above cases (namely 3 and 4) are shown.

The first step, of the validation, was to check the particle input spectrum. Both, muons and pions are produced flat in η (similar to the minimum bias events, see section 4.1), as shown in fig. A.11.

Since the incoming generated particle distribution is flat in η, the number of measurements on each tracker layer depends on the η-coverage of the respective layer, which is shown in fig. A.12.

When also overlap is taken into account, the number of cluster measurements should roughly stay constant, at each layer, when dividing by the pseudorapidity coverage:

$$\frac{\mathrm{d}n}{\mathrm{d}\eta} \approx \text{const} \tag{A.12}$$

For the barrel layers, the overlap, of the modules, needs to be calculated with respect to a cylinder. In the endcap region, the overlap with respect to a disc needs to be considered.

This was tested using muons in fig. A.13 for the barrel and in fig. A.15 for the endcaps, for the four different cases described above. The green curve show the values without taking overlaps of

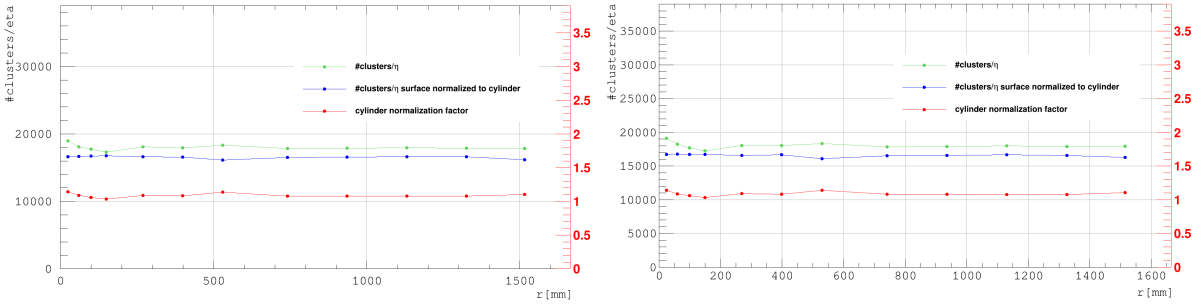

(a) *no magnetic field, no secondaries*

(c) *with magnetic field, no secondaries*

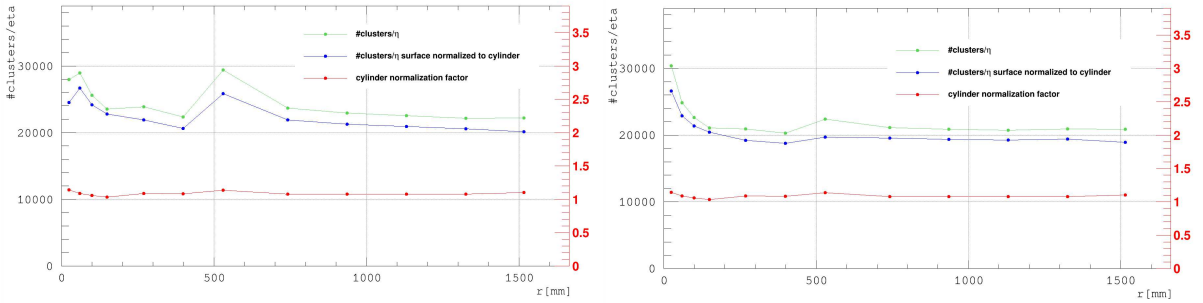

(b) *no magnetic field, with secondaries*

(d) *with magnetic field, with secondaries*

fig. A.13: Each point displays the number of cluster-measurements for the **muon** case divided by the η-coverage of each barrel layer, plotted against the barrel layer's radial position. Four different variations are shown: turning on/off the magnetic field and including/excluding secondary particles produced in the detector during simulation. The green line shows the pure value, while the blue line shows the the values, when dividing by the surface normalization factor (accounting for overlap) of each layer. The factor, which corrects for overlap, is displayed in red, with the corresponding axis labels on the right in red.

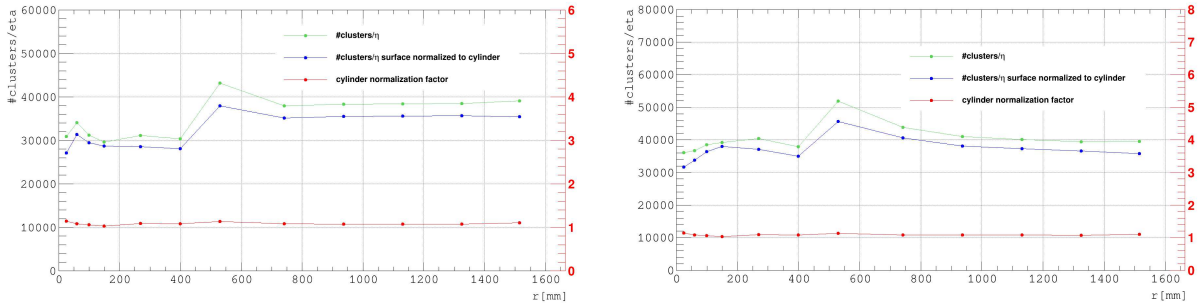

(a) *no magnetic field, with secondaries*

(b) *with magnetic field, with secondaries*

fig. A.14: Each point displays the number of cluster-measurements for the **pion** case divided by the η-coverage of each barrel layer, plotted against the barrel layer's radial position. Four different variations are shown: turning on/off the magnetic field and including/excluding secondary particles produced in the detector during simulation. The green line shows the pure value, while the blue line shows the the values, when dividing by the surface normalization factor (accounting for overlap) of each layer displayed in red, with the corresponding axis labels on the right in red.

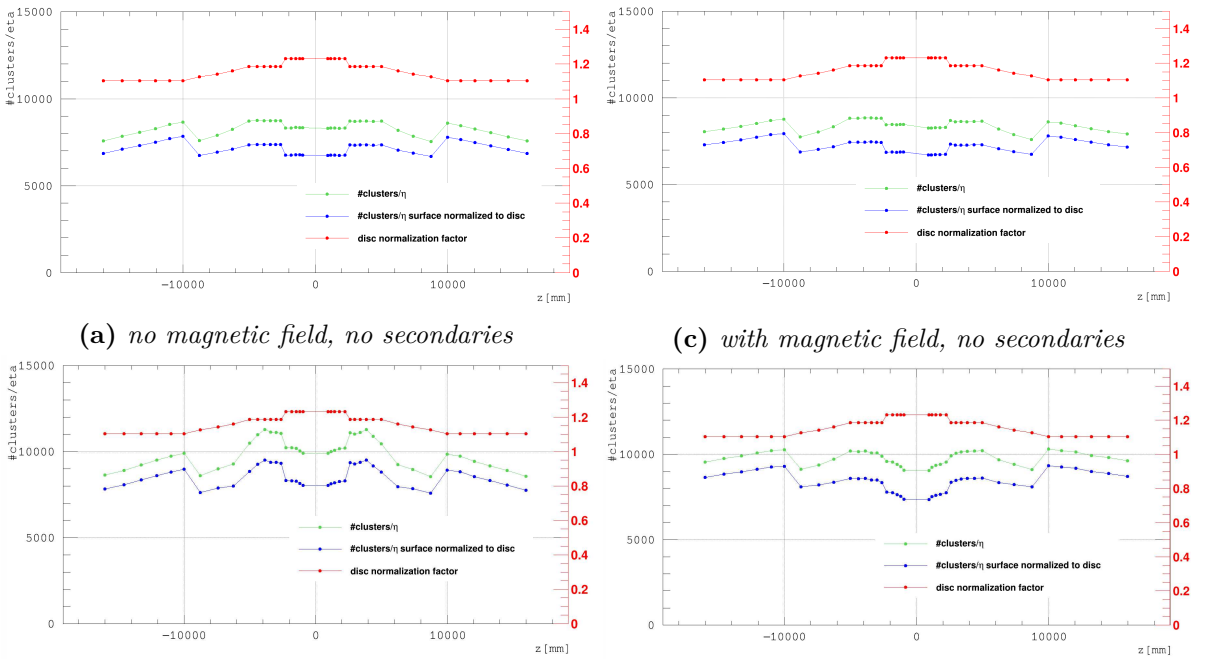

(a) *no magnetic field, no secondaries*

(c) *with magnetic field, no secondaries*

(b) *no magnetic field, with secondaries*

(d) *with magnetic field, with secondaries*

fig. A.15: Each point displays the number of cluster-measurements for the **muon** case divided by the η-coverage of each endcap disc layer, plotted against the endcap layer's position in z. Four different variations are shown: turning on/off the magnetic field and including/excluding secondary particles produced in the detector during simulation. The green line shows the pure value, while the blue line shows the the values, when dividing by the surface normalization factor (accounting for overlap) of each layer displayed in red, with the corresponding axis labels on the right in red.

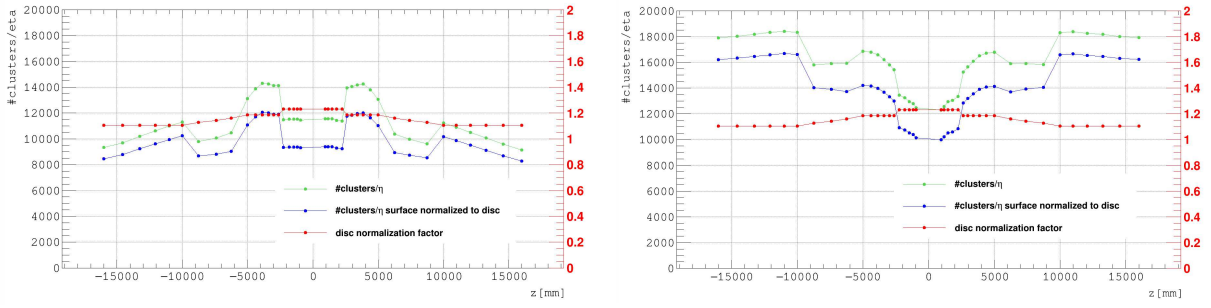

(a) *no magnetic field, with secondaries*

(b) *with magnetic field, with secondaries EC*

fig. A.16: Each point displays the number of cluster-measurements for the **pion** case divided by the η-coverage of each endcap disc layer, plotted against the endcap layer's position in z. Four different variations are shown: turning on/off the magnetic field and including/excluding secondary particles produced in the detector during simulation. The green line shows the pure value, while the blue line shows the the values, when dividing by the surface normalization factor (accounting for overlap) of each layer displayed in red, with the corresponding axis labels on the right in red

modules into account. The blue curve shows the corrected distribution. The correction is done by dividing by the *surface normalization factor = total surface of modules/surface of respective cylinder or disc of the layer*, which is displayed in red, with the corresponding axis to the right. If, for the barrel region (fig. A.13), the magnetic field is turned off and no secondary particles are included (upper left), the number of clusters, as theoretically assumed, stays roughly constant over η. Since the produced muons have a high transverse momentum, they are almost not affected by the magnetic field (upper right). Taking secondaries produced along the track within the detector material by the moun into account (bottom left), which are essentially ionized electrons, has a strong effect on the number of clusters, which are raised by $30-70\,\%$ for the different layers. The overlap and the module material thickness (see fig. 4.3b) lead to significant higher production of secondary particles and the number of measurements, stays no longer constant with variation of up to 1/3 in the number of clusters. When turning on the magnetic field and including secondaries (bottom right), the magnetic field has a significant effect on the mostly soft produced secondary particles. It even slightly increases the total number of clusters in the first layers (due to increased interactions also of the secondaries coming from the beampipe), but smooths the distribution for the outer layers, since less secondaries are surviving. For the endcap discs the results are similar as shown in fig. A.15. Looping particles tend to accumulate in the endcaps.
The effect of secondaries is particulary strong for pions (see fig. A.14 and fig. A.16), which make approximately $1.6-2.4$ times more number of hits than the muons. Different then for the muon case, the magnetic field even reinforces this effect by $15-20\,\%$. The secondary particles created through hadronic interaction (see fig. 4.6b) have higher momentum than ionized electrons and form tracks of their own which are deviated by the magnetic field, creating more hits.

As a next step, the fluence, which is the number of measurements per area, was investigated. In simulation this quantity can be calculated by dividing the number of measurements through the total module area. This is equal to the number of pixels times the pixel size. To receive one value for a layer, the average fluence of all detector modules constituting the layer, is calculated. The fluence distribution can also be estimated analytically, by dividing the η-coverage (which is proportional to the number of clusters) per layer by the total area of the layer, including the module overlaps:

$$\Phi = \frac{\mathrm{dn}}{\mathrm{dA}} \propto \frac{\eta}{\mathrm{A}} \tag{A.13}$$

Since this only gives a proportion and not a quantity it is scaled to the first entry of the fluence obtained by simulation, to compare the distribution. For muons, as shown in fig. A.17 the values for the first case are nearly identical (upper left), also when including magnetic field without including secondaries (upper right). When secondaries are included the fluence is raised, consistent with the previous observations and especially the first layers are affected (bottom left), due to the secondaries from the beampipe. When including magnetic field, this effect is more pronounced (bottom right). Similar behavior can be observed for the endcaps fig. A.19. Secondaries have a stronger effect on the inner disc layers and the fluence is raised. Particles arriving in the more forward parts, are less affected by the magnetic field, due to lower transverse momentum. The fluence, including magnetic field with secondaries, is slightly below the expectation for the inner discs, when scaling the reference fluence to the outermost layer. This is due to the fact, that more low momentum secondaries are present. For pions, this effect is more pronounced (see fig. A.20). In the barrel region (fig. A.18), the fluence in the outer layers is raised, because more material is passed, which increases the probability of hadronic interaction.

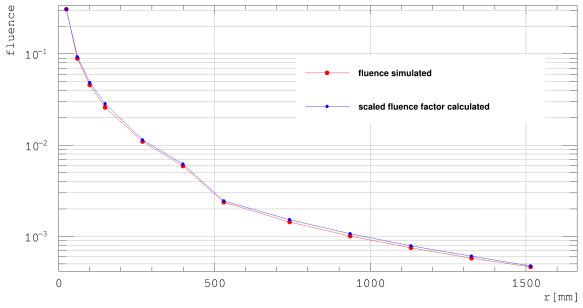

(a) *no magnetic field, no secondaries*

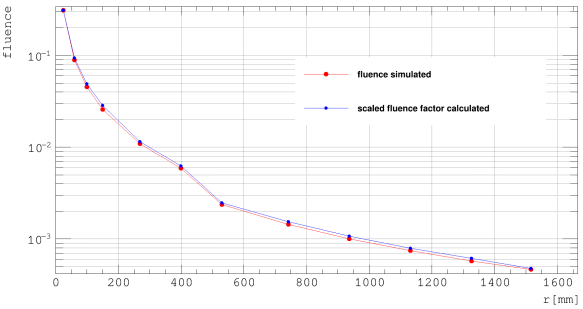

(c) *with magnetic field, no secondaries*

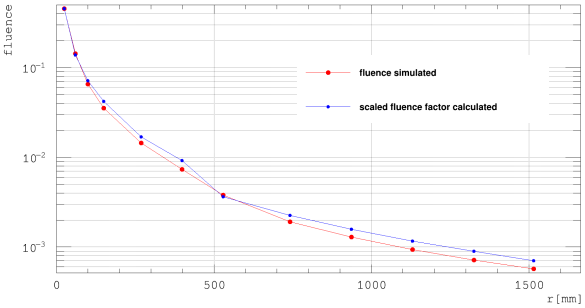

(b) *no magnetic field, with secondaries*

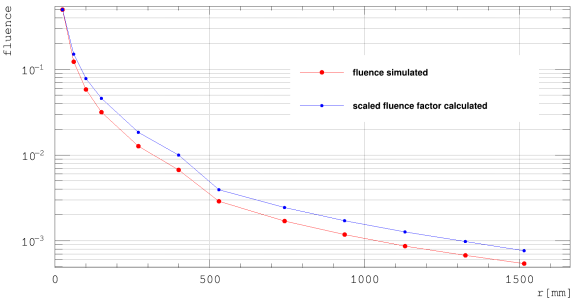

(d) *with magnetic field, with secondaries*

fig. A.17: Each red point displays the averaged fluence as obtained from simulation of **muon**s for the barrel region plotted against the layer's position in r. The blue points show the analytically calculated fluence distribution scaled to the first entry. Four different variation of turning on/off the magnetic field and including/excluding secondary particles produced in the detector during simulation are shown.

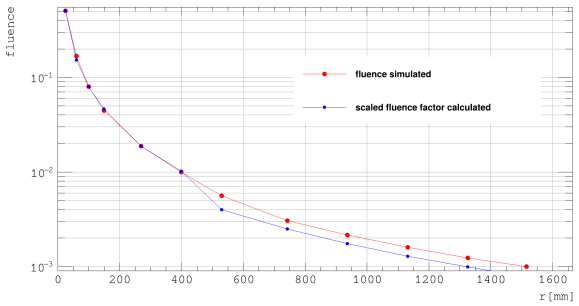

(a) *no magnetic field, with secondaries*

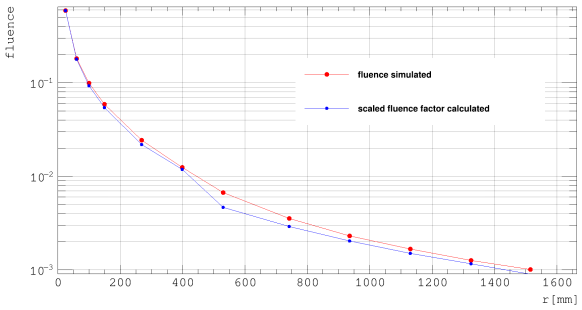

(b) *with magnetic field, with secondaries*

fig. A.18: Each red point displays the averaged fluence as obtained from simulation of **pion**s for the barrel region plotted against the layer's position in r. The blue points show the analytically calculated fluence distribution scaled to the first entry. Four different variation of turning on/off the magnetic field and including/excluding secondary particles produced in the detector during simulation are shown.

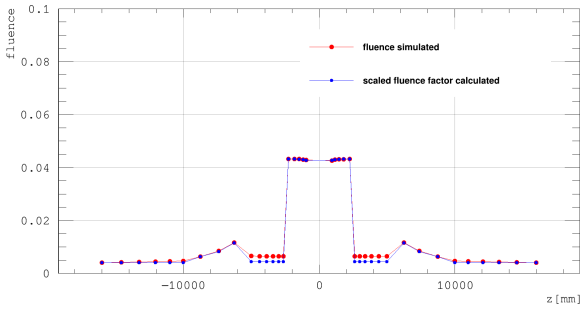

(a) *no magnetic field, no secondaries*

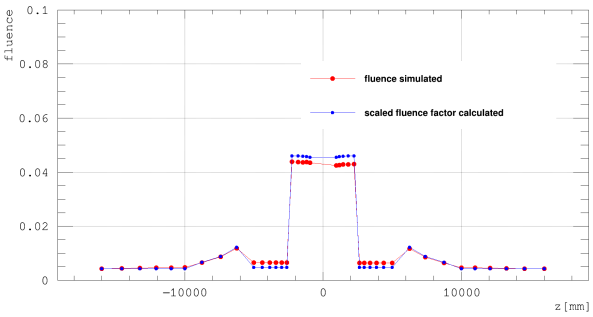

(c) *with magnetic field, no secondaries*

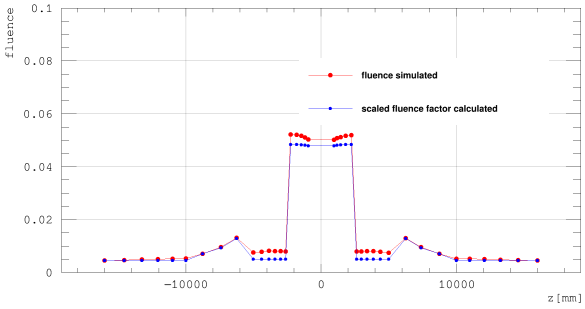

(b) *no magnetic field, with secondaries*

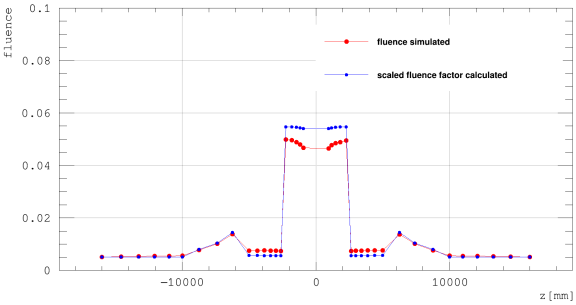

(d) *with magnetic field, with secondaries*

fig. A.19: Each red point displays the averaged fluence as obtained from simulation of **muon**s for the endcap region plotted against the layer's position in z. The blue points show the analytically calculated fluence distribution scaled to the first entry. Four different variation of turning on/off the magnetic field and including/excluding secondary particles produced in the detector during simulation are shown.

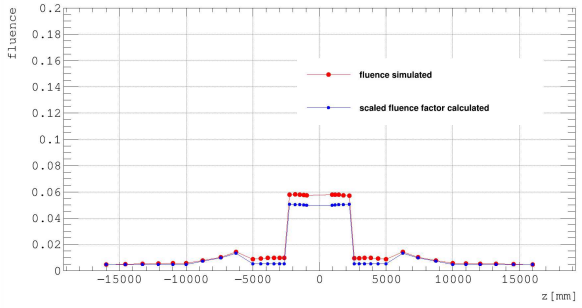

(a) *no magnetic field, with secondaries*

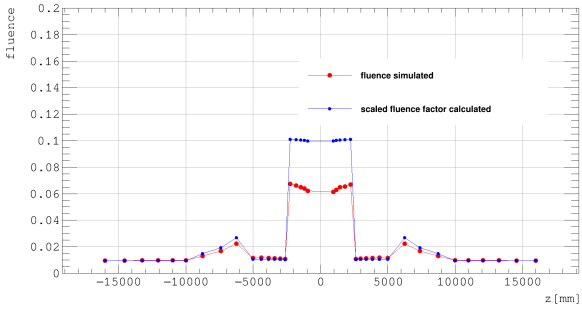

(b) *with magnetic field, with secondaries EC*

fig. A.20: Each red point displays the averaged fluence as obtained from simulation of **pion**s for the endcap region plotted against the layer's position in z. The blue points show the analytically calculated fluence distribution scaled to the first entry. Four different variation of turning on/off the magnetic field and including/excluding secondary particles produced in the detector during simulation are shown.

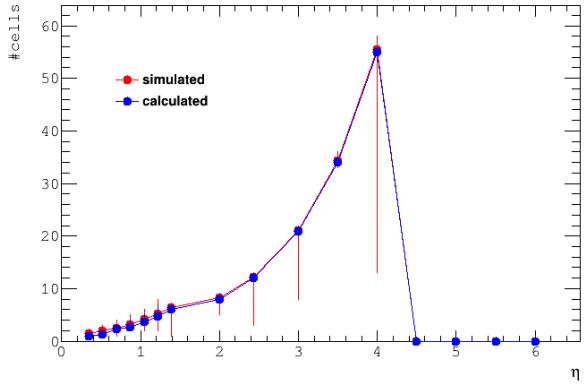

(a) barrel, using $N^{cells} = t/(\tan\vartheta * pitch)$, with ϑ taken from the generated particles momentum direction

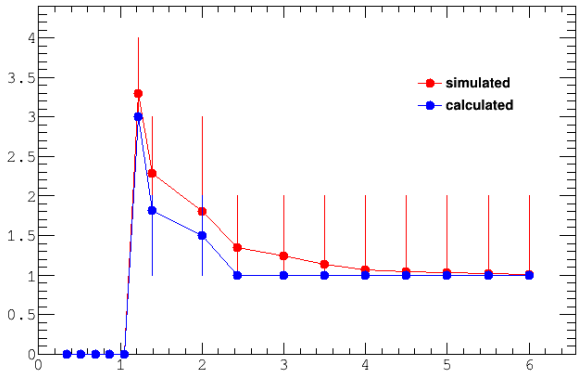

(c) endcap, using $N^{cells} = (t * \tan\vartheta)/pitch$, with ϑ taken from the generated particles momentum direction

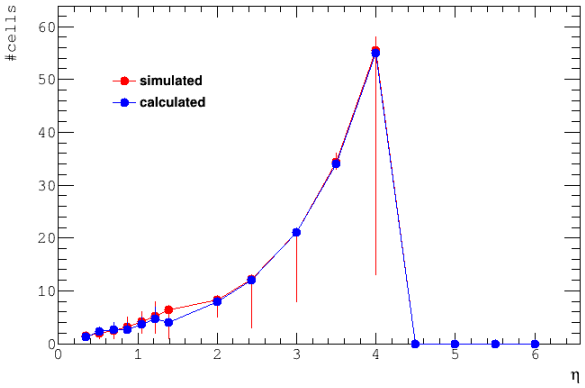

(b) barrel, using $N^{cells} = (t * z)/(r * pitch)$, with z/r taken from the cluster position

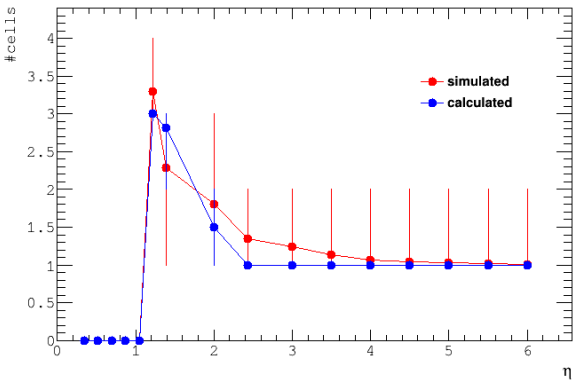

(d) endcap, using $N^{cells} = (t * r)/(z * pitch)$, with r/z taken from the cluster position

fig. A.21: Comparison of the analytically (blue) and simulated (red) cluster size, using **muon**s without magnetic field and secondaries, tested for different pseudorapdity values of the particle. Two different methods to calculate the analytical value have been used for both the barrel (left) and the endcap (right) regions.

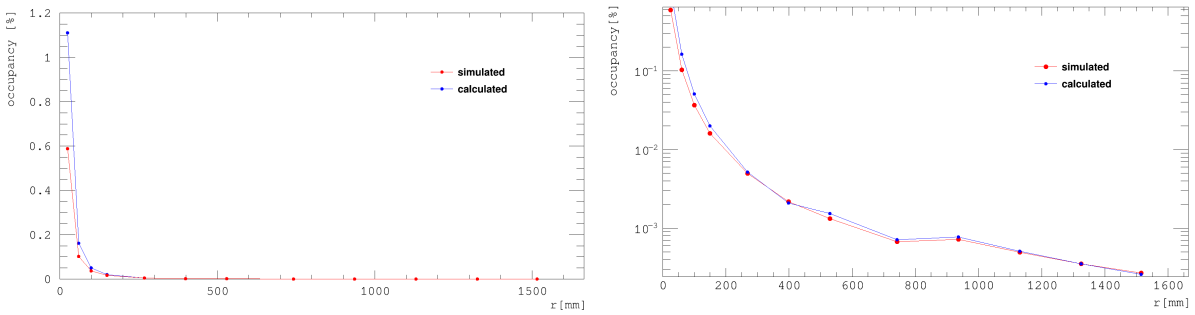

(a) *no magnetic field, no secondaries*

(c) *with magnetic field, no secondaries*

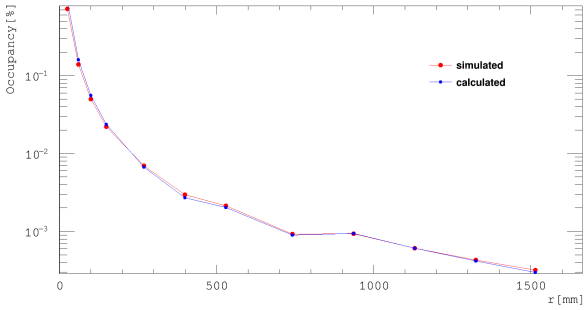

(b) *no magnetic field, with secondaries*

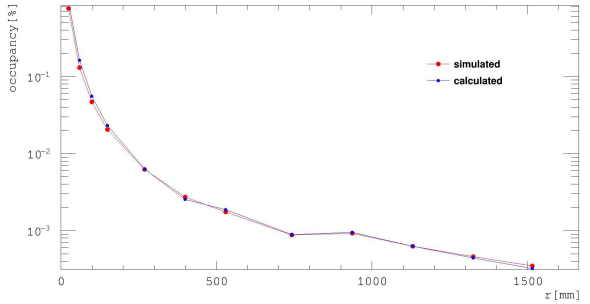

(d) *with magnetic field, with secondaries*

fig. A.22: Each red point displays the averaged occupancy of each layer as obtained from simulation of **muon**s for the barrel region plotted against the layer's radial position. The blue points show the calculated occupancy. Four different variation of turning on/off the magnetic field and including/excluding secondary particles produced in the detector during simulation are shown.

As part of the validation a cross-check of the obtained cluster sizes[1] from simulation with the analytically expected values was done. To be independent from any intangible effects, only pure muons with varied incident angle ϑ, without taking secondaries into account and with magnetic field turned off, have been used. For the barrel region, the number of activated cells, when a particle traverses a planar module can be estimated as (see fig. 4.6a)

$$N^{cells} = \frac{t}{\tan\vartheta * p} = \frac{t * z}{r * p} \tag{A.14}$$

and for the endcap as:

$$N^{cells} = \frac{t * \tan\vartheta}{p} = \frac{t * r}{z * p} \tag{A.15}$$

with p, being the pitch size.
The result of the comparison is shown in fig. A.21. Good agreement of the analytically calculated value and the value obtained by simulation can be observed. In the endcap region at higher $\eta = 1.2 - 5$, the agreement is reduced: due to the high incident angle in that region the amount of traversed material and hence multiple scattering effects are non-negligible. For the upper plots of fig. A.21, the analytically calculated values have been obtained, by using $\tan\vartheta$ of the generated muons (first part of the above equation). Due to multiple scattering effects, the second part of the above formula using r/z of the each cluster is closer to simulation.

[1] cluster size = the number of cells contributing to one cluster

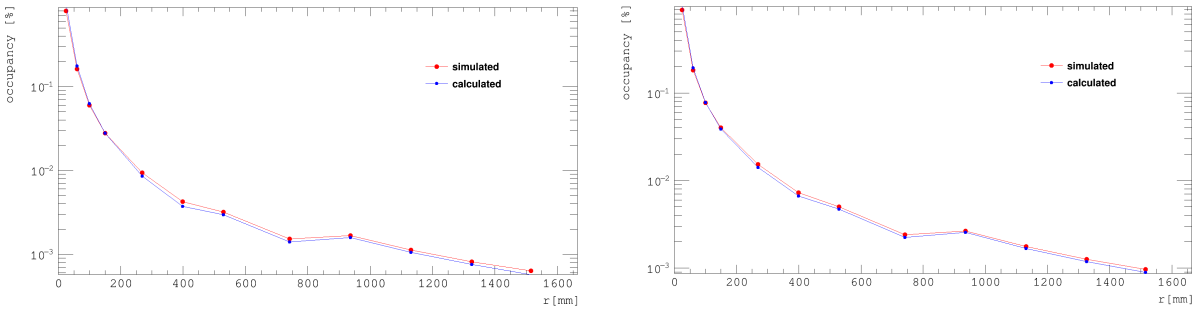

(a) *no magnetic field, with secondaries* **(b)** *with magnetic field, with secondaries*

fig. A.23: Each red point displays the averaged occupancy of each layer as obtained from simulation of **pion**s for the barrel region plotted against the layer's radial position. The blue points show the calculated occupancy. Four different variation of turning on/off the magnetic field and including/excluding secondary particles produced in the detector during simulation are shown.

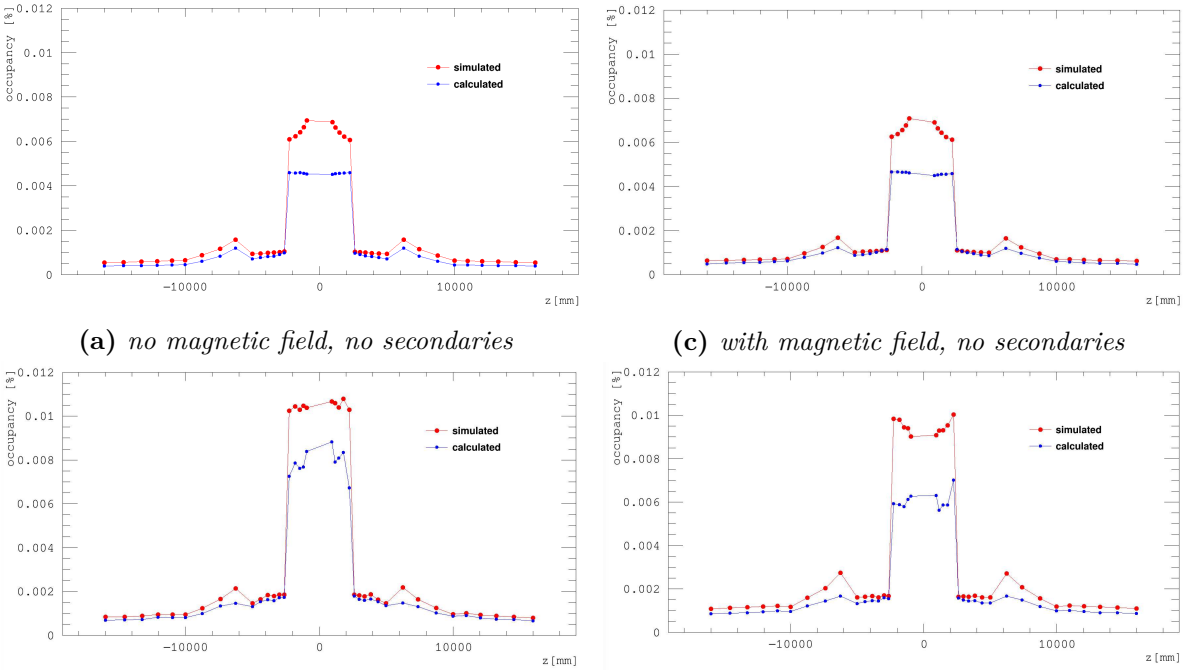

(a) *no magnetic field, no secondaries* **(c)** *with magnetic field, no secondaries*

(b) *no magnetic field, with secondaries* **(d)** *with magnetic field, with secondaries*

fig. A.24: Each red point displays the averaged occupancy of each layer as obtained from simulation of **muon**s for the endcap region plotted against the layer's position in z. The blue points show the calculated occupancy. Four different variation of turning on/off the magnetic field and including/excluding secondary particles produced in the detector during simulation are shown.

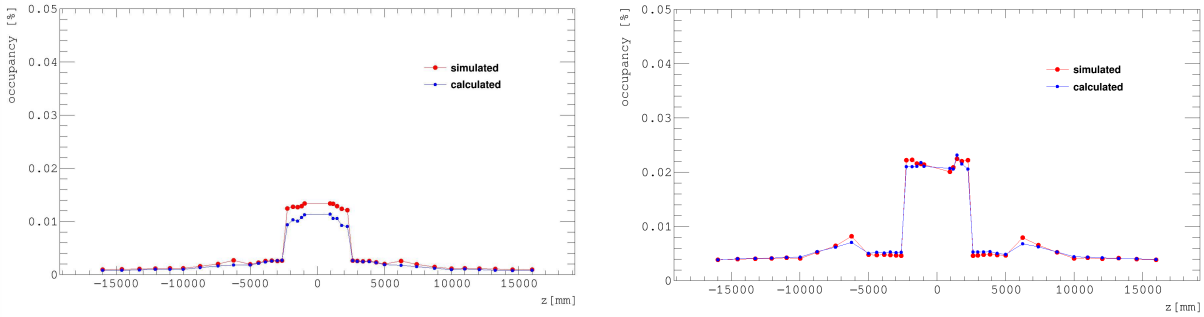

(a) *no magnetic field, with secondaries* **(b)** *with magnetic field, with secondaries EC*

fig. A.25: Each red point displays the averaged occupancy of each layer as obtained from simulation of **pion**s for the endcap region plotted against the layer's position in z. The blue points show the calculated occupancy. Four different variation of turning on/off the magnetic field and including/excluding secondary particles produced in the detector during simulation are shown.

Finally, the channel occupancy obtained from simulation can be compared to the calculated value. From simulation, the channel occupancy is calculated by dividing the number of activated cells of a module, by the total number of channels of the module.

$$\text{occupancy}_{\text{sim}} = \frac{\text{N}^{\text{channels}}_{\text{activated}}}{\text{N}^{\text{channels}}} \quad \text{per module} \tag{A.16}$$

This value is averaged for all modules of a layer and can be compared to the following calculated value, for each layer:

$$\text{occupancy}_{\text{calc}} \propto \frac{\text{dn}}{\text{dA}} * \text{average cluster size} * \text{pitch} \tag{A.17}$$

Good agreement between the calculated and the simualted value is observed in fig. A.22, fig. A.23, fig. A.24 and fig. A.25. For the endcaps, the statistics sample is too small and therefore the distributions are partly asymmetric. As explained when estimating the fluence, the occupancy in the inner endcaps is underestimated by the calculation for the muon case, because the calculated value, is scaled to the outermost disc. Including secondary particles increases the occupancy up to a factor of 8. Including the magnetic field, the increase is $1-2$.

In addition to unit tests, the physical validity of the digitization and clusterization within FCCSW (and Acts) could be shown, by comparing simulated with expected values and distributions. Beginning from the number of measurements, more complex tests including the fluence, the cluster sizes and channel occupancies have been done for different scenarios. The effect of secondary particles, increasing the number of clusters and hence, the fluence and the occupancy is very strong, especially when taking hadronic interaction into account. Also the magnetic field can lead to a moderate increase for particles with high p_T, while decreasing the effect for soft particles.

A.7 Two-body particle decay kinematics

This section shortly explains the kinematics of an unstable moving particle decaying into two daughter particles, which was needed for the study of disappearing tracks in chapter 6 and

follows [207]. The final goal is to determine the four-momenta of the daughter particles, given a moving and decaying mother particle.
First, the daughter momenta are determined in the rest frame of the mother. The four-momentum of the mother particle at rest is $P = (M, 0, 0, 0)$, while the unknown daughter momenta are denoted as $p_1 = (E_1, \vec{p_1})$ and $p_2 = (E_2, \vec{p_2})$. Applying the law of 4-momentum conservation (energy and momentum conservation) $P = p_1 + p_2$, the following relations are found:

$$\vec{p_2} = -\vec{p_1} \coloneqq \vec{p} \tag{A.18}$$

$$E_1 + E_2 = \sqrt{m_1^2 + p^2} + \sqrt{m_2^2 + p^2} = M \tag{A.19}$$

This can be solved for the value of p:

$$p = \frac{1}{2M}\sqrt{[M^2 - (m_1 - m_2)^2][M^2 - (m_1 + m_2)]} \tag{A.20}$$

The energies of the daughters are fixed by their masses

$$E_1 = \frac{1}{2M} * (M^2 + m_1^2 - m_2^2) \tag{A.21}$$

$$E_2 = \frac{1}{2M} * (M^2 + m_2^2 - m_1^2) \tag{A.22}$$

Hence, the mass of the mother particle must at least be equal or exceed the sum of its daughter masses to allow a decay. The momentum direction can not be exactly determined by theory, because the angular distributions of the daughter particles are isotropic. In simulation, this behaviour is mimicked by generating random numbers for the two angles ϑ and φ. In an experiment the direction of one particle is determined, when it is measured. As soon as the momentum direction of one daughter particle fixed, according to eq. (A.18) the second daughter particle has the same momentum direction with opposite sign.
Now the momenta and energies of the daughters have been determined in the rest frame of the mother particle. Since the mother is not at rest, but is moving, usually with relativistic velocities (close to the speed of light), the calculated momenta and energies need to be boosted to the lab frame by using a lorentz boost, which is in general direction described as:

$$\vec{x'} = \vec{x} - \frac{(\gamma - 1)}{\beta^2} * (\vec{\beta} * \vec{x}) * \vec{\beta} - \gamma\beta t \quad [208] \tag{A.23}$$

A.8 Track and tracklet resolutions using the Riemann fit method

To estimate the track fitting capability in chapter 6, a simple fitting method was used. Assuming, that the particle's movement in the longitudinal and transverse (with respect to the beamline) plane is independent, the fitting is done separately. A homogeneous field along z is assumed. In the longitudinal plane a straight line fit is performed, using least squares method [209]. In the transverse plane the particle is bent due to the magnetic field and a circle fit based on the Riemann fit method is performed. The Riemann fit method [210] is extremely fast compared to other circle-fitting methods, since it is a non-iterativ method. This is achieved by mapping the measurements of the transverse plane onto a Riemann sphere, which transforms the 2D-circle fit into fitting a plane to the transformed measurements, using least squares method. The implementation follows [210], as described in *section 3*.
To estimate the SM background in section 6.6.3, single electron- and pion-tracklets have been fitted using the Riemann fit. Figure A.26 shows the reconstructed transverse momentum versus

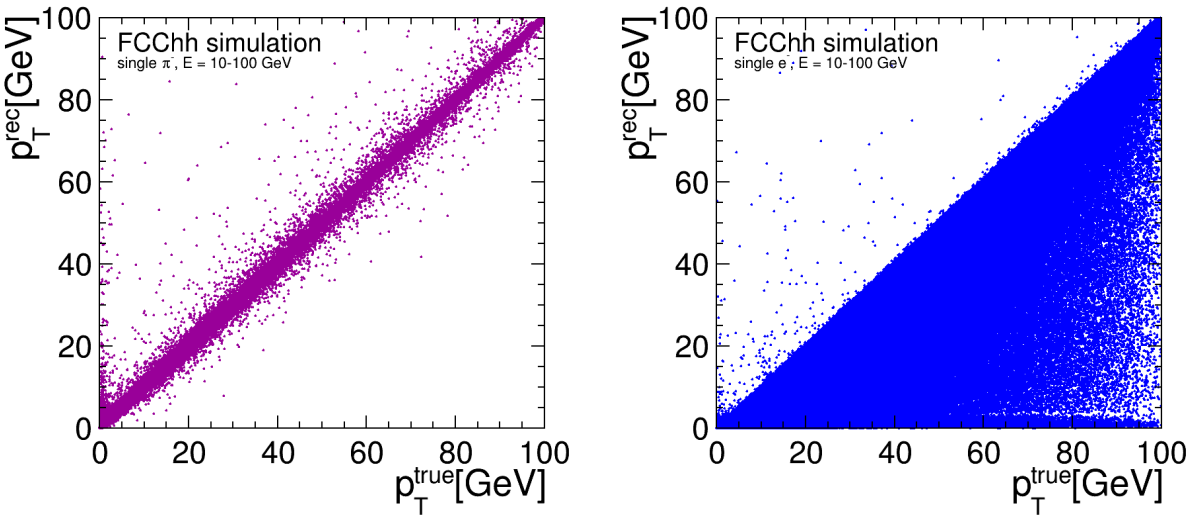

(a) single pions **(b)** single electrons

fig. A.26: Reconstructed versus true transverse momentum for single particles using the Riemann fit method.

the true transverse momentum of pions (left) and electrons (right). Figure A.27 shows $\Delta p_T/p_T$ for the full tracks and for tracklets with four, five and six different layers hit. For the pions the resolution is symmetric. The best value is achieved using all measurements along the track. As expected the resolution worsens with decreasing number of measurements on different layers used. Highly energetic electrons with energies above 1 GeV lose most of their energy via *Bremsstrahlung* (see [124], *chapter 33.4*)). Therefore, a tail due to Bremsstrahlung can be observed in fig. A.27b. The energy loss rate due to Bremsstrahlung $dE/dx \approx E/X_0$ is approximately proportional to the electron's energy and the material crossed. Hence, the tail is more pronounced for highly energetic electrons and for more measurements along the track, while the resolution increases with more measurements.

For all transverse momenta above 100 GeV, single particle resolutions created with a "toy"-model have been used. This toy model randomly creates track parameters (see definition in section 2.3), for tracks contained within the barrel region. It then calculates the positions of the clusters created by those tracks, by determining the intersection of the barrel layers with the circle corresponding to the track in the transverse plane and with the straight line in the r/z plane (see fig. 2.4). To account for the limited tracker resolution and multiple scattering, the cluster positions are smeared with the tracker resolutions plus a 5 µm tolerance, using gaussian random distribution. The received scatter plot of the truth p_T, versus the reconstructed p_T as well as the total relative error are shown in fig. A.28. The resolution is high for lower transverse momenta ($p_T < 50$ GeV) and degrades for higher momenta as shown in fig. A.28a. The fit performs worse using less number hits (see fig. A.28b): the central peaks stems from the particles with lower transverse momentum, while the second offset peaks are due to the high momentum particles. The toy model is very similar to the resolution of the physical particles and hence gives a realistic estimate. Only for very low momenta, the fit might be too optimistic, since the multiple scattering contribution can not be neglected at low momenta. In any case, the toy model resolutions are only used for $p_T > 100$ GeV.

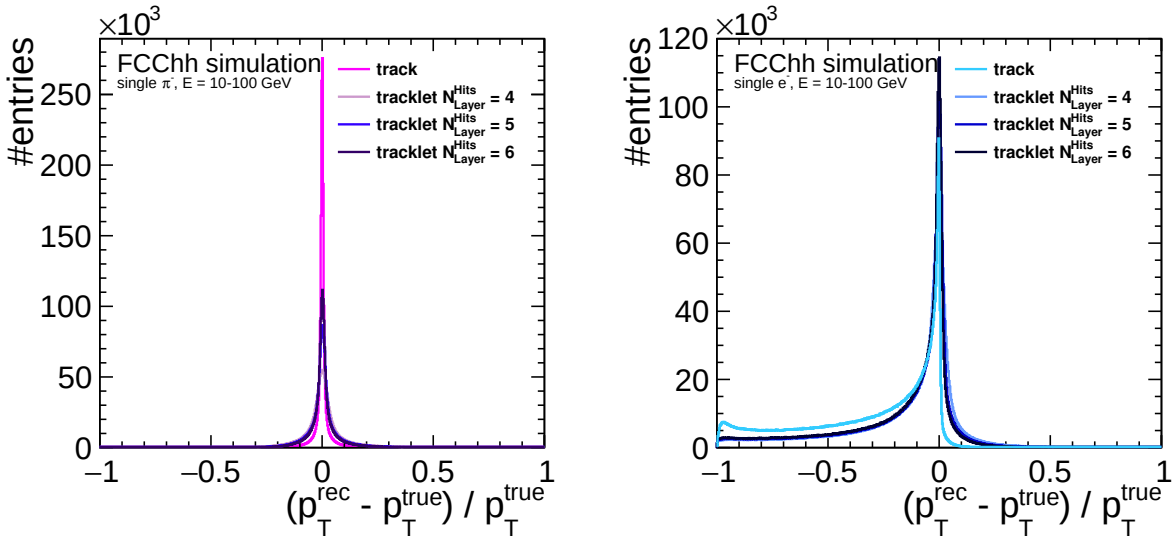

(a) single pions **(b)** single electrons

fig. A.27: Relative error of the reconstructed transverse momentum when using all measurements along the track and using at maximum four, five or six measurements on different layers.

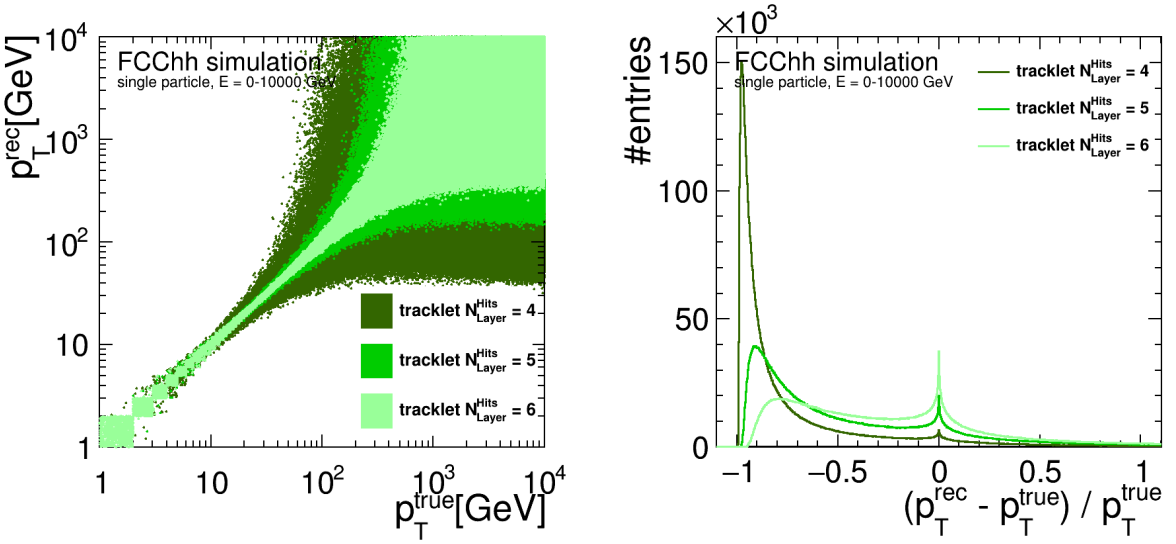

(a) Reconstructed versus true transverse momentum for single particle tracks using the Riemann fit method.

(b) Relative error of the reconstructed transverse momentum when using at maximum four, five or six measurements on different layers.

fig. A.28: Transverse momentum resoultion for single particle tracks. The tracks have been created using a "toy"-model.

A.9 Charginos and background simulation samples of disappearing track study

Since per default BSM-particles are not defined in Geant4 the $\widetilde{\chi}_1^+$,$\widetilde{\chi}_1^-$ and the $\widetilde{\chi}_1^0$ needed to be introduced in FCCSW, following a Geant4 interface class (`G4ParticleDefinition`). Since the masses and lifetimes (and hence the decay width) of those particles are not fixed by theory, they are configurable parameters. Before simulation, a simple python script does a look-up of those parameters in the LHE-file configuration[2] and configures the job via python job-options. Also the physics processes of the charginos had to be defined in Geant4 (the neutralino does not interact with the tracker material). The standard Geant4 multiple scattering and ionization processes, as described in [211] (*chapters 8* and *10*) have been defined for the chargino. In addition, the decay of the charginos always decaying to a neutralino and a charged pion have been introduced. The decay kinematics are described by a phase space decay with isotropic angular distribution in the centre-of-mass frame of the mother (the chargino) and are then boosted into the lab-frame and following the laws as described in appendix A.7. The decay time of the charginos can be configured using the job-options.
In tables A.2 to A.5, the simulation samples used for the disappearing track study in chapter 6 are listed.

SampleID	name	σ[pb]	N^{Events}
550	`mgp8_pp_w0123j_4f_HT_5000_100000`	11.11	889 817
551	`mgp8_pp_w0123j_4f_HT_2000_5000`	273.7	481 090
552	`mgp8_pp_w0123j_4f_HT_1000_2000`	1917	514 471
553	`mgp8_pp_w0123j_4f_HT_500_1000`	1.037×10^4	528 015
554	`mgp8_pp_w0123j_4f_HT_300_500`	2.493×10^4	534 826
555	`mgp8_pp_w0123j_4f_HT_15_300`	8.377×10^4	513 873
556	`mgp8_pp_w0123j_4f_HT_0_150`	1.478×10^6	1 426 809

tab. A.2: Summary of SM W + jets background simulation samples used in section 6.6.3. Samples are taken from v0.2 of the Delphes FCC physics events, generated with madgraph8 [193] and simulated with DELPHES [85, 192]. The samples cover different regions of transverse energies of the partons (HT) from 0 – 100 000 GeV. Cross-section are calculated with madgraph8 at leading order.

A.10 Estimation of probabilities for a chargino to create a tracklet

This section explains how a "toy"-model was used to obtain the rates of charginos surviving until a given layer, used in chapter 6. The probability that a particle, with a mean lifetime of τ and mass M, travels a certain path x is given by

$$P(x) = e^{\frac{Mx}{|p|\tau}} = e^{-\frac{x}{\beta\gamma c\tau}} \tag{A.24}$$

[2] Input files for particle generation, see chapter 6 and [164]

SampleID	name	σ[pb]	N^{Events}
550	mgp8_pp_z0123j_4f_HT_5000_100000	4.196	1 297 409
551	mgp8_pp_z0123j_4f_HT_2000_5000	102.3	485 744
552	mgp8_pp_z0123j_4f_HT_1000_2000	703.8	506 495
553	mgp8_pp_z0123j_4f_HT_500_1000	3756	515 419
554	mgp8_pp_z0123j_4f_HT_300_500	8958	526 584
555	mgp8_pp_z0123j_4f_HT_15_300	2.944×10^4	512 577
556	mgp8_pp_z0123j_4f_HT_0_150	$4.658e \times 10^5$	1 372 327

tab. A.3: Summary of SM Z + jets background simulation samples used in section 6.6.3. Samples are taken from v0.2 of the Delphes FCC physics events, generated with madgraph8 [193] and simulated with DELPHES [85, 192]. The samples cover different regions of transverse energies of the partons (HT) from 0 – 100 000 GeV. Cross-section are calculated with madgraph8 at leading order.

Given the probability, the path a particle can travel can be calculated the following:

$$x(P) = -\beta\gamma c\tau \ln(P) \tag{A.25}$$

Given the momenta of the generated chargino samples (see tables A.4 and A.5) and a randomly drawn probability, the expected path can be evaluated for a given mean decay time. When calculating the path several times, with varying probabilities, the survival distributions as shown in Figure A.29 can be obtained.

A.11 Definitions for hypothesis testing

This section explains in detail the used definitions for hypothesis testing in chapter 6.
The sensitivity of a search for new physics can be obtained by hypothesis testing, estimating the probability that a certain number of signal events could emerge from statistical fluctuations of pure background, which is expressed by the *p-value*. The smaller the p-value (under assumption of the background only hypothesis), the higher is the possible discovery reach, if signal is present. In addition, the significance of the presence of signal can be calculated (see [213], *chapter 39.5*). The probability of the realization of a certain number of events, can be described by the poisson distribution [209]:

$$f(n;\lambda) = \frac{\lambda^n}{n!} e^{-\lambda} \tag{A.26}$$

For a large number of events the poisson distribution can be described by a gaussian distribution with a mean value of λ and a standard deviation of $\sqrt{\lambda}$.

The p-value, can then be calculated the following (see [213], *(39.79)*):

$$p_0 = \Phi\left(\frac{n-b}{\sqrt{b}}\right) \tag{A.27}$$

SampleID	process	mass	σ[pb]
902100	$\tilde{\chi}_1^{\pm}\tilde{\chi}_1^0$	700	$2.670 \times 10^{-01} + 1.722 \times 10^{-01}$
902000	$\tilde{\chi}_1^{\pm}\tilde{\chi}_1^{\mp}$	700	2.190×10^{-01}
902101	$\tilde{\chi}_1^{\pm}\tilde{\chi}_1^0$	800	$1.684 \times 10^{-01} + 1.050 \times 10^{-01}$
902001	$\tilde{\chi}_1^{\pm}\tilde{\chi}_1^{\mp}$	800	1.370×10^{-01}
902102	$\tilde{\chi}_1^{\pm}\tilde{\chi}_1^0$	900	$1.103 \times 10^{-01} + 6.783 \times 10^{-02}$
902002	$\tilde{\chi}_1^{\pm}\tilde{\chi}_1^{\mp}$	800	9.033×10^{-02}
902103	$\tilde{\chi}_1^{\pm}\tilde{\chi}_1^0$	1000	$7.707 \times 10^{-02} + 4.635 \times 10^{-02}$
902003	$\tilde{\chi}_1^{\pm}\tilde{\chi}_1^{\mp}$	1000	6.274×10^{-02}
902104	$\tilde{\chi}_1^{\pm}\tilde{\chi}_1^0$	1100	$5.799 \times 10^{-02} + 3.424 \times 10^{-02}$
902004	$\tilde{\chi}_1^{\pm}\tilde{\chi}_1^{\mp}$	1100	4.598×10^{-02}
902105	$\tilde{\chi}_1^{\pm}\tilde{\chi}_1^0$	1200	$4.261 \times 10^{-02} + 2.477 \times 10^{-02}$
902005	$\tilde{\chi}_1^{\pm}\tilde{\chi}_1^{\mp}$	1200	3.353×10^{-02}
902106	$\tilde{\chi}_1^{\pm}\tilde{\chi}_1^0$	1300	$3.125 \times 10^{-02} + 1.776 \times 10^{-02}$
902006	$\tilde{\chi}_1^{\pm}\tilde{\chi}_1^{\mp}$	1300	2.442×10^{-02}
902107	$\tilde{\chi}_1^{\pm}\tilde{\chi}_1^0$	1400	$2.401 \times 10^{-02} + 1.343 \times 10^{-02}$
902007	$\tilde{\chi}_1^{\pm}\tilde{\chi}_1^{\mp}$	1400	1.859×10^{-02}
902108	$\tilde{\chi}_1^{\pm}\tilde{\chi}_1^0$	1500	$1.885 \times 10^{-02} + 1.033 \times 10^{-02}$
902008	$\tilde{\chi}_1^{\pm}\tilde{\chi}_1^{\mp}$	1500	1.371×10^{-02}
902109	$\tilde{\chi}_1^{\pm}\tilde{\chi}_1^0$	1600	$1.410 \times 10^{-02} + 7.605 \times 10^{-03}$
902009	$\tilde{\chi}_1^{\pm}\tilde{\chi}_1^{\mp}$	1600	1.075×10^{-02}
902110	$\tilde{\chi}_1^{\pm}\tilde{\chi}_1^0$	1700	$1.129 \times 10^{-02} + 5.989 \times 10^{-03}$
902010	$\tilde{\chi}_1^{\pm}\tilde{\chi}_1^{\mp}$	1700	8.552×10^{-03}
902111	$\tilde{\chi}_1^{\pm}\tilde{\chi}_1^0$	1800	$1.015 \times 10^{-02} + 5.281 \times 10^{-03}$
902011	$\tilde{\chi}_1^{\pm}\tilde{\chi}_1^{\mp}$	1800	6.866×10^{-03}
902112	$\tilde{\chi}_1^{\pm}\tilde{\chi}_1^0$	1900	$7.437 \times 10^{-03} + 3.831 \times 10^{-03}$
902012	$\tilde{\chi}_1^{\pm}\tilde{\chi}_1^{\mp}$	1900	5.572×10^{-03}
902113	$\tilde{\chi}_1^{\pm}\tilde{\chi}_1^0$	2000	$6.129 \times 10^{-03} + 3.120 \times 10^{-03}$
902013	$\tilde{\chi}_1^{\pm}\tilde{\chi}_1^{\mp}$	2000	4.563×10^{-03}
902114	$\tilde{\chi}_1^{\pm}\tilde{\chi}_1^0$	2100	$5.499 \times 10^{-03} + 2.763 \times 10^{-03}$
902014	$\tilde{\chi}_1^{\pm}\tilde{\chi}_1^{\mp}$	2100	4.070×10^{-03}
902115	$\tilde{\chi}_1^{\pm}\tilde{\chi}_1^0$	2200	$(4.200 \times 10^{-03} + 4.505 \times 10^{-03})/2 + (2.075 \times 10^{-03} + 2.233 \times 10^{-03})/2$
902015	$\tilde{\chi}_1^{\pm}\tilde{\chi}_1^{\mp}$	2200	$(3.088 \times 10^{-03} + 3.314 \times 10^{-03})/2$
902116	$\tilde{\chi}_1^{\pm}\tilde{\chi}_1^0$	2300	$3.507 \times 10^{-03} + 1.709 \times 10^{-03}$
902016	$\tilde{\chi}_1^{\pm}\tilde{\chi}_1^{\mp}$	2300	2.558×10^{-03}
902117	$\tilde{\chi}_1^{\pm}\tilde{\chi}_1^0$	2400	$2.958 \times 10^{-03} + 1.423 \times 10^{-03}$
902017	$\tilde{\chi}_1^{\pm}\tilde{\chi}_1^{\mp}$	2400	2.142×10^{-03}
902118	$\tilde{\chi}_1^{\pm}\tilde{\chi}_1^0$	2500	$2.647 \times 10^{-03} + 1.261 \times 10^{-03}$
902018	$\tilde{\chi}_1^{\pm}\tilde{\chi}_1^{\mp}$	2500	1.913×10^{-03}
902119	$\tilde{\chi}_1^{\pm}\tilde{\chi}_1^0$	2600	$2.135 \times 10^{-03} + 1.001 \times 10^{-03}$
902019	$\tilde{\chi}_1^{\pm}\tilde{\chi}_1^{\mp}$	2600	1.532×10^{-03}

tab. A.4: Summary I of chargino simulation samples used in chapter 6. The cross sections have been calculated in NLO with by M.Saito using Prospino 2.1 [212] (see [188] for details).

SampleID	process	mass	σ[pb]
902120	$\tilde{\chi}_1^{\pm}\tilde{\chi}_1^0$	2700	$1.972 \times 10^{-03} + 9.116 \times 10^{-04}$
902020	$\tilde{\chi}_1^{\pm}\tilde{\chi}_1^{\mp}$	2700	1.402×10^{-03}
902121	$\tilde{\chi}_1^{\pm}\tilde{\chi}_1^0$	2800	$1.688 \times 10^{-03} + 7.708 \times 10^{-04}$
902021	$\tilde{\chi}_1^{\pm}\tilde{\chi}_1^{\mp}$	2800	1.190×10^{-03}
902122	$\tilde{\chi}_1^{\pm}\tilde{\chi}_1^0$	2900	$1.488 \times 10^{-03} + 6.765 \times 10^{-04}$
902022	$\tilde{\chi}_1^{\pm}\tilde{\chi}_1^{\mp}$	2900	1.055×10^{-03}
902123	$\tilde{\chi}_1^{\pm}\tilde{\chi}_1^0$	3000	$1.230 \times 10^{-03} + 5.502 \times 10^{-04}$
902023	$\tilde{\chi}_1^{\pm}\tilde{\chi}_1^{\mp}$	3000	8.640×10^{-04}
902124	$\tilde{\chi}_1^{\pm}\tilde{\chi}_1^0$	3100	$1.090 \times 10^{-03} + 4.822 \times 10^{-04}$
902024	$\tilde{\chi}_1^{\pm}\tilde{\chi}_1^{\mp}$	3100	7.602×10^{-04}
902125	$\tilde{\chi}_1^{\pm}\tilde{\chi}_1^0$	3200	$9.480 \times 10^{-04} + 4.153 \times 10^{-04}$
902025	$\tilde{\chi}_1^{\pm}\tilde{\chi}_1^{\mp}$	3200	6.587×10^{-04}
902126	$\tilde{\chi}_1^{\pm}\tilde{\chi}_1^0$	3300	$8.016 \times 10^{-04} + 3.460 \times 10^{-04}$
902026	$\tilde{\chi}_1^{\pm}\tilde{\chi}_1^{\mp}$	3300	5.549×10^{-04}
902127	$\tilde{\chi}_1^{\pm}\tilde{\chi}_1^0$	3400	$7.199 \times 10^{-04} + 3.076 \times 10^{-04}$
902027	$\tilde{\chi}_1^{\pm}\tilde{\chi}_1^{\mp}$	3400	4.954×10^{-04}
902128	$\tilde{\chi}_1^{\pm}\tilde{\chi}_1^0$	3500	$6.341 \times 10^{-04} + 2.682 \times 10^{-04}$
902028	$\tilde{\chi}_1^{\pm}\tilde{\chi}_1^{\mp}$	3500	4.351×10^{-04}
902129	$\tilde{\chi}_1^{\pm}\tilde{\chi}_1^0$	3600	$5.610 \times 10^{-04} + 2.349 \times 10^{-04}$
902029	$\tilde{\chi}_1^{\pm}\tilde{\chi}_1^{\mp}$	3600	3.829×10^{-04}
902130	$\tilde{\chi}_1^{\pm}\tilde{\chi}_1^0$	3700	$5.082 \times 10^{-04} + 2.114 \times 10^{-04}$
902030	$\tilde{\chi}_1^{\pm}\tilde{\chi}_1^{\mp}$	3700	3.444×10^{-04}
902131	$\tilde{\chi}_1^{\pm}\tilde{\chi}_1^0$	3800	$4.482 \times 10^{-04} + 1.849 \times 10^{-04}$
902031	$\tilde{\chi}_1^{\pm}\tilde{\chi}_1^{\mp}$	3800	3.029×10^{-04}
902132	$\tilde{\chi}_1^{\pm}\tilde{\chi}_1^0$	3900	$3.939 \times 10^{-04} + 1.605 \times 10^{-04}$
902032	$\tilde{\chi}_1^{\pm}\tilde{\chi}_1^{\mp}$	3900	2.659×10^{-04}
902133	$\tilde{\chi}_1^{\pm}\tilde{\chi}_1^0$	4000	$3.563 \times 10^{-04} + 1.442 \times 10^{-04}$
902033	$\tilde{\chi}_1^{\pm}\tilde{\chi}_1^{\mp}$	4000	2.385×10^{-04}
902134	$\tilde{\chi}_1^{\pm}\tilde{\chi}_1^0$	4100	$3.187 \times 10^{-04} + 1.273 \times 10^{-04}$
902034	$\tilde{\chi}_1^{\pm}\tilde{\chi}_1^{\mp}$	4100	2.127×10^{-04}
902135	$\tilde{\chi}_1^{\pm}\tilde{\chi}_1^0$	4200	$2.861 \times 10^{-04} + 1.130 \times 10^{-04}$
902035	$\tilde{\chi}_1^{\pm}\tilde{\chi}_1^{\mp}$	4200	1.902×10^{-04}
902136	$\tilde{\chi}_1^{\pm}\tilde{\chi}_1^0$	4300	$2.563 \times 10^{-04} + 1.006 \times 10^{-04}$
902036	$\tilde{\chi}_1^{\pm}\tilde{\chi}_1^{\mp}$	4300	1.692×10^{-04}
902137	$\tilde{\chi}_1^{\pm}\tilde{\chi}_1^0$	4400	$2.309 \times 10^{-04} + 8.998 \times 10^{-05}$
902037	$\tilde{\chi}_1^{\pm}\tilde{\chi}_1^{\mp}$	4400	1.522×10^{-04}
902138	$\tilde{\chi}_1^{\pm}\tilde{\chi}_1^0$	4500	$2.086 \times 10^{-04} + 8.034 \times 10^{-05}$
902038	$\tilde{\chi}_1^{\pm}\tilde{\chi}_1^{\mp}$	4500	1.367×10^{-04}
902139	$\tilde{\chi}_1^{\pm}\tilde{\chi}_1^0$	4600	$1.876 \times 10^{-04} + 7.196 \times 10^{-05}$
902039	$\tilde{\chi}_1^{\pm}\tilde{\chi}_1^{\mp}$	4600	1.229×10^{-04}

tab. A.5: Summary II of chargino simulation samples used in chapter 6. The cross sections have been calculated in NLO with by M.Saito using Prospino 2.1 [212] (see [188] for details).

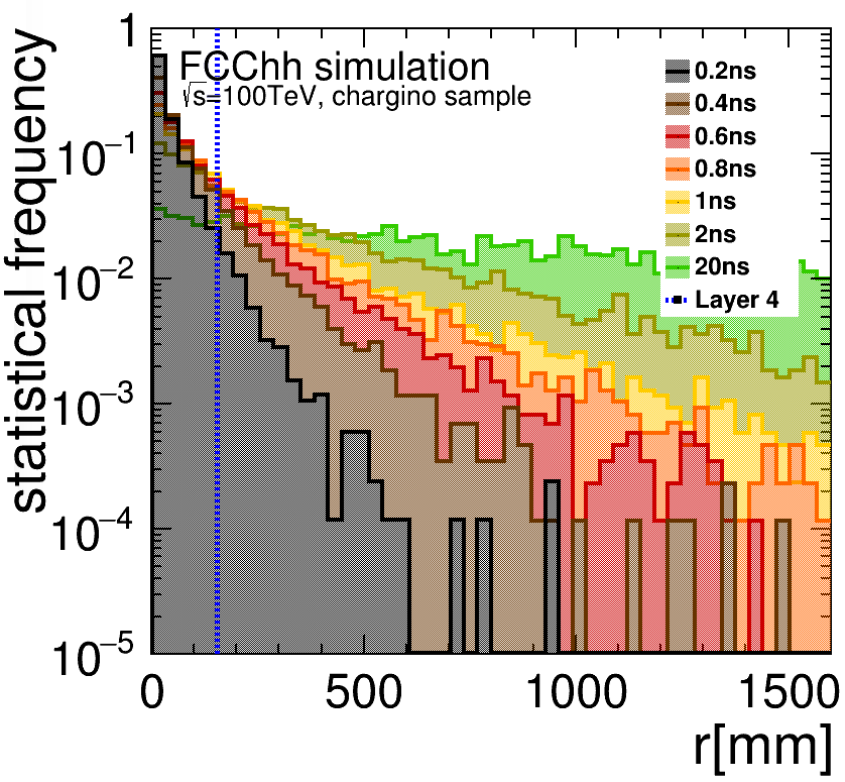

fig. A.29: Statistical frequency of charginos surviving a certain path in radial direction, for different decay times.

with Φ being the standard gaussian cumulative distribution. The corresponding significance is defined the following (see [213], *(39.79-39.80)*):

$$Z_0 = \Phi^{-1}(1 - p_0) = (n - b)/\sqrt{b} \tag{A.28}$$

A.11.1 Goodness of fit

To test the goodness of fit of the randomly generated tracklets, for emulation of the combinatorial background in section 6.7.1, the method of least squares [213] was used to calculate the χ^2. Correlations between the parameters and the uncertainty of the track parameters have not been taken into account and the χ^2 is calculated the following (see [213]):

$$\chi^2 = \Sigma_{i=1}^{N} = \frac{(x_{track} - x_{measurement})^2}{\sigma_x} \tag{A.29}$$

for each measurement position on a layer. The measurements are gaussian distributed with a mean of $x_{measurement}$ and a standard deviation of σ_x. The total χ^2 was calculated as the sum of the three values obtained separately for x, y and z. The smaller the value for the χ^2, the better the fit. For σ_x the squared layer resolutions have been used. Finally, the probability that the observed χ^2 should be less than the observed value, assuming a correct model, is calculated using the χ^2 distribution [213]. The cut is passed only, if this probability is less than 5 %. The test shows how well the track fit conforms with the actual measurements.

Appendix B

Definitions and acronyms

For clarity, specific definitions and acronyms used in this thesis are listed in the following. The descriptions are specific, as used in the context of this thesis and might not be generally applicable.

Acts
: A common tracking software - a general tracking software toolkit co-developed and used in the context of this thesis.

boosted particle
: Particle with high momentum to lab frame.

BSM
: Short for Beyond the Standard Model physics.

chargino
: Hypothetical *charged* particles of SUSY, possibly arising from mixed degrees of freedom of gaugino and higgsino.

cluster/measurement
: Neighbouring, activated pixels form a cluster, which is the readout measurement of the tracking detector.

cluster size
: Number of channels contributing to one cluster.

clusterization
: Part of track reconstruction. Clusters neighbouring activated detector channels to form a measurement, using pattern recognition algorithms.

DD4hep
: Detector Description for high energy physics - a general detector geometry description package used for the FCC study.

digitization
: Part of simulation. Emulates the detector response, when a particle passes through material. Depends on detector technology.

electronweakinos
: Hypothetical particles of SUSY, possibly arising from mixed degrees of freedom of gaugino and higgsino. General term for neutralinos and charginos.

E_T^{miss}
: Missing transverse energy, which is defined as $E_T^{miss} = -\sum p_T$ of all measured particles, following the law of transverse momentum conservation at a collider experiment, which should be zero in total.

η
: The pseudorapidity given by $-\ln\tan(\frac{\vartheta}{2})$, which is invariant under lorentz-boost along the beam-axis.

event
: A physics event in high energy physics refers to a particle collision at a particle collider and its subsequently produced particles.

fakes/fake tracks
: Tracks formed by a random combination of hits, without any physical meaning.

FCC-hh
: Short for the hadron-hadron (proton-proton) collider option of the FCC study.

FCCSW
: The FCC software package - co-developed and used in the context of this thesis.

gauginos
: The supersymmetric partners of the gauge bosons.

generated particles/primary particles
: Input particles from event generator.

HL-LHC
: Short for High Luminosity LHC, with planned operation after 2025.

higgsino
: The supersymmetric partner of the Higgs-boson.

integrated luminosity
: The luminosity integrated over time.

ISR-jet
: Jet resulting fro initial state radiation.

jet
: A dense region of particle tracks, stemming from hadronization processes.

jet clustering
: Jet reconstruction method, which bundles all particles/clusters belonging to the same jet, using an algorithm.

L_0
: The nuclear interaction length, which is a material specific parameter.

leading jet
: Jet with highest transverse momentum.

longitudinal axis
: The axis along the beamline of the detector.

LSP
Short for Lightest Supersymmetric Particle.

luminosity
Quantifies the possible number of collisions per cm^2 and second.

MC
Short for Monte Carlo methods used for particle generation and simulation.

merged cluster
If two clusters are next to each other, they merge to one cluster.

$\langle\mu\rangle$
Average number of simultaneous proton-proton collisions per bunch crossing (pile-up).

neutralino
Hypothetical *neutralino* particles of SUSY, possibly arising from mixed degrees of freedom of gaugino and higgsino.

Phase-II upgrade
Detector upgrades for the High Luminosity LHC.

parton
The hypothetical protons constituents are called partons.

passive detector part/material
Part of the detector, which does not do the measurement. It is usually support material or material needed for e.g. cooling. Opposite to sensitive detector material.

φ
The polar angle, which is the angle in x/y plane, transverse to the beam-axis.

pile-up/PU
Number of simultaneous proton-proton collisions per bunch crossing.

p_T
The transverse component of the particle momentum.

QCD
Short for quantum chromodynamics.

secondary particles/secondaries
Particles produced during simulation through interaction with the detector.

sensitive detector part/material
Part of the detector, which is sensitive to the passage of particles, i.e. where the particle passage is measured. Opposite to passive detector material.

shared cluster
When more than one particle contributes to the same cluster, the cluster is "shared".

soft particle/soft p_T-spectrum
Particles with low transverse momentum are called "soft".

SM
Short for the Standard Model of particle physics.

SUSY
Short for Supersymmetry, which are theoretical supersymmetric extension of the Standard Model.

ϑ
The azimuth angle, which is the angle in the r/z plane with the beampipe along the z-axis. The angle opens from the positive z-axis.

tracklet
A tracklet is a short track. It arises, when a particle only passes a few detection layers.

transverse plane
The plane transverse to the the beamline of the detector.

truth jets
Jets obtained by clustering generated particles, describing true location and spread of jet most accurately.

WIMP
Short for Weakly Interacting Massive Particles, which are dark matter candidates.

underlying event
Soft part of hard scatter of two protons.

wino
The supersymmetric partner of the W-boson.

X_0
The radiation length, which is a material specific parameter.

Bibliography

[1] Oscar Barbalat. Applications of particle accelerators; rev. version. (CERN-AC-93-04-BLIT-REV):23 p, Feb 1994. URL https://cds.cern.ch/record/260280.

[2] Paul Langacker. *The standard model and beyond*. Series in High Energy Physics, Cosmology and Gravitation. Taylor and Francis, Boca Raton, FL, 2010. URL https://cds.cern.ch/record/1226768.

[3] A. Einstein. Ist die Trägheit eines Körpers von seinem Energieinhalt abhängig? (Annalen der Physik. Band 323, Nr. 13):639–643, 1905. URL http://myweb.rz.uni-augsburg.de/~eckern/adp/history/einstein-papers/1905_18_639-641.pdf.

[4] M. Tanabashi et al. (Particle Data Group). Big-Bang Cosmology. *Phys. Rev. D 98*, (030001 (2018)), . Revised September 2017 by K.A. Olive (University of Minnesota) and J.A. Peacock (University of Edinburgh).

[5] A. P. Chernyaev and S. M. Varzar. Particle accelerators in modern world. *Physics of Atomic Nuclei*, 77(10):1203–1215, Oct 2014. ISSN 1562-692X. doi: 10.1134/S1063778814100032. URL https://doi.org/10.1134/S1063778814100032.

[6] CERN. Applications of CERN Technologies in Society. (online compilation). URL https://kt.cern/cern-technologies-society.

[7] Massimo Florio and Stefano Forte and Emanuela Sirtori. Forecasting the Socio-Economic Impact of the Large Hadron Collider: a Cost-Benefit Analysis to 2025 and Beyond. 2016. doi: 10.1016/j.techfore.2016.03.007.

[8] E Chesta, F Caspers, W Wuensch, S Sgobba, T Stora, P Chiggiato, and M Taborelli. Overview of CERN Technology Transfer Strategy and Accelerator-Related Activities. (CERN-ACC-2013-0199):3 p, May 2013. URL http://cds.cern.ch/record/1595493.

[9] The Large Hadron Collider. Jan 2014. URL https://cds.cern.ch/record/1998498.

[10] The official CERN website, 2019. URL https://home.cern.

[11] The ATLAS Collaboration. The ATLAS Experiment at the CERN Large Hadron Collider. *Journal of Instrumentation*, 3(08):S08003, 2008. URL http://stacks.iop.org/1748-0221/3/i=08/a=S08003.

[12] The CMS Collaboration. The CMS experiment at the CERN LHC. The Compact Muon Solenoid experiment. *JINST*, 3:S08004. 361 p, 2008. URL https://cds.cern.ch/record/1129810. Also published by CERN Geneva in 2010.

[13] The LHCb Collaboration. The LHCb Detector at the LHC. *JINST*, 3(LHCb-DP-2008-001. CERN-LHCb-DP-2008-001):S08005, 2008. URL https://cds.cern.ch/record/1129809. Also published by CERN Geneva in 2010.

[14] The ALICE Collaboration. The ALICE experiment at the CERN LHC. A Large Ion Collider Experiment. *JINST*, 3:S08002. 259 p, 2008. URL https://cds.cern.ch/record/1129812. Also published by CERN Geneva in 2010.

[15] R Mankel. Pattern recognition and event reconstruction in particle physics experiments. *Reports on Progress in Physics*, 67(4):553, 2004. URL http://stacks.iop.org/0034-4885/67/i=4/a=R03.

[16] Claus Grupen, Armin Böhrer, and Ludek Smolik. *Particle detectors*. Cambridge monographs on particle physics, nuclear physics, and cosmology. Cambridge Univ. Press, Cambridge, 1996. URL https://cds.cern.ch/record/306826.

[17] C. Patrignani et al. (Particle Data Group). Particle Detectors at Accelerators. *Chin. Phys. C ,40*, (100001 (2016) and 2017 update), . Revised 2017.

[18] Roderik Bruce, Gianluigi Arduini, Hannes Bartosik, Riccardo De Maria, Massimo Giovannozzi, Giovanni Iadarola, John Jowett, Kevin Shing Bruce Li, Mike Lamont, Anton Lechner, Elias Metral, Daniele Mirarchi, Tatiana Pieloni, Stefano Redaelli, Giovanni Rumolo, Benoit Salvant, Rogelio Tomas Garcia, and Jorg Wenninger. LHC Run 2: Results and challenges. (CERN-ACC-2016-0103):MOAM5P50. 7 p, Jul 2016. URL http://cds.cern.ch/record/2201447.

[19] Oliver Sim Brüning, Paul Collier, P Lebrun, Stephen Myers, Ranko Ostojic, John Poole, and Paul Proudlock. *LHC Design Report*. CERN Yellow Reports: Monographs. CERN, Geneva, 2004. URL https://cds.cern.ch/record/782076.

[20] The ATLAS Collaboration. Observation of a new particle in the search for the Standard Model Higgs boson with the ATLAS detector at the LHC. 2012. doi: 10.1016/j.physletb.2012.08.020.

[21] The CMS Collaboration. Observation of a new boson at a mass of 125 GeV with the CMS experiment at the LHC. 2012. doi: 10.1016/j.physletb.2012.08.021.

[22] F. Englert and R. Brout. Broken Symmetry and the Mass of Gauge Vector Mesons. *Phys. Rev. Lett.*, 13:321–323, Aug 1964. doi: 10.1103/PhysRevLett.13.321. URL https://link.aps.org/doi/10.1103/PhysRevLett.13.321.

[23] G. S. Guralnik, C. R. Hagen, and T. W. B. Kibble. Global Conservation Laws and Massless Particles. *Phys. Rev. Lett.*, 13:585–587, Nov 1964. doi: 10.1103/PhysRevLett.13.585. URL https://link.aps.org/doi/10.1103/PhysRevLett.13.585.

[24] M. Tanabashi et al. (Particle Data Group). Accelerator Physics of Colliders. *Phys. Rev. D 98*, (030001 (2018)), . Revised March 2018 by M.J. Syphers (NIU/FNAL) and F. Zimmermann (CERN).

[25] Rende Steerenberg. LHC Report: Another run is over and LS2 has just begun. December 2018. URL https://home.cern/news/news/accelerators/lhc-report-another-run-over-and-ls2-has-just-begun.

[26] Eckhard Elsen and Frédérick Bordry. A successful conclusion to Run 2. December 2018. URL https://home.cern/news/opinion/accelerators/successful-conclusion-run-2.

[27] The ATLAS collaboration. Measurement of the W-boson mass in pp collisions at $\sqrt{s} = 7$ TeV with the ATLAS detector. *The European Physical Journal C*, 78(2):110, Feb 2018. ISSN 1434-6052. doi: 10.1140/epjc/s10052-017-5475-4. URL `https://doi.org/10.1140/epjc/s10052-017-5475-4`.

[28] The CMS Collaboration. Measurement of the top quark mass in the all-jets final state at $\sqrt{s} = 13$ TeV and combination with the lepton+jets channel. Technical Report arXiv:1812.10534. CMS-TOP-17-008-003, CERN, Geneva, Dec 2018. URL `https://cds.cern.ch/record/2652747`. * Temporary entry *.

[29] ATLAS and CMS Collaborations. Combined Measurement of the Higgs Boson Mass in pp Collisions at $\sqrt{s} = 7$ and 8 TeV with the ATLAS and CMS Experiments. 2015. doi: 10.1103/PhysRevLett.114.191803.

[30] M. Tanabashi et al. (Particle Data Group). Status of Higgs Boson Physics. *Phys. Rev. D 98*, (030001 (2018)), . Revised September 2017 by M. Carena (Fermi National Accelerator Laboratory and the University of Chicago), C. Grojean (DESY, Hamburg, and Humboldt University, Berlin), M. Kado (Laboratoire de l'Accélérateur Linéaire, Orsay), and V. Sharma (University of California, San Diego).

[31] The CMS Collaboration. Observation of $t\bar{t}H$ Production. *Phys. Rev. Lett.*, 120:231801, Jun 2018. doi: 10.1103/PhysRevLett.120.231801. URL `https://link.aps.org/doi/10.1103/PhysRevLett.120.231801`.

[32] ATLAS Collaboration. Observation of Higgs boson production in association with a top quark pair at the LHC with the ATLAS detector. 2018. doi: 10.1016/j.physletb.2018.07.035.

[33] ATLAS Collaboration. Observation of $H \to b\bar{b}$ decays and VH production with the ATLAS detector. 2018. doi: 10.1016/j.physletb.2018.09.013.

[34] ATLAS Collaboration. Cross-section measurements of the Higgs boson decaying into a pair of tau-leptons in proton-proton collisions at $\sqrt{s} = 13$ TeV with the ATLAS detector, 2018.

[35] CMS Collaboration. Observation of the Higgs boson decay to a pair of tau leptons with the CMS detector. 2017. doi: 10.1016/j.physletb.2018.02.004.

[36] Giuseppe Degrassi, Stefano Di Vita, Joan Elias-Miró, José R. Espinosa, Gian F. Giudice, Gino Isidori, and Alessandro Strumia. Higgs mass and vacuum stability in the Standard Model at NNLO. *arXiv:1205.6497*, 2012. doi: 10.1007/JHEP08(2012)098.

[37] M. Tanabashi et al. (Particle Data Group). Dark Matter. *Phys. Rev. D 98*, (030001 (2018)), . Revised September 2017 by M. Drees (Bonn University) and G. Gerbier (Queen's University, Canada).

[38] M. Tanabashi et al. (Particle Data Group). Neutrino Masses, Mixing, and Oscillations. *Phys. Rev. D 98*, (030001 (2018)), . Updated November 2017 by K. Nakamura (Kavli IPMU (WPI), U. Tokyo, KEK), and S.T. Petcov (SISSA/INFN Trieste, Kavli IPMU (WPI), U. Tokyo, Bulgarian Academy of Sciences).

[39] Gian F. Giudice. Naturalness after LHC8. *arXiv:1307.7879*, 2013.

[40] M. Tanabashi et al. (Particle Data Group). 109. Supersymmetry, part I (theory). *Phys. Rev. D 98*, (030001 (2018)), . Revised September 2017 by Howard E. Haber (UC Santa Cruz).

[41] Diogo Buarque Franzosi, Giacomo Cacciapaglia, Haiying Cai, Aldo Deandrea, and Mads Frandsen. Vector and axial-vector resonances in composite models of the higgs boson. *Journal of High Energy Physics*, 2016(11):76, Nov 2016. ISSN 1029-8479. doi: 10.1007/JHEP11(2016)076. URL https://doi.org/10.1007/JHEP11(2016)076.

[42] Johannes Erdmann. Beyond Standard Model searches by ATLAS and CMS. Technical Report ATL-PHYS-PROC-2018-185, CERN, Geneva, Dec 2018. URL https://cds.cern.ch/record/2649929.

[43] H. S. Bawa. Recent results from Beyond Standard Model (BSM) searches at LHC. Technical Report ATL-PHYS-PROC-2018-160, Department of Physics, California State University Fresno, USA-93740, Nov 2018. URL http://cds.cern.ch/record/2647217.

[44] Apollinari G., Béjar Alonso I., Brüning O., Fessia P., Lamont M., Rossi L., and Tavian L. *High-Luminosity Large Hadron Collider (HL-LHC): Technical Design Report V. 0.1*. CERN Yellow Reports: Monographs. CERN, Geneva, 2017. URL http://cds.cern.ch/record/2284929.

[45] Burkhard Schmidt. The High-Luminosity upgrade of the LHC: Physics and Technology Challenges for the Accelerator and the Experiments. *J. Phys.: Conf. Ser.*, 706(2):022002. 42 p, 2016. URL https://cds.cern.ch/record/2263093.

[46] S. F. King. Neutrino Mass Models. 2003. doi: 10.1088/0034-4885/67/2/R01.

[47] P. J. Fox R. Torre K. A. Ulmer X. Cid Vidal, M. D'Onofrio. Beyond the Standard Model Physics at the HL-LHC and HE-LHC. Technical Report arXiv:1812.07831, CERN, Geneva, 2018. URL http://cds.cern.ch/record/2650173.

[48] P.Nason A.Tricoli D.Zeppenfeld et al. P.Azzi, S.Farry. Standard Model Physics at the HL-LHC and HE-LHC. Technical Report arXiv:1902.04070, CERN, Geneva, 2018. URL https://cds.cern.ch/record/2650160.

[49] Michael Benedikt, Alain Blondel, Olivier Brunner, Mar Capeans Garrido, Francesco Cerutti, Johannes Gutleber, Brennan Goddard, Patrick Janot, Jose Miguel Jimenez, Max Klein, Daniel Schulte, Michelangelo Mangano, Attilio Milanese, Volker Mertens, Katsunobu Oide, John Andrew Osborne, Thomas Otto, Yannis Papaphilippou, John Poole, Werner Riegler, Laurent Jean Tavian, Davide Tommasini, and Frank Zimmermann. Future Circular Collider - European Strategy Update Documents. Technical Report CERN-ACC-2019-0007, CERN, Geneva, Jan 2019. URL https://cds.cern.ch/record/2653673.

[50] The official Future Cirular Collider (FCC) conceptual design report (CDR) homepage, 2019. URL https://fcc-cdr.web.cern.ch/.

[51] Michelangelo Mangano, Patrizia Azzi, Michael Benedikt, Alain Blondel, Daniel Andreas Britzger, Andrea Dainese, Mogens Dam, Jorge de Blas, David Enterria, Oliver Fischer, Christophe Grojean, Johannes Gutleber, Claire Gwenlan, Clement Helsens, Patrick Janot, Max Klein, Uta Klein, Matthew Philip Mccullough, Stephane Monteil, John Poole, Michael Ramsey-Musolf, Christian Schwanenberger, Michele Selvaggi, Frank Zimmermann, and Tevong You. Future Circular Collider - FCC Physics Opportunities. Technical Report CERN-ACC-2018-0056, CERN, Geneva, Dec 2018. URL https://cds.cern.ch/record/2651294. Submitted for publication to Eur. Phys. J. C.

[52] Michael Benedikt, Mar Capeans Garrido, Francesco Cerutti, Brennan Goddard, Johannes Gutleber, Jose Miguel Jimenez, Michelangelo Mangano, Volker Mertens, John Andrew Osborne, Thomas Otto, John Poole, Werner Riegler, Daniel Schulte, Laurent Jean Tavian, Davide Tommasini, and Frank Zimmermann. Future Circular Collider, Volume 3 - The Hadron Collider (FCC-hh). Technical Report CERN-ACC-2018-0058, CERN, Geneva, Dec 2018. URL `https://cds.cern.ch/record/2651300`. Submitted for publication to Eur. Phys. J. ST.

[53] ATLAS Phase-II Upgrade Scoping Document. Technical Report CERN-LHCC-2015-020. LHCC-G-166, CERN, Geneva, Sep 2015. URL `https://cds.cern.ch/record/2055248`.

[54] A.J. Barr, C.G. Lester, Michael Andrew Parker, B.C. Allanach, and P. Richardson. Discovering anomaly-mediated supersymmetry at the LHC. Technical Report hep-ph/0208214. ATLAS-COM-PHYS-2002-034. CAVENDISH-HEP-2002-11. CERN-TH-2002-190. hep-ph/0208214, Cavendish Lab. High Energy Phys. Group, Cambridge, Aug 2002. URL `http://cds.cern.ch/record/577789`.

[55] H. Damerau A. Funken B. Goddard A. M. Lombardi D. Manglunki S. Mataguez M. Meddahi B. Mikulec G. Rumolo R. Scrivens E. Shaposhnikova M. Vretenar K. Hanke, J. Coupard. THE LHC INJECTORS UPGRADE (LIU) PROJECT AT CERN: PROTON INJECTOR CHAIN. Technical Report Proceedings of IPAC2017, Copenhagen, Denmark, CERN, Geneva, 2017. URL `http://accelconf.web.cern.ch/AccelConf/ipac2017/papers/wepva036.pdf`.

[56] Michelangelo Mangano. *Physics at the FCC-hh, a 100 TeV pp collider*. CERN Yellow Reports: Monographs. CERN, Geneva, 2017. URL `https://cds.cern.ch/record/2270978`.

[57] Helen Brooks and Peter Skands. Average Event Properties from LHC to FCC-hh. 2018. doi: 10.1140/epjc/s10052-018-6460-2.

[58] E. Fretwurst, G. Lindstrom, J. Stahl, and I. Pintilie. Radiation damage in silicon detectors caused by hadronic and electromagnetic irradiation. In *Radiation effects on semiconductor materials, detectors and devices. Proceedings, 4th International Conference, RESMDD'02, Florence, Italy, July 10-12, 2002*, 2002.

[59] J (CERN) Chistiansen and M (LBNL) Garcia-Sciveres. RD Collaboration Proposal: Development of pixel readout integrated circuits for extreme rate and radiation. Technical Report CERN-LHCC-2013-008. LHCC-P-006, CERN, Geneva, Jun 2013. URL `https://cds.cern.ch/record/1553467`. The authors are editors on behalf of the participating institutes. the participating institutes are listed in the proposal.

[60] F. Arteche Gonzalez, N. Bacchetta, M. Barbero, T. Benka, G. Bilei, G. Calderini, D. Christian, J. Christiansen, L. Demaria, M. Garcia-Sciveres, A. Grillo, M. Havranek, M. Karagounis, R. Kluit, H. Krueger, J. Leveque, V. Liberali, F. Loddo, A. Lounis, C. Munoz, F. Palla, P. Placidi, M. Prydderch, V. Re, S. Seidel, and B. Stugu. Extension of RD53. Technical Report CERN-LHCC-2018-028. LHCC-SR-008, CERN, Geneva, Sep 2018. URL `http://cds.cern.ch/record/2637453`.

[61] Wolfgang Demtroeder. *Experimentalphysik 2: Elektrizität und Optik*. ISBN 3-540-20210-2 3. Auflage. Springer-Verlag Berlin Heidelberg New York, 2004. chapter 3.3.

[62] Zbynek Drasal. Status & Challenges of Tracker Design for FCC-hh. *PoS*, Vertex 2017:030. 10 p, 2018. doi: 10.22323/1.309.0030. URL http://cds.cern.ch/record/2674721.

[63] J. Hrdinka E. Perez V. Volkl Z. Drasal, W. Fawcett. An FCC-hh CDR Chapter on Vertex and Tracker Detector. Technical report, CERN, Geneva. unpublished.

[64] Zbynek Drasal and Werner Riegler. An extension of the Gluckstern formulas for multiple scattering: analytic expressions for track parameter resolution using optimum weights. 2018. doi: 10.1016/j.nima.2018.08.078.

[65] R.L. Gluckstern. Uncertainties in track momentum and direction, due to multiple scattering and measurement errors. *Nuclear Instruments and Methods*, 24:381 – 389, 1963. ISSN 0029-554X. doi: https://doi.org/10.1016/0029-554X(63)90347-1. URL http://www.sciencedirect.com/science/article/pii/0029554X63903471.

[66] E-J Buis, R. J. Dankers, S. Haywood, and A. Reichold. Parameterisation of the Inner Detector Performance. 1997.

[67] Z. Drasal. The Basics of Tracking Formalism by GLS Method: An Application to Optimal Design of Tracking Detectors. Technical report, CERN, Geneva, 2018.

[68] CMS Collaboration. The Phase-2 Upgrade of the CMS Tracker. Technical Report CERN-LHCC-2017-009. CMS-TDR-014, CERN, Geneva, June 2017. URL http://cds.cern.ch/record/2272264.

[69] Aranzazu Ruiz-Martinez and ATLAS Collaboration. The Run-2 ATLAS Trigger System. Technical Report ATL-DAQ-PROC-2016-003, CERN, Geneva, Feb 2016. URL https://cds.cern.ch/record/2133909.

[70] The CMS Collaboration. The CMS trigger system. The CMS trigger system. *JINST*, 12 (CMS-TRG-12-001. 01):P01020. 122 p, Sep 2016. URL https://cds.cern.ch/record/2212926. Replaced with the published version. Added the journal reference and DOI. All the figures and tables can be found at http://cms-results.web.cern.ch/cms-results/public-results/publications/TRG-12-001/index.html.

[71] Mark Peter Whitehead. The upgrade of the LHCb trigger for Run III. Jul 2017. URL https://cds.cern.ch/record/2274115.

[72] ATLAS Collaboration. Technical Design Report for the Phase-II Upgrade of the ATLAS TDAQ System. Technical Report CERN-LHCC-2017-020. ATLAS-TDR-029, CERN, Geneva, Sep 2017. URL https://cds.cern.ch/record/2285584.

[73] CMS Collaboration. The Phase-2 Upgrade of the CMS L1 Trigger Interim Technical Design Report. Technical Report CERN-LHCC-2017-013. CMS-TDR-017, CERN, Geneva, Sep 2017. URL https://cds.cern.ch/record/2283192. This is the CMS Interim TDR devoted to the upgrade of the CMS L1 trigger in view of the HL-LHC running, as approved by the LHCC.

[74] William James Fawcett, Anna Sfyrla, and Giuseppe Iacobucci. A self-seeded track trigger for the FCC-hh. Technical Report CERN-ACC-2018-0046, CERN, Geneva, Oct 2018. URL https://cds.cern.ch/record/2645273.

[75] M (CERN) Aleksa, W (Pittsburgh) Cleland, Y (Tokyo) Enari, M (Victoria) Fincke-Keeler, L (CERN) Hervas, F (BNL) Lanni, S (Oregon) Majewski, C (Victoria) Marino, and I (LAPP) Wingerter-Seez. ATLAS Liquid Argon Calorimeter Phase-I Upgrade Technical Design Report. Technical Report CERN-LHCC-2013-017. ATLAS-TDR-022, Sep 2013. URL `https://cds.cern.ch/record/1602230`. Final version presented to December 2013 LHCC.

[76] C. Neubüser. Performance Studies and Requirements on the Calorimeters for a FCC-hh Experiment. *Springer Proc. Phys.*, 213:37–43, 2018. doi: 10.1007/978-981-13-1316-5_7.

[77] J. Faltova. Design and performance studies of a hadronic calorimeter for a FCC-hh experiment. *JINST*, 13(03):C03016, 2018. doi: 10.1088/1748-0221/13/03/C03016.

[78] Ana Maria Henriques Correia. The ATLAS Tile Calorimeter. Technical Report ATL-TILECAL-PROC-2015-002, CERN, Geneva, Mar 2015. URL `https://cds.cern.ch/record/2004868`.

[79] ATLAS Collaboration. Topological cell clustering in the atlas calorimeters and its performance in lhc run 1. 2016. doi: 10.1140/epjc/s10052-017-5004-5.

[80] Electron and photon reconstruction and performance in ATLAS using a dynamical, topological cell clustering-based approach. Technical Report ATL-PHYS-PUB-2017-022, CERN, Geneva, Dec 2017. URL `https://cds.cern.ch/record/2298955`.

[81] Arabella Martelli. The CMS HGCAL detector for HL-LHC upgrade, 2017.

[82] H. Kroha, R. Fakhrutdinov, O. Kortner, A. Kozhin, K. Schmidt-Sommerfeld, and E. Takasugi. New High-Precision Drift-Tube Detectors for the ATLAS Muon Spectrometer. 2017. doi: 10.1088/1748-0221/12/06/C06007.

[83] Nicholas Metropolis and S. Ulam. The Monte Carlo Method. *Journal of the American Statistical Association*, 44(247):335–341, 1949. doi: 10.1080/01621459.1949.10483310. URL `https://www.tandfonline.com/doi/abs/10.1080/01621459.1949.10483310`. PMID: 18139350.

[84] Z. Drasal et al. Official FCC-hh tracker layout repository: Tracker in tilted configuration - v4.01, 2017. URL `http://fcc-tklayout.web.cern.ch/fcc-tklayout/FCChh_v4.01/index.html`.

[85] J. de Favereau, C. Delaere, P. Demin, A. Giammanco, V. Lemaître, A. Mertens, and M. Selvaggi. DELPHES 3, A modular framework for fast simulation of a generic collider experiment. 2013. doi: 10.1007/JHEP02(2014)057.

[86] A Clark, M Elsing, N Hessey, P Mättig, N Styles, P Wells, S Burdin, T Cornelissen, T Todorov, P Vankov, I Watson, and S Wenig. Final Report: ATLAS Phase-2 Tracker Upgrade Layout Task Force. Technical Report ATL-UPGRADE-PUB-2012-004, CERN, Geneva, Oct 2012. URL `https://cds.cern.ch/record/1482960`.

[87] D Contardo, M Klute, J Mans, L Silvestris, and J Butler. Technical Proposal for the Phase-II Upgrade of the CMS Detector. Technical Report CERN-LHCC-2015-010. LHCC-P-008. CMS-TDR-15-02, Geneva, Jun 2015. URL `https://cds.cern.ch/record/2020886`.

[88] J. Hrdinka. A coherent framework for full, fast and parametric detector simulation for the FCC project. Technical Report CERN-LHCC-2015-020. LHCC-G-166, Technische Universität Wien | Fakultät für Physik | Atominstitut | E141, Wien, Techn. Univ., Dipl.-Arb., 2015, 2015. URL http://katalog.ub.tuwien.ac.at/AC12652767.

[89] Bjarne Stroustrup. *The C++ Programming Language (Third ed.)*. Number 1. 1997.

[90] The C++ programming language, 2019. URL http://www.cplusplus.com/doc/tutorial/.

[91] Z. Drasal B. Hegner C Helsens J. Hrdinka J. Lingemann A. Robson A. Salzburger V. Volkl C. Bernet, A. Dell'Acqua and A. Zaborowska. The FCC Software: how to keep software experiment independent.

[92] Julia Hrdinka, Anna Zaborowska, Andreas Salzburger, and Benedikt Hegner. Prototyping a coherent framework for full, fast and parameteric detector simulation for the FCC project. Prototyping a coherent framework for full, fast and. *PoS*, EPS-HEP2015:248, 2015. URL https://cds.cern.ch/record/2159230.

[93] G. Barrand et al. GAUDI - A software architecture and framework for building HEP data processing applications. *Comput. Phys. Commun.*, 140:45–55, 2001. doi: 10.1016/S0010-4655(01)00254-5.

[94] The python programming language, 2019. URL https://www.python.org.

[95] GaudiHive: Concurrent Framework Project (CF4Hep), 2019. URL http://concurrency.web.cern.ch/GaudiHive.

[96] F Gaede, B Hegner, and P Mato. PODIO: An Event-Data-Model Toolkit for High Energy Physics Experiments. *J. Phys. : Conf. Ser.*, 898(10.1088/1742-6596/898/7/072039. 7): 072039. 6 p, 2017. URL https://cds.cern.ch/record/2296801.

[97] R. Brun and F. Rademakers. ROOT: An object oriented data analysis framework. *Nucl. Instrum. Meth.*, A389:81–86, 1997. doi: 10.1016/S0168-9002(97)00048-X.

[98] Torbjörn Sjöstrand, Stephen Mrenna, and Peter Skands. A Brief Introduction to PYTHIA 8.1. *Comput. Phys. Commun.*, 178(arXiv:0710.3820. CERN-LCGAPP-2007-04. LU TP 07-28. FERMILAB-PUB-07-512-CD-T):852–867. 27 p, Oct 2007. URL https://cds.cern.ch/record/1064095.

[99] Peter Skands, Stefano Carrazza, and Juan Rojo. Tuning PYTHIA 8.1: the Monash 2013 Tune. *Eur. Phys. J. C*, 74(arXiv:1404.5630. CERN-PH-TH-2014-069. MCNET-14-08. OUTP-14-05P. 8):3024. 57 p, Apr 2014. URL https://cds.cern.ch/record/1695787. Comments: 57 pages.

[100] Daniel Funke, Thomas Hauth, V Innocente, G Quast, P Sanders, and D Schieferdecker. Parallel track reconstruction in CMS using the cellular automaton approach. *J. Phys.: Conf. Ser.*, 513:052010. 7 p, 2014. URL https://cds.cern.ch/record/2026343.

[101] Elmar Ritsch, Emmerich Kneringer, Daniel Froidevaux, and Andreas Salzburger. ATLAS Detector Simulation in the Integrated Simulation Framework applied to the W Boson Mass Measurement, Dec 2014. URL https://cds.cern.ch/record/2221649. Presented 27 Feb 2015.

[102] GEANT4 Collaboration. GEANT4: A Simulation toolkit. *Nucl. Instrum. Methods Phys. Res., A*, 506(CERN-IT-2002-003. SLAC-PUB-9350. 3):250–303. 86 p, Jul 2002. URL https://cds.cern.ch/record/602040.

[103] A Zaborowska. Geant4 fast and full simulation for Future Circular Collider studies. *J. Phys. : Conf. Ser.*, 898(4):042053. 8 p, 2017. URL https://cds.cern.ch/record/2298621.

[104] M Frank, F Gaede, and P Mato. DD4hep: A Detector Description Toolkit for High Energy Physics Experiments. *J. Phys.: Conf. Ser.*, 513(AIDA-CONF-2014-004):022010, Oct 2013. URL https://cds.cern.ch/record/1670270.

[105] The AIDA-2020 Collaboration. AIDA-2020: 2nd periodic report. Technical Report AIDA-2020-NOTE-2018-002, CERN, Geneva, Jun 2018. URL https://cds.cern.ch/record/2628353.

[106] R Brun, A Gheata, and M Gheata. The root geometry package. *Nuclear Instruments and Methods in Physics Research Section A: Accelerators, Spectrometers, Detectors and Associated Equipment*, 502(2):676 – 680, 2003. ISSN 0168-9002. doi: https://doi.org/10.1016/S0168-9002(03)00541-2. URL http://www.sciencedirect.com/science/article/pii/S0168900203005412. Proceedings of the VIII International Workshop on Advanced Computing and Analysis Techniques in Physics Research.

[107] Andreas Salzburger, Dietmar Kuhn, and Markus Elsing. Track Simulation and Reconstruction in the ATLAS experiment, 2008. URL https://cds.cern.ch/record/2224514.

[108] John Backus. The History of FORTRAN I, II and III. Technical report, IBM Corporation, Research Division, November 2014. URL http://www.softwarepreservation.org/projects/FORTRAN/paper/p25-backus.pdf.

[109] Andreas Salzburger. Optimisation of the ATLAS Track Reconstruction Software for Run-2. *Journal of Physics: Conference Series*, 664(7):072042, 2015. URL http://stacks.iop.org/1742-6596/664/i=7/a=072042.

[110] M. Aaboud et al. Performance of the ATLAS Track Reconstruction Algorithms in Dense Environments in LHC Run 2. *Eur. Phys. J.*, C77(10):673, 2017. doi: 10.1140/epjc/s10052-017-5225-7.

[111] ATLAS Collaboration. Reconstruction of primary vertices at the ATLAS experiment in Run 1 proton–proton collisions at the LHC. Reconstruction of primary vertices at the ATLAS experiment in Run 1 proton-proton collisions at the LHC. *Eur. Phys. J. C*, 77(CERN-EP-2016-150. CERN-EP-2016-150. 5):332. 52 p, Nov 2016. URL https://cds.cern.ch/record/2235651. 52 pages in total, author list starting at page 36, 17 figures, 4 tables, final version published in EPJC. All figures including auxillary figures are available at http://atlas.web.cern.ch/Atlas/GROUPS/PHYSICS/PAPERS/PERF-2015-01.

[112] Georges Aad et al. Muon reconstruction performance of the ATLAS detector in proton–proton collision data at $\sqrt{s}$ =13 TeV. *Eur. Phys. J.*, C76(5):292, 2016. doi: 10.1140/epjc/s10052-016-4120-y.

[113] E Lund, L Bugge, E W Hughes, D Lopez Mateos, A Salzburger, and A Strandlie. Treatment of energy loss and multiple scattering in the context of track parameter and covariance matrix propagation in continuous material in the ATLAS experiment. Technical Report ATL-SOFT-PUB-2008-003. ATL-COM-SOFT-2008-008, CERN, Geneva, Jul 2008. URL https://cds.cern.ch/record/1114577.

[114] Christian Gumpert, Andreas Salzburger, Moritz Kiehn, Julia Hrdinka, and Noemi Calace. ACTS: from ATLAS software towards a common track reconstruction software. Technical Report ATL-SOFT-PROC-2017-030. 4, CERN, Geneva, Jan 2017. URL https://cds.cern.ch/record/2243297.

[115] The Acts website, 2019. URL http://acts.web.cern.ch/ACTS/.

[116] The eigen math library, 2019. URL http://eigen.tuxfamily.org.

[117] The boost library, 2019. URL https://www.boost.org.

[118] Intel VTune Amplifier, 2019. URL https://software.intel.com/en-us/vtune.

[119] Laura Barranco Navarro. Alignment of the ATLAS Inner Detector in the LHC Run II. Technical Report ATL-PHYS-PROC-2015-190, CERN, Geneva, Dec 2015. URL http://cds.cern.ch/record/2114708.

[120] CMS Tracker Alignment Performance Results 2018. Nov 2018. URL https://cds.cern.ch/record/2650977.

[121] Root TGeoNode, 2019. URL https://root.cern.ch/doc/master/classTGeoNode.html.

[122] FileFormat.Info: Wavefront OBJ File Format Summary, 2019. URL https://www.fileformat.info/format/wavefrontobj/egff.html.

[123] A Salzburger, S Todorova, and M Wolter. The ATLAS Tracking Geometry Description. Technical Report ATL-SOFT-PUB-2007-004. ATL-COM-SOFT-2007-009, CERN, Geneva, Jun 2007. URL https://cds.cern.ch/record/1038098.

[124] M. Tanabashi et al. (Particle Data Group). Passage of Particles Through Matter. *Phys. Rev. D 98*, (030001 (2018)), . Revised August 2015 by H. Bichsel (University of Washington), D.E. Groom (LBNL) and S.R. Klein (LBNL).

[125] ATLAS Insertable B-Layer Technical Design Report Addendum. Technical Report CERN-LHCC-2012-009. ATLAS-TDR-19-ADD-1, May 2012. URL https://cds.cern.ch/record/1451888. Addendum to CERN-LHCC-2010-013, ATLAS-TDR-019.

[126] H H J ten Kate. ATLAS superconducting toroids and solenoid. *IEEE Trans. Appl. Supercond.*, 15(2 pt.2):1267–1270. 4 p, 2005. URL http://cds.cern.ch/record/912244.

[127] K Edmonds, S Fleischmann, T Lenz, C Magass, J Mechnich, and A Salzburger. The Fast ATLAS Track Simulation (FATRAS). Technical Report ATL-SOFT-PUB-2008-001. ATL-COM-SOFT-2008-002, CERN, Geneva, Mar 2008. URL http://cds.cern.ch/record/1091969.

[128] Performance of the Fast ATLAS Tracking Simulation (FATRAS) and the ATLAS Fast Calorimeter Simulation (FastCaloSim) with single particles. Technical Report ATL-SOFT-PUB-2014-001, CERN, Geneva, Mar 2014. URL https://cds.cern.ch/record/1669341.

[129] The Acts FATRAS package, 2019. URL https://gitlab.cern.ch/acts/acts-fatras.

[130] C++ STL UniformRandomBitGenerators concept, 2019. URL https://en.cppreference.com/w/cpp/numeric/random/UniformRandomBitGenerators.

[131] K S Kölbig. Landau Distribution. Aug 1985. URL https://cds.cern.ch/record/2050932. CERN Program Library Short Writeups.

[132] The unordered map implementation of the C++ standard library, 2019. URL https://en.cppreference.com/w/cpp/container/unordered$_$map.

[133] M. Tanabashi et al. (Particle Data Group). Quantum Chromodynamics. *Phys. Rev. D 98*, (030001 (2018)), . Revised September 2017 by S. Bethke (Max-Planck-Institute of Physics, Munich), G. Dissertori (ETH Zurich), and G.P. Salam (CERN).

[134] Rick Field. Min-Bias and the Underlying Event at the LHC. *Acta Phys. Pol. B*, 42 (arXiv:1110.5530):2631–2656, Oct 2011. URL https://cds.cern.ch/record/1393621. Comments: Lectures presented at the 51st Cracow School of Theoretical Physics: 'The Soft Side of the LHC'.

[135] Ringaile Placakyte. Parton distribution functions, 2011.

[136] Valentina Maria Cairo. Latest Minimum Bias and Underlying Event measurements with the ATLAS Detector. Technical Report ATL-PHYS-PROC-2018-058, CERN, Geneva, Jun 2018. URL http://cds.cern.ch/record/2627860.

[137] CMS collaboration. Measurement of charged particle spectra in minimum-bias events from proton-proton collisions at $\sqrt{s} = 13$ TeV. *Eur. Phys. J. C*, 78(arXiv:1806.11245. CMS-FSQ-16-011-003. 9):697. 39 p, Jun 2018. URL https://cds.cern.ch/record/2627556. Replaced with the published version. Added the journal reference and the DOI. All the figures and tables can be found at http://cms-results.web.cern.ch/cms-results/public-results/publications/FSQ-16-011 (CMS Public Pages).

[138] F Pisano and N O Reis. Natural units, numbers and numerical clusters. Technical Report hep-ph/0112097, Dec 2001. URL http://cds.cern.ch/record/529676.

[139] ATLAS Collaboration. Technical Design Report for the ATLAS Inner Tracker Pixel Detector. Technical Report CERN-LHCC-2017-021. ATLAS-TDR-030, CERN, Geneva, Sep 2017. URL https://cds.cern.ch/record/2285585.

[140] Sven Wonsak. High fluence effects on silicon detectors: An overview of the state of the art of radiation resistant detector characterisation by the CERN RD50 collaboration. High fluence effects on silicon detectors: damage and defects characterization: An overview of the state of the art of radiation resistance detectors. *PoS*, Vertex2016:032. 10 p, 2017. URL https://cds.cern.ch/record/2634249.

[141] G Kramberger, V Cindro, I Mandić, M Mikuž, and M Zavrtanik. Charge collection studies on custom silicon detectors irradiated up to 1.6×10^{17}n eq /cm^2 . *Journal of Instrumentation*, 8(08):P08004, 2013. URL http://stacks.iop.org/1748-0221/8/i=08/a=P08004.

[142] L. Pacher, E Monteil, A Paternò, S Panati, L Demaria, A Rivetti, M Da Rocha Rolo, G Dellacasa, G Mazza, F Rotondo, R Wheadon, F Loddo, F Licciulli, F Ciciriello, C Marzocca, L Gaioni, G Traversi, V Re, F De Canio, L Ratti, S Marconi, P Placidi, G Magazzù, A Stabile, and S Mattiazzo. A Prototype of a New Generation Readout ASIC in 65 nm CMOS for Pixel Detectors at HL-LHC. Sep 2016. URL https://cds.cern.ch/record/2623575.

[143] M. Tanabashi et al. (Particle Data Group). Quark Model. *Phys. Rev. D 98*, (030001 (2018)), . Revised August 2017 by C. Amsler (Stefan Meyer Institute for Subatomic Physics,

Vienna), T. DeGrand (University of Colorado, Boulder), and B. Krusche (University of Basel).

[144] Kazuhiko Nishijima Masud Chaichian. An Essay on Color Confinement. 1999.

[145] Bryan R Webber. Hadronization. (hep-ph/9411384. CAVENDISH-HEP-94-17), 1994. URL https://cds.cern.ch/record/272660.

[146] Jonathan M Butterworth, Guenther Dissertori, and Gavin P Salam. Hard Processes in Proton-Proton Collisions at the Large Hadron Collider. *Annu. Rev. Nucl. Part. Sci.*, 62 (arXiv:1202.0583):387–405. 24 p, Feb 2012. URL http://cds.cern.ch/record/1421725. Comments: 24 pages, 10 figures. Invited contribution to the Annual Review of Nuclear and Particle Science.

[147] M. Tanabashi et al. (Particle Data Group). Quarks. *Phys. Rev. D 98*, (030001 (2018)), .

[148] M. Tanabashi et al. (Particle Data Group). Production and Decay of b-flavored Hadrons. *Phys. Rev. D 98*, (030001 (2018)), . Updated September 2017 by P. Eerola (U. of Helsinki, Helsinki, Finland), M. Kreps (U. of Warwick, Coventry, UK), and Y. Kwon (Yonsei U., Seoul, Korea).

[149] V. Faraoni. Special Relativity. *Springer International Publishing Switzerland 2013*, 2013. doi: DOI:10.1007/978-3-319-01107-3_2. Undergraduate Lecture Notes in Physics, Chapter 2.

[150] Luca Scodellaro. b tagging in ATLAS and CMS. Technical Report CMS-CR-2017-225, Sep 2017. URL https://cds.cern.ch/record/2282521. 6 pages, Proceeding for the Fifth Annual Large Hadron Collider Physics (LHCP2017) conference.

[151] Estel Perez Codina and Philipp Gerhard Roloff. Hit multiplicity approach to b-tagging in FCC-hh. Technical Report CERN-ACC-2018-0023, CERN, Geneva, Jul 2018. URL https://cds.cern.ch/record/2631478.

[152] CMS Collaboration. Observation of Higgs boson decay to bottom quarks. 2018. doi: 10.1103/PhysRevLett.121.121801.

[153] Luca Lista. Top quark measurements in the CMS experiment. 2017. doi: 10.1051/epjconf/201818202074.

[154] Richard Nisius. Measurements of the top quark mass with the ATLAS detector, 2017.

[155] ATLAS Collaboration. Combination of searches for heavy resonances decaying into bosonic and leptonic final states using 36 fb^{-1} of proton-proton collision data at $\sqrt{s} = 13$ TeV with the ATLAS detector. 2018. doi: 10.1103/PhysRevD.98.052008.

[156] CMS Collaboration. Search for heavy resonances decaying into two Higgs bosons or into a Higgs boson and a W or Z boson in proton-proton collisions at 13 TeV, 2018.

[157] Rachel Emma Clarke Smith. Exploring the $Z' \to t\bar{t}$ heavy resonance at FCC-hh. FCC-hh = Future Circular Collider (hadron hadron). Aug 2017. URL https://cds.cern.ch/record/2278304.

[158] J. Katharina Behr, Daniela Bortoletto, James A. Frost, Nathan P. Hartland, Cigdem Issever, and Juan Rojo. Boosting Higgs pair production in the $b\bar{b}b\bar{b}$ final state with multivariate techniques. 2015. doi: 10.1140/epjc/s10052-016-4215-5.

[159] Sebastian Sapeta. QCD and Jets at Hadron Colliders. 2015. doi: 10.1016/j.ppnp.2016.02.002. chapter 2.

[160] Matteo Cacciari, Gavin P. Salam, and Gregory Soyez. FastJet user manual. 2011. doi: 10.1140/epjc/s10052-012-1896-2.

[161] ATLAS Collaboration. Jet reconstruction and performance using particle flow with the ATLAS Detector. 2017. doi: 10.1140/epjc/s10052-017-5031-2.

[162] Particle-Flow Event Reconstruction in CMS and Performance for Jets, Taus, and MET. Technical Report CMS-PAS-PFT-09-001, CERN, Geneva, Apr 2009. URL `https://cds.cern.ch/record/1194487`.

[163] FCC-hh simulation package. URL `https://github.com/FCC-hh-framework/FCCSimJobs`.

[164] J. Alwall, A. Ballestrero, P. Bartalini, S. Belov, E. Boos, A. Buckley, J. M. Butterworth, L. Dudko, S. Frixione, L. Garren, S. Gieseke, A. Gusev, I. Hinchliffe, J. Huston, B. Kersevan, F. Krauss, N. Lavesson, L. Lönnblad, E. Maina, F. Maltoni, M. L. Mangano, F. Moortgat, S. Mrenna, C. G. Papadopoulos, R. Pittau, P. Richardson, M. H. Seymour, A. Sherstnev, T. Sjöstrand, P. Skands, S. R. Slabospitsky, Z. Wcas, B. R. Webber, M. Worek, and D. Zeppenfeld. A standard format for Les Houches Event Files. 2006. doi: 10.1016/j.cpc.2006.11.010.

[165] Estel Perez Codina and Philipp Gerhard Roloff. Tracking and Flavour Tagging at FCC-hh. Technical Report CERN-ACC-2018-0027, CERN, Geneva, Aug 2018. URL `https://cds.cern.ch/record/2635893`.

[166] ATLAS collaboration. A neural network clustering algorithm for the ATLAS silicon pixel detector. 2014. doi: 10.1088/1748-0221/9/09/P09009.

[167] ATLAS Collaboration. Technical Design Report for the ATLAS Inner Tracker Strip Detector. Technical Report CERN-LHCC-2017-005. ATLAS-TDR-025, CERN, Geneva, Apr 2017. URL `https://cds.cern.ch/record/2257755`.

[168] Felix Cormier. Tracking in Dense Environments for the HL-LHC ATLAS Detector. Mar 2018. URL `http://cds.cern.ch/record/2310670`.

[169] ISBN 978-0-521-76368-4. *PARTICLE DARK MATTER: Observations, Models and Searches.* Cambridge University Press. Frontmatter.

[170] Y. Akrami et al. Planck 2018 results. I. Overview and the cosmological legacy of Planck. 2018.

[171] Virginia Trimble. Existence and Nature of Dark Matter in the Universe. *Ann. Rev. Astron. Astrophys.*, 25:425–472, 1987. doi: 10.1146/annurev.aa.25.090187.002233.

[172] W. K. Jr.; Thonnard N. Rubin, V. C.; Ford. Rotational properties of 21 SC galaxies with a large range of luminosities and radii, from NGC 4605 /R = 4kpc/ to UGC 2885 /R = 122 kpc/. *Astrophysical Journal, Part 1*, 238:471–487, 1980. doi: 10.1086/158003.

[173] Adel Bilal. Introduction to supersymmetry. *arXiv*, hep-th/0101055:NEIP–01–001, 2001.

[174] Gerard Jungman, Marc Kamionkowski, and Kim Griest. Supersymmetric dark matter. *Phys. Rept.*, 267:195–373, 1996. doi: 10.1016/0370-1573(95)00058-5.

[175] Lisa Randall and Raman Sundrum. Out of this world supersymmetry breaking. *Nucl. Phys.*, B557:79–118, 1999. doi: 10.1016/S0550-3213(99)00359-4.

[176] Gian F. Giudice, Markus A. Luty, Hitoshi Murayama, and Riccardo Rattazzi. Gaugino mass without singlets. *JHEP*, 12:027, 1998. doi: 10.1088/1126-6708/1998/12/027.

[177] R. Martinez Rodolfo A. Diaz. The custodial symmetry. *arXiv*, hep-th/0302058, 2003.

[178] Masahiro Ibe, Shigeki Matsumoto, and Ryosuke Sato. Mass Splitting between Charged and Neutral Winos at Two-Loop Level. *Phys. Lett.*, B721:252–260, 2013. doi: 10.1016/j.physletb.2013.03.015.

[179] Scott D. Thomas and James D. Wells. Phenomenology of Massive Vectorlike Doublet Leptons. *Phys. Rev. Lett.*, 81:34–37, 1998. doi: 10.1103/PhysRevLett.81.34.

[180] Marco Cirelli, Alessandro Strumia, and Matteo Tamburini. Cosmology and Astrophysics of Minimal Dark Matter. Technical Report arXiv:0706.4071. IFUP-TH-2007-12 AND SACLAY-T07-052, Jun 2007. URL `http://cds.cern.ch/record/1043625`. Comments: 24 pages, 10 figures.

[181] Morad Aaboud et al. Search for long-lived charginos based on a disappearing-track signature in pp collisions at $\sqrt{s} = 13$ TeV with the ATLAS detector. *JHEP*, 06:022, 2018. doi: 10.1007/JHEP06(2018)022.

[182] M. Tanabashi et al. (Particle Data Group). Structure Functions. *Phys. Rev. D 98*, (030001 (2018)), . Updated February 2018 by B. Foster (University of Hamburg/DESY/Oxford), R.S. Thorne (University College London) and M.G. Vincter (Carleton University)..

[183] M. Tanabashi et al. (Particle Data Group). Kinematics. *Phys. Rev. D 98*, (030001 (2018)), . Revised August 2017 by D.R. Tovey (Sheffield) and January 2000 by J.D. Jackson (LBNL).

[184] J Cranshaw, T Cuhadar-Donszelmann, E Gallas, J Hrivnac, M Kenyon, H McGlone, D Malon, M Mambelli, M Nowak, F Viegas, E Vinek, and Q Zhang. Event selection services in ATLAS. *Journal of Physics: Conference Series*, 219(4):042007, apr 2010. doi: 10.1088/1742-6596/219/4/042007.

[185] Mia Tosi. The CMS trigger in Run 2. Technical Report CMS-CR-2017-340, CERN, Geneva, Oct 2017. URL `https://cds.cern.ch/record/2290106`.

[186] David Krohn, Lisa Randall, and Lian-Tao Wang. On the Feasibility and Utility of ISR Tagging, 2011.

[187] Search for long-lived charginos based on a disappearing-track signature in pp collisions at $\sqrt{s} = 13$ TeV with the ATLAS detector. Technical Report ATLAS-CONF-2017-017, CERN, Geneva, Apr 2017. URL `https://cds.cern.ch/record/2258131`.

[188] Masahiko Saito, Ryu Sawada, Koji Terashi, and Shoji Asai. Discovery reach for wino and higgsino dark matter with a disappearing track signature at a 100 TeV pp collider, 2019.

[189] J. Alwall, R. Frederix, S. Frixione, V. Hirschi, F. Maltoni, O. Mattelaer, H. S. Shao, T. Stelzer, P. Torrielli, and M. Zaro. The automated computation of tree-level and next-to-leading order differential cross sections, and their matching to parton shower simulations. 2014. doi: 10.1007/JHEP07(2014)079.

[190] M. Tanabashi et al. (Particle Data Group). Gauge and Higgs bosons. *Phys. Rev. D 98*, (030001 (2018)), .

[191] M. Tanabashi et al. (Particle Data Group). Top Quark. *Phys. Rev. D 98*, (030001 (2018)), . Updated September 2017 by T.M. Liss (The City College of New York), F. Maltoni (Univ. Catholique de Louvain), and A. Quadt (Univ. Göttingen).

[192] C. Helsens. FCCSW DELPHES simulation samples, 2019. URL `http://fcc-physics-events.web.cern.ch/fcc-physics-events/Delphesevents$_$fcc$_$v02.php`.

[193] Madgraph gridpacks, 2019.

[194] Glen Cowan, Kyle Cranmer, Eilam Gross, and Ofer Vitells. Asymptotic formulae for likelihood-based tests of new physics. 2010. doi: 10.1140/epjc/s10052-011-1554-0.

[195] ATLAS sensitivity to winos and higgsinos with a highly compressed mass spectrum at the HL-LHC. Technical Report ATL-PHYS-PUB-2018-031, CERN, Geneva, Nov 2018. URL `https://cds.cern.ch/record/2647294`.

[196] Performance of tracking and vertexing techniques for a disappearing track plus soft track signature with the ATLAS detector. Technical Report ATL-PHYS-PUB-2019-011, CERN, Geneva, Mar 2019. URL `https://cds.cern.ch/record/2669015`.

[197] Performance of vertex reconstruction algorithms for detection of new long-lived particle decays within the ATLAS inner detector. Technical Report ATL-PHYS-PUB-2019-013, CERN, Geneva, Mar 2019. URL `https://cds.cern.ch/record/2669425`.

[198] Json (javascript object notation) file format, 2019. URL `https://json.org/`.

[199] Lucie Linssen, Akiya Miyamoto, Marcel Stanitzki, and Harry Weerts. *Physics and Detectors at CLIC: CLIC Conceptual Design Report*. CERN Yellow Reports: Monographs. CERN, Geneva, 2012. doi: 10.5170/CERN-2012-003. URL `https://cds.cern.ch/record/1425915`. Comments: 257 p, published as CERN Yellow Report CERN-2012-003.

[200] CLIC, 2019. URL `https://clic.cern/`.

[201] Vladimir Prus. Chapter 21. Boost Program Options, 2002-2004. URL `https://www.boost.org/doc/libs/1$_$58$_$0/doc/html/program$_$options.html`.

[202] Geant4 webpage, 2019. URL `https://geant4.web.cern.ch/support`.

[203] R. Chytracek, J. McCormick, W. Pokorski, and G. Santin. Geometry description markup language for physics simulation and analysis applications. *IEEE Trans. Nucl. Sci.*, 53:2892, 2006. doi: 10.1109/TNS.2006.881062. URL `https://gdml.web.cern.ch/GDML/`.

[204] S Meroli, D Passeri, and L Servoli. Energy loss measurement for charged particles in very thin silicon layers. *Journal of Instrumentation*, 6(06):P06013–P06013, jun 2011. doi: 10.1088/1748-0221/6/06/p06013.

[205] Wolfgang Demtröder. *Experimentalphysik 2: Elektrizität und Optik*. ISBN 3-540-20210-2 3. Auflage. Springer-Verlag Berlin Heidelberg New York, 2004. chapter 1.

[206] Wolfgang Demtröder. *Experimentalphysik 4: Kern-, Teilchen- und Astrophysik*. ISBN3-540-21451-8 2.Auflage. Springer-Verlag Berlin Heidelberg New York, 2004. chapter 2.2.

[207] Hok-Chuen Cheng. Two-body decay kinematics. Technical report, University of Michigan, Ann Arbor, April 2015. URL https://indico.cern.ch/event/391122/contributions/928962/attachments/782786/1073126/twoBodyDecay.pdf.

[208] Bernard R. Durney. Lorentz Transformations, 2011.

[209] Rudolf Fruehwirth. *Wahrscheinlichkeitsrechnung und Statistik für Studierende der Physik*. Chapter 9.2.1. Institut für Hochenergiephysik der Österreichischen Akademie der Wissenschaften, Nikolsdorfer Gasse 18, 1050 Wien,Österreich, 2014. URL http://www.hephy.at/project/ilc/reports/ASEpub/14_eBook_by_RF.pdf.

[210] A Strandlie, J Wroldsen, R Frühwirth, and B Lillekjendlie. Particle tracks fitted on the Riemann sphere. *Comput. Phys. Commun.*, 131(1-2):95–108, 2000. URL https://cds.cern.ch/record/500989.

[211] GEANT4 Collaboration. GEANT4: Physics Reference Manual. Technical Report release 10.5, CERN, Geneva, Dec 2018. URL http://geant4-userdoc.web.cern.ch/geant4-userdoc/UsersGuides/PhysicsReferenceManual/fo/PhysicsReferenceManual.pdf.

[212] W. Beenakker, R. Hopker, and M. Spira. PROSPINO: A Program for the Production of Supersymmetric Particles in Next-to-leading Order QCD. Technical Report hep-ph/9611232, Nov 1996. URL http://cds.cern.ch/record/314229. 12 pages, latex, no figures, Complete postscript file and FORTRAN source codes available from http://wwwcn.cern.ch/ mspira/prospino/.

[213] M. Tanabashi et al. (Particle Data Group). Statistics. *Phys. Rev. D 98*, (030001 (2018)), . Revised September 2017 by G. Cowan (RHUL).